THE CENTIMETER- AND MILLIMETER-WAVELENGTH AMMONIA ABSORPTION SPECTRA UNDER JOVIAN CONDITIONS

A Dissertation
Presented to
The Academic Faculty

by

Kiruthika Devaraj

In Partial Fulfillment
of the Requirements for the Degree
Doctor of Philosophy in
Electrical and Computer Engineering

School of Electrical and Computer Engineering
Georgia Institute of Technology
December 2011

THE CENTIMETER- AND MILLIMETER-WAVELENGTH AMMONIA ABSORPTION SPECTRA UNDER JOVIAN CONDITIONS

Approved by:

Professor Paul G. Steffes, Advisor
School of Electrical and Computer Engineering
Georgia Institute of Technology

Professor Oliver Brand
School of Electrical and Computer Engineering
Georgia Institute of Technology

Professor Waymond R. Scott
School of Electrical and Computer Engineering
Georgia Institute of Technology

Professor Carol Paty
School of Earth and Atmospheric Science
Georgia Institute of Technology

Professor Gregory D. Durgin
School of Electrical and Computer Engineering
Georgia Institute of Technology

Date Approved: September 19, 2011

To my parents

ACKNOWLEDGEMENTS

I express my deepest gratitude to my advisor Professor Paul Steffes for his support and guidance throughout the course of this research. I am grateful for his tremendous encouragement and constant faith in my abilities as a researcher. I also thank my committee members, Professor Oliver Brand, Professor Gregory Durgin, Professor Carol Paty, and Professor Waymond Scott for spending the time and effort in reviewing this work.

I acknowledge the NASA Planetary Atmospheres Program and the NASA Juno Mission Team for their financial support of this work. This work was supported by NASA Contract NNM06AA75C from the Marshall Space Flight Center supporting the Juno Mission Science Team, under Subcontract 699054X from the Southwest Research Institute and by the NASA Planetary Atmospheres Program under Grants NNG06GF34G and NNX11AD66G.

I spent two summers at the National Radio Astronomy Observatory (NRAO) in Soccoro, NM as a graduate summer student and I thank NRAO for providing me with an opportunity to work on planetary radio astronomy. I thank Dr. Bryan Butler for his guidance on planetary radio observations, data reduction, and analysis. I wish to express my gratitude to Dr. Brigette Hesman for her guidance on radiative transfer models of planetary atmospheres and her constant support and encouragement ever since.

The success of the laboratory experiments was made possible as a result of many contributions over the years. I wish to thank Dr. Thomas Hanley for automating the microwave measurement subsystem and data processing and Dr. Bryan Karpowicz for building the high-pressure system, both of which were utilized in this research work.

I thank them and Danny Duong for their support and many conversations. Thanks to the all the staff in the school of ECE for keeping the department operational.

My graduate student experience would not have be complete had it not been for all the wonderful friends I made over the years I was at Georgia Tech. I thank Manali Tare for being my friend, and confidant, and for introducing me to masala chai, which I consumed religiously every morning for a good part of four years. I also thank my friends for making my stay at Georgia Tech nothing short of wonderful: Nandita Yeshala, Smita Vemulapalli, Vibhore Kumar, Sonali Tare, Karan Singhal, Nagesh and Deepthi Adiga, Swanand Gupte, Shreekrisha, Manoj Agarwal, Yogish Gopala, and Sai Kumar Thumuluru.

The constant support and encouragement from my family sustained me throughout these years. My parents Shanthamani Soundirarajan and Devaraj Ranganathan have always supported me and I cannot thank them enough for their unconditional love and unshakable belief in me. My brother Karthik Vignesh Devaraj, without whom growing up would have been boring, ensured my life was filled with fun and happiness, and the occasional squabbles. I spent a good part of my childhood with my grandparents and I cannot express my gratitude for their unconditional love. I thank my wonderful husband Lakshmi Narasimhan Chakrapani, without whom this dissertation would not have been possible. His passion for research and curiosity to understand the animate and the inanimate world continuously fueled and strengthened my research interests. I thank him for his support, love, and endless patience.

TABLE OF CONTENTS

LIST OF TABLES

LIST OF FIGURES

LIST OF SYMBOLS OR ABBREVIATIONS

α	Multiple uses: Absorption, reduced Helmholtz free energy.
AIPS	Astronomical Image Processing Software.
ALMA	Atacama Large Millimeter Array.
AMC	Active multiplier chain.
AU	Astronomical unit. 1 AU = 149597870.691 km.
arcsec	1 arcsecond is 1/3600 of a degree.
a	Helmholtz free energy.
A	Absorption at the line center.
A_s	Asymmetry of resonance.
β	Phase constant.
BW	Bandwidth.
B	Confidence coefficient of a two-tailed distribution.
CH_4	Methane.
CW	Continuous wave.
C band	Electromagnetic frequencies from 4 to 8 GHz.
c	Speed of light.
c_p	Heat capacity.
$\Delta\nu$	Linewidth (half width at half-maximum).
D	Multiple uses: Distance of separation between the mirrors in a Fabry–Perot resonator, scale factor in the Ben-Reuven lineshape.
dB	Decibel.
dBm	Decibel with respect to 1 mW.
DC	Direct current.
DW	Data weight.
$\mathcal{E}$	Electric field.

EMIR	Eight MIxer Receiver frontend on IRAM 30-m telescope.
EPL	Effective path length.
ESA	European Space Agency.
ε	Permittivity of the medium.
E	Energy.
ε'	Real part of permittivity of the medium.
ε''	Imaginary part of permittivity of the medium.
FPR	Fabry–Perot resonator.
FSR	Free spectral range.
FS	Full scale.
FWHM	Full width at half maximum.
F band	Electromagnetic frequencies from 90 to 140 GHz.
f	Frequency.
F	Lineshape function.
f_0	Resonant frequency.
GEISA	Gestion et Etude des Informations Spectroscopiques Atmosphériques: Management and Study of Spectroscopic Information.
GE	General Electric.
GPIB	General Purpose Interface Bus.
G band	Electromagnetic frequencies from 140 to 220 GHz.
$\mathcal{H}$	Magnetic field.
H_2	Hydrogen.
He	Helium.
h	Planck constant.
h^0	Ideal gas enthalpy.
h_t	Height of the cylindrical cavity resonator.
HP	Hewlett-Packard.

HPBW	Multiple uses: Half-power bandwidth, half-power beamwidth.
HWHM	Half width at half maximum.
IF	Intermediate frequency.
IRAM	Institut de Radioastronomie Millimétrique.
I	Line intensity.
JPL	Jet Propulsion Lab.
Jy	Jansky. Unit of spectral flux density. 1 Jy = 10^{-26} W/(m^2.Hz).
J	Total angular momentum vector.
K band	Electromagnetic frequencies from 18 to 26.5 GHz.
Ka band	Electromagnetic frequencies from 26.5 to 40 GHz.
Ku band	Electromagnetic frequencies from 12 to 18 GHz.
K	Projection of the angular momentum vector onto the molecular axis.
k	Wavenumber.
λ	Wavelength.
LNA	Low noise amplifier.
LO	Local oscillator.
LSD	Least significant digit.
L band	Electromagnetic frequencies from 1 to 2 GHz.
MWR	Microwave radiometer on board the Juno spacecraft.
mBWR	Modified Benedict-Webb-Rubin equation of state.
μ	Permeability of the medium.
M	Molecular weight.
NASA	National Aeronautics and Space Administration.
NH_3	Ammonia.
NIST	National Institute of Standards and Technology.
NPT	National pipe thread.

NRAO	National Radio Astronomy Observatory.
ν	Frequency (cm^{-1}).
ν_0	Center frequency of line transition.
ν_2	Higher energy state.
N	Refractivity.
n	Number density of a gas.
N_H	Harmonic number.
n_{ri}	Refractive index of a gas.
$N_{samples}$	Number of samples.
ω	Radial frequency.
P	Pressure.
Q band	Electromagnetic frequencies from 33 to 50 GHz.
Q	Quality factor.
RBW	Resolution bandwidth.
ρ	Density.
ϱ	Reduced density.
R	Specific gas constant.
R_0	Ideal or universal gas constant.
r_d	Radius of the cylindrical cavity resonator.
REFPROP	Reference fluid thermodynamic and transport properties database.
RF	Radio frequency.
RFI	Radio frequency interference.
RTD	Resistance temperature detector.
RTM	Radiative transfer model.
SCPI	Standard commands for programmable instruments.
SNR	Signal to noise ratio.
S-parameter	Elements of a scattering matrix.

SiO_2	Silicon dioxide.
σ	Multiple uses: Standard deviation, measurement uncertainty.
S	Insertion loss of resonator.
s^0	Ideal gas entropy.
S_N	Standard deviation of measurements.
TCM	Thermochemical model.
TEM	Transverse electromagnetic mode.
TE	Transverse electric mode.
TM	Transverse magnetic mode.
TP	Temperature-Pressure.
$\tan\delta$	Loss tangent.
τ	Reciprocal of the reduced temperature.
T	Temperature.
t	Transmissivity.
UHP	Ultra-high-purity.
USB	Universal serial bus.
UT	Universal time.
VLA	Very Large Array.
VSWR	Voltage standing wave ratio.
V	Volume.
W band	Electromagnetic frequencies from 75 to 110 GHz.
X band	Electromagnetic frequencies from 8 to 12 GHz.
ζ	Line-to-line coupling element in the Ben-Reuven lineshape.
Z	Compressibility.

SUMMARY

Accurate knowledge of the centimeter- and millimeter-wavelength absorptivity of ammonia is necessary for the interpretation of the emission spectra of the jovian planets. The objective of this research has been to advance the understanding of the centimeter- and millimeter-wavelength opacity spectra of ammonia under jovian conditions using a combination of laboratory measurements and theoretical formulations. As part of this research, over 1000 laboratory measurements of the 2–4 mm-wavelength properties of ammonia under simulated upper and middle tropospheric conditions of the jovian planets, and approximately 1200 laboratory measurements of the 5–20 cm-wavelength properties of ammonia under simulated deep tropospheric conditions of the jovian planets have been conducted. Using these and pre-existing measurements, a consistent mathematical formalism has been developed to reconcile the centimeter- and millimeter-wavelength opacity spectra of ammonia. This formalism can be used to estimate the opacity of ammonia in a hydrogen/helium atmosphere in the centimeter-wavelength range at pressures up to 100 bar and temperatures in the 200 to 500 K range and in the millimeter-wavelength range at pressures up to 3 bar and temperatures in the 200 to 300 K range. In addition, a preliminary investigation of the influence of water vapor on the centimeter-wavelength ammonia absorptivity spectra has been conducted.

This work addresses the areas of high-sensitivity centimeter- and millimeter-wavelength laboratory measurements, and planetary science, and contributes to the body of knowledge that provides clues into the origin of our solar system. The laboratory measurements and the model developed as part of this doctoral research work can be used for interpreting the emission spectra of jovian atmospheres obtained from

ground-based and spacecraft-based observations. The results of the high-pressure ammonia opacity measurements will also be used to support the interpretation of the microwave radiometer (MWR) measurements on board the NASA Juno spacecraft at Jupiter.

CHAPTER I

INTRODUCTION

If we could understand how the jovian system formed and evolved, we could unlock vital clues to the beginning and ultimate fate of the entire solar system.
— Morrison and Samz, Voyage to Jupiter, 1980

The jovian planets (Jupiter, Saturn, Uranus, and Neptune) are the most massive planetary bodies in the solar system, and together they comprise 99.56% of the planetary mass of the solar system. Because of strong gravity fields and relatively low temperatures, the jovian planets, unlike the terrestial planets, have retained a large portion of the composition of the primordial cloud from which our solar system was formed. Hence, understanding their molecular composition and distribution could reveal much information about the formation of our solar system and provide vital clues to the formation of similar planetary systems.

For more than half a century, Jupiter has been one of the most extensively studied astronomical radio and microwave sources because of the fascinating diversity of its emission characteristics. The discovery of radio emission from Jupiter was made serendipitously at a frequency of 22.2 MHz by Burke and Franklin (1955). This complex high-intensity emission was non-thermal in nature and was later found to be synchrotron radiation originating from the relativistic electrons accelerating through the planet's magnetosphere. The microwave radiation from Jupiter is dominated by thermal emission from its atmosphere at frequencies above 3 GHz and synchrotron emission at frequencies below 3 GHz. The ammonia resonant structure at microwave frequencies in Jupiter's atmosphere was first measured by Law and Staelin (1968).

Since then, numerous other ground-based and spacecraft-based observations have been made through the microwave region. Jupiter is also the only giant planet from which *in situ* measurements of the atmospheric composition have been made (by the *Galileo* entry probe; Niemann et al., 1996). Saturn was first detected at the radio-wavelengths by Smith and Douglas (1957). Lindal et al. (1985) interpreted Voyager radio occultation measurements at Saturn and attributed the absorption encountered at 2.3 GHz and 8.4 GHz to ammonia. To comprehensively study Saturn, the Cassini mission was conceptualized in the 1980s and launched in 1997. One of the objectives of the Cassini mission is to study the atmospheric structure of Saturn using radio occultation experiments conducted at 2.3 GHz, 8.4 GHz, and 32 GHz. Uranus and Neptune, being the outermost planets in our solar system were the last to be scrutinized closely. Voyager 2 made its closest approach to Uranus on January 24, 1986 and Neptune on August 25, 1987, providing a wealth of information on the ice giants.

To interpret the observed emission spectra of the jovian atmospheres, the emission spectra are compared with appropriate jovian atmospheric models, and the atmospheric composition and distribution of various constituents are obtained. The observable atmospheres of the jovian planets are dominated by hydrogen and helium with small amounts of methane, water vapor, ammonia, hydrogen sulfide, and other gases. A lack of laboratory measurements of the centimeter- and millimeter-wavelength (microwave region) properties of various gases has been cited as a major hindrance for modeling the atmospheres of the jovian planets (de Pater and Mitchell, 1993; de Pater et al., 2005).

The objective of this work has been to improve our understanding of the centimeter- and millimeter-wavelength absorption spectra of ammonia under jovian conditions using a combination of laboratory measurements and theoretical formulations (absorption formalism). The ammonia absorption formalism has been incorporated into a radiative transfer model of the atmosphere of Jupiter to predict the emission from

the planet in the millimeter-wavelength region. Finally, observations of Jupiter have been made with the Institut de Radioastronomie Millimétrique (IRAM) telescope facility to search for the 140 GHz ν_2 inversion transition of ammonia.

1.1 Motivation

The motivation for this doctoral research work has been to improve our understanding of the absorption spectra of ammonia in the centimeter- and millimeter-wavelength region under jovian conditions. An aggressive campaign of laboratory measurements of the centimeter-wavelength opacity of ammonia in a hydrogen/helium atmosphere under deep jovian conditions and the millimeter-wavelength opacity of ammonia under upper tropospheric jovian conditions has been undertaken. Using these and pre-existing laboratory measurements, a consistent ammonia opacity formalism that can be used in the 1 mm–30 cm wavelength range in a hydrogen/helium environment under jovian conditions has been developed. Additionally, laboratory measurements and modeling of ammonia broadened by water vapor under jovian conditions have been conducted for the first time to study the influence of water vapor on the ammonia absorption spectra. Finally, the ammonia opacity model has been used to interpret the emission spectra of Jupiter at 140 GHz.

Why conduct laboratory measurements?

Absorptivity data for planetary atmospheres obtained from ground-based and spacecraft-based observations can be used to infer abundances of centimeter- and millimeter-wavelength absorbing constituents in those atmospheres, as long as reliable information regarding the absorbing properties of potential constituents is available. Theoretical calculations of the absorption spectrum of gaseous molecules can be made from classical theories using resonant line strengths and frequencies that exist in spectral line catalogs such as the JPL catalog (Pickett et al., 1998) and the GEISA catalog (Jacquinet-Husson et al., 2011). However, these theoretical calculations of

opacity are limited by the knowledge of the lineshapes and the broadening parameters of various molecules with the appropriate broadening agents under the temperature and pressure conditions found in planetary atmospheres. For example, the centimeter-wavelength laboratory measurements of the opacity of phosphine under simulated jovian conditions reported by Hoffman et al. (2001) showed that the opacity of gaseous phosphine is an order of magnitude higher than theory had predicted. Even under terrestrial conditions, it has been known since the measurements near atmospheric pressure by Becker and Autler (1946) that absorption of microwaves by water vapor cannot be accounted for by standard lineshape theory. Models for atmospheric water vapor absorption therefore include an empirical "continuum" component (Rosenkranz, 1998). Hence, there is a need to conduct laboratory measurements of the properties of gases under simulated planetary atmospheric conditions over a range of temperatures and pressures that correspond to the altitudes probed by astronomical observations, and over a range of frequencies that correspond to those used in astronomical observations. These measurements can be used in the empirical determination of the broadening parameters, temperature coefficients, and lineshapes of various gases under simulated planetary conditions. These laboratory measurements can also form the basis for developing accurate mathematical formalisms to model the centimeter- and millimeter-wavelength properties of gases under those planetary conditions.

Why use centimeter and millimeter waves?

Centimeter- and millimeter-wavelength astronomy are powerful tools for studying the jovian atmospheres. Centimeter waves probe the middle and deep atmospheres of jovian planets (pressures up to hundreds of bar), and hence help infer the interior composition and dynamics of the planetary atmospheres. Millimeter waves probe the upper and middle tropospheres of jovian planets (pressures less than a few bar)

providing unique insights into the atmospheric composition, chemistry, and dynamics of those layers in the planetary atmospheres. Furthermore, the millimeter-wavelength range is often more sensitive than any other spectral range for the detection of minor species (trace gases).

Why study ammonia?

Gaseous ammonia contributes to strong absorption in the jovian planets in the centimeter- and millimeter-wavelength range because of the presence of a series of strong inversion transitions around 1.25 cm, several strong rotational transitions in the sub-millimeter region, and a strong ν_2 inversion transition at 2.15 mm. Hence, knowledge of the opacity of gaseous ammonia directly impacts the accuracy of interpretation of the observed emission spectra of the jovian atmospheres. Furthermore, since ammonia is one of the predominant absorbers in the jovian planets, its opacity must be known before the potential effects of other absorbing constituents can be assessed. There has been tremendous interest in understanding the absorption properties of ammonia in the centimeter-wavelength region since they were first measured in the laboratory by Cleeton and Williams (1934) (see, e.g., Hanley et al., 2009). Recently, Hanley et al. (2009) made close to 2000 high-accuracy measurements of the centimeter-wavelength properties of ammonia under simulated jovian atmospheric conditions (pressures up to 12 bar and temperatures up to 450 K) and developed a model to estimate the opacity of ammonia in the centimeter-wavelength range. The millimeter-wavelength absorptivity of pure ammonia was first investigated more than 50 years ago by Nethercot et al. (1952) who measured the absorption of one atmosphere of pure ammonia up to 260 GHz. A few 3.2 mm-wavelength measurements of ammonia gas properties under simulated jovian conditions were made by Joiner

and Steffes (1991) and Mohammed and Steffes (2004). However, these millimeter-wavelength measurements had large uncertainties because of the coarse instrumentation used at that time and also did not account properly for the adsorption of ammonia on the surface of the resonator and pressure vessel.

Several ammonia opacity models are currently used to estimate the centimeter- and/or millimeter-wavelength opacity of gaseous ammonia under jovian conditions (Berge and Gulkis, 1976; Spilker, 1990; Joiner and Steffes, 1991; Mohammed and Steffes, 2003, 2004; Hanley et al., 2009). The models that were derived based on centimeter-wavelength measurements (Berge and Gulkis, 1976; Spilker, 1990; Hanley et al., 2009) cannot be used to accurately estimate the absorptivity in the millimeter-wavelength range because they do not account for the presence of all the absorption lines in the millimeter and sub-millimeter region. The models that were derived based on a limited number of millimeter-wavelength measurements (Joiner and Steffes, 1991; Mohammed and Steffes, 2003, 2004) do not accurately represent the absorptivity of ammonia over the entire millimeter-wavelength region because of the limited wavelength ranges measured and the large uncertainties associated with those measurements. Furthermore, none of the models account for the non-ideal nature of gases under high pressures, and hence cannot be used to study the deep interiors of the jovian planets. There were also difficulties in reconciling the centimeter- and millimeter-wavelength opacity of ammonia (see, e.g., Mohammed and Steffes, 2004). Hence, there has been a strong impetus to conduct a large number of highly accurate measurements of the centimeter-wavelength properties of ammonia under simulated deep jovian conditions and the millimeter-wavelength properties of ammonia under simulated upper tropospheric jovian conditions, and to develop a model to estimate the opacity of ammonia in a hydrogen/helium atmosphere over a wide range of pressures, temperatures, and mixing ratios, that is consistent in both the centimeter- and millimeter-wavelength range.

1.2 Science Objectives and Applications

The scientific objective of this research has been to advance the understanding of the centimeter- and millimeter-wavelength absorption spectra of gaseous ammonia under jovian conditions. Specifically, the research focused on conducting highly accurate laboratory measurements of the 2–4 mm-wavelength opacity of ammonia under simulated jovian conditions at pressures up to three bar and temperatures between 200 and 300 K, and the 5–20 cm-wavelength opacity of ammonia under simulated deep jovian conditions at pressures up to 100 bar and temperatures up to 500 K. These new measurements and close to 1500 centimeter-wavelength measurements of the opacity of ammonia conducted by Hanley et al. (2009) were used to develop a consistent ammonia opacity model to provide accurate interpretation of ground-based and spacecraft-based observations of jovian planetary atmospheres in the 1 mm–30 cm wavelength range. The results of the high-pressure centimeter-wavelength measurements will also be used to support the interpretation of the microwave radiometer (MWR) measurements on board the NASA New Frontiers Juno spacecraft that is scheduled to arrive at Jupiter in 2016.

Millimeter-wavelength applications

Millimeter-wavelength astronomy is a powerful tool for studying the temperature structure, composition, and dynamics of jovian planetary atmospheres. To date, ground-based millimeter-wavelength observations have been used for disk-averaged emission measurements of the jovian planets (Ulich, 1974; Griffin et al., 1986; Muhleman and Berge, 1991; Griffin and Orton, 1993; Kramer et al., 2008), interferometric mapping of Saturn (Dowling et al., 1987; van der Tak et al., 1999; Dunn et al., 2005), and interferometric observations of limb darkening of Jupiter (Valdes et al., 1982). At millimeter-wavelengths, the planets Uranus and Neptune, with small apparent diameters and large flux densities, are frequently used as primary calibrators

of astronomical sources and telescope parameters (Ulich, 1981; Kramer et al., 2008). Future millimeter-wavelength observations with the Atacama Large Millimeter Array (ALMA) will represent a major step forward in the study of planetary atmospheres because of its high angular resolution, fast imaging capabilities, and wide instantaneous bandwidth. Combined millimeter-wavelength observations using the ALMA in conjunction with space telescopes such as the Planck space telescope (Lamarre et al., 2003) will greatly enhance studies of planetary atmospheres. The ammonia opacity model developed as part of this work can be used for interpreting the millimeter-wavelength emission spectra of jovian atmospheres observed by such facilities.

Centimeter-wavelength applications

The ammonia opacity model developed as part of this work will be used for interpreting the MWR measurements made by the Juno spacecraft at Jupiter, in addition to its application to the interpretation of past and future centimeter-wavelength ground-based and spacecraft-based observations, radio occultation experiments, and entry-probe observations of the jovian planets. The NASA mission Juno is a robotic spacecraft scheduled to arrive at Jupiter in July 2016. Using a spinning, solar-powered spacecraft, Juno will make maps of the gravity, magnetic fields, and atmospheric composition of Jupiter from a unique polar orbit. During its one-year mission, Juno will complete 33 eleven-day-long orbits and will sample Jupiter's full range of latitudes and longitudes. The primary goal of the Juno MWR is to probe the deep atmosphere of Jupiter at radio wavelengths ranging from 1.3–50 cm using six separate radiometers to measure the planet's thermal emissions and determine the atmospheric composition beneath the cloud layers, down to hundreds of bar of pressure. These thermal emission measurements with the aid of a radiative transfer model can help infer planet-wide concentration and distribution of water vapor and ammonia, provided the radiative transfer model has accurate absorption models for ammonia and water vapor that are

valid at the pressures and temperatures probed by the six MWR channels.

1.3 Organization

This dissertation addresses five main areas: theoretical discussion of microwave spectroscopy, laboratory measurements of the centimeter- and millimeter-wavelength absorption spectra of ammonia under simulated jovian conditions, discussion of the compressibility of fluids under deep jovian conditions, development of a consistent model to represent the absorption spectra of ammonia under jovian conditions, and an application of this model for the interpretation of ground-based millimeter-wavelength observations of the emission spectra of Jupiter. Each of these topics is discussed within its own chapter.

Chapter 2 provides a brief description of microwave spectroscopy and presents the fundamental theory of the absorption spectra of ammonia. Chapter 3 provides a discussion of approaches for measuring absorption and refraction of gases in the centimeter- and millimeter-wavelength region and a description of the millimeter-wavelength system and the high-pressure centimeter-wavelength system used for performing measurements of the properties of gases under simulated jovian conditions. This chapter also provides a discussion of the laboratory measurement procedure, and methods for processing the raw data and the uncertainties involved.

Chapter 4 introduces the concept of non-ideal gases (real gases) and provides a thermodynamic framework for handling pure fluids under high-pressure conditions that are characteristic of the deep jovian atmospheres. Chapter 5 provides a summary of the centimeter- and millimeter-wavelength laboratory measurements, and the consistent ammonia absorption formalism developed based on laboratory measurements and theoretical models. The performance of the new model is compared with the previous models in the 1 mm–30 cm wavelength range. Additionally, a brief discussion

of the preliminary investigation (laboratory measurements and model) of the influence of water vapor on the ammonia absorption spectra in the centimeter-wavelength range is provided.

Chapter 6 shows an application of the new ammonia opacity model for the interpretation of ground-based observations of the 2.1 mm-wavelength emission spectra of Jupiter. Chapter 7 concludes this dissertation with a summary of main contribution and explores the future directions of research.

CHAPTER II

MICROWAVE SPECTROSCOPY AND AMMONIA SPECTRA

Electromagnetic radiation incident on a gaseous molecule produces absorption or emission of energy at a particular wavelength. Radiation incident on a molecule is absorbed when the molecule transitions from a lower energy state to a higher energy state, emission is the reverse process. The frequency associated with this energy change is given by

$$f = \frac{\Delta E}{h}, \tag{2.1}$$

where ΔE is the change in energy between the upper and lower states, h = 6.624×10^{-34} Jsec (Planck's constant), and f is the frequency of absorption or emission. An isolated molecule's internal energies consist primarily of electronic, vibrational, and rotational, typically associated with absorption or emission in the visible, infrared, and microwave regions, respectively. Electronic transitions occur when electrons in a molecule are excited from one energy level to a higher energy level. The energy associated with the electronic transition is very large and correspond to the visible region of the electromagnetic spectrum. Vibrational transitions occur when the atoms in a molecule are in periodic motion while the molecule as a whole has a constant rotational motion. A linear molecule with N atoms has 3N-5 normal modes of vibration since the rotation about the molecular axis cannot be observed, and a non-linear molecule with N atoms has 3N-6 normal modes of vibration. The energy associated with vibrational motion is considerably larger than that associated with rotational motion, and hence the frequency associated with these transitions is in the infrared region of the spectrum. The energy studied in the microwave region results mostly from

rotational motion with the exception of molecular inversion, which is a form of vibrational motion. Rotational transitions occur when a molecule that possesses either a magnetic or electric dipole moment rotates about its center of mass. Polar molecules have a structure that naturally possesses a permanent dipole moment creating an asymmetry in the charge distribution which occurs as a result of the covalent bonding. Polar molecules interact with electromagnetic radiation and are active absorbers in the microwave region. A large portion of the centimeter- and millimeter-wavelength absorption in the jovian planets stems from the presence of polar molecules such as ammonia, hydrogen sulfide, water vapor, and phosphine. Non-polar molecules do not possess permanent dipole moment and are not active absorbers in the microwave region, but they do exhibit pressure-induced absorption. This absorption occurs because of the formation of transient collisionally-induced dipoles. Since the bulk of jovian atmospheres consist of hydrogen, helium, and methane, it is important to consider the collisionally-induced dipoles of H_2-H_2, H_2-He, and H_2-CH_4.

2.1 Absorption Spectra of Ammonia

Ammonia is a symmetric top molecule with a trigonal pyramidal shape and a bond angle of 107.8° (Figure 2.1). The central nitrogen atom has five outer electrons and each of the hydrogen atom has an electron, resulting in a total of eight electrons or four electron pairs, which are arranged tetrahedrally. Three of these electron pairs are used as nitrogen-hydrogen bond pairs, which leaves one lone pair of electrons. The lone pair of electrons repel more strongly than bond pairs, therefore the bond angle is 107.8° and not 109.5° as expected for a regular tetrahedral arrangement. This shape gives the ammonia molecule an electric dipole moment and makes it polar.

Ammonia has been a prime candidate to test theoretical and experimental microwave spectroscopy techniques because of the presence of a large number of easily observable lines (Townes and Schawlow, 1955). Ammonia also provides a rich and

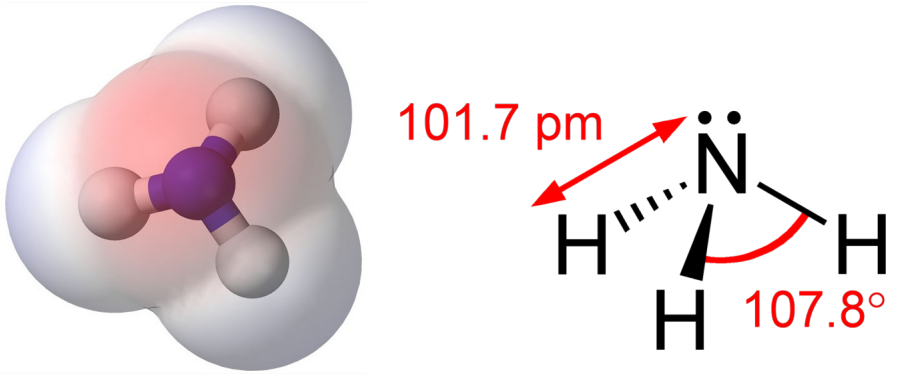

Figure 2.1: Ammonia molecule.

intense spectra involving hindered motion arising from quantum mechanical tunneling effect. The central nitrogen atom cannot be allowed in the plane of the hydrogen atoms because of the large potential-energy hump at this position. However, the nitrogen atom can "tunnel" through the plane of the hydrogen atoms and vibrate from one side to the other. These hindered motions are in principal vibrational transitions, but are called inversion transitions. Although the vibrational transitions absorb or emit infrared frequencies, the inversion transitions occur in the microwave region because they are slowed down by the hindering potential.

The potential energy curve between the nitrogen atom and the plane of the hydrogen atoms shows two minima that correspond to the equilibrium position of the nitrogen atom on either side of the plane of the hydrogen atoms (see, e.g., Townes and Schawlow, 1955). The nitrogen atom may vibrate rapidly with respect to the plane of the hydrogen atoms in one of the potential minima resulting in vibrational transitions in the infrared region, and also may penetrate the potential barrier resulting in inversion transitions in the microwave region and begin vibrating in the other potential minima. The height of the potential hill above the minimum is $\sim$ 2077 cm^{-1} and the ground-state inversion transitions occur in the microwave region ($\sim$ 23.8 GHz). Comparison of the ammonia potential hill with other symmetric hydrides such as phosphine and arsine can be made. The height of the potential hill

above the minimum for phosphine is ~ 6085 cm^{-1} resulting in ground-state inversion transitions in the radio wavelength range (~ 0.14 MHz) and for arsine is ~ 11220 cm^{-1} resulting in a ground-state inversion frequency of $\sim 1/2$ cycle/year. Thus, the ground-state inversion transitions of ammonia are rapid and provide a large number of easily observable lines, whereas arsine takes two years to go through a cycle of inversion and does not provide any observable transitions.

The interaction between the rotational and vibrational motion of ammonia results in a series of closely spaced lines in the rotational spectrum, each corresponding to different vibrational states. The interaction between inversion and rotational transitions of ammonia results in a series of lines in the inversion spectrum, each corresponding to a different rotational state.

Due to the symmetric nature of the ammonia molecule, the quantum numbers J and K are used to describe the rotation of the molecule. J represents the total angular momentum vector of the ammonia molecule (rotational quantum number) and K is the projection of J onto the molecular axis. Since K represents a component of the rotational quantum number J, it can never be larger than J, and due to the symmetry of the coordinate system negative values are not used. It is not possible to have to have a molecule with zero angular momentum because of the uncertainty principle, and hence J cannot be equal to zero. However, K can be equal to zero in pure rotational states, but this does not correspond to inversion. Hence, while considering inversion transitions, the quantum numbers are counted up from one, with $J \geq K$ and the inversion transitions are represented as (J, K). Inversion splitting of the rotational spectrum corresponds to different spins of the nitrogen nucleus that are recognized through molecular inversion, giving rise to a third quantum number S that can have a value of either 1 or 0. Inversion transition (1,1) occurs at 23.67 GHz, but the strongest inversion transition is the (3,3) transition that occurs at 23.87 GHz (Poynter and Kakar, 1975). A more complete description of the ammonia

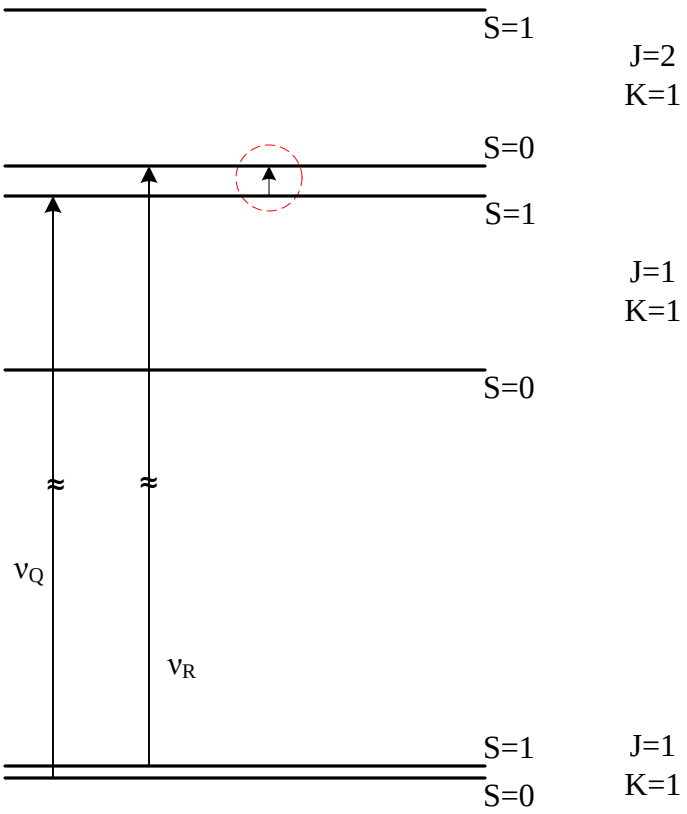

Figure 2.2: The 140.14 GHz $\nu_2 = 1$ inversion transition occurs when the ammonia molecule transitions between the lower inversion level of the ground-state J = 2, K = 1 rotational transition and the upper inversion level of the ground-state J = 1, K = 1 rotational transition.

spectrum and hindered motion can be found in Townes and Schawlow (1955).

In addition to the ground-state transitions ($\nu_2 = 0$), ammonia can have transitions that occur at higher-states ($\nu_2 = 1$, 2, 3, and so on). The higher state transitions (also called ν_2 transitions) that influence the centimeter- and millimeter-wavelength opacity of ammonia are similar to the ground state transitions, except that the transition occurs from a higher-energy state. For example, the strongest millimeter-wavelength $\nu_2 = 1$ inversion transition that occurs at 140.14 GHz is a transition between the lower inversion level of the ground-state J = 2, K = 1 rotational transition and the upper inversion level of the ground-state J = 1, K = 1 rotational transition (Figure 2.2).

Microwave and sub-millimeter spectral line catalogs such as the JPL catalog (Pickett et al., 1998) provide a database of the line strengths and frequencies of transitions of various molecules in the centimeter, millimeter and sub-millimeter region. The JPL spectral line catalogs for ground-state NH_3 transitions and higher-energy state $NH_3 - \nu_2$ transitions were recently updated (Yu et al., 2010a,b,c), and the line transitions in the 0.3–1300 GHz frequency range and their intensities are shown in Figure 2.3. The NH_3 catalog has a total of 1716 ground-state transitions that include 415 inversion transitions in the 0.3–220 GHz frequency range and 1301 rotational transitions in the 0.3–20 THz frequency range. The higher-state $NH_3 - \nu_2$ catalog has a total of 4198 inversion-rotational transitions in the 0.02–46 THz frequency range. To effectively model the centimeter- and millimeter-wavelength opacity of ammonia, it is critical to consider the contribution from all the line transitions that influence its opacity in that spectral region.

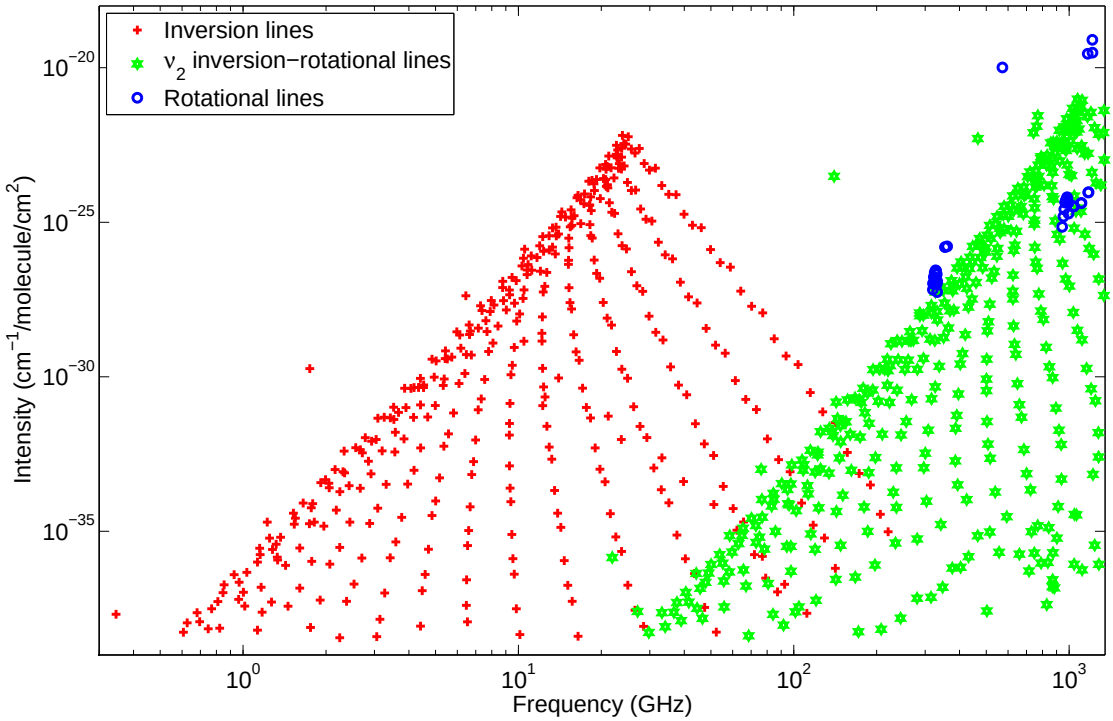

Figure 2.3: Line positions and intensities of the NH_3 and $NH_3 - \nu_2$ transitions from 0.3–1300 GHz (Yu et al., 2010a,b,c).

2.2 Linewidths

Transitions of an isolated, undisturbed, and stationary molecule occur at very specific energies and frequencies since these transitions are quantized. However, various types of disturbances change the energy levels, giving a width to the spectral lines and varying the center frequency, thereby broadening the line. The full width at half maximum (FWHM) is defined as the width that causes transition in at least half of the molecules of a particular species. Spectral linewidth, nominally called the half width at half maximum (HWHM), is half of the FWHM.

The sources of line-broadening include natural line broadening, Doppler broadening, saturation broadening, molecular collisions against walls, and pressure broadening. Zero-point ambient electromagnetic energy, present in free space, disturbs the molecules and results in natural line broadening or radiation broadening (Townes and Schawlow, 1955). This width is negligible when compared to the other types of broadening in the microwave region. Molecular motion relative to the direction of propagation of the electromagnetic radiation results in a frequency shift due to the Doppler effect. The linewidth that results from Doppler broadening is given as (Townes and Schawlow, 1955)

$$\Delta\nu_{\text{Doppler}} = 3.581 \times 10^{-7} \nu \sqrt{\frac{T}{M}}, \tag{2.2}$$

where ν is the center frequency of the line, T is the temperature of the molecules in a gas, and M is the molecular weight. For the ammonia ν_2=1 transition at 140.14 GHz, the Doppler linewidth at room temperature is $\sim$ 210 kHz. The Doppler broadening is significant for very low density gas mixtures. However, under the jovian temperature and pressure conditions studied in this work, the Doppler effect is negligible. Saturation broadening results when the intensity of the microwave radiation is so large that absorbing molecules cannot get rid of the absorbed energy rapidly

enough and the Beer-Lambert's law breaks down. While gases under low-pressures show significant saturation effect (see, e.g., Townes and Schawlow, 1955), it is negligible for the pressure conditions studied in this work. Additionally, collisions with the walls of a test chamber in a laboratory setting can cause broadening. As an example, at room temperature, gaseous ammonia in a parallel plate waveguide cell with a spacing of 4 mm between the plates has a wall collision linewidth of 12 kHz (Townes and Schawlow, 1955). Although the line broadening due to wall collisions could be significant for small waveguide cells (Danos and Geschwind, 1953), this effect is negligible for large test chambers such as those used in this work.

Under the pressure and temperature conditions used in this study, the greatest source of line broadening arises from pressure broadening due to molecular collisions. These collisions allow for the transfer of kinetic energy and interactions between the molecules due to van der Waals force. Almost all collision theories assume bimolecular collisions and most collision theories also assume that these collisions are instantaneous, i.e., the time between collisions is very large compared to the duration of a collision. While these assumptions are adequate for low pressure conditions, they are invalid under very high pressure conditions. Each molecular species has a broadening cross-section (collision diameter) that depends on its size and dipole moment. These broadening cross-sections are critical in characterizing the microwave absorption by various molecular species. When a molecule collides with another molecule of the same species, the resulting broadening is called self-broadening. If the collision is between two molecules of different species, the resulting broadening is called foreign-gas-broadening. The foreign-gas-broadening occurs even if the colliding molecules do not have any microwave absorption lines themselves, as in the case of hydrogen and helium.

2.3 Lineshapes

The lineshape of molecular collisions is used to describe the spectral dependence of broadening. Lorentz (1906) was the first to model the pressure broadening of gases. Debye (1929) described the absorption and refraction in polar molecules with a theory that differed from that of Lorentz at the zero resonant frequency. Van Vleck and Weisskopf (1945) combined the two theories to derive the Van Vleck–Weisskopf lineshape given as

$$F_{VVW}(\nu, \nu_{(0,j)}, \Delta\nu_j) = \frac{1}{\pi}\left(\frac{\nu}{\nu_{(0,j)}}\right)^2 \left[\frac{\Delta\nu_j}{(\nu_{(0,j)} - \nu)^2 + \Delta\nu_j^2} + \frac{\Delta\nu_j}{(\nu_{(0,j)} + \nu)^2 + \Delta\nu_j^2}\right], \tag{2.3}$$

where for the line j, $\Delta\nu_j$ is the half width at half-maximum, $\nu_{(0,j)}$ is the center frequency of the line transition, and ν is the frequency of the incident electromagnetic wave. Gross (1955) assumed a Maxwellian distribution of molecular velocities, instead of the Boltzmann one used by Lorentz and Van Vleck and Weisskopf and derived the Gross or the Kinetic lineshape given by

$$F_G(\nu, \nu_{(0,j)}) = \frac{1}{\pi}\left(\frac{\nu}{\nu_{(0,j)}}\right)\left[\frac{4\nu\nu_{(0,j)}\Delta\nu_j}{(\nu_{(0,j)}^2 - \nu^2)^2 + 4\nu^2\Delta\nu_j^2}\right]. \tag{2.4}$$

Although the Van Vleck–Weisskopf and Gross lineshapes converge at the line center, the Gross lineshape has higher skirts away from the linecenter than the Van Vleck–Weisskopf lineshape. Ben-Reuven (1966) derived a lineshape with two additional parameters, a line shift term (δ) proportional to the gas density, and a line-to-line coupling element (ζ). The Ben–Reuven lineshape is given by

$$F_{BR}(\nu, \nu_{(0,j)}, \gamma_j, \zeta_j, \delta_j) = \frac{2}{\pi}\left(\frac{\nu}{\nu_{(0,j)}}\right)^2 \left[\frac{(\gamma_j - \zeta_j)\nu^2 + (\gamma_j + \zeta_j)[(\nu_{(0,j)} + \delta_j)^2 + \gamma_j^2 - \zeta_j^2]}{[\nu^2 - (\nu_{(0,j)} + \delta_j)^2 - \gamma_j^2 + \zeta_j^2]^2 + 4\nu^2\gamma_j^2}\right], \tag{2.5}$$

where for the line j, $\gamma_j = \Delta\nu_j$ is the linewidth. The Gross lineshape is a special case of the Ben–Reuven lineshape under the assumption that only sense-reversing collisions take place, in which case $\gamma_j = \zeta_j$ and $\delta = 0$ (Waters, 1976).

2.4 Line Intensity

The absorption from a collisionally broadened gas is a function of the absorption at the line center, the linewidth, and the lineshape function. The absorption at each line center is calculated using the line intensity information from the latest JPL catalog as per Pickett et al. (1998)

$$A_j = \frac{nI_j(T)}{\pi\Delta\nu_j}, \tag{2.6}$$

where for the line j, n is the number density of the gas, $I_j(T)$ is the intensity of the line at temperature T, and $\Delta\nu_j$ is the linewidth. The line intensity is a measure of the amount of energy associated with any particular molecular transition. The line intensity at the measurement temperature (T) is calculated as per Pickett et al. (1998), using the values of the line intensity at the reference temperature (T_0), lower state energy of the transition, and temperature dependence parameter. The temperature dependence parameter for a diatomic or linear molecule is 1 and for a symmetric rotor is 3/2. The line intensities (at the reference temperature), lower state energies, and transition frequencies used in this study are provided by the JPL spectral line catalog (Pickett et al., 1998). A detailed description on calculating the absorption of a collisionally broadened gas is provided in Section 5.4.

CHAPTER III

LABORATORY MEASUREMENTS OF AMMONIA

One of the outstanding problems in the millimeter-wavelength spectroscopy of planets is the lack of adequate information on lineshapes and linewidths of gases at relevant pressures and temperatures, and with appropriate broadening agents. On the other hand, at centimeter-wavelengths, although there is adequate information on lineshapes and linewidths of gases, there is a lack of understanding of the influence of the far-wings of the rotational lines on the continuum absorption spectrum and a very poor understanding of the effects of compressibility of gases under the high-pressure conditions typical of the deep jovian atmospheres. These problems may be addressed by developing accurate opacity models grounded in accurate laboratory measurements. This chapter describes the theory, laboratory apparatus, measurement procedure, and uncertainties in the measurements of the centimeter- and millimeter-wavelength absorptivity of gaseous ammonia under simulated jovian atmospheric conditions.

3.1 Electromagnetic Propagation in a Homogeneous, Isotropic Medium

The phasor expressions for the electric and magnetic fields of an electromagnetic wave propagating in a homogeneous, isotropic, and lossy medium in the $+x$ direction are

$$\mathcal{E}(x) = \mathcal{E}_0 e^{-jkx} = \mathcal{E}_0 e^{-j\alpha x} e^{-j\beta x}, \tag{3.1}$$

$$\mathcal{H}(x) = \mathcal{H}_0 e^{-jkx} = \mathcal{H}_0 e^{-j\alpha x} e^{-j\beta x}, \tag{3.2}$$

respectively, where $\mathcal{E}_0$ and $\mathcal{H}_0$ are the amplitudes of the electric and magnetic fields, respectively, k is the wavenumber, and α is the attenuation constant, and β is the phase constant. The wavenumber k is given as

$$k = \omega\sqrt{\mu\varepsilon}, \tag{3.3}$$

where ω is the radial frequency, μ is the permeability, and ε is the permittivity. For most gases under jovian conditions, μ may be assumed to be entirely real and equal to μ_0, the permeability of free space. However, for lossy gases, the permittivity is complex and is given as

$$\varepsilon = \varepsilon' - j\varepsilon'', \tag{3.4}$$

so that the wavenumber of the electromagnetic wave equations becomes

$$k = \omega\sqrt{\mu(\varepsilon' - j\varepsilon'')}. \tag{3.5}$$

The frequency dependence of the real and imaginary parts of the permittivity are not independent and are related by the Kramer-Kronig relation as (see, e.g., Ramo et al., 1994)

$$\varepsilon'(\omega) = \varepsilon_0 + \frac{2}{\pi}\int_0^\infty \frac{\omega'\varepsilon''(\omega')d\omega'}{(\omega'^2 - \omega^2)}, \tag{3.6}$$

$$\varepsilon''(\omega) = -\frac{2\omega}{\pi}\int_0^\infty \frac{[\varepsilon'(\omega') - \varepsilon_0]d\omega'}{(\omega'^2 - \omega^2)}, \tag{3.7}$$

where ω and ω' are the radial frequencies. A fully accurate characterization of ε' from ε'' requires knowledge of the value of ε'' over an infinite frequency range,

and vice versa. Practical calculations of the unknown quantity using the Kramer-Kronig relation use all available information about the known quantity, while using appropriate interpolations to fill any gaps, and assumptions at the extreme frequencies where information is not available.

The wavenumber can be separated into the attenuation and phase constants α and β (see, e.g., Ramo et al., 1994)

$$jk = \alpha + j\beta = j\omega\sqrt{\mu\varepsilon'\left[1 - j\left(\frac{\varepsilon''}{\varepsilon'}\right)\right]}, \tag{3.8}$$

where

$$\alpha = \omega\sqrt{\left(\frac{\mu\varepsilon'}{2}\right)\left[\sqrt{1 + \left(\frac{\varepsilon''}{\varepsilon'}\right)^2} - 1\right]}, \tag{3.9}$$

and

$$\beta = \omega\sqrt{\left(\frac{\mu\varepsilon'}{2}\right)\left[\sqrt{1 + \left(\frac{\varepsilon''}{\varepsilon'}\right)^2} + 1\right]}. \tag{3.10}$$

The frequency dependence can be removed by taking the ratio of α and β as

$$\frac{\alpha}{\beta} = \sqrt{\frac{\sqrt{1 + \left(\frac{\varepsilon''}{\varepsilon'}\right)^2} - 1}{\sqrt{1 + \left(\frac{\varepsilon''}{\varepsilon'}\right)^2} + 1}}. \tag{3.11}$$

The term $\frac{\varepsilon''}{\varepsilon'}$ is the *loss tangent* ($\tan\delta$) of the medium. The inverse of loss tangent is the *quality factor* of the medium $Q = \frac{\varepsilon'}{\varepsilon''}$. For a gaseous medium that is not very lossy,

$$\frac{\varepsilon''}{\varepsilon'} = \tan\delta = \frac{1}{Q_{gas}} << 1, \tag{3.12}$$

where Q_{gas} is the quality factor of the gaseous medium. Hence, for a low-loss gas, the terms in Equation 3.11 can be expanded using Taylor series and approximated as

$$\frac{\alpha}{\beta} \approx \frac{\varepsilon''}{2\varepsilon'}. \tag{3.13}$$

This approximation estimates $\frac{\alpha}{\beta}$ within 0.5% when the loss tangent is less than 0.01 (or absorptivity less than 10^4 dB/km) and the loss tangents of gaseous media are almost always less than 0.01 (Spilker, 1990).

3.2 Measurement Theory

The reduction in the quality factor (Q) of a resonant mode of a resonator in the presence of a low-loss gas is used to measure the absorption of the gas (see, e.g., Hanley and Steffes, 2007). The quality factor of a resonance is given as (Matthaei et al., 1980)

$$Q = \frac{2\pi f_0 \times \text{Energy Stored}}{\text{Average Power Loss}}, \tag{3.14}$$

where f_0 is the resonant frequency. The Q can be computed as the resonant frequency divided by its half-power bandwidth (HPBW).

$$Q = \frac{f_0}{\text{HPBW}}. \tag{3.15}$$

The Q of the lossy gas and its opacity are related by

$$\alpha \approx \frac{\varepsilon''\pi}{\varepsilon'\lambda} = \frac{1}{Q_{gas}}\frac{\pi}{\lambda}, \tag{3.16}$$

where ε' and ε'' are the real and imaginary permittivity of the gas, λ is the wavelength in km, and α is the absorptivity of the gas in Nepers/km (1 Neper = 8.686 dB). The quality factor of a resonator filled with the lossy gas is given by

$$\frac{1}{Q^m_{loaded}} = \frac{1}{Q_{gas}} + \frac{1}{Q_r} + \frac{1}{Q_{ext1}} + \frac{1}{Q_{ext2}}, \tag{3.17}$$

where Q^m_{loaded} is the measured quality factor of the loaded resonator, Q_{gas} is the quality factor of the gas under test, Q_r is the quality factor of the evacuated resonator, less coupling losses, and Q_{ext1} and Q_{ext2} are the external coupling losses in the resonator. For symmetric resonators such as the ones used in this work, we can assume $Q_{ext1} = Q_{ext2}$. The coupling losses can be calculated by measuring the transmissivity $t = 10^{-S/10}$, where S is the insertion loss of the resonator in decibels (dB) at the frequency of a particular resonance, and using the relation (Matthaei et al., 1980)

$$t = \left[2\frac{Q^m}{Q_{ext}}\right]^2, \tag{3.18}$$

$$Q_{ext} = \frac{2Q^m}{\sqrt{t}}. \tag{3.19}$$

The value of Q_r is related to the measured Q at vacuum (Q^m_{vac}) by

$$\frac{1}{Q^m_{vac}} = \frac{1}{Q_r} + \frac{1}{Q_{ext1}} + \frac{1}{Q_{ext2}}. \tag{3.20}$$

Substituting Equation 3.19 in equations 3.17 and 3.20, we get

$$\frac{1}{Q_{gas}} = \frac{1-\sqrt{t_{loaded}}}{Q^m_{loaded}} - \frac{1-\sqrt{t_{vac}}}{Q^m_{vac}}, \tag{3.21}$$

where t_{loaded} and t_{vac} are the transmissivities of the resonances in the loaded and vacuum conditions, respectively. The addition of the test gas causes a shift in the center frequency of the resonances corresponding to the refractive index of the test gas.

There is a change in the quality factor of the resonances when the center frequency changes owing to the changes in coupling to the resonator. This effect is called dielectric loading (DeBoer and Steffes, 1994) and can be removed by performing additional measurement of the quality factor of the resonances with a lossless gas present and shifting the center frequency of the resonances by the exact same amount as with the lossy gas. These matched measurements are used in place of the vacuum measurements in Equation 3.21, and converting the units from Nepers/km to dB/km (1 Neper/km=8.686 dB/km), the absorptivity is given as

$$\alpha = 8.686\frac{\pi}{\lambda}\left(\frac{1-\sqrt{t_{loaded}}}{Q^m_{loaded}} - \frac{1-\sqrt{t_{matched}}}{Q^m_{matched}}\right) \quad \text{(dB/km)}. \tag{3.22}$$

The dielectric loading of resonances gives information about the refractive index of a gas. The refractive index (n_{ri}) of gases, albeit very close to one, should be known to a very high accuracy since small changes in the refractive index can significantly alter the propagation of electromagnetic radiation through an atmosphere. Refractivity (N) of a gas mixture is defined as refractive index less one multiplied by 10^6

$$N = 10^6(n_{ri} - 1). \tag{3.23}$$

Refractivity is measured by the change of the center frequency of the resonances compared to their vacuum values and is given as

$$N = 10^6 \times \frac{f_{vac} - f_{gas}}{f_{gas}}, \tag{3.24}$$

where f_{vac} and f_{gas} are the center frequencies of the resonances measured with the system under vacuum and with the test gases, respectively (Tyler and Howard, 1969). For the pure ammonia experiments, the refractivity of ammonia can be directly calculated using the above equation. However, for ammonia mixture experiments, the

measured refractivity represents the total refractivity of the test mixture which is the sum of the individual constituents' refractivities weighted by their mole fraction. Refractivity depends on pressure (P) and temperature (T), and the normalized refractivity is calculated as

$$N' = \frac{NR_0T}{P}, \tag{3.25}$$

where R_0 is the universal gas constant.

3.3 Millimeter-Wavelength Measurement System

A new high-sensitivity millimeter-wavelength measurement system developed as part of this work has been used to measure the 2–4 millimeter-wavelength properties of gases under simulated planetary conditions. The measurement system consists of a planetary atmospheric simulator, millimeter-wavelength subsystems: W band (3–4 mm) and F band (2–3 mm), and a data handling subsystem. For the study described in this dissertation, the W band and F band systems have been used for the measurements of the opacity of pure ammonia and ammonia/hydrogen/helium mixtures under simulated jovian conditions. Additional applications of the millimeter-wavelength system for the study of hydrogen sulfide under jovian conditions, and sulfur dioxide and sulfuric acid vapor under Venus conditions are discussed by Devaraj and Steffes (2011).

3.3.1 Planetary Atmospheric Simulator

The planetary atmospheric simulator controls and monitors the environment experienced by the measurement system, including the pressure and temperature conditions of the gas under test. The simulator consists of a pressure vessel, temperature chamber, gas-handling subsystem, and various measurement gauges. The main component of the atmospheric simulator is a pressure vessel capable of withstanding pressures

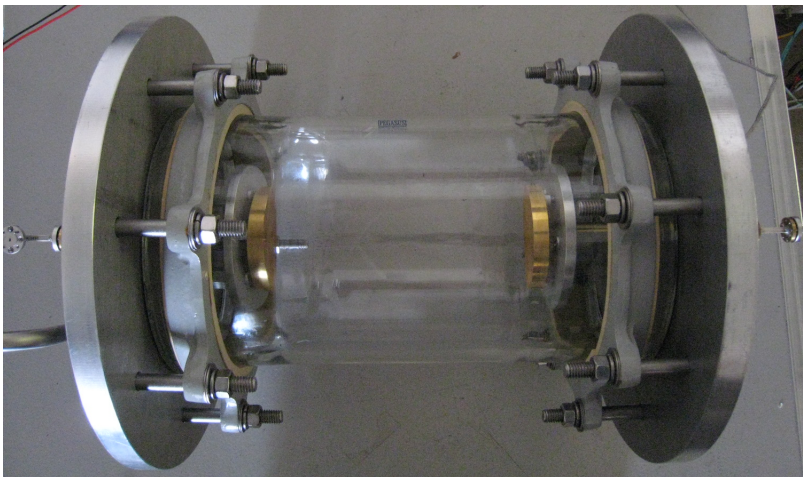

Figure 3.1: A picture of the glass pressure vessel enclosing the Fabry–Perot resonator used for simulating the jovian atmospheric conditions.

up to three bar. This pressure vessel is a Pegasus® conical glass pipe (6x9 inches) with aluminum endplates. The endplates are sealed with Viton® O-rings sandwiched between the lip of the glass and the flat endplate which is bolted to an inner flange. The pressure vessel encloses the Fabry–Perot resonator used for making measurements and is shown in Figure 3.1.

The pressure vessel and a part of the millimeter-wavelength measurement system are contained in a temperature-controlled chamber which is a Revco® ultra-low temperature freezer capable of operating between 173 K and 218 K. The temperature chamber has a stability of approximately ±0.5 K. The freezer does not operate warmer than 218 K, and hence measurements cannot be conducted in the 218–290 K range. Room temperature measurements are also conducted with the system placed inside the temperature chamber (with the cooling system shut-off) since the chamber helps to maintain thermal stability. When the system is operating at cold temperatures, the thermal stability is increased by placing iron blocks inside the freezer so that the temperature fluctuations inside the pressure vessel do not exceed ±0.5 °C as verified by *in situ* temperature measurements. The temperature inside the pressure vessel is monitored by an Omega® Model HH21 Microprocessor Thermometer (display unit)

connected to a Type T (copper/copper-nickel) thermocouple probe threaded into a 1/4" NPT fitting on one side of the aluminum endplate of the resonator. This allows the probe to be in direct contact with the test gases and provides a very accurate measurement of the temperature inside the vessel. The thermometer display unit has a resolution of 0.1 °C and a 3σ accuracy of 0.3% of the displayed value plus an additional ±0.6 °C uncertainty at temperatures below 0 °C. Above 0 °C, the additional uncertainty remains the same, but the accuracy improves to 0.1%. The thermocouple itself has an accuracy of 1.0 °C or 0.75% of the reading, whichever is greater.

Pressure measurements in the 2–3 bar range are made with an Omega® DPG7000-30 Digital Test Gauge, and pressure measurements in the 0–2 bar range (vacuum to 2 bar) are made with an Omega® DPG7000-VAC/15 Digital Test Gauge. These gauges have a resolution of 1 mbar and 0.05% full scale total error band accuracy. The gauges only display differential pressure between the closed system and the ambient laboratory environment, and hence the gauge readouts can vary as the ambient pressure varies even if the absolute pressure in the system remains constant. To correct for this effect, digital barometers (Davis® Weather Monitor II 7440 and Young® 61202L) are used to measure the ambient pressure inside the laboratory.

A Welch DuoSeal® vacuum pump Model 1376B-01 is used to evacuate the gases from the system from 1 bar down to vacuum. Gases at higher pressures are vented through an exhaust valve. A glass cylinder with a volume of approximately 7.2 L is connected to the venting line along with an Analytical Technology, Inc. PortaSens II portable gas leak detector so as to detect any trace amounts of gas through a series of interchangeable electrochemical cartridge sensors. Gases are fed into the pressure vessel through a series of regulators and valves. All components in the gas handling system are connected with seamless 3/8" outer diameter stainless tubing and Swagelok® fittings.

3.3.2 Millimeter-Wavelength Subsystem

Currently, the 2–4 mm-wavelength measurements are made with two different subsystems, namely the W band and F band systems. At the heart of both the measurement systems is a spherical mirror Fabry–Perot resonator (FPR) in a near confocal configuration enclosed in the pressure vessel.

Fabry–Perot resonator

Resonant microwave cylindrical cavities have been used to observe molecular resonances in gases and their absorption coefficients for over 60 years (Bleaney and Penrose, 1947; Weidner, 1947; Gordy, 1948). In the millimeter-wavelength region, FPRs provide low loss, high coupling efficiency, and high precision in measurements (Culshaw, 1960, 1961, 1962; Zimmerer, 1963). FPRs have been successfully employed for the measurement of atmospheric gas losses in the millimeter-wavelength range for more than 40 years (Valkenburg and Derr, 1966). Absorptivity of gases under simulated planetary conditions have also been measured using an FPR in the past (Joiner and Steffes, 1991; Fahd and Steffes, 1992).

The FPR used in the millimeter-wavelength system consists of two concave gold-plated mirrors whose surface is polished to μm tolerance (Figure 3.2). Electromagnetic energy is coupled to and from the resonator (which acts as a band-pass filter) through irises located in the center of each of the mirrors via WR-8 waveguides which pass through the endplates to the exterior of the pressure vessel. The end of each waveguide section is pressure-sealed by a circular piece of mica window held in place by a low temperature O-ring and vacuum grease. The resonator is symmetrical and the input/output ports are interchangeable. One of the ports is connected to the signal source through a waveguide section and the other end is connected to a high-resolution spectrum analyzer through a harmonic mixer and diplexer.

The spherical mirror FPR is used in a near-confocal configuration which has a

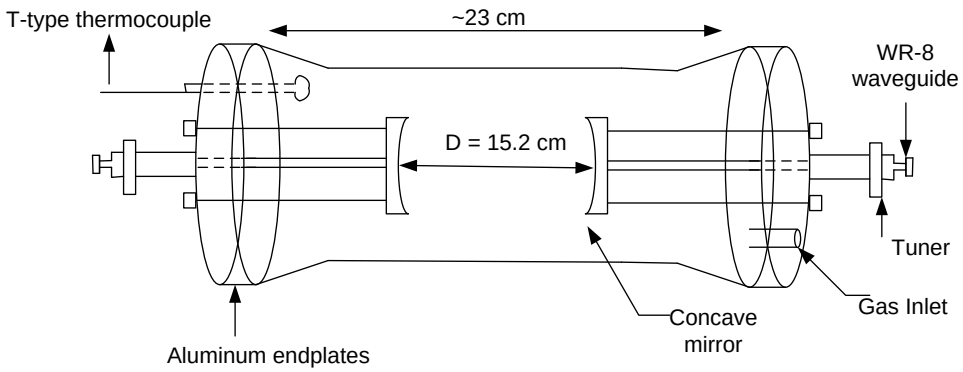

Figure 3.2: Block diagram of the spherical mirror Fabry–Perot resonator placed in a near-confocal configuration.

number of advantages such as high quality factor and very good tolerance to the alignment of mirrors (Herriott et al., 1964). The radius of curvature of the spherical mirrors is approximately 30 cm and the distance of separation (D) between the mirrors is adjustable thereby making it possible to measure resonances (transmission peaks) at desired frequencies. For the measurements that were made with this resonator, a mirror spacing of approximately 15.2 cm provided minimum diffraction losses and optimal free spectral range (FSR). FSR is the frequency interval between adjacent axial mode resonances and is given by

$$\mathrm{FSR} = \frac{c}{2D}, \tag{3.26}$$

where c is the speed of light. For the current resonator set-up, FSR $\sim$ 1GHz.

There are three kinds of losses in an FPR: resistive losses (on the surface of the mirrors), coupling losses (due to the energy coupling in/out of the resonator through the irises), and diffraction losses (around the sides of the mirrors) (Culshaw, 1960, 1962). When a spherical mirror interferometer is illuminated by an off-axis ray of light, the repeated reflections cause several ray paths and these ray paths give rise to additional resonances (Herriott et al., 1964). These additional off-axis resonances

adversely affect the performance of the interferometer. Furthermore, diffraction loss is caused by energy spilling over the sides of the mirrors because of poor mirror alignment. To suppress the off-axis resonances and to reduce diffraction losses, the mirrors need to be very precisely aligned. This was achieved using a beam from a helium-neon laser, which was directed to the input waveguide of the resonator. The other mirror was adjusted so that the reflected beam focused precisely on the output iris. The coupling losses are a function of frequency due to the standing waves between the input/output irises and the signal source/detector. The coupling losses were reduced by ensuring a good waveguide to mirror joint. The resistive losses were minimized by using highly reflective gold-plated mirror surfaces with minimal surface irregularities. However, the mirror resistive losses increase at higher frequencies because of the shallow skin depth of the gold-plated mirrors. The coupling losses also increase at higher frequencies. Neglecting diffraction losses, the quality factor of the resonances are dependent on the mirror resistive and coupling losses. For the resonator used in this work, the mirror resistive and coupling losses increase faster as a function of frequency compared to the theoretical increase in Q as a function of frequency and become dominant at higher frequencies. Hence, the quality factor of the system decreases as a function of frequency (Figure 3.3).

In order to achieve a high system sensitivity (which corresponds to a high Q), all losses in an FPR should be minimized. After the alignments were made, the quality factor of the resonator at vacuum and T=297 K in the 2–4 mm-wavelength range was between 45,000 and 190,000 (Figure 3.3). The effective path length (EPL) of the electromagnetic energy is given as (Valkenburg and Derr, 1966)

$$\mathrm{EPL} = \frac{Q\lambda}{2\pi}. \tag{3.27}$$

For example, consider a resonance at 77.08 GHz (3.89 mm). The observed Q of this particular resonance was 185,800. Hence, the effective path length is about

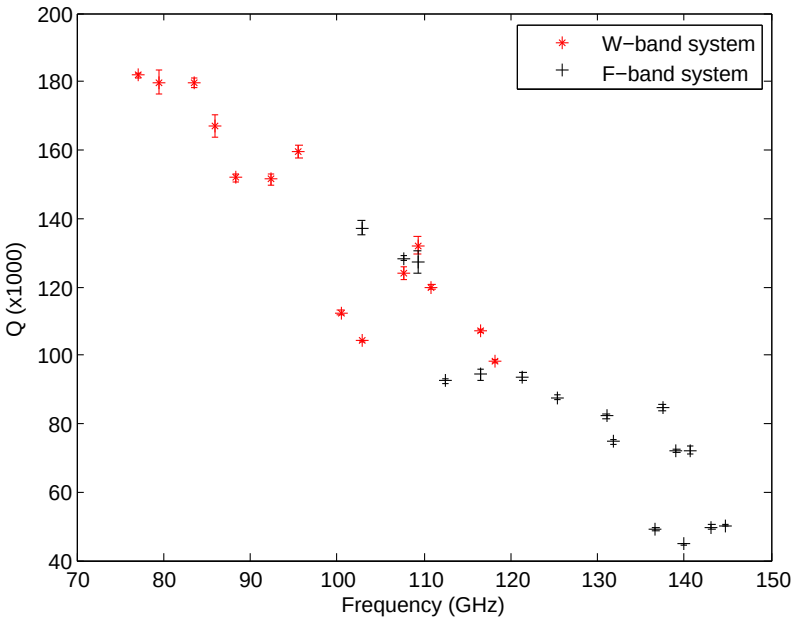

Figure 3.3: Quality factor of the resonances of the Fabry–Perot resonator measured at vacuum and room temperature (T=297 K).

115.01 m. Figure 3.4 shows a plot of the effective path length of the resonances as a function of frequency as measured at room temperature. The performance of the FPR improves slightly at lower temperatures.

W band system

The W band measurement system is used to measure the 3–4 mm-wavelength properties of ammonia, and is shown in Figure 3.5.

A swept signal generator (HP 83650B) is used to generate signals in the 12.5–18.3 GHz range which is fed to a times six active multiplier chain (AMC) via flexible, low-loss, high frequency 2.9 mm male–2.9 mm male coaxial cable assembly. All coax connections are tightened with an 8 in-lb (0.90 N-m) torque wrench to ensure reliable connections. The operating temperature of the AMC is 0°C–45°C. Hence, the AMC is heat sunk to keep the case temperature below +45°C when it is used at room temperature. When the AMC is used at cold temperatures, the heat sink is removed

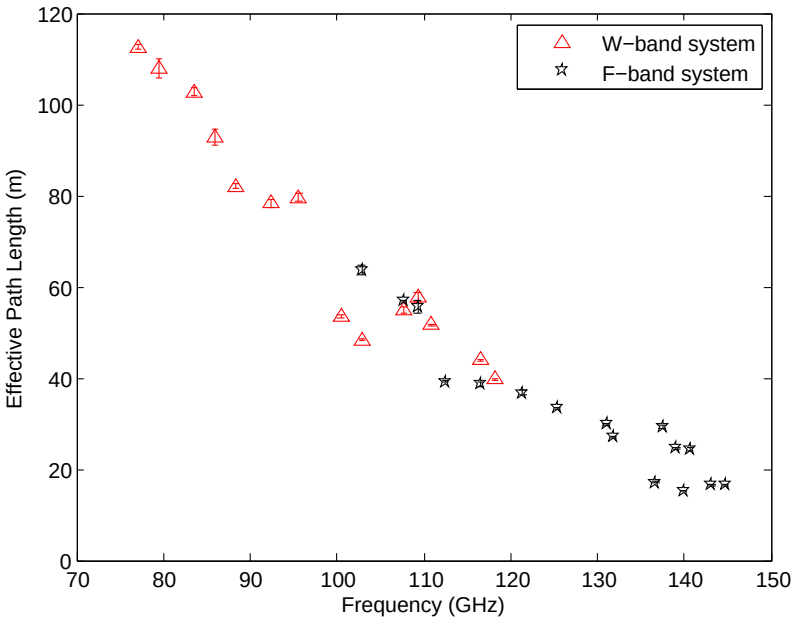

Figure 3.4: Effective path length of the resonances of the Fabry–Perot resonator measured at vacuum and room temperature (T=297 K).

and thermal insulation is provided so that the heat generated by the AMC could sustain its own operation even if the external temperature is -100°C. The AMC is hermetically sealed to prevent ice deposition at cold temperatures. The output from the AMC is fed to one of the ports of the FPR via a solid WR-8 waveguide section.

The radio frequency (RF) signal from the output port of the FPR is fed to a QuinStar Technology QMH series harmonic mixer via solid WR-8/WR-10 waveguide sections so as to enable down-conversion of 3–4 mm-wavelength signal. The QMH series harmonic mixer has a common SMA port for the local oscillator (LO) and intermediate frequency (IF) signals, and hence an external diplexer (model MD1A) is used to combine/separate the LO and IF signals. The typical conversion loss of this mixer is approximately 40 dB. Both the mixer and the diplexer are hermetically sealed when used in the freezer. The harmonic mixer locked to the 18th harmonic is used in the "external mixer" mode with a spectrum analyzer (HP 8564E). The detector within the spectrum analyzer operates in a positive peak mode, which displays the

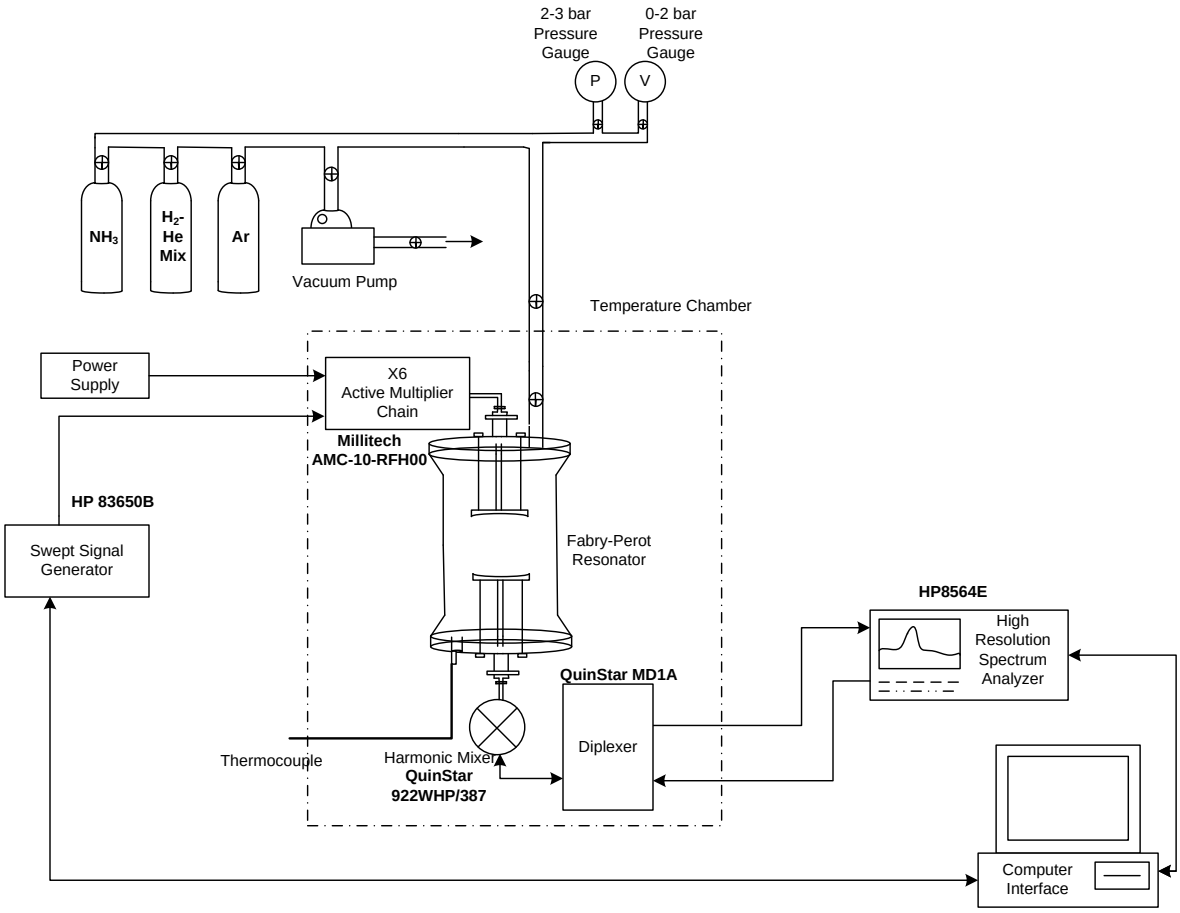

Figure 3.5: Block diagram of the W band measurement system for studying ammonia gas properties under simulated upper tropospheric jovian conditions. Solid lines represent the electrical connections and the arrows show the direction of signal propagation. Valves controlling the flow of gases are shown by the small crossed circles.

maximum power level received during the integration time of each point on each individual sweep. This mode is used primarily because it maximizes the data return to the computer. The normal mode detects both the high and low signal (noise floor) intensities at each frequency point, but when transferring to the computer, the spectrum analyzer is limited to 601 points in both the frequency and amplitude axes. In the normal mode, the peak level data becomes interspersed with the noise floor data, which would result in only half the data transferred being of practical use for these measurements and consequently would halve the frequency resolution. The mixer can also be used as a down-converter with an external LO, but a different diplexer is used (model MD2A).

As shown in Figure 3.5, the AMC and the harmonic mixer are placed as close to the resonator input/output ports as possible to reduce the signal loss and increase the signal to noise ratio (SNR) of the resonances. The signal power generated by the signal source, the loss through the FPR, and the conversion loss of the mixer are dependent on the frequency. Hence, the signal to noise ratio of the received signal is also dependent on the frequency. For example, the swept signal generator is used to generate a 10 dBm signal at 12.5 GHz. This is fed to the AMC, which produces the RF signal at 75 GHz with a signal power of 5 dBm. At 75 GHz, the loss through the FPR is approximately 20 dB and the conversion loss of the mixer is approximately 40 dB. Hence, the signal power that reaches the spectrum analyzer is approximately -55 dBm at 75 GHz. Additional information on the various components of the W band subsystem is provided in Appendix A.

F band system

The F band measurement system is used to measure the 2–3 mm-wavelength properties of ammonia and is shown in Figure 3.6.

The signal generated by a swept signal generator (HP 83650B) in the 33–50 GHz

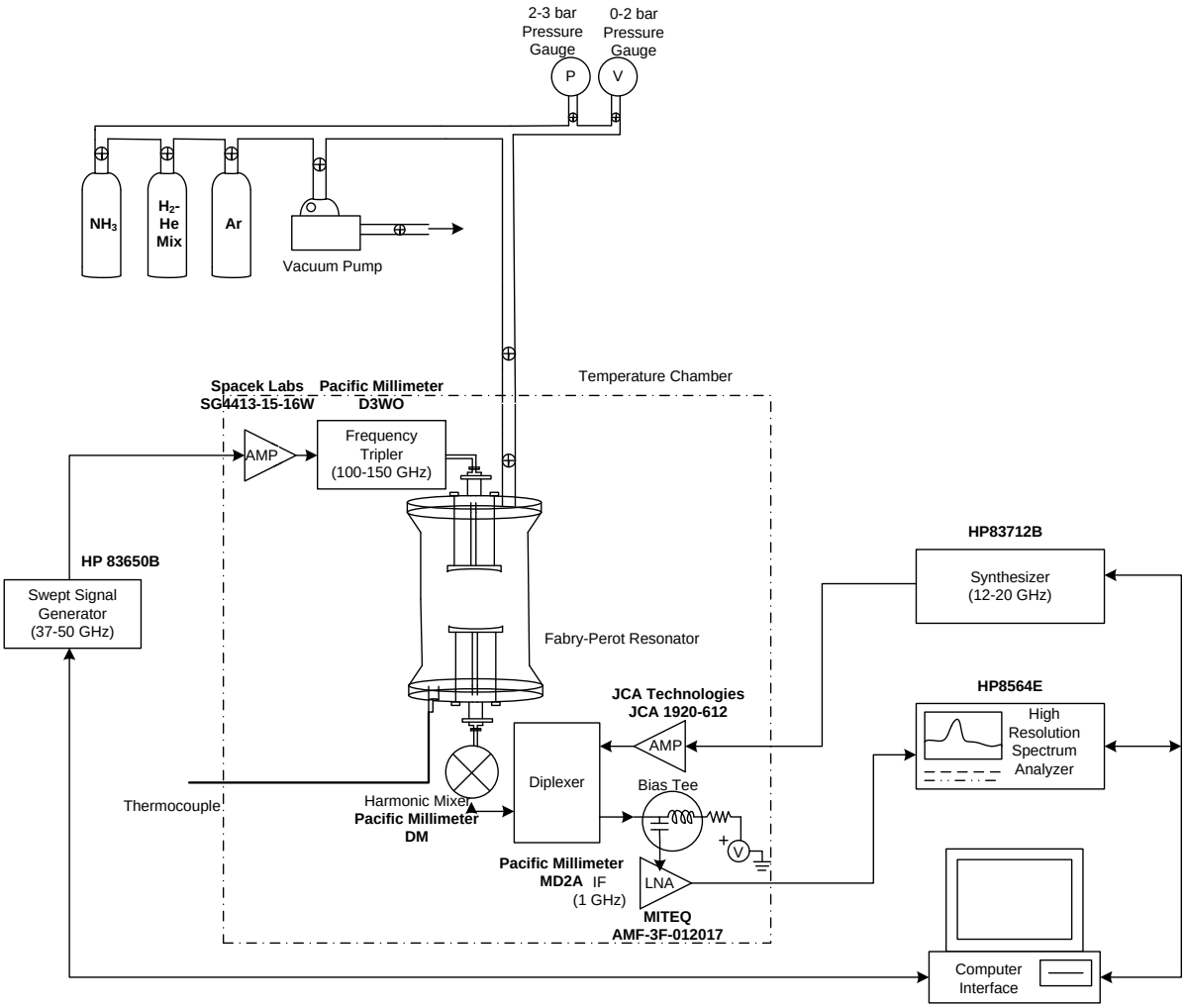

Figure 3.6: Block diagram of the F band measurement system for studying ammonia gas properties under simulated upper tropospheric jovian conditions. Solid lines represent the electrical connections and the arrows show the direction of signal propagation. Valves controlling the flow of gases are shown by the small crossed circles.

range is amplified (Spacek model SG 4413-15-16W) and fed to a frequency tripler. To facilitate the operation of the amplifier inside the freezer, the heat sink mounted on the amplifier is removed and adequate thermal insulation is provided. Both the amplifier and the tripler are hermetically sealed while operating at cold temperatures. The output from the tripler is fed to one of the ports of the FPR via a solid WR-8 waveguide section.

The RF signal from the output port of the FPR is fed to a harmonic mixer (Pacific Millimeter Products model DM) via a solid WR-8 waveguide section to enable down-conversion of 2–3 mm-wavelength signal. The harmonic mixer can operate with an LO frequency as high as 18 GHz and has a common SMA port for LO and IF signals. An external diplexer (model MD2A) is used to combine/separate LO and IF signals. For a particular RF and IF frequency, LO frequency can be computed using

$$f_{LO} = \frac{f_{RF} - f_{IF}}{N_H}, \tag{3.28}$$

where N_H is the lowest integer such that $f_{LO} < 18$ GHz. The harmonic mixer has one diode, and requires a DC return path for the diode current. This DC return path follows the IF path in the diplexer, and the device attached to the IF port of the diplexer must have provision for a bias-tee. Mixer conversion loss is dependent upon the frequency, the harmonic number, applied LO power, and the diode current. For the 10th harmonic (LO frequency=11–17 GHz for RF=110–170 GHz) conversion loss is approximately 40 dB. Sensitivity of the receiver system will depend on the receiver bandwidth, but the mixer conversion loss sets a minimum noise contribution for the receiver system of 40 dB. If the internal spectrum analyzer local oscillator (3–6 GHz LO frequency) is used, an even higher conversion loss associated with the low LO frequency and high harmonic mixing number results. Hence, a separate CW signal generator (HP 83712B) along with an amplifier (JCA Technologies model JCA 1920-612) are used as the LO, and harmonics less than the tenth order are used.

The IF signal is then enhanced using a low noise amplifier (MITEQ model AMF-3F-012017) and displayed on the spectrum analyzer. The IF is chosen such that there is minimal radio frequency interference (RFI). RFI is further mitigated by wrapping aluminum foil tapes around the microwave components and connectors at the IF end. Additional information on the various components of the F band subsystem is provided in Appendix A.

3.3.3 Data Handling Subsystem

The data acquisition system consists of a computer connected to the spectrum analyzer (HP 8564E), swept signal generator (HP 83650B), and CW signal generator (HP 83712B) via a general purpose interface bus (National Instruments GPIB Controller for Hi-Speed USB). The instruments are controlled via Matlab® and the Standard Commands for Programmable Instruments (SCPI). The software used is similar to that used by (Hanley and Steffes, 2007) with modifications to account for the suite of instruments used in this measurement system.

3.4 High-Pressure Measurement System

A high-pressure measurement system was used to conduct measurements of the 5–20 cm-wavelength absorptivity of ammonia under deep jovian conditions at pressures up to 100 bar and temperatures up to 500 K. The high-pressure measurement system consists of a planetary atmospheric simulator, centimeter-wavelength subsystem, and a data handling system.

3.4.1 High-Pressure Planetary Atmospheric Simulator

The planetary atmospheric simulator was designed by Karpowicz and Steffes (2011). The simulator consists of a high-pressure vessel, temperature chamber, water-reservoir, mass flow meter, temperature and pressure gauges, vacuum pump, various gas bottles, gas handling valves, and pipes. The main component of the planetary atmospheric

simulator is a high-pressure vessel that operates at pressures up to 100 bar and temperatures up to 520 K custom built by Hays Fabrication and Welding. The custom pressure vessel was designed with two 1/2" NPT ports, one 1/4" NPT port, and two CF-1.33 flanges with 3.38 cm diameter for microwave feedthroughs. One of the 1/2" NPT ports is used as a gas inlet while the other 1/2" NPT port is used for a temperature sensor. The 1/4" NPT port serves as the gas outlet. A composite glass fiber/nitrile butadiene rubber KLINGERsil®C-4430 O-ring is used to seal the pressure vessel along with twenty 6 cm diameter nuts torqued to 1760 Nm. The pressure vessel is constructed out of a 30.48 cm section of schedule 100 pipe that is 35.56 cm in diameter (outer dimension). An elliptical head is welded to the bottom of the pressure vessel giving it a maximum interior height of approximately 46 cm. The top of the pressure vessel is an ANSI class 900 flange that is 10.16 cm thick, and the top plate is 9.2 cm thick. The pressure vessel has a volume of approximately 32.3 liters and weighs approximately 545 kgs.

The pressure vessel is contained in a temperature chamber, which is a Grieve® industrial oven (model AB-650) that is rated to a temperature of 615 K and weighs approximately 740 kgs. The combined weight of the pressure vessel and the oven far exceeded the load capacity of the laboratory floor. It was determined that an outdoor concrete pad on which a decommissioned crane once stood would be ideal for such a load. Hence, all the system components, except the network analyzer and the data acquisition system, are placed on the outdoor concrete pad. A metallic EZEE shed was built around the system components for protection.

A water reservoir made of a 304 stainless steel pipe that is 46 cm long and 3.8 cm in diameter is connected the pressure-vessel and placed inside the oven to produce water vapor. Various gas bottles (hydrogen, helium, ammonia, pre-mixed hydrogen/helium, and argon) required for simulating the jovian atmosphere and for dielectric matching measurements are placed on a six-pack gas cylinder rack adjacent to the EZEE shed.

The gases and mixtures are ultra-high-purity UHP300 grade and supplied by Airgas. Gas delivery pressure regulators, Matheson® model 3030-580 were used for argon and helium, Matheson® model 3030-350 was used for hydrogen, and Airgas® model Y11E444B660 was used for ammonia. A Teledyne-Hastings HFM-I-401 industrial flow meter capable of operating up to 103 bar pressure is used for mass flow sensing. When the gases are added to the pressure vessel, the flow *totalizer* function of the flow meter is used to estimate the system volume since the volume changes by a small but measurable amount with temperature. All components in the gas handling subsystem are connected with seamless 3/8" outer diameter stainless steel tubing and Swagelok® fittings. Gases are vented down to ambient pressure though an exhaust valve and a Welch DuoSeal® vacuum pump model 1376B-01 is used to evacuate the pressure vessel from 1 bar down to vacuum.

Pressure measurements are made with a GE Druck DPI 10430A Digital Test Gauge in the 0 to 2 bar range, GE Druck DPI 104300A Digital Test Gauge in the 2 to 20 bar range, and an Omega® PX1009L0-1.5KAV pressure transducer for pressures up to 100 bar. The GE Druck DPI 10430A gauge has a resolution of 0.1 mbar and the GE Druck DPI 104300A gauge has a resolution of 1 mbar. Both the pressure gauges have a 0.05% full scale total error band accuracy and display the absolute pressure within the pressure vessel. The pressure gauges are powered externally with a 9 V power supply and have an RS-232 serial interface for data acquisition. The Omega® pressure transducer has an accuracy of ±0.25% full scale output and measures the absolute pressure. The voltage from the pressure transducer is read via a HP 34401A multimeter.

The temperature of the gases in the pressure vessel is monitored with an Omega® resistance temperature detector (RTD) (PR-11-2-100-1/8-9-E). The RTD has a 0.01°C resolution and the accuracy is IEC/DIN Class A (±0.15°C at 0°C and ±0.55°C at 200°C). The RTD is connected to the 1/2" NPT port of the pressure vessel via a 1/8"

Swagelok® tube to 1/2" NPT adapter (SS-200-1-8BT). For experiments conducted below 450 K, a high temperature thermometer/hydrometer assembly (E+E Elektronik EE33-MFTI9205HA07D05/AB6-T52) inserted into the 1/2" NPT port of the pressure vessel was used to measure the temperature. The temperature resolution of the thermometer/hygrometer is 0.01°C and the accuracy is between ±0.25°C at 0°C and ±0.5°C at 180°C. The temperature of the pressure vessel is maintained within ±0.1°C of the measurement temperature throughout an experiment sequence. The temperature inside and outside the oven are monitored by various T type thermocouple probes. A block diagram of the EZEE-shed along with all the system components are shown in Figure 3.7. The valves shown in blue in Figure 3.7 are high temperature Swagelok® SS-1RS6-PK valves rated to 315°C at a maximum pressure of 215 bar, and the valves shown in black are Swagelok® SS-1RS6 valves rated to 93°C at a maximum pressure of 295 bar. Table 3.1 lists the instruments used in the planetary atmospheric simulator of the high-pressure system along with their operating conditions and 3σ precision. Figure 3.8 shows the high-pressure system in assembly along with the EZEE shed and the gas cylinder rack and Figure 3.9 shows the high-pressure vessel in and after assembly.

3.4.2 Centimeter-Wavelength Subsystem

The centimeter-wavelength subsystem has greatly benefited by continuous improvement over the past twenty years (see, e.g., DeBoer and Steffes, 1996; Hanley and Steffes, 2007). At the heart of the subsystem is a type 304 stainless steel cylindrical cavity resonator placed inside the high-pressure vessel. The inside of the cavity resonator is plated with gold to improve the quality factor of the resonances, and to prevent reaction with corrosive gases. The interior dimension of the cavity resonator is approximately 13.1 cm in diameter and 25.5 cm in height, and is ideal for measurements in the 5–20 cm wavelength range. The resonator consists of two closed-loop

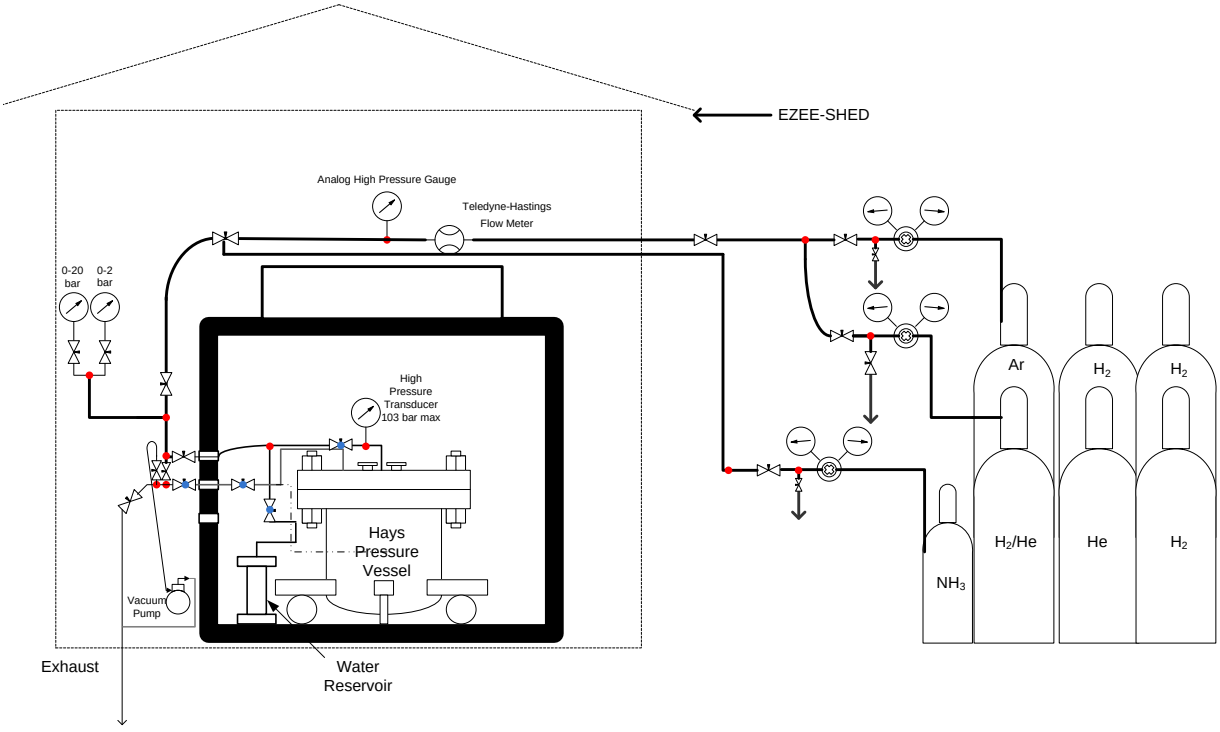

Figure 3.7: The Georgia Tech high-pressure system used for studying the centimeter-wavelength properties of ammonia under simulated jovian conditions (Karpowicz and Steffes, 2011). The valves shown with a blue dot are high temperature valves.

Figure 3.8: Assembly of the high-pressure system.

Table 3.1: High-pressure planetary atmospheric simulator instruments.

Instrument	Operating Range (°C)	Measurement Parameter	3σ Precision
GE Druck DPI 10430A	-10 to 50	Pressure (0–2 bar absolute)	±0.05% FS
GE Druck DPI 104300A	-10 to 50	Pressure (0–20 bar absolute)	±0.05% FS
Omega® PX1009L0-1.5KAV	-54 to 343	Pressure (0–103 bar absolute)	±0.25% FS
HP® 34401A multimeter	23±5	Voltage (pressure transducer output)	±(0.0035% of reading + 0.0005% of range)
Omega® PR-11-2-100-1/8-9-E	-50 to 450	Temperature (50 to 450°C)	±(0.15 + 0.002 of reading)°C
Omega® DP41B	0 to 50	Temperature (-200 to 900°C)	±0.2°C
Type T thermocouple	-200 to 400	Temperature (-200 to 400°C)	greater of ±1.0°C or 0.75% of reading
E+E Elektronik EE33-MFTI9205HA07D05/AB6-T52	-40 to 180	Temperature (-40 to 180°C)	±0.25–0.5°C
Teledyne-Hastings HFM-I-401	-20 to 70	Flowrate 0–10 slm, operates up to 103 bar	±(0.2% FS + 0.5% reading)

(a) Microwave cavity resonator and SiO_2 cables inside pressure vessel.

(b) Assembled pressure vessel and water reservoir inside the oven.

Figure 3.9: Pictures of the pressure vessel in and after assembly.

(a) Gold-plated resonator with the top plate removed.

(b) Resonator with dielectric spacers.

Figure 3.10: Cylindrical cavity resonator.

antenna probes mounted on the top plate and oriented to maximize the Q of the $\mathrm{TEM}_{(0,M,L)}$ mode (Hanley et al., 2009). The resonator has two horizontal slits on its circular side near the top plate to suppress unwanted degenerate TM resonant modes and also to allow gases to enter the interior. Additionally, the top and the bottom plates of the resonator are isolated by approximately 1.75 mm from the cylinder by a series of Teflon® washers around the connecting screws. This isolation eliminates the degenerate $\mathrm{TM}_{(1,M,L)}$ mode and greatly improves the sensitivity of the system, but increases the microwave energy leaking out of the resonator. Hence, the resonator is wrapped with a stainless steel mesh screen to damp interference of the microwave energy reflected off the pressure vessel walls back into the resonator. The two ports of the resonator are essentially symmetric and Qs of the resonances range from 30,000 to 80,000. The resonator with the top-plate removed and the assembled resonator with dielectric spacers are shown in Figure 3.10.

The center frequencies of the transverse electric (TE) and transverse magnetic (TM) mode resonances in a cylindrical cavity resonator are calculated as

$$f_{TE(N,M,L)} = \frac{c}{2\pi\sqrt{\mu_r \varepsilon_r}} \sqrt{\left(\frac{p_{NM}}{r_d}\right)^2 + \left(\frac{L \times \pi}{h_t}\right)^2}, \tag{3.29}$$

$$f_{TM(N,M,L)} = \frac{c}{2\pi\sqrt{\mu_r \varepsilon_r}} \sqrt{\left(\frac{q_{NM}}{r_d}\right)^2 + \left(\frac{L \times \pi}{h_t}\right)^2}, \tag{3.30}$$

where N, M, and L refer to the zeros in the standing wave patterns in the circumferential, radial, and axial dimensions, respectively, μ_r and ε_r are the relative permeability and permittivity of the material contained in the resonator, c is the speed of light in cm/s, r_d and h_t are radius and height of the cylindrical resonator in cm, q_{NM} is the M^{th} zero of the N^{th} order Bessel function, and p_{NM} is the M^{th} zero of the first derivative of the N^{th} order Bessel function of the first kind (Pozar, 1998). In this work, only TE mode resonances are used because of their high quality factors. The TM modes have been intentionally suppressed to minimize interference with the neighboring TE mode resonances. One dozen high-Q, low-asymmetry resonances were selected and used as "standard resonances" for all the measurements. A detailed description of the selection criteria for the resonances was provided by Hanley et al. (2009).

The resonator is connected to the high-pressure Ceramtec® microwave feedthroughs (model 16545-01-CF) on the top-plate of the pressure-vessel using Times Microwave® SiO_2 microwave cables, to couple microwave energy in and out of the pressure vessel. The SiO_2 cables are rated to 875 K and the SMA Ceramtec feedthroughs are rated to 103 bar and 625 K. Exterior to the pressure vessel, two 1 m long sections of high-temperature Times Microwave M17/86-00001 (RG-225) cables fitted with type-N connectors are connected to the Ceramtec feedthroughs via high-temperature type-N to SMA adapters. These cable assemblies were assembled in the laboratory with high-temperature solder rated to 500 K. One end of these cables with type-N bulkheads are positioned outside of the oven via holes that were drilled on the side

wall of the oven. Two sections of approximately 24.4 m length Andrews®CNT 600 microwave cables, rated to 350 K are connected to the type-N bulkheads on the RG-225 cable assemblies outside the oven and connect to an Agilent® E5071C vector network analyzer that is situated inside the laboratory. The network analyzer operates from 300 kHz to 8.5 GHz with a high-stability timebase (Option 1E5). The long CNT 600 microwave cables are required to enable the placement of the network analyzer within the laboratory environment to ensure its temperature stability. The S-parameters measured by the network analyzer are read into the data acquisition system via GPIB.

3.4.3 Data Acquisition System

The data acquisition subsystem consists of a laptop computer connected to the network analyzer and multimeter via a GPIB connected to a National Instruments NI-488.2 interface card, and a data logging computer connected to the various pressure and temperature sensors via extended USB buses and USB to RS-232 adapters. The extended USB buses allow the data logging computer to remain inside the laboratory. A schematic of the centimeter-wavelength subsystem and the data-acquisition components of the high-pressure measurement system are shown in Figure 3.11. The network analyzer is controlled via Matlab® and the Standard Commands for Programmable Instruments (SCPI) and the suite of pressure and temperature sensors are controlled via Python®. The Matlab software used is similar to that used by Hanley and Steffes (2007) and a detailed description of the data acquisition system is provided by Karpowicz (2010).

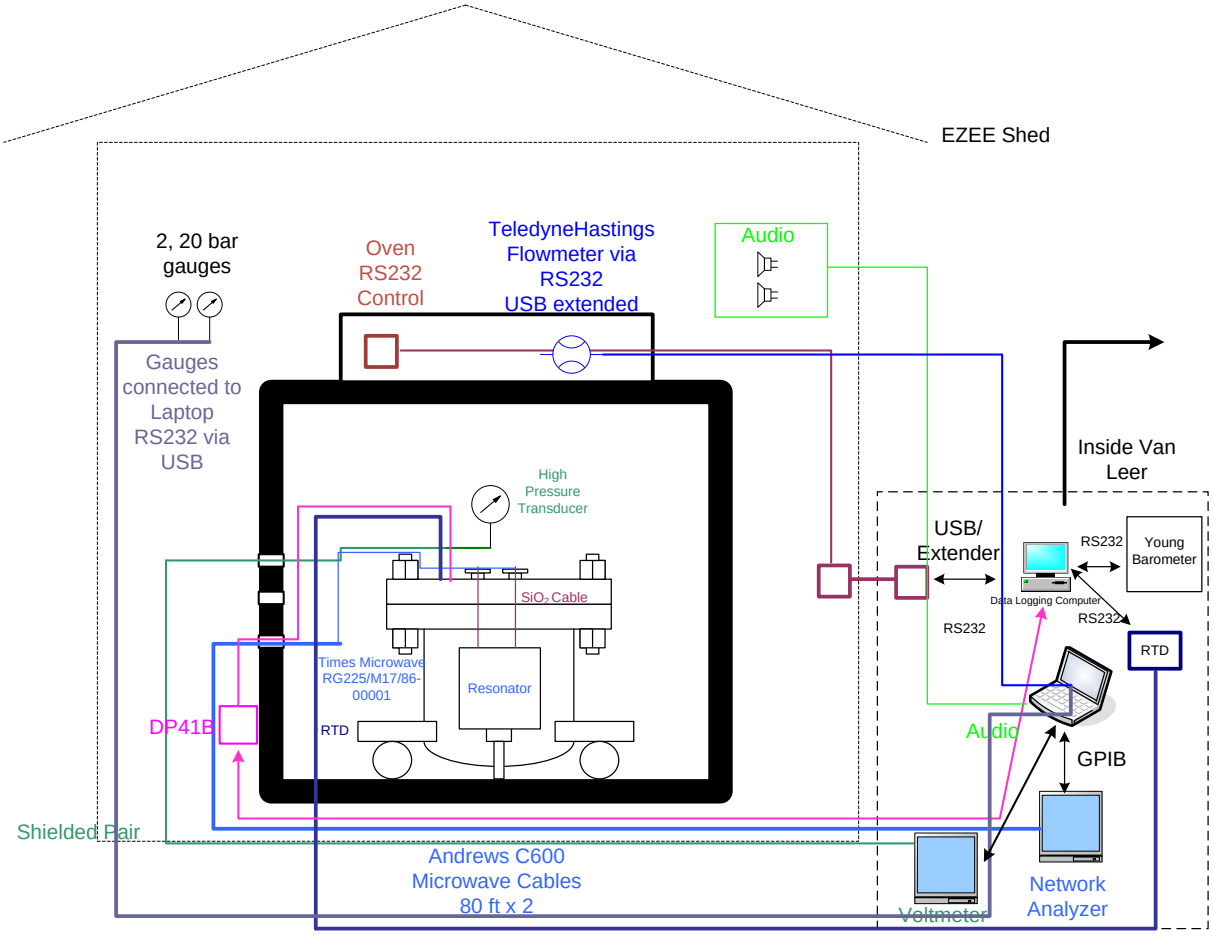

Figure 3.11: The centimeter-wavelength subsystem and the data-acquisition components of the high-pressure system (Karpowicz and Steffes, 2011).

3.5 Measurement Procedure

One of the most important prerequisites for performing the measurements of gas properties is a leak-proof system. Leak-proofing the system not only reduces the uncertainties in the experiments, but also ensures that no toxic or flammable gases leak from the system and pose a health-hazard. The pressure vessel is assembled and sealed at the coldest operating temperature, which ensures that it remains leak-proof at warmer temperatures since warming expands the materials and only improves the seal. The pressure vessel, gas handling pipes, valves, and gas regulators are positive pressure-tested with a liquid leak detection compound at the highest permissible pressure. Further tightening of the pressure vessel is achieved after drawing a vacuum since there is additional compression force on the surface of the pressure vessel due to normal atmospheric pressure. Once a good seal is established, the pressure vessel is filled with argon (three bar for the glass pressure vessel and 95 bar for the high-pressure vessel) and the pressure is monitored for several days to ensure that there is a good pressure seal.

Once a good pressure seal is established in the millimeter-wavelength system, the measurement process begins by characterizing the resonances of the FPR at the measurement temperature. Whenever the temperature of the FPR changes, the metal stand-offs that hold the mirrors in place and the mirrors themselves expand/contract, and hence the distance between the mirrors and their alignment change slightly. Any change in mirror alignment affects the off-axis resonances which move in frequency with respect to the axial mode resonances. As a result, some axial mode resonances become contaminated with the off-axis resonances, resulting in compound asymmetric resonances. Asymmetry (A_s) is defined as

$$A_s = 100 \times \frac{(f_{high} - f_{center}) - (f_{center} - f_{low})}{(f_{high} - f_{low})}\%, \tag{3.31}$$

(DeBoer and Steffes, 1994), where f_{high}, f_{center}, f_{low}, represent the higher frequency half power point, center frequency, and lower frequency half power point of the resonances, respectively. Since asymmetric resonances might broaden disproportionately when lossy gases are added, only those resonances with $A_s \leq 5\%$ are used for the measurements. About a dozen high-Q, low-asymmetry resonances that are roughly uniformly spaced in frequency are selected to be used as the "standard resonances" for all the measurement sequences at a particular measurement temperature. For the centimeter-wavelength system, one dozen high-Q, low-asymmetry "standard resonances" were chosen based on the selection criteria provided by Hanley et al. (2009) and used for all the measurements.

Owing to the difficulties in frequently changing the measurement temperature, and because changes in pressure and mixing ratios can be achieved quickly, the gas properties are measured at a particular temperature for different sets of mixing ratios and gas pressures. Once the desired set of measurements are conducted at a particular temperature, the temperature of the chamber is changed and a new set of measurements are made at the new temperature.

When gas molecules are added to the pressure vessel, they have a tendency to adhere (physically or chemically adsorb) to the surface of the pressure vessel. Physisorption is the process of gaseous molecules of one substance, the adsorbate, adhering to the surface of a liquid or solid substance, the substrate, due to weak attractive van der Waals forces between the adsorbate and the substrate. This does not result in any sharing of electrons and is not to be confused with chemisorption that requires the formation of a chemical bond between the substrate and the adsorbate. The formation of physically adsorbed layer may be likened to the condensation of a vapor to form a liquid and most likely occurs when the gas is near its condensation point, but can occur under warmer, lower pressure conditions (Young and Crowell, 1962). If p is the equilibrium pressure of the adsorbed film and p_0 is the saturation vapor pressure

of the gas at the experimental temperature, then below $p/p_0 = 0.01$ no significant adsorption takes place (Young and Crowell, 1962). While all molecules can encounter physisorption, polar molecules are more prone to it, especially when the substrates are conductors. An analogue is a dipole interacting electromagnetically with its image in the plane of the conductor. Adsorbed molecules have limited degrees of freedom, and hence do not interact with the incident electromagnetic energy to the extent they would in the gaseous phase. Adsorbed molecules, however, do change the electrical conductivity of the surfaces, to which they adsorb (Young and Crowell, 1962). In this measurement system, the effect of adsorbed ammonia on the conductivity and resulting Qs of the resonator was found to be negligible. Desorption is the process by which the adsorbed molecules are returned to the gas phase. The most effective ways for molecules to desorb are by the reduction of the partial pressure of the adsorbate or by the increase of the temperature of the substrate to provide enough energy for the adsorbate to break the weak attractive van der Waals forces that hold them in place.

A particular example of ammonia adsorption/desorption is discussed here, but it should be noted that most polar molecules behave in a similar fashion. A study by Rodrigues and Moraes Jr. (2002) found that at all temperatures the physisorption capacity of ammonia increased with increasing ammonia concentration, but an increase in temperature at any concentration led to a decrease in the adsorption capacity of ammonia. The study also concluded that the effect of temperature more significantly affected desorption than ammonia concentration. Non-polar molecules such as hydrogen and helium on the other hand do not adhere to the substrate at our experimental conditions. It is difficult to quantify or predict adsorption due to its dependence on the fine molecular structure of the substrate. Hence, precautions must be taken to account for adsorption, whenever gas mixtures are added to the system where one component adsorbs more than another. Earlier studies of ammonia

opacity made under simulated jovian conditions did not properly account for adsorption (Mohammed and Steffes, 2004; Spilker, 1990). When manufactured mixtures of hydrogen, helium and ammonia are used (Mohammed and Steffes, 2004), some ammonia in the mixture adsorbs to the surface of the measurement system thereby reducing its concentration in the gas phase, and there is no effective method to determine the exact concentration of ammonia left in the measurement system. When a series of progressive dilutions are employed to arrive at mixtures with a small ammonia concentration (Spilker, 1990), there is a shift in the adsorption/desorption equilibrium since the concentration of ammonia decreases after partial venting. This leads to additional desorption and disproportionate increase of the concentration of that gas.

One way to compensate for adsorption is to presaturate the surface of the measurement system with the adsorbate so that no more adsorption occurs since there are only so many layers of adsorbate that can form on the substrate. This is achieved by adding ammonia to the pressure vessel first and letting the system completely saturate while simultaneously monitoring the Qs of the resonances. After ammonia is added, there is a reduction in the Qs of the resonances because of the absorption of electromagnetic energy by ammonia in the gas phase. Once ammonia starts adhering to the surface of the resonator, its concentration is reduced, and hence the Qs increase slightly. After ammonia completely saturates the surface of the pressure vessel, the Qs stabilize, and at this stage adsorption equals desorption. After this stage, hydrogen and helium are added to the system. Measurements of gas properties are made starting at the lowest pressure by adding ammonia and working up to higher pressures by adding hydrogen and helium. Measurements are never made by venting the gas mixture down to lower pressures because of the possibility of enhanced ammonia desorption from the substrate due to the reduction in the partial pressure of ammonia thereby leading to a disproportionate increase in the concentration of ammonia.

Each measurement cycle consists of first measuring the pre-selected standard resonances of the resonator at vacuum. Test gases (eg. ammonia, hydrogen and helium) are added to the system and after the system stablizies, the frequency shifted resonances are measured at different pressures. Because of the large volume and thermal inertia, it takes much longer for the centimeter-wavelength system to stabilize when compared to the millimeter-wavelength system. For the centimeter-wavelength system, it takes about 8–10 hours for the system to stabilize after the test gases are added and for the millimeter-wavelength system, it takes about 2–3 hours for system stabilization. After the frequency shifted resonances are measured, the pressure vessel is vented down to the ambient pressure and a vacuum is drawn for at least 12 hours to remove the test gases. A second set of vacuum measurements of the resonances is made. A non-absorbing gas such as argon or carbon dioxide is then added to the system to shift the frequency of the resonances by the exact same amount as the test gases and the dielectrically matched measurements are made. The dielectric matching process is aided by a series of tones produced by the data acquisition computer to help the experimenter precisely match the center frequency of the resonances. The system is evacuated once again to remove the matching gas and a third set of vacuum measurements is made. After this step, three sets of straight-through measurements of signal levels are made (without the resonator present) under the same conditions at each pressure/frequency point of the test gas, so as to correct the measurements of transmissivities (loaded and matched) for losses in the cables or waveguides. For the millimeter-wavelength system, these measurements involve disconnecting the W band/F band signal generator and detector from the resonator and coupling 1/100th of the RF signal power (via a WR-10 20 dB directional coupler) from the generator to the detector and making multiple measurements at the standard resonant frequencies. For the centimeter-wavelength system, these measurements involve disconnecting the RG-225 cables from the Ceramtec feedthroughs and connecting the cables together

via a high-temperature female-to-female SMA adapter and making multiple measurements at the standard resonant frequencies. Between the repeated signal level measurements, all the waveguide/coax connections are disconnected and reconnected to better statistically characterize the reproducibility of the electrical connections. Signal levels are only measured at the end of the experiments so as to ensure that the resonator stays at a constant temperature ($\pm$ 0.5°C for the millimeter-wavelength system and $\pm$0.1°C for the centimeter-wavelength system) throughout the measurement cycle. (Signal level measurements involve opening the temperature chamber to disconnect/reconnect the signal generator, detector, waveguides, and/or coax assembly, and this might temporarily alter the temperature of the chamber.)

3.6 Data Processing

The data are processed after each measurement cycle is completed. Software written in Matlab® is used to automatically load and process the raw data. The software used is similar to that described by Hanley and Steffes (2007), but with modifications to account for the topology of the new measurement systems. The automated software loads the raw data files, runs smoothing algorithms, and calculates the absorptivity of the test gas at the measured frequencies, pressures, temperatures, and mixing ratios.

The shape of any major variation in the straight-through signal level measurements of the cables/waveguides/adapters over the measurement frequency range of the resonances are deconvolved from the sweeps. Since this variation is $< \pm 0.25$ dB for the centimeter-wavelength system, this effect is omitted. The cable/waveguide losses at the center frequency of the resonances under each pressure, temperature, and mixing ratio condition is calculated by averaging the values of the mean of each set of sweeps of the signal level measurements. The loaded insertion loss (S_l) and matched insertion loss (S_m) are obtained by subtracting the cable/waveguide losses from the peak power measurements of the test gas and the dielectric matching gas,

respectively. The insertion losses are used to generate the quantities t_{loaded} and $t_{matched}$ in Equation 3.22.

For the millimeter-wavelength system that employs the spectrum analyzer, the measured bandwidth ($\mathrm{BW}_{measured}$) of a resonance is a function of the resolution bandwidth (RBW) and the filter response (shape) of the spectrum analyzer which is approximately Gaussian (1 MHz < RBW < 2 MHz) or synchronously tuned 4-pole filter (300 Hz < RBW < 300 kHz). RBW is chosen to be $\sim 1/100$th of the frequency span. The actual bandwidth is calculated from the measured bandwidth by

$$BW_{actual} = \sqrt{BW^2_{measured} - RBW^2}. \tag{3.32}$$

This correction is unnecessary for the centimeter-wavelength system that employs the network analyzer, since it is programmed to display the true response of the device under test.

3.7 Measurement Uncertainties

The uncertainties associated with the measurements include instrumental errors (σ_n), errors in dielectric matching (σ_{diel}), transmissivity errors (σ_{trans}), errors due to asymmetry in resonances (σ_{asym}), and errors in measurement conditions (σ_{cond}) due to uncertainties in measurement temperature, pressure, and mixing ratio.

The instrumental errors and electrical noise arise because of the sensitivity of the electrical devices and their ability to accurately measure the center frequency (f_o) and bandwidth ($BW_{measured}$). Electrical noise arises from the noise of the internal electronics and the accuracies of the frequency references. Electrical noise is uncorrelated and the best estimate of instrumental uncertainty is the mean of multiple measurements. The variance of the best error estimate is given by the sample variance (S^2_N) weighted by the confidence coefficient (B) as

$$\sigma^2_N = B \times \frac{S^2_N}{N_{samples}}, \tag{3.33}$$

where $N_{samples}$ is the number of independent measurements of the sample. For the millimeter-wavelength system that employs the spectrum analyzer, five sets of independent measurements of each resonances are taken, and for the centimeter-wavelength system that employs the network analyzer, 30 sets of independent measurements of each resonances are taken. A confidence coefficient corresponding to the 95% confidence interval (approximately 2σ) is used. The confidence coefficient is equal to the critical value of the Student t test (Student, 1908) for a two-tailed significance of 0.05 and the degrees of freedom ($N_{samples} - 1$). This means that the true mean will fall above the confidence interval 2.5% of the time and below the confidence interval 2.5% of the time. The critical value of B for 95% confidence for five samples is 2.776 and for 30 samples is 2.045. The center frequency sample standard deviation of the measurements is very small and its effect on the uncertainty in Q is negligible. Hence, S_N refers only to sample standard deviation of the bandwidth of the measurements.

The HP 8564E spectrum analyzer is used for measuring the resonances in the millimeter-wavelength system and the manufacturer specified instrumental uncertainties are the 3σ values (Hewlett-Packard, 1997). The 3σ standard deviation for the center frequency and bandwidth measurements, respectively, are estimated by

$$\sigma_o \leq \pm\left(f_o \times f_{ref\ acc} + 0.05 \times \mathrm{SPAN} + 0.15 \times \mathrm{RBW} + 10\right) \quad \text{(Hz)}, \tag{3.34}$$

$$\sigma_{BW} \leq \pm(BW_{measured} \times f_{ref\ acc}) + 4 \times N_H + 2 \times \mathrm{LSD} \quad \text{(Hz)}, \tag{3.35}$$

where $f_{ref\ acc}$ is given as

$$f_{ref\ acc} = (aging \times time\ since\ calibration) + initial\ achievable\ accuracy + temperature\ stability, \tag{3.36}$$

and f_o, SPAN, RBW, N_H, and LSD are the center frequency, frequency span, resolution bandwidth, harmonic number, and least significant digit of the bandwidth

measurement, respectively. LSD is calculated as LSD = 10^x for the smallest positive integer value of x such that SPAN $< 10^{x+4}$. These formulae are for SPAN > 2 MHz$\times N_H$, which is a wide-span scenario. For SPAN ≤ 2 MHz$\times N_H$, SPAN multiplication factor of 0.05 is replaced with 0.01. For the spectrum analyzer used in the experiments, $f_{ref\ acc}$ reduces to

$$f_{ref\ acc} = (10^{-7} \times \textit{years since calibrated}) + 3.2 \times 10^{-8}. \tag{3.37}$$

There is a 3σ uncertainty associated with the RBW ($\pm 25\%$). However, this changes the value of BW_{actual} (Equation 3.32) by less than 0.01%, and hence can be omitted for all practical purposes in the computation of the measurement uncertainties.

For measurements made with the Agilent E5071C-ENA Vector Network Analyzer, the relative uncertainty in measured frequency is calculated as

$$\sigma_o = f_{measured} \times \left(5 \times 10^{-8} + 5 \times 10^{-7} \times \textit{years since calibrated}\right) \quad \text{(Hz)}, \tag{3.38}$$

with $f_{measured}$ given in Hz. The absolute uncertainty in measured frequency is as low as 1 ppm of the frequency reading (Hanley et al., 2009) and hence can be ignored. Since no specifications were available for calculating uncertainties in measured bandwidth for the network analyzer, the formula provided by Hanley et al. (2009) was used

$$\sigma_{BW} = \sqrt{2} \times BW_{measured} \times \left(5 \times 10^{-8} + 5 \times 10^{-7} \times \textit{years since calibrated}\right) \quad \text{(Hz)}, \tag{3.39}$$

where $BW_{measured}$ is given in Hz.

The formulae for calculating σ_o and σ_{BW} for the spectrum analyzer and the network analyzer represent the 3σ uncertainties and are scaled by 2/3 to obtain the 2σ uncertainties. The instrumental uncertainties are also based on the specifications provided by the manufacturer and the instruments are typically more accurate than this. However, these formulae represent the worst case condition for instrumental uncertainties and are used in our calculations.

The worst case scenario (greatest error) is considered in the computation of uncertainties of the instrumental error and electrical noise and is computed as given by DeBoer and Steffes (1994)

$$\sigma_\psi^2 = \langle F_l^2 \rangle + \langle F_m^2 \rangle - 2\langle F_l F_m \rangle, \tag{3.40}$$

where

$$\langle F_i^2 \rangle = \frac{\Upsilon_i^2}{f_{oi}^2}\left[\frac{\sigma_o^2}{Q_i^2} + \sigma_{BW}^2 + \sigma_{Ni}^2 + \frac{2\sigma_o\sigma_{BW}}{Q_i}\right], i= l,m, \tag{3.41}$$

$$\langle F_l F_m \rangle = -\frac{\Upsilon_l \Upsilon_m}{f_{ol} f_{om}} \times \left[\frac{\sigma_o^2}{Q_l Q_m} + \sigma_{BW}^2 + \frac{\sigma_o\sigma_{BW}}{Q_l} + \frac{\sigma_o\sigma_{BW}}{Q_u}\right], \tag{3.42}$$

$$Q_i = \frac{f_{oi}}{f_{BWi}}, \quad i = l, m, \tag{3.43}$$

$$\Upsilon_i = 1 - \sqrt{t}, \quad i = l, m, \tag{3.44}$$

where l, m denote loaded and dielectrically matched cases, respectively, and $f_{ol,om}$ and $f_{BWl,BWm}$ represent center frequency, and bandwidth of loaded and dielectrically matched cases, respectively. The 2σ uncertainty of the measured gas absorption due to instrumental errors and electrical noise is given by

$$\sigma_n = \frac{8.686\pi}{\lambda}\sigma_\psi \quad (\text{dB/km}), \tag{3.45}$$

where λ is the wavelength in km.

Errors due to dielectric matching, transmissivity, and asymmetry are computed in a fashion similar to that used by Hanley et al. (2009), but with modifications to account for the topologies of the new measurement systems. Errors in dielectric matching are due to the minor mis-alignments in the center frequency between the loaded and the matched measurements. This is the most trivial error because of the highly accurate software-controlled matching of the center frequency between the

loaded and matched measurements. Though the gas used for dielectric matching is lossless, the Q of the resonator can change slightly from that of vacuum values. The magnitude of this effect is calculated by comparing the Q of the three vacuum measurements to that of the dielectric matched measurements.

$$\left(\frac{dQ}{df}\right)_i = \left|\frac{Q_{vac,i} - Q_{matched}}{f_{vac,i} - f_{matched}}\right| \text{ for } i = 1, 2, \text{ and } 3. \tag{3.46}$$

The maximum of the three values is used to calculate a dQ value

$$dQ = \left(\frac{dQ}{df}\right)_{\max} \times \left|f_{loaded} - f_{matched}\right|, \tag{3.47}$$

where f_{loaded} and $f_{matched}$ are the center frequencies of the resonances under loaded and matched conditions, respectively. The error in absorptivity due to imperfect dielectric matching is then computed by propagating $\pm dQ$ through Equation 3.22

$$\begin{aligned}\sigma_{diel} = &\frac{8.686\pi}{\lambda} \\ &\times \left|\left(\frac{1-\sqrt{t_{loaded}}}{Q^{\,m}_{\,loaded}} - \frac{1-\sqrt{t_{matched}}}{Q^{\,m}_{\,matched} + dQ}\right)\right. \\ &\left. - \left(\frac{1-\sqrt{t_{loaded}}}{Q^{\,m}_{\,loaded}} - \frac{1-\sqrt{t_{matched}}}{Q^{\,m}_{\,matched} - dQ}\right)\right| \quad \text{(dB/km)}.\end{aligned} \tag{3.48}$$

Transmissivity errors are due to the uncertainties in the measurement amplitude. This is caused by the centimeter- and millimeter-wavelength instruments (signal generators, spectrum analyzer, and network analyzer), cables, adapters, and waveguides used in the system. Absolute magnitude uncertainties for the signal sources can be safely disregarded since the loaded, matched, and signal level measurements are all made with the same signal power. The greatest uncertainty in the signal level measurements results from disconnecting and reconnecting the waveguides and cables. Since the waveguides and cables have to be disconnected at least once from the system to characterize their loss, this procedure is repeated two more times to ensure a better statistical bound on the uncertainty parameters. The standard deviation (S_N) of these measurements is calculated and is weighted by the confidence coefficient for

a two-tailed distribution for three samples with a 95% confidence interval (Student, 1908) and is divided by the square root of the number of measurements to yield

$$\sigma_{msl} = \frac{4.303}{\sqrt{3}} S_N. \tag{3.49}$$

For the millimeter-wavelength system, the signal level measurements involve sampling the RF power with a WR-10 20 dB directional coupler to feed to the harmonic mixer for down-conversion and detection. This procedure ensures that RF power input to the harmonic mixer does not exceed its maximum allowed input power of -10 dBm. However, the WR-10 directional coupler does not uniformly sample the input signal throughout the entire frequency range. Hence, an additional 1.5 dB uncertainty is included in the calculation of the uncertainty due to insertion loss ($\sigma_{ins\ loss}$). The signal generator has a temperature stability of 1 dB/10 °C, but an internal temperature equilibrium is reached after two hours of operation at a stable ambient temperature (Hewlett-Packard, 1997). Since the measurement environment outside the temperature chamber is maintained at a constant temperature throughout the measurement cycle, this uncertainty can be disregarded. The total uncertainty in insertion loss for the millimeter-wavelength system is calculated by

$$\sigma_{ins\ loss} = \sigma_{msl} + 1.5 \quad \text{(dB)}. \tag{3.50}$$

For the centimeter-wavelength system, the signal level measurements involve disconnecting the RG-225 cables from the resonator and connecting them in a thru configuration so that the cable losses can be measured at each resonant frequency. Cable losses are measured three times by disconnecting and reconnecting the cables to statistically characterize their loss and the measured signal level uncertainty σ_{msl} is calculated using Equation 3.49. While σ_{msl} takes into account the variations in the cables that arise when they are disconnected and reconnected, it does not account for the variabilities in the SiO_2 cables internal to the pressure vessel that cannot be removed. To account for the variability in these SiO_2 cables, a value 0.25 dB is

assumed based on worst case models of cable performance (Karpowicz and Steffes, 2011). An additional uncertainty of 0.5 dB is included to account for the variations in the cable losses due to ambient temperature variations in the approximately 8.5 m long outdoor section of each of the 24.4 m Andrews® CNT 600 microwave cable. The total uncertainty in insertion loss for the centimeter-wavelength system is given as

$$\sigma_{ins\ loss} = \sqrt{\sigma_{msl}^2 + 0.25^2 + 0.5^2} \quad \text{(dB)}. \tag{3.51}$$

The error in insertion loss is used to compute the transmissivity error

$$\sigma_{t,i} = \frac{1}{2}\left(10^{-(S_i - \sigma_{ins\ loss})} - 10^{-(S_i + \sigma_{ins\ loss})}\right), \tag{3.52}$$
$$i = l, m,$$

where l, m are the loaded and matched cases, respectively, and S is the insertion loss of the resonator. This is used to compute the 2σ uncertainties in opacity and is expressed as

$$\sigma_{trans} = \frac{8.686\pi}{2\lambda} \times \left(\frac{\sqrt{t_l + \sigma_{t,l}} - \sqrt{t_l - \sigma_{t,l}}}{Q^{\,m}_{loaded}} - \frac{\sqrt{t_m - \sigma_{t,m}} - \sqrt{t_m + \sigma_{t,m}}}{Q^{\,m}_{matched}}\right) \quad \text{(dB/km)}. \tag{3.53}$$

Errors from asymmetry are due to the asymmetric nature of the measured resonances which are caused by the overlapping of the off-axis/TM mode resonances on the axial/TE mode resonances. The asymmetric nature of the resonances are more prominent at the shorter wavelength and colder temperatures. Errors due to asymmetry result from the disproportionate asymmetric broadening of the loaded measurements compared to the matched measurements. Equivalent full bandwidths based on assuming symmetry of the high and low sides of the resonances are calculated as

$$BW_{high} = 2 \times (f_{high} - f_{center}), \tag{3.54}$$

$$BW_{low} = 2 \times (f_{center} - f_{low}), \tag{3.55}$$

where BW_{high}, BW_{low}, f_{high}, f_{center}, and f_{low} are the high bandwidth, low bandwidth, higher frequency half power point, center frequency, and lower frequency half power point, respectively. The difference between the opacities calculated using BW_{high} and BW_{low} (treated as 2σ errors) is defined as σ_{asym} and calculated as

$$\begin{aligned}\sigma_{asym} = & \frac{8.686\pi}{\lambda} \\ & \times \left| \left(\frac{1-\sqrt{t_{loaded}}}{Q^{m}_{loaded,high}} - \frac{1-\sqrt{t_{matched}}}{Q^{m}_{matched,high}} \right) \right. \\ & \left. - \left(\frac{1-\sqrt{t_{loaded}}}{Q^{m}_{loaded,low}} - \frac{1-\sqrt{t_{matched}}}{Q^{m}_{matched,low}} \right) \right| \quad \text{(dB/km)},\end{aligned} \tag{3.56}$$

where $Q^{m}_{loaded,high/low}$ and $Q^{m}_{matched,high/low}$ are the measured Qs evaluated using the high and low bandwidths for loaded and matched cases, respectively.

The measured uncertainty in temperature, pressure, and concentration contribute to the total uncertainties due to the measurement conditions (σ_{cond}). Although σ_{cond} does not directly affect the measurements, it still needs to be accounted for while creating accurate models for opacity based on experimental data, and is computed as

$$\sigma_{cond} = \sqrt{\sigma^2_{temp} + \sigma^2_p + \sigma^2_c}, \tag{3.57}$$

with σ_{temp}, σ_p, and σ_c representing the 2σ uncertainties in opacity corresponding to the uncertainties in temperature, pressure, and concentration, respectively. Each of these uncertainties is calculated by halving the difference between the maximum modeled opacity and the minimum modeled opacity, with each measurement uncertainty. Since σ_{cond} dependence on the opacity and refractivity are not known while making the measurements, this uncertainty is maintained separately from σ_{tot}. Thus, the total 95% confidence for the measurement uncertainty is expressed in dB/km as per Hanley et al. (2009)

$$\sigma_{tot} = \sqrt{{\sigma_n}^2 + {\sigma_{diel}}^2 + {\sigma_{trans}}^2 + {\sigma_{asym}}^2}. \tag{3.58}$$

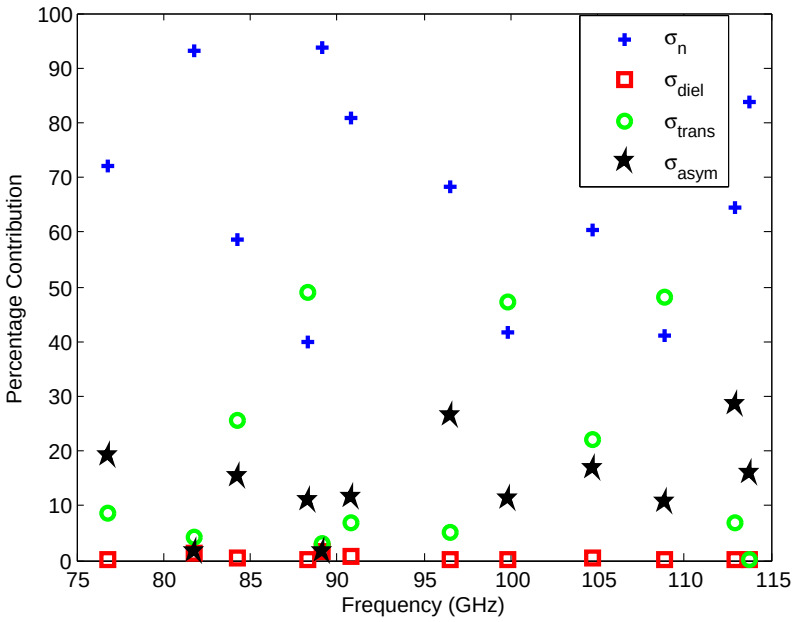

Figure 3.12: Percentage contribution of the different measurement uncertainties to the total uncertainty of the W band system at room temperature (T=297 K).

The centimeter-wavelength system exhibits a maximum 2σ sensitivity in the opacity ranging from 0.01 dB/km at 1.5 GHz to 0.1 dB/km at 6 GHz (Hanley et al., 2009). For the W band and F band systems, the percentage contribution of different uncertainties to the total 2σ uncertainty of a typical measurement are shown in Figures 3.12 and 3.13. The dominant factor in the total uncertainty in most cases for the W band system is σ_n and that for the F band system is σ_{trans}. For the cold temperature measurements, σ_{asym} starts to dominate at the shorter wavelengths. The aggregate sensitivities of the millimeter-wavelength system are shown in Figure 3.14.

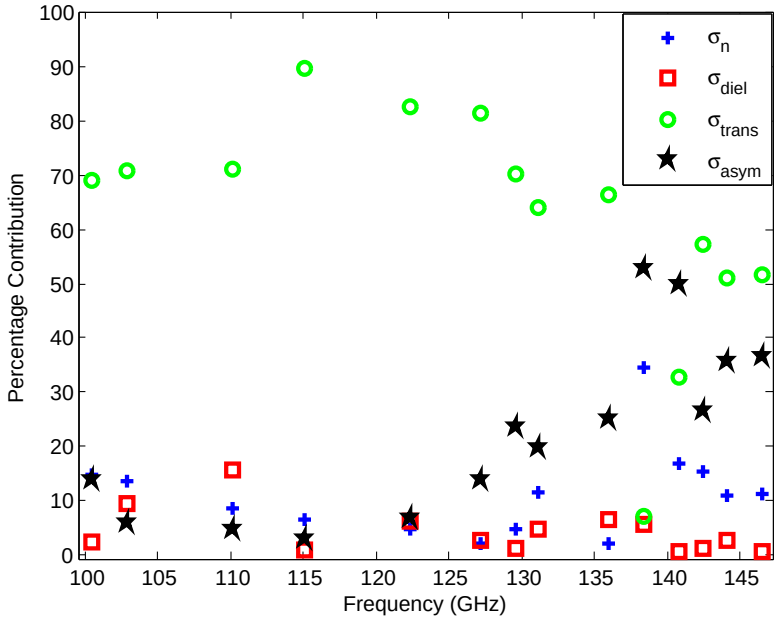

Figure 3.13: Percentage contribution of the different measurement uncertainties to the total uncertainty of the F band system at T=218 K.

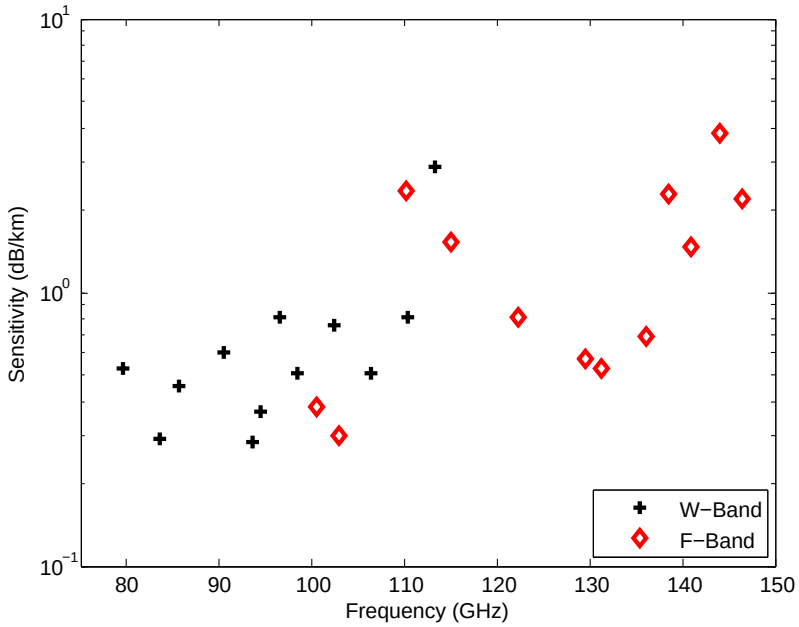

Figure 3.14: Measured system sensitivity at room temperature (T=297 K) in the 2–4 millimeter-wavelength range.

CHAPTER IV

COMPRESSIBILITY OF FLUIDS

The thermodynamic and transport behavior of pure fluids and their mixtures are controlled by the nature of the molecules and the intermolecular forces that exist between them. The simplest theory, the theory for ideal gases, assumes that point mass molecules with negligible volume are in constant, random motion, and elastically collide with each other. The duration of collision is assumed to be negligible when compared to the time between collisions and the intermolecular forces are assumed to be negligible when compared to the kinetic energy generated by the molecular collisions. The theory for ideal gases assumes that pressure arises because of molecular collisions and not because of static repulsions between molecules. The common form of the ideal gas law is

$$PV = nRT, \tag{4.1}$$

where P is the absolute pressure, V is the volume occupied by the gas, n is the molar density, R is the specific gas constant, and T is the absolute temperature. The ideal gas equation may also be written as

$$P = \rho RT, \tag{4.2}$$

where ρ is the density of the gas. Gases are hardly ideal under the conditions found in the deep planetary atmospheres. Real gases, as opposed to ideal gases, exhibit compressibility effects. For real gases, the intermolecular forces are very large and the force fields exhibited by the molecules are larger than the size of individual

molecules. Hence, there is indeed an action at a distance, albeit very weak. Real gases also undergo inelastic collisions (kinetic energy is not conserved). An approximate formulation for the behavior of real gases was first proposed by van der Waals (1873). Although the van der Waals equation of state provides a simple intuitive way to account for real gas behavior, it is rarely accurate. Over the years, numerous expressions have been developed to account for the behavior of real gases. To correct for non-ideality, the simplest equation of state uses a correction factor, known as the compressibility factor (Z):

$$PV = nZRT. \tag{4.3}$$

The Z factor can be considered as being the ratio of the volume occupied by the real gas to the volume occupied under the same temperature and pressure conditions if the gas were ideal. The factor Z is a function of temperature, pressure, and gas composition, and is often determined experimentally. If $Z = 1$, then the gas is considered ideal. If $Z <1$, then the molecular attractive forces dominate and hence the measured pressure (real pressure) appears to be less than the ideal pressure. If $Z >1$, the molecular repulsive forces dominate and hence the measured pressure appears to be greater than the ideal pressure.

To accurately study the thermophysical and thermochemical properties of the jovian atmospheres, highly precise equations of state of various molecular species are required. Pressure-explicit equations of state, such as the modified Benedict-Webb-Ruben (mBWR) equation of state, can be used for directly deriving pressure for a given gas density and temperature (Span, 2000). The Helmholtz free energy form is also frequently used to accurately represent the fundamental equations of state of pure substances. The thermodynamic fluid properties used in this work were obtained from the REFPROP database of the National Institute of Standards and Technology (NIST) (Lemmon et al., 2007) and subroutines were written in Matlab to access the

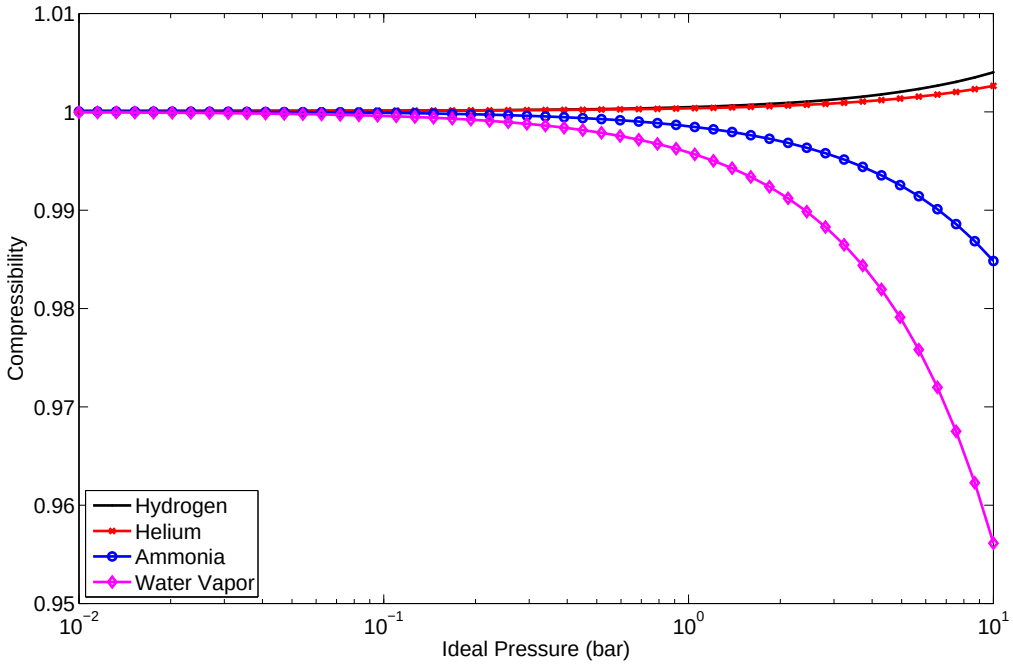

Figure 4.1: The compressibility of various pure fluids at 500 K as a function of pressure. For H_2 and He, the molecular repulsive forces dominate under these conditions and hence the measured pressure is greater than the ideal pressure. For NH_3 and H_2O, the molecular attractive forces dominate under these conditions and hence the measured pressure is less than the ideal pressure.

database. An example of the compressibilities of hydrogen, helium, ammonia, and water, in the 0.01–10 bar pressure range at 500 K, computed using the state of the art equations of state for these fluids (described later in this chapter) is shown in Figure 4.1.

In this work, the latest equations of state for pure fluids have been employed to compute their thermodynamic properties at pressures up to 100 bar. Under the ultra-high-pressure conditions characteristic of the very deep interiors of the jovian planets (pressures much greater than 100 bar), in addition to the breakdown of the ideal gas law for pure substances, Dalton's law of partial pressures also breaks down. Hence, in the ultra-high-pressure realm (while modeling the very deep interiors of the jovian atmospheres), the non-ideal nature of fluid mixtures should also be included, in addition to accounting for the non-ideality of pure fluids (Span, 2000).

4.1 Hydrogen

Hydrogen is the most abundant molecular species in the universe and constitutes more than 80% of the atmospheric composition of the jovian planets (Irwin, 2003). Depending on the relative orientation of the nuclear spin of the individual atoms in the hydrogen molecule, diatomic hydrogen can exist in either the lower-energy singlet "para" state (the nuclear spins are antiparallel) or higher-energy triplet "ortho" state (the nuclear spins are parallel). The equilibrium ratio of orthohydrogen and parahydrogen depends on the temperature. At very low temperatures, there is insufficient thermal energy to populate higher energy states and hence hydrogen exists exclusively in the "para" form (e.g., at 19 K, a sample of gaseous hydrogen is 99.75% parahydrogen, Leachman et al., 2009). As temperature is increased, the higher energy states are populated and the equilibrium shifts towards the "ortho" form. At 80 K, the equilibrium concentration is approximately 50% parahydrogen and 50% orthohydrogen. At room temperature, an equilibrium distribution of 75% orthohydrogen and 25% parahydrogen is reached. This 3:1 distribution, commonly referred as "normal hydrogen", is also maintained at temperatures above ambient room temperature since each of the four possible energy states will remain equally populated. Under the deep jovian conditions, hydrogen exists in the normal form and this section contains information about the currently accepted formulations for the thermodymanic properties of normal hydrogen available in REFPROP (Lemmon et al., 2007).

The equation of state for normal hydrogen has been formulated using the Helmholtz energy as the fundamental property with density and temperature as independent variables. The Helmholtz free energy (a) is expressed as

$$\frac{a(T,\rho)}{RT} = \alpha(\tau,\varrho), \tag{4.4}$$

where α is the reduced Helmholtz free energy, τ is the reciprocal of the reduced

temperature, and ϱ is the reduced density, given as

$$\tau = \frac{T_c}{T}, \tag{4.5}$$

$$\varrho = \frac{\rho}{\rho_c}, \tag{4.6}$$

where the subscript c denotes a critical-point property. The critical values for normal hydrogen are (Leachman et al., 2009)

$$T_c = 33.145 \quad \text{(K)}, \tag{4.7}$$

$$P_c = 1.2964 \quad \text{(MPa)}, \tag{4.8}$$

$$\rho_c = 31.26 \quad \text{(kg/m}^3\text{)}. \tag{4.9}$$

The reduced Helmholtz free energy is composed of the ideal gas component (α^0) and the residual component (α^r) which corresponds to the intermolecular forces:

$$\alpha(\tau, \varrho) = \alpha^0(\tau, \varrho) + \alpha^r(\tau, \varrho). \tag{4.10}$$

All thermodynamic properties can be calculated as the derivative of the Helmholtz free energy and are given in Span (2000). For example, pressure can be calculated from the Helmholtz free energy as

$$P = \rho RT \left(1 + \varrho \left(\frac{\partial \alpha^r}{\partial \varrho}\right)_\tau\right), \tag{4.11}$$

and compressibility is obtained as

$$Z = \frac{P}{\rho RT} = 1 + \varrho \left(\frac{\partial \alpha^r}{\partial \varrho}\right)_\tau. \tag{4.12}$$

The ideal gas Helmholtz free energy is expressed as

$$\alpha^0 = \frac{h^0}{RT} - 1 - \frac{s^0}{R}, \tag{4.13}$$

Table 4.1: Coefficients of the normal hydrogen ideal gas heat capacity equation.

k	u_k	v_k
1	1.616	531
2	-0.4117	751
3	-0.792	1989
4	0.758	2484
5	1.217	6859

where h^0 is the ideal gas enthalpy and s^0 is the ideal gas entropy. The ideal gas enthalpy is given as

$$h^0 = h_0^0 + \int_{T_0}^{T} c_p^0 dT, \tag{4.14}$$

and the ideal gas entropy is given as

$$s^0 = s_0^0 + \int_{T_0}^{T} \frac{c_p^0}{T} dT - R \log\left(\frac{\rho T}{\rho_0 T_0}\right), \tag{4.15}$$

where ${c_p}^0$ is the ideal gas heat capacity, and s_0^0 and h_0^0 are the ideal gas entropy and enthalpy at a reference density (ρ_0) and temperature (T_0). The ideal gas heat capacity (c_p^0) equation is given as

$$c_p^0 = 2.5R + R\sum_{k=1}^{N_l} u_k \left(\frac{v_k}{T}\right)^2 \frac{\exp(v_k/T)}{[\exp(v_k/T)-1]^2}, \tag{4.16}$$

and the coefficients u_k and v_k are listed in Table 4.2

Combining Equations 4.13-4.15, the reduced Helmholtz equation for normal hydrogen is given as

$$\alpha^0 = \frac{h_0^0 \tau}{RT_c} - \frac{s_0^0}{R} - 1 + \log\frac{\varrho\tau_0}{\varrho_0\tau} - \frac{\tau}{R}\int_{\tau_0}^{\tau} \frac{c_p^0}{\tau^2} d\tau + \frac{1}{R}\int_{\tau_0}^{\tau} \frac{c_p^0}{\tau} d\tau, \tag{4.17}$$

where $\varrho_0 = \rho_0/\rho_c$ and $\tau_0 = T_c/T_0$.

A computationally convenient parametrized form of the ideal part of the reduced Helmholtz free energy is given as (Leachman et al., 2009)

$$\alpha^0 = \log\varrho + 1.5\log(\tau) + a_1 + a_2\tau + \sum_{k=3}^{N_l} a_k \log[1-\exp(b_k\tau)]. \tag{4.18}$$

Table 4.2: Coefficients and parameters of the ideal part of the reduced Helmholtz free energy equation for normal hydrogen.

k	a_k	b_k
1	-1.4579856475	
2	1.888076782	
3	1.616	-16.0205159149
4	-0.4117	-22.6580178006
5	-0.792	-60.0090511389
6	0.758	-74.9434303817
7	1.217	-206.9392065168

For normal hydrogen, $N_l = 7$ and the coefficients a_k and b_k are listed in Table 4.2.

The residual contribution to the reduced Helmholtz free energy is given as

$$\alpha^r(\tau,\varrho) = \sum_{i=1}^{l} N_i \varrho^{d_i} \tau^{t_i} + \sum_{i=l+1}^{m} N_i \varrho^{d_i} \tau^{t_i} \exp(-\varrho^{p_i}) + \sum_{i=m+1}^{n} N_i \varrho^{d_i} \tau^{t_i} \exp[-\varphi_i(\varrho - \vartheta_i)^2 - \varkappa_i(\tau - \varsigma_i)^2], \tag{4.19}$$

where the first summation is a polynomial comprising seven terms ($l = 7$), with exponents d_i and t_i on the reduced density and temperature, respectively. The second summation consists of an exponential density component comprising two terms ($m = 9$) to aid in the calculation of liquid and critical-region properties. The third summation comprises of five modified Gaussian bell-shaped terms ($n = 14$) to accurately model the critical region. The values of the parameters and coefficients are given by Leachman et al. (2009) and listed in Table 4.3. The compressibility of pure normal hydrogen computed using the reduced Helmholtz free energy as a function of temperature and pressure is shown in Figure 4.2.

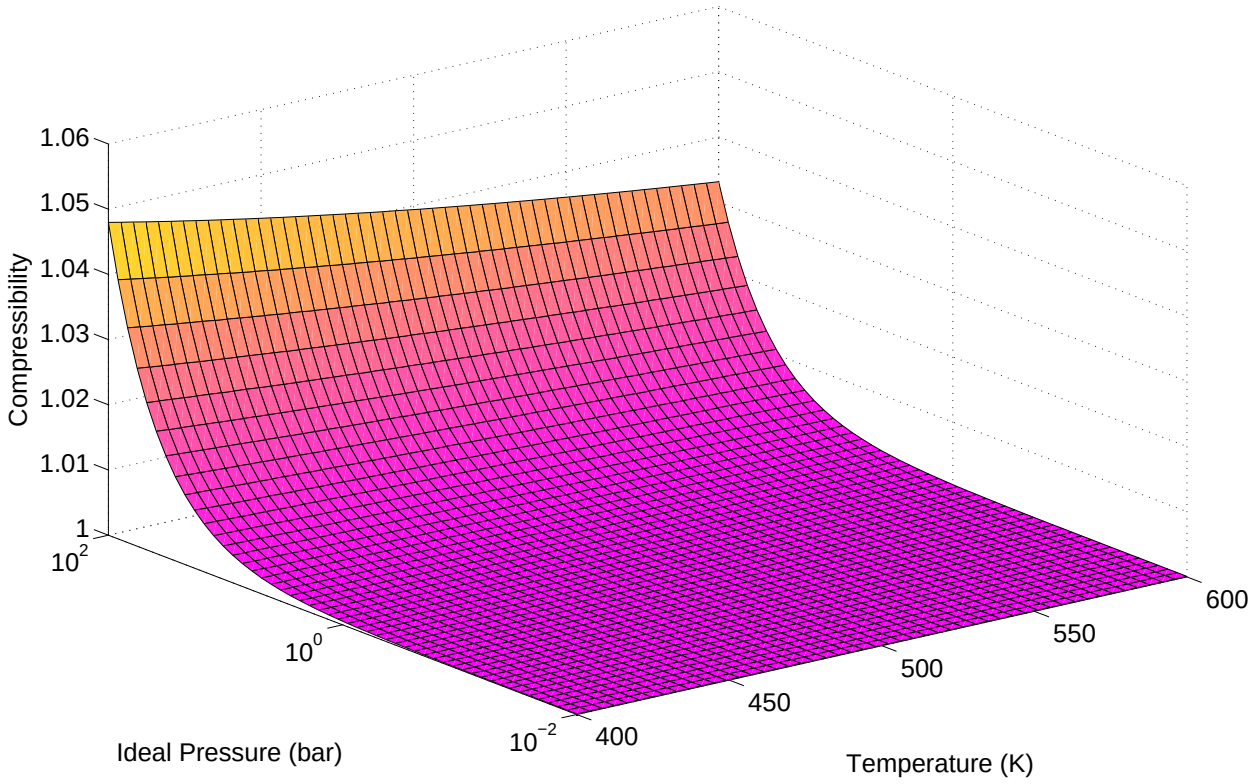

Figure 4.2: The compressibility (Z) of pure normal hydrogen.

Table 4.3: Parameters and coefficients of the residual part of the reduced Helmholtz free energy term for normal hydrogen.

i	N_i	t_i	d_i	p_i	φ_i	$\varkappa_i$	ς_i	ϑ_i
Polynomial								
1	-6.93643	0.6844	1					
2	0.01	1	4					
3	2.1101	0.989	1					
4	4.52059	0.489	1					
5	0.732564	0.803	2					
6	-1.34086	1.1444	2					
7	0.130985	1.409	3					
Exponential								
8	-0.777414	1.754	1	1				
9	0.351944	1.311	3	1				
Gaussian								
10	-0.0211716	4.187	2		1.685	0.171	0.7164	1.506
11	0.0226312	5.646	1		0.489	0.2245	1.3444	0.156
12	0.032187	0.791	3		0.103	0.1304	1.4517	1.736
13	-0.0231752	7.249	1		2.506	0.2785	0.7204	0.67
14	0.0557346	2.986	1		1.607	0.3967	1.5445	1.662

4.2 Helium

For pure helium, a modified Benedict-Webb-Rubin (mBWR) pressure-explicit equation of state developed by McCarty and Arp (1990) was used. The mBWR equation of state is given as

$$\begin{aligned} P = \rho R_0 T &+ \rho^2(N_1 T + N_2 T^{1/2} + N_3 + N_4/T + N_5/T^2) + \rho^3(N_6 T + N_7 + N_8/T + N_9/T^2) \\ &+ \rho^4(N_{10} T + N_{11} + N_{12}/T) + \rho^5(N_{13}) + \rho^6(N_{14}/T + N_{15}/T^2) + \rho^7(N_{16}/T) \\ &+ \rho^8(N_{17}/T + N_{18}/T^2) + \rho^9(N_{19}/T^2) + \rho^3(N_{20}/T^2 + N_{21}/T^3)\exp(-\Psi\rho^2) \\ &+ \rho^5(N_{22}/T^2 + N_{23}/T^4)\exp(-\Psi\rho^2) + \rho^7(N_{24}/T^2 + N_{25}/T^3)\exp(-\Psi\rho^2) \\ &+ \rho^9(N_{26}/T^2 + N_{27}/T^4)\exp(-\Psi\rho^2) + \rho^{11}(N_{28}/T^2 + N_{29}/T^3)\exp(-\Psi\rho^2) \\ &+ \rho^{13}(N_{30}/T^2 + N_{31}/T^3 + N_{32}/T^4)\exp(-\Psi\rho^2), \end{aligned} \tag{4.20}$$

Table 4.4: Coefficients of the mBWR equation of state for helium.

$N_1 = 0.4558980227431 \times 10^{-4}$	$N_{17} = 0.6446881346448 \times 10^{-12}$
$N_2 = -0.1260692007853 \times 10^{-2}$	$N_{18} = 0.3298960057071 \times 10^{-10}$
$N_3 = -0.7139657549318 \times 10^{-2}$	$N_{19} = -0.3555585738784 \times 10^{-12}$
$N_4 = 0.9728903861441 \times 10^{-2}$	$N_{20} = -0.6885401367690 \times 10^{-2}$
$N_5 = -0.1589302471562 \times 10^{-1}$	$N_{21} = 0.9166109232806 \times 10^{-2}$
$N_6 = 0.1454229259623 \times 10^{-5}$	$N_{22} = -0.6544314242937 \times 10^{-5}$
$N_7 = -0.4708238429298 \times 10^{-4}$	$N_{23} = -0.3315398880031 \times 10^{-4}$
$N_8 = 0.1132915223587 \times 10^{-2}$	$N_{24} = -0.2067693644676 \times 10^{-7}$
$N_9 = 0.2410763742104 \times 10^{-2}$	$N_{25} = 0.3850153114958 \times 10^{-7}$
$N_{10} = -0.5093547838381 \times 10^{-8}$	$N_{26} = -0.1399040626999 \times 10^{-10}$
$N_{11} = 0.2699726927900 \times 10^{-5}$	$N_{27} = -0.1888462892389 \times 10^{-11}$
$N_{12} = -0.3954146691114 \times 10^{-4}$	$N_{28} = -0.4595138561035 \times 10^{-14}$
$N_{13} = 0.1551961438127 \times 10^{-8}$	$N_{29} = 0.6872567403738 \times 10^{-14}$
$N_{14} = 0.1050712335785 \times 10^{-7}$	$N_{30} = -0.6097223119177 \times 10^{-18}$
$N_{15} = -0.5501158366750 \times 10^{-7}$	$N_{31} = -0.7636186157005 \times 10^{-17}$
$N_{16} = -0.1037673478521 \times 10^{-9}$	$N_{32} = 0.3848665703556 \times 10^{-17}$
$R = 0.008314310$	

where $\Psi = 1/\rho_c^2$. The critical values for helium are (McCarty and Arp, 1990)

$$T_c = 5.1953 \quad \text{(K)}, \tag{4.21}$$

$$P_c = 0.22746 \quad \text{(MPa)}, \tag{4.22}$$

$$\rho_c = 69.3 \quad (\text{kg/m}^3) \quad = \quad 17.399 \quad \text{(mol/L)}. \tag{4.23}$$

The coefficients used in the mBWR equation are provided in Table 4.4. The pressure P is in MPa, density ρ is in mol/L, and temperature T in K. The compressibility of pure helium computed using the mBWR equation as a function of temperature and pressure is shown in Figure 4.3.

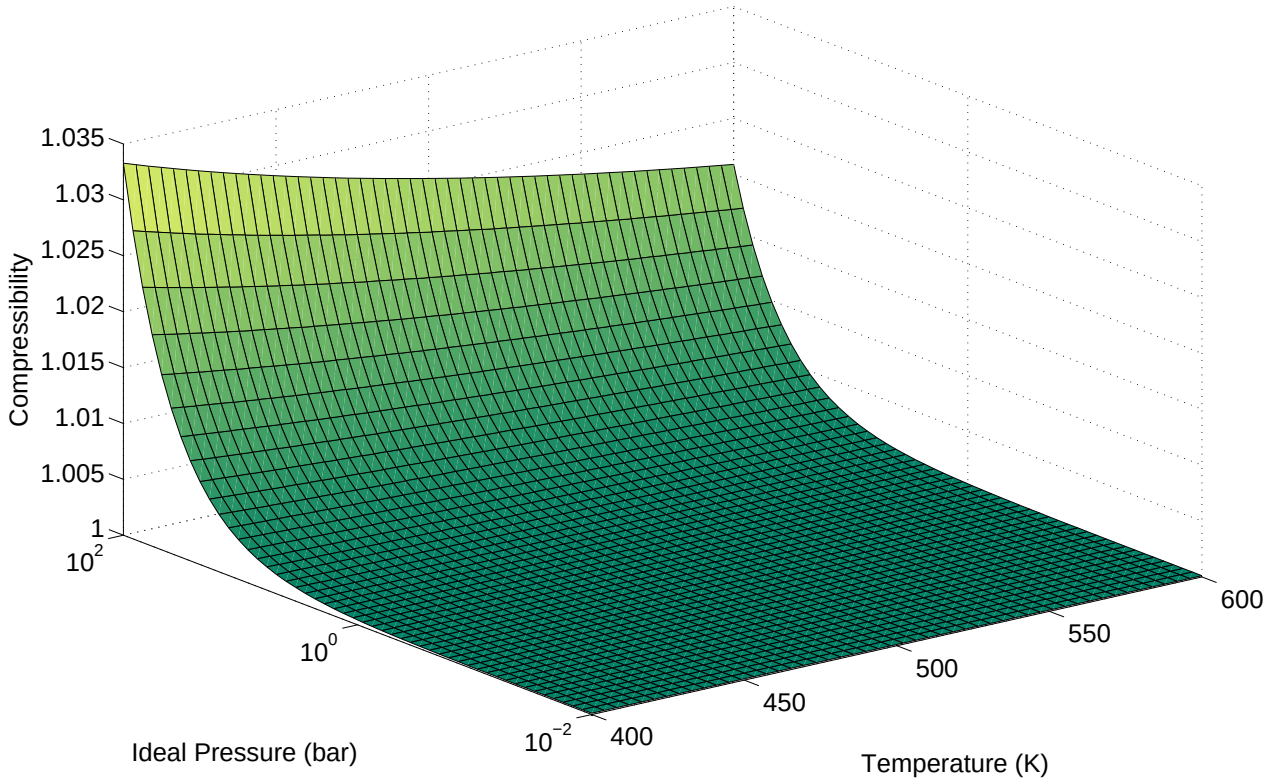

Figure 4.3: The compressibility (Z) of pure helium.

4.3 Ammonia

For modeling the equation of state for pure ammonia, the formulations given by Tillner-Roth et al. (1993) was used. The critical quantities for ammonia are taken as (Tillner-Roth et al., 1993)

$$T_c = 404.45 \quad (\mathrm{K}), \tag{4.24}$$

$$P_c = 11.333 \quad (\mathrm{MPa}), \tag{4.25}$$

$$\rho_c = 225 \quad (\mathrm{kg/m^3}). \tag{4.26}$$

The ideal part of the reduced Helmholtz free energy is expressed as (Tillner-Roth et al., 1993)

$$\alpha^0(\tau, \varrho) = ln(\varrho) + a_1^0 + a_2^0\tau - ln(\tau) + a_3^0\tau^{1/3} + a_4^0\tau^{-3/2} + a_5^0\tau^{-7/4}, \tag{4.27}$$

where the coefficients are listed in Table 4.5.

The residual part of the reduced Helmholtz free energy for ammonia is expressed as (Tillner-Roth et al., 1993)

$$\begin{aligned}\alpha^r = &\sum_{i=1}^{5} a_i\tau^{t_i}\varrho^{d_i} + \exp(-\varrho)\sum_{i=6}^{10} a_i\tau^{t_i}\varrho^{d_i} \\ &+ \exp(-\varrho^2)\sum_{i=11}^{17} a_i\tau^{t_i}\varrho^{d_i} + \exp(-\varrho^3)\sum_{i=18}^{21} a_i\tau^{t_i}\varrho^{d_i},\end{aligned} \tag{4.28}$$

Table 4.5: Coefficients of the ideal part of the reduced Helmholtz free energy for ammonia.

k	a_k
1	-15.81502
2	4.255726
3	11.47434
4	-1.296211
5	0.5706757

Table 4.6: Parameters and coefficients of the residual part of the reduced Helmholtz free energy for ammonia.

i	a_i	t_i	d_i
Polynomial			
1	0.04554431	-0.5	2
2	0.7238548	0.5	1
3	0.01229470	1	4
4	-1.858814	1.5	1
5	0.2141882×10^{-10}	3	15
Exponential			
6	-0.0143002	0	3
7	0.3441324	3	3
8	-0.2873571	4	1
9	0.2352589×10^{-4}	4	8
10	-0.03497111	5	2
11	0.02397852	3	1
12	0.001831117	5	8
13	-0.04085375	6	1
14	0.2379275	8	2
15	-0.03548972	8	3
16	-0.1823729	10	2
17	0.02281556	10	4
18	-0.006663444	5	3
19	-0.008847486	7.5	1
20	0.002272635	15	2
21	-0.0005588655	30	4

where the first summation is a polynomial comprising five terms, with exponents d_i and t_i on the reduced density and temperature, respectively. The remaining summation terms consists of exponential density components to aid in the calculation of liquid and critical-region properties. The values of the parameters and coefficients are given by Tillner-Roth et al. (1993) and listed in Table 4.6. The compressibility of pure ammonia computed using the reduced Helmholtz free energy equation as a function of temperature and pressure is shown in Figure 4.4.

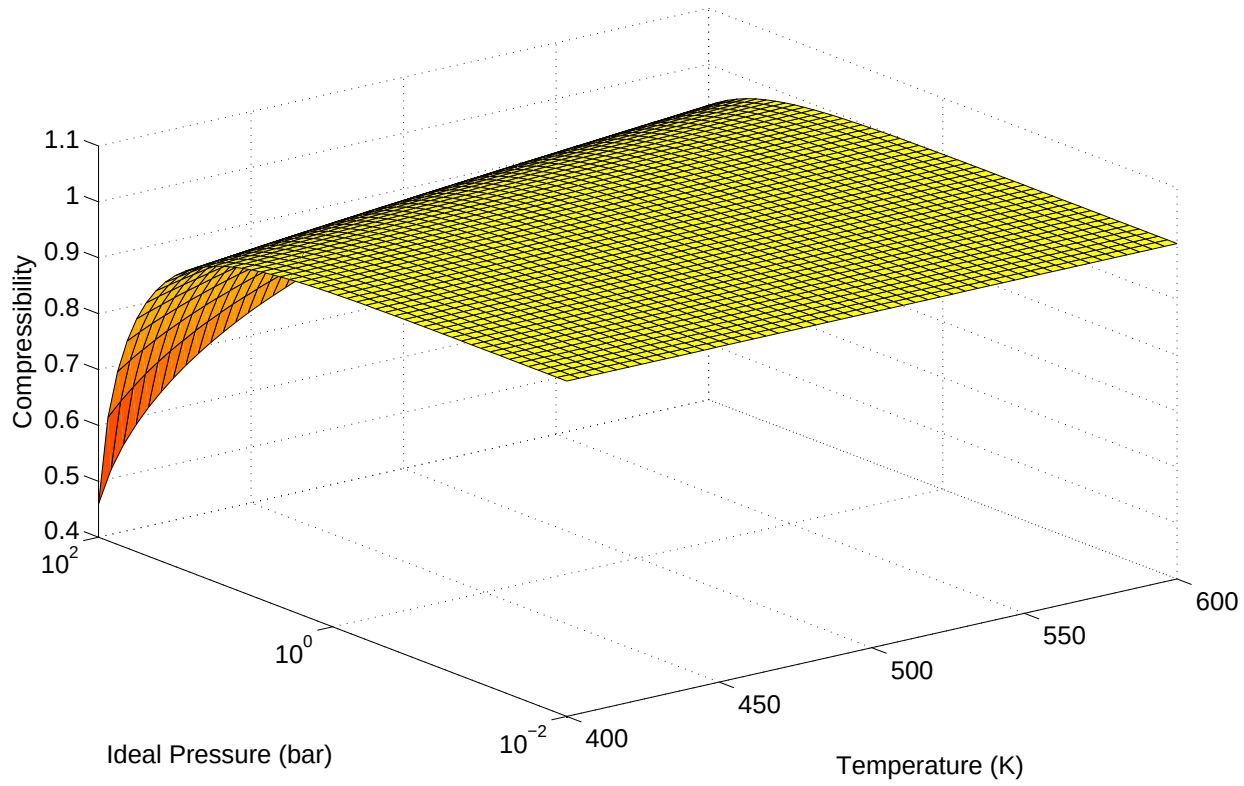

Figure 4.4: The compressibility (Z) of pure ammonia.

4.4 Water

The latest formulation for the equation of state for water employs the reduced Helmholtz free energy equation. The critical quantities for water are taken as (Wagner and Pruß, 2002)

$$T_c = 647.096 \quad (\mathrm{K}), \tag{4.29}$$

$$P_c = 22.064 \quad (\mathrm{MPa}), \tag{4.30}$$

$$\rho_c = 322 \quad (\mathrm{kg/m^3}). \tag{4.31}$$

The ideal part of the reduced Helmholtz free energy for water is given as (Wagner and Pruß, 2002)

$$\alpha_0 = ln(\varrho) + n_1^0 + n_2^0\tau + n_3^0 ln(\tau) + \sum_{i=4}^{8} n_i^0 ln(1 - \exp(-\gamma_i^0\tau)). \tag{4.32}$$

The coefficients and parameters of the ideal part of the reduced Helmholtz free energy for water are listed in Table 4.7.

The residual contribution to the reduced Helmholtz free energy is given as

$$\begin{aligned}\alpha^r(\tau,\varrho) = &\sum_{i=1}^{l} N_i \varrho^{d_i} \tau^{t_i} + \sum_{i=l+1}^{m} N_i \varrho^{d_i} \tau^{t_i} \exp(-\varrho^{p_i}) \\ &+ \sum_{i=m+1}^{n} N_i \varrho^{d_i} \tau^{t_i} \exp[-\varphi_i(\varrho - \vartheta_i)^2 - \varkappa_i(\tau - \varsigma_i)^2] + \sum_{i=n+1}^{p} N_i \Upsilon^{b_i} \varrho\psi,\end{aligned} \tag{4.33}$$

Table 4.7: Coefficients and parameters of the ideal part of the reduced Helmholtz free energy for water.

i	n_i^0	γ_i^0
1	-8.32044648201	-
2	6.6832105268	-
3	3.00632	-
4	0.012436	1.28728967
5	0.97315	3.53734222
6	1.27950	7.74073708
7	0.96956	9.24437796
8	0.24873	27.5075105

where the first summation is a polynomial comprising seven terms ($l = 7$), with exponents d_i and t_i on the reduced density and temperature, respectively. The second summation consists of an exponential density component comprising 45 terms ($m = 51$), the third summation comprises of three modified Gaussian bell-shaped terms ($n = 54$), and the fourth summation comprises of two critical terms ($p = 56$). The critical term components are given as

$$\Upsilon = \Theta^2 + B_i[(\varrho - 1)^2]^{a_i}, \tag{4.34}$$

$$\Theta = (1 - \tau) + A_i[(\varrho - 1)^2]^{1/2\beta_i}, \tag{4.35}$$

$$\psi = \exp(-C_i[\varrho - 1]^2 - D_i[\tau - 1]^2). \tag{4.36}$$

The values of the parameters and coefficients are given by Wagner and Pruß (2002) and listed in Table 4.8. The compressibility of pure water computed using the reduced Helmholtz energy formulation as a function of temperature and pressure is shown in Figure 4.5.

Table 4.8: Parameters and coefficients of the residual part of the reduced Helmholtz free energy for water.

i	c_i	d_i	t_i	N_i
Polynomial				
1	-	1	-0.5	$0.12533547935523\times10^{-1}$
2	-	1	0.875	$0.78957634722828\times10^{1}$
3	-	1	1	$-0.87803203303561\times10^{1}$
4	-	2	0.5	0.31802509345418
5	-	2	0.75	-0.26145533859358
6	-	3	0.375	$-0.78199751687981\times10^{-2}$
7	-	4	1	$0.88089493102134\times10^{-2}$
Exponential				
8	1	1	4	-0.66856572307965

i	c_i	d_i	t_i	N_i
9	1	1	6	0.20433810950965
10	1	1	12	-0.66212605039687$\times 10^{-4}$
11	1	2	1	-0.19232721156002
12	1	2	5	-0.25709043003438
13	1	3	4	0.16074868486251
14	1	4	2	-0.40092828925807$\times 10^{-1}$
15	1	4	13	0.39343422603254$\times 10^{-6}$
16	1	5	9	-0.75941377088144$\times 10^{-5}$
17	1	7	3	0.56250979351888$\times 10^{-3}$
18	1	9	4	-0.15608652257135$\times 10^{-4}$
19	1	10	11	0.11537996422951$\times 10^{-8}$
20	1	11	4	0.36582165144204$\times 10^{-6}$
21	1	13	13	-0.13251180074668$\times 10^{-11}$
22	1	15	1	-0.62639586912454$\times 10^{-9}$
23	2	1	7	-0.10793600908932
24	2	2	1	0.17611491008752$\times 10^{-1}$
25	2	2	9	0.22132295167546
26	2	2	10	-0.40247669763528
27	2	3	10	0.58083399985759
28	2	4	3	0.49969146990806$\times 10^{-2}$
29	2	4	7	-0.31358700712549$\times 10^{-1}$
30	2	4	10	-0.74315929710341
31	2	5	10	0.47807329915480
32	2	6	6	0.20527940895948$\times 10^{-1}$
33	2	6	10	-0.13636435110343
34	2	7	10	0.14180634400617$\times 10^{-1}$
35	2	9	1	0.83326504880713$\times 10^{-2}$
36	2	9	2	-0.29052336009585$\times 10^{-1}$
37	2	9	3	0.38615085574206$\times 10^{-1}$
38	2	9	4	-0.20393486513704$\times 10^{-1}$
39	2	9	8	-0.16554050063734$\times 10^{-2}$
40	2	10	6	0.19955571979541$\times 10^{-2}$
41	2	10	9	0.15870308324157$\times 10^{-3}$
42	2	12	8	-0.16388568342530$\times 10^{-4}$
43	3	3	16	0.43613615723811$\times 10^{-1}$
44	3	4	22	0.34994005463765$\times 10^{-1}$
45	3	4	23	-0.76788197844621$\times 10^{-1}$

i	c_i	d_i	t_i	N_i				
46	3	5	23	$0.224462773320\times10^{-1}$				
47	4	14	10	$-0.62689710414685\times10^{-4}$				
48	6	3	50	$-0.55711118565645\times10^{-9}$				
49	6	6	44	-0.19905718354408				
50	6	6	46	0.31777497330738				
51	6	6	50	-0.11841182425981				
Gaussian								
i	c_i	d_i	t_i	N_i	φ_i	$\varkappa_i$	ς_i	ϑ_i
52	-	3	0	$-0.31306260323435\times10^{2}$	20	150	1.21	1
53	-	3	1	$0.31546140237781\times10^{2}$	20	150	1.21	1
54	-	3	4	$-0.25213154341695\times10^{4}$	20	250	1.25	1
Critical								
i	c_i	d_i	t_i	N_i	C_i	D_i	A_i	β_i
55	3.5	0.85	0.2	-0.14874640856724	28	700	0.32	0.3
56	3.5	0.95	0.2	0.31806110878444	32	800	0.32	0.3

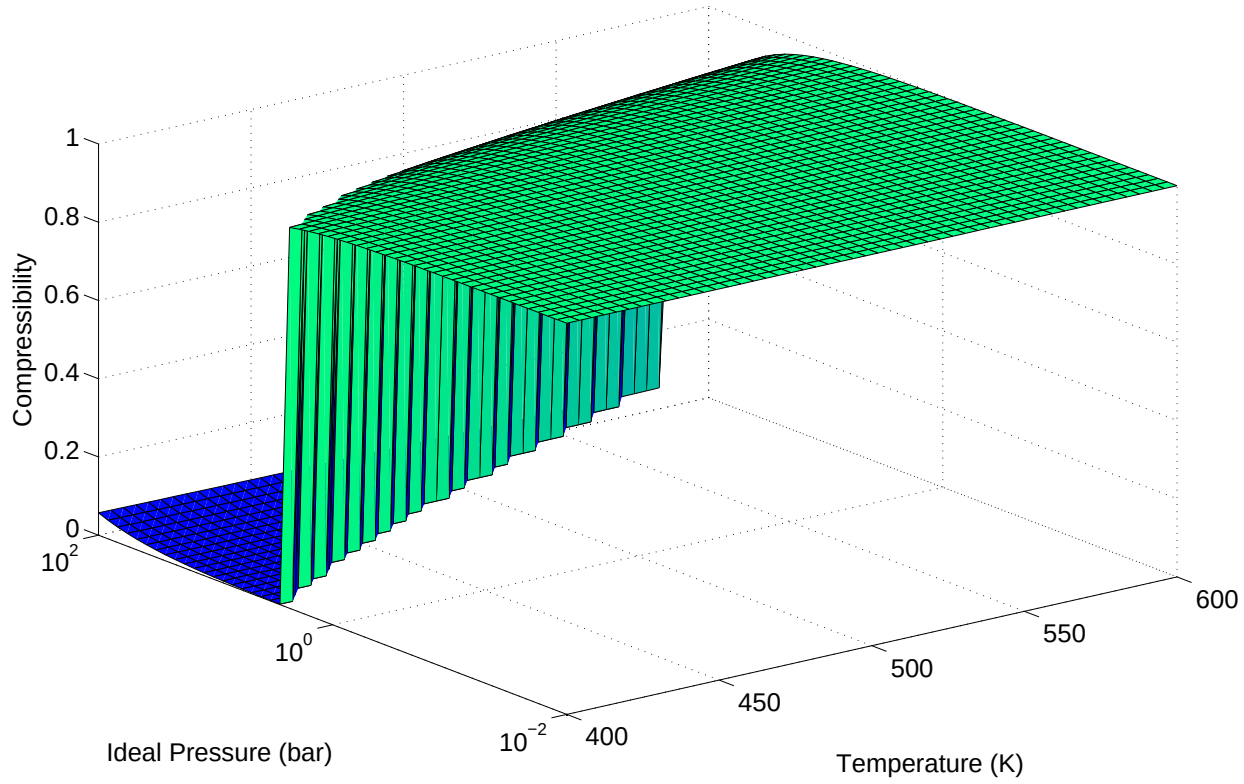

Figure 4.5: The compressibility (Z) of pure water.

CHAPTER V

MEASUREMENTS AND MODEL

One of the primary objectives of this work has been to develop a consistent formalism for the centimeter- and millimeter-wavelength opacity of ammonia under jovian atmospheric conditions. The model is based on an extensive set of measurements of the opacity of ammonia conducted as part of this work and previous measurements conducted by Hanley et al. (2009). A dry jovian adiabatic temperature-pressure (TP) profile overlayed with the TP distribution of the centimeter- and millimeter-wavelength measurement points that were used in the model development and/or assessment of the model performance are shown in Figure 5.1.

5.1 Millimeter-Wavelength Ammonia Opacity Measurements

Over 1000 high-accuracy measurements of the 2–4 mm-wavelength absorptive properties of pure ammonia and ammonia pressure-broadened by hydrogen and helium have been conducted using the millimeter-wavelength measurement system. Certified ultra-high-purity (UHP grade) ammonia and premixed hydrogen/helium gas cylinders from Airgas, Inc. were used for the experiments and certified UHP grade argon and carbon dioxide gas cylinders were used for dielectric matching experiments. In the premixed hydrogen/helium cylinder, the helium mixing ratio was (13.6±0.272)% and the remainder was hydrogen. This is approximately the helium mole fraction at Jupiter measured by von Zahn et al. (1998). A total of 718 data points of the opacity of ammonia in a hydrogen/helium environment and 295 data points of the opacity of pure ammonia were measured with each data point uniquely representing a combination of pressure, temperature, mixing ratio, and frequency.

Table 5.1: Listing of all experimental conditions for the 2–4 mm-wavelength ammonia opacity measurements conducted using the Fabry–Perot resonator as part of this work.

Experiment Dates	Temperature (K)	Pressure (bar)	NH_3 Mole Fraction	Frequency (GHz)
06/2007–10/2007	295	1–3	0.02–0.04	75–120
12/2007–02/2008	222	1–3	0.02	75–120
08/2008–09/2008	295	1–3	0.02–0.04	110–150
10/2008–11/2008	295	0.1–1	1	110–150
11/2008–12/2008	295	0.1–1	1	75–120
01/2009–02/2009	222	0.1–3	0.02–1	110–150
02/2009–03/2009	222	0.1–3	0.02–1	75–120
03/2009–04/2009	205	0.1–3	0.02–1	110–150
04/2009–05/2009	205	0.1–3	0.02–1	75–120

Pure ammonia opacity measurements were made to accurately characterize its self-broadening parameters. Table 5.1 lists the measurements taken along with the experiment dates. The processed data are provided online (*NH3_mmwavelength.dat*) at `http://users.ece.gatech.edu/~psteffes/palpapers/models.html`.

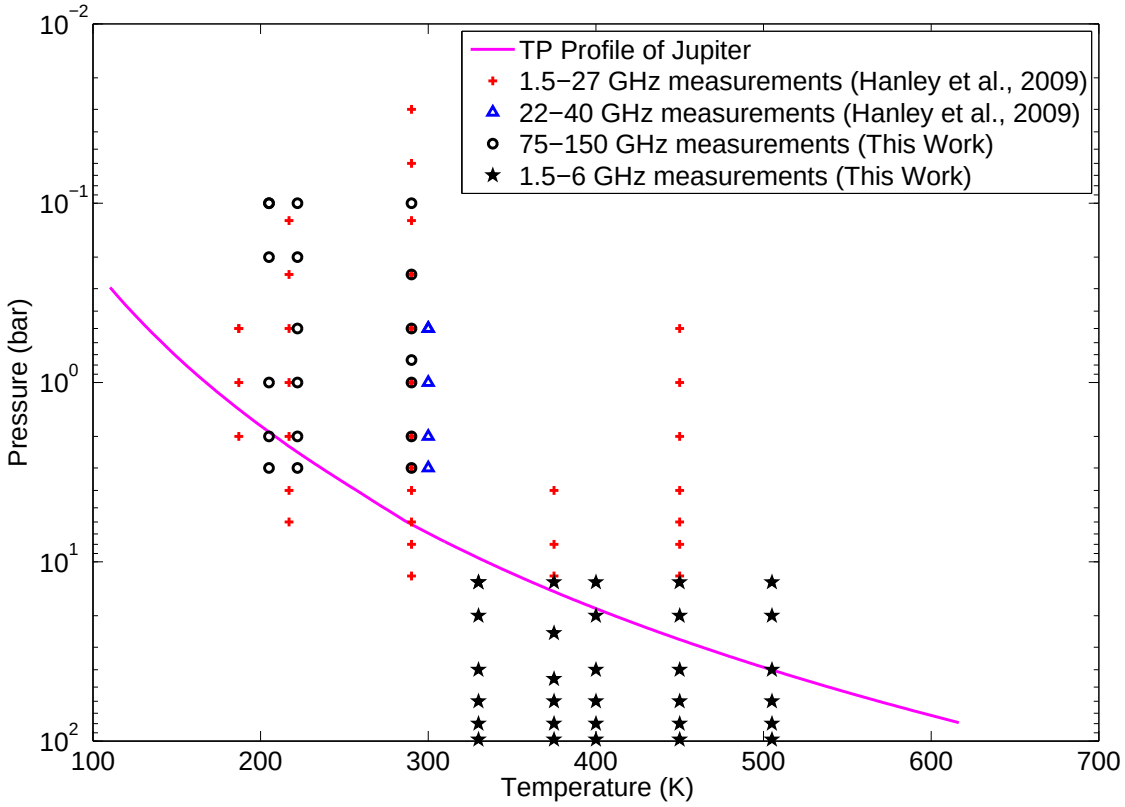

Figure 5.1: Dry jovian adiabatic temperature-pressure (TP) profile along with the TP space measurement points used in the model development and/or evaluation of the new model performance. Red crosses are the 1.5–27 GHz cavity resonator TP space points measured by Hanley et al. (2009), blue triangles are the 22–40 GHz FPR TP space points measured by Hanley et al. (2009), black circles are the 75–150 GHz FPR TP space points measured as part of this work, and black asterisks are the 1.5–6 GHz high-pressure TP space points measured as part of this work.

5.2 High-Pressure Centimeter-Wavelength Ammonia Opacity Measurements

This measurement process involved an extensive series of measurements of the opacity of ammonia under simulated deep jovian conditions at pressures up to 100 bar and temperatures up to 500 K. A total of 1176 measurements of the 5–20 cm-wavelength absorptive properties of pure ammonia and ammonia broadened by hydrogen and/or helium have been made using the high-pressure centimeter-wavelength measurement system. Certified UHP grade ammonia, helium, hydrogen, and argon gas cylinders from Airgas, Inc. were used for the experiments and dielectric matching. Each measurement sequence first involved the addition of gaseous ammonia to an evacuated chamber up to the desired pressure, and pure ammonia measurements were made to accurately characterize its self-broadening parameters. In this work, pure ammonia measurements were made in the 0.046–0.133 bar pressure range. Gaseous helium was then added to the system up to the desired pressure and ammonia/helium mixture measurements were made to accurately characterize the helium-broadening parameters. The ammonia/helium mixture measurements were made in the 7–20 bar pressure range. Gaseous hydrogen was then added to the pressure vessel, in 10–20 bar pressure increments, and the ammonia/helium/hydrogen mixture measurements were made at pressures up to 100 bar. A few measurements of the ammonia/hydrogen mixture opacity at pressures up to 100 bar were also made to accurately characterize the hydrogen-broadening parameters. A total of 180 data points of the opacity of pure ammonia, 156 data points of the opacity of ammonia/helium mixture, 120 data points of the opacity of ammonia/hydrogen mixture, and 720 data points of the opacity of ammonia/helium/hydrogen mixture were measured, with each data point uniquely representing a combination of pressure, temperature, mixing ratio, and frequency. Table 5.2 lists the measurements taken along with the experiment dates. The pressure values provided in the table correspond to the measured

Table 5.2: Listing of all experiment sequences of the 5–20 cm-wavelength ammonia opacity measurements conducted using the high-pressure system as part of this work.

Experiment Dates	Temperature (K)	Maximum Pressure (bar)	NH_3 Pressure (bar)	He Pressure (bar)
09/2009	376.0	94.66	0.0899	12.53
09/2009	375.5	95.51	0.0798	13.63
10/2009	375.2	96.11	0.0580	14.0
10/2009	373.2	95.59	0.1096	11.92
11/2009	446.5	95.34	0.1	7.35
12/2009	446.8	93.54	0.0824	0
12/2009	446.6	94.01	0.0805	19.07
01/2010	322.6	92.66	0.0838	16.55
02/2010	332.9	91.73	0.0462	15.58
02/2010	401.0	96.17	0.0813	11.98
03/2010	452.1	97.6	0.133	12.42
09/2010	503.6	94.17	0.0850	16.64
10/2010	502.8	89.99	0.0662	9.40
11/2010	502.6	96.47	0.1046	0
11/2010	502.1	98.44	0.1248	10.75

maximum pressure readings of the DPI pressure gauges or the pressure transducer. The processed data are provided online (*NH3_cmwavelength_highpressure.dat*) at `http://users.ece.gatech.edu/~psteffes/palpapers/models.html`.

5.3 Data Fitting

One of the primary goals of this work has been to develop a model, based on highly accurate laboratory measurements, that can be used to estimate the opacity of ammonia in a hydrogen/helium atmosphere under diverse conditions in the frequency/temperature/ pressure/concentration (fTPC) space. For the data fitting process, the FPR measurements of the 75–150 GHz opacity of ammonia and the high-pressure cavity resonator measurements of the 1.5–6 GHz opacity of ammonia, made as part of this work, along with the cavity resonator measurements of the 1.5–27 GHz opacity of ammonia made by Hanley et al. (2009) were utilized so as to obtain a consistent model in the fTPC space. The FPR measurements of the 22–40 GHz opacity

of ammonia made by Hanley et al. (2009) were not used in the model development process, but instead were used to evaluate the model performance. The method used for data fitting was a Levenberg–Marquardt optimization technique (Levenberg, 1944; Marquardt, 1963) with a minimization function

$$\chi = \frac{\sqrt{DW} \times (\alpha_{measured} - \alpha_{model})}{\sigma_{measured}}, \tag{5.1}$$

where DW is the data weight assigned to each data point, $\alpha_{measured}$, α_{model}, and $\sigma_{measured}$ are the measured opacity, modeled opacity of the model under optimization, and measured uncertainty in opacity, respectively. The measured uncertainty in opacity is calculated as

$$\sigma_{measured} = \sigma_{tot} + \sigma_{cond}, \tag{5.2}$$

where σ_{tot} is the total measurement uncertainty and σ_{cond} is the uncertainty due to measurement conditions. The sum of squared value of the χ function was minimized multiple times using random input seed values until a convergent solution was found. The data weight is given as (Hanley et al., 2009)

$$DW = \frac{1}{n_f} + \frac{1}{n_T} + \frac{1}{n_P} + \frac{1}{n_C}, \tag{5.3}$$

where n_f, n_T, n_P, and n_C represent the number of measurements conducted at each frequency, temperature, pressure, and gas concentration range, in the four-dimensional fTPC space. The approach used divides the data points into roughly equally spaced bins that span the fTPC space and each data point is scaled with its data weight so as to prevent the accuracy of the derived model from being skewed toward the most often measured conditions. The data fitting process was done in two stages in this work. In the first stage, the free parameters for the rotational and ν_2 roto-vibrational transitions were estimated using a measurement database consisting

of the 75–150 GHz FPR measurements made as part of this work and the 1.5–27 GHz cavity resonator measurements conducted by Hanley et al. (2009). Nominal values of the free parameters for the inversion transitions were also obtained in this stage and later revised during the second stage of data fitting. In the second stage, the 1.5–6 GHz high-pressure data points were added to the measurement database and the free parameters for the inversion transitions were estimated.

In the first stage of data fitting, the 75–150 GHz FPR measurements and the 1.5–27 GHz cavity resonator measurements were used to create the fTPC space. The breakdown of the fTPC space is listed in Table 5.3. The free parameters for pure ammonia were estimated before those for hydrogen/helium. The pure ammonia measurements were divided into two groups with one group constituting the data points with $f \leq$100 GHz (group I) and the other group constituting the data points with $f >$ 100 GHz (group II). For the data points in group I, the inversion and rotational transitions of ammonia contribute significantly to the measured opacity and the contribution from the ν_2 roto-vibrational transitions is negligible. The ν_2 roto-vibrational transitions contribute significantly to the measured opacity when $f >$ 100 GHz. Data fitting was achieved for group I by optimizing the ammonia free parameters for the inversion and rotational transitions. After this step, group II data points were used for optimization of the ammonia free parameters for the ν_2 roto-vibrational transitions. Subsequent optimization steps involved assigning the values obtained from the previous optimization steps to the ammonia free parameters and optimizing only the hydrogen and helium free parameters using the ammonia/hydrogen/helium mixture measurements. The mixture measurements were subdivided into two groups: group III comprising the data points with $f \leq$ 100 GHz and group IV comprising the data points with $f >$ 100 GHz. The hydrogen and helium free parameters for the inversion and rotational transitions were optimized using group III data points and the hydrogen and helium free parameters for the ν_2 roto-vibrational transitions were optimized

Table 5.3: The breakdown in the fTPC space of the measurement database consisting of the 75–150 GHz FPR measurements (this work) and the 1.5–27 GHz cavity resonator measurements (Hanley et al., 2009) used in the first stage of optimization.

Frequency range (GHz)	n_f	Temperature range (K)	n_T	Pressure range (bar)	n_P	Concentration range (%)	n_C
f<6	874	T<210	291	P<0.5	459	C<0.5	380
6≤f<27	557	210≤T<230	650	0.5≤P<1	213	0.5≤C<1	578
75≤f<100	329	230≤T<300	1195	1≤P<2	533	1≤C<4	481
100≤f< 120	393	300≤T<380	112	2≤P<5	761	4≤C<10	557
120≤f<150	291	380≤T<450	196	5≤P≤12.5	478	10≤C≤100	448

using group IV data points. This procedure was repeated several times with different input seed values for the free parameters, until a convergent solution was obtained. The final values for the free parameters for the rotational and ν_2 roto-vibrational transitions of ammonia were obtained after the first stage of optimization. The nominal values for the free parameters for the inversion transitions that were obtained after the first stage of optimization were revised during the second stage of optimization.

The nominal values that were obtained for the inversion transitions of ammonia after the first stage of optimization, could in fact be used to estimate the centimeter-wavelength ammonia opacity under jovian conditions at pressures up to 12 bar (Devaraj et al., 2011). However, these nominal values cannot be used under the deep jovian conditions because they were not optimized to perform under those conditions. To obtain a consistent formalism that can operate under diverse pressure conditions, two sets of free parameters for the inversion transitions of ammonia were estimated in the second stage of optimization. One set of parameters is used for modeling ammonia opacity at pressures less than 15 bar and a second set of parameters is used for modeling the ammonia opacity at pressures greater than 15 bar and up to 100 bar. It was possible to obtain a consistent model that performs well in both the low-pressure and the high-pressure regimes, by using two sets of parameters for the inversion transitions and incorporating a pressure-dependent switch.

The fTPC space for the second stage of data fitting includes the 1.5–6 GHz high-pressure measurements in addition to the 1.5–27 GHz measurements conducted by Hanley et al. (2009), and the 75–150 GHz FPR measurements conducted as part of this work. The breakdown in the fTPC space of the measurement database used in the second stage of optimization is listed in Table 5.4. In this stage of data fitting, only the free parameters for the inversion transitions were optimized. To best fit the measured data, two sets of parameters for the inversion transitions were derived, and a pressure-dependent switch was included in the model to assure consistent results over the wide pressure range (a few bar to hundreds of bar) characteristic of the middle and deep tropospheres of the jovian planets. This was, however, not required for the rotational and the ν_2 roto-vibrational transitions of ammonia since these transitions occur at very high frequencies (the first rotational transition of ammonia occurs at 572 GHz and the first strong ν_2 inversion transition of ammonia occurs at 140.14 GHz) and the jovian atmospheric layers that contribute to the emission at these frequencies have pressures less than a few bar (upper and middle tropospheres of the jovian planets). For example, the atmospheric layers of Jupiter that contribute to the emission at 140 GHz have pressures between 0.5 and 3 bar, whereas at 1 GHz, the contribution is from the atmospheric layers with pressures between 20 and 300 bar. Hence, it was sufficient to derive two sets of parameters (low-pressure and high-pressure) for the inversion transitions alone.

In the second stage of data fitting, the measurements were split into two groups (group V and group VI), with group V consisting of the data points with $P <= 15$ bar and group VI consisting of data points with $P > 15$ bar. The pure ammonia measurements were used to obtain the ammonia free parameters for the inversion transitions. Since the pure ammonia measurements were made under low-pressure conditions ($P < 0.8$ bar), only one set of parameters were estimated. The ammonia/helium mixture measurements with $P <= 15$ bar (group V) were used to obtain

Table 5.4: The breakdown in the fTPC space of the measurement database consisting of the 75–150 GHz FPR measurements (this work), 1.5–27 GHz cavity resonator measurements (Hanley et al., 2009), and the 1.5–6 GHz high-pressure measurements (this work) used in the second stage of optimization.

Frequency range (GHz)	n_f	Temperature range (K)	n_T	Pressure range (bar)	n_P	Concentration range (%)	n_C
f<5	1340	T<230	941	P<1	852	C<0.1	208
5≤f<10	847	230≤T<310	1195	1≤P<3	914	0.1≤C<0.5	1000
10≤f<27	420	310≤T<385	592	3≤P<12	867	0.5≤C<1	710
75≤f<100	329	385≤T< 460	592	12≤P<40	363	1≤C<10	1074
100≤f<150	684	460≤T<510	300	40≤P≤100	624	10≤C≤100	628

the low-pressure helium-broadening free parameters for the inversion transitions and the ammonia/helium mixture measurements with $P > 15$ bar (group VI) were used to obtain the high-pressure helium-broadening free parameters for the inversion transitions. The ammonia/hydrogen mixture measurements with $P <= 15$ bar (group V) were used to obtain the low-pressure hydrogen-broadening free parameters for the inversion transitions and the ammonia/hydrogen mixture measurements with $P >$ 15 bar (group VI) were used to obtain the high-pressure hydrogen-broadening free parameters for the inversion transitions. After this step, the low-pressure and high-pressure inversion transition parameters were further adjusted by optimizing over the ammonia/helium/hydrogen mixture measurements. This procedure was repeated several times with different input seed values for the free parameters, until convergent solutions were obtained.

5.4 New Consistent Ammonia Absorption Formalism

The absorption from a collisionally broadened gas can be expressed as

$$\alpha = \sum_j A_j \pi \Delta\nu_j F_j(\nu, \nu_{(0,j)}, \ldots) \quad (\mathrm{cm}^{-1}), \tag{5.4}$$

where for the line j, A_j is the absorption at the line center in cm^{-1}, $\Delta\nu_j$ is the

linewidth (half width at half max) in cm^{-1}, $F_j(\nu, \nu_{0,j}, \ldots)$ is the lineshape function in cm, $\nu_{(0,j)}$ is the frequency at the line center in cm^{-1}, and ν is the frequency of the incident electromagnetic wave in cm^{-1} (see, e.g., Townes and Schawlow, 1955).

The absorption at each line center is calculated using the line intensity information from the latest JPL catalog as per Pickett et al. (1998)

$$A_j = \frac{nI_j(T)}{\pi \Delta\nu_j} \quad (\mathrm{cm}^{-1}), \tag{5.5}$$

where n is the number density of the gas in molecules/cm^3, $I_j(T)$ is the intensity of the line in $\mathrm{cm}^{-1}/(\mathrm{molecule}/\mathrm{cm}^2)$ at temperature T, and with $\Delta\nu_j$ expressed in cm^{-1}. The number density n is calculated as

$$n = \frac{0.1 \times P_{ideal}}{k_B T}, \tag{5.6}$$

where P_{ideal} is the ideal partial pressure of the gas under consideration in bar, T is the temperature in K, and $k_B = 1.38 \times 10^{-23}$J/K (Boltzmann's constant). The ideal partial pressure of a gas is computed from its density and temperature. In this work, the density of a gas is computed from its equation of state and further details are provided in Chapter 4. The ideal pressure (in bar) is computed as,

$$P_{ideal} = \rho \frac{R_0}{M} T, \tag{5.7}$$

where ρ is the density in g/m^3, R_0 is the ideal gas constant for the gas, M is the molecular mass of the gas in g/mol and T is the measured temperature in K. The value for R_0 used in this work is equal to $8.314472 \times 10^{-5} \left(\frac{\mathrm{m}^3\mathrm{bar}}{\mathrm{Kmol}}\right)$ for all the gases except helium. For helium, the equation of state requires the use of the older value $8.31431 \times 10^{-5} \left(\frac{\mathrm{m}^3\mathrm{bar}}{\mathrm{Kmol}}\right)$. The line intensity at the measurement temperature (T) is calculated as

$$I_j(T) \approx I_j(T_0) \left(\frac{T_0}{T}\right)^{\eta+1} \exp^{\left(\left(\frac{1}{T_0}-\frac{1}{T}\right)E_{(l,j)}(hc/k_B)\right)}, \tag{5.8}$$

where $I_j(T_0)$ is the intensity of the line at the reference temperature T_0, $E_{(l,j)}$ is the lower state energy of transition in cm^{-1}, c is the speed of light in cm/s, h is the Planck's constant in Jsec, and η is the temperature dependence and is $\approx 3/2$ for non-linear and symmetric-top molecules such as ammonia, and 1 for linear molecules. The values of $\nu_{(0,j)}, I_j(T_0)$, and $E_{(l,j)}$ at the reference temperature are taken from the latest JPL spectral line catalog (Pickett et al., 1998) (Version 5, September 2010). The values of $I_j(T_0)$ given in the JPL catalog have units of $\log_{10}(\mathrm{nm}^2\mathrm{MHz})$ and must be taken as the exponent of 10 and then divided by $2.99793458 \times 10^{18}$ to be converted to $\mathrm{cm}^{-1}/(\mathrm{molecule/cm}^2)$. The linewidth for a gas mixture is calculated by

$$\Delta\nu_j = \sum_i \Delta\nu^o_{(i,j)} P_{(i,ideal)} \left(\frac{T_0}{T}\right)^{\xi_{ij}} \quad (\mathrm{cm}^{-1}), \tag{5.9}$$

where for the gas i and line j, $\Delta\nu^o_{(i,j)}$ is the line broadening parameter in cm^{-1}/bar, $P_{(i,ideal)}$ is the ideal partial pressure of the gas in bar (computed using Equation 5.7), and ξ_{ij} is the temperature dependence of the line broadening parameter. The temperature dependence is calculated as (e.g., Townes and Schawlow, 1955)

$$\Delta\nu_j \propto T^{-(m+1)/2(m-1)} = T^{-\xi}, \tag{5.10}$$

where $1 < \mathrm{m} < \infty$. For neutral gases, $m = 3$ is a lower limit and hence $0.5 < \xi < 1.0$.

5.4.1 Line Parameters

The JPL spectral line catalogs for NH_3 and $NH_3 - \nu_2$ have been recently updated (Yu et al., 2010a,b,c). The NH_3 catalog has a total of 1716 transitions that include

415 inversion transitions in the 0.3–220 GHz frequency range and 1301 rotational transitions in the 0.3–20 THz frequency range. The $NH_3 - \nu_2$ catalog has a total of 4198 roto-vibrational transitions in the 0.02–46 THz frequency range. A total of 5914 transitions are used in the new opacity formalism for ammonia.

For the development of the new ammonia opacity model described in this work, different lineshapes were investigated in order to obtain the best fit for the measurements. By using a modified Ben–Reuven lineshape (Ben-Reuven, 1966) for the inversion transitions, and a modified Gross lineshape (Gross, 1955) for the rotational and ν_2 roto-vibrational transitions, it was possible to achieve a robust fit for the measurements. The lineshapes rely on the knowledge of the linewidths of the gases being studied. Laboratory measurements of the self- and foreign-gas-broadening parameters of various line transitions were used where those data were available. When laboratory measurements of the broadening parameters were not available, those parameters were made free variables in the optimization process and the values closest to the average of the available measured broadening parameters that best fit the opacity measurements described in this work were used.

5.4.2 Ammonia Opacity Formalism

The new model for the hydrogen- and helium-broadened opacity of ammonia uses a modified Ben–Reuven lineshape for the inversion transitions and a modified Gross lineshape for the rotational and ν_2 roto-vibrational transitions. The cumulative opacity is calculated by

$$\alpha = (\alpha_{inv} + \alpha_{rot} + \alpha_{\nu_2}) \times 434294.5 \quad (\text{dB/km}), \tag{5.11}$$

where α_{inv}, α_{rot}, and α_{ν_2} are the opacities from the inversion, rotational, and ν_2 transitions, respectively, in cm^{-1}. The multiplication factor of 434294.5 converts the total absorptivity from cm^{-1} to dB/km.

The opacity from the inversion transitions is calculated using a modified Ben–Reuven lineshape in a fashion similar to that described by Hanley et al. (2009) but with different sets of values for the model constants than those used by Hanley. Two sets of model constants were obtained by optimizing the free parameters for the inversion transitions. When $P <= 15$ bar, the low-pressure model constants are used and when $P > 15$ bar, the high-pressure model constants are used. The opacity from the inversion lines is given as

$$\alpha_{inv} = \frac{0.1 D_{inv} P_{NH_3}}{k_B T} \left(\frac{2}{\pi}\right) \left(\frac{T_0}{T}\right)^{\eta+1} \times \sum_j \left(I_j(T_0) \exp^{\left(\left(\frac{1}{T_0}-\frac{1}{T}\right)E_{(l,j)}\left(\frac{hc}{k_B}\right)\right)} \left(\frac{\nu}{\nu_{(0,j)}}\right)^2 \left[\frac{(\gamma_j-\zeta_j)\nu^2 + (\gamma_j+\zeta_j)[(\nu_{(0,j)}+\delta_j)^2+\gamma_j^2-\zeta_j^2]}{[\nu^2-(\nu_{(0,j)}+\delta_j)^2-\gamma_j^2+\zeta_j^2]^2+4\nu^2\gamma_j^2}\right] \right) \quad (\mathrm{cm}^{-1}), \tag{5.12}$$

where for the inversion line j, $\nu_{(0,j)}$, γ_j, ζ_j, and δ_j are the center frequency, linewidth, coupling parameter, and shift parameter, respectively, in cm^{-1}, and D_{inv} is a unitless scale factor. The frequency, linewidth, coupling, and shift parameters are nominally expressed in GHz and should be converted to cm^{-1} before they are used in the equation for opacity. (Note that 1 $\mathrm{cm}^{-1} \sim 30$ GHz.) The linewidth and coupling parameter of the lines are calculated by summing the contribution from different gases and are given by

$$\gamma_j = \gamma_{H_2} P_{H_2} \left(\frac{300}{T}\right)^{\Gamma_{H_2}} + \gamma_{He} P_{He} \left(\frac{300}{T}\right)^{\Gamma_{He}} + \gamma_{NH_3}\gamma_{(0,j)} P_{NH_3} \left(\frac{295}{T}\right)^{\Gamma_{NH_3}} \quad (\mathrm{GHz}), \tag{5.13}$$

$$\zeta_j = \zeta_{H_2} P_{H_2} \left(\frac{300}{T}\right)^{Z_{H_2}} + \zeta_{He} P_{He} \left(\frac{300}{T}\right)^{Z_{He}} + \zeta_{NH_3}\gamma_{(0,j)} P_{NH_3} \left(\frac{295}{T}\right)^{Z_{NH_3}} \quad (\mathrm{GHz}), \tag{5.14}$$

where for the inversion line j and i = H_2, He, and NH_3, γ_i and ζ_i are constant scale terms, and Γ_i and Z_i represent the constant temperature dependences of the broadening of each of the gases, P_i are the ideal partial pressures in bar, and $\gamma_{(0,j)}$ are the self-broadening linewidths of the inversion transitions of ammonia in MHz/Torr. The units of $\gamma_{(0,j)}$ remain in MHz/Torr and the conversion to GHz/bar is incorporated in the scale terms γ_{NH_3} and ζ_{NH_3} in Equations 5.13 and 5.14. The values for $\gamma_{(0,j)}$ are from the calculations of Poynter and Kakar (1975) assuming a T_0 of 295 K. For the lines with center frequencies below 7.2 GHz and $J > 16$, where J represents the total angular momentum vector for the ammonia molecule, γ_0 is expressed as

$$\gamma_0(J,K) = 25.923\frac{K}{\sqrt{J(J+1)}} \quad \text{(MHz/Torr)}, \tag{5.15}$$

where K is the projection of J onto the molecular axis. The $\gamma_{(0,j)}$ of all the other inversion lines which are not listed by Poynter and Kakar (1975) and whose $J < 16$ or center frequency > 7.2 GHz are assigned a constant value equal to the average of the γ_0 of the lines calculated by Poynter and Kakar. The pressure shift parameter is calculated by

$$\delta_j = d \times \gamma_j \quad \text{(GHz)}, \tag{5.16}$$

where d is an empirically derived constant. All the inversion transitions are assigned the same set of model constants (either low-pressure or high-pressure), even though each line transition behaves differently (see, e.g., Hanley et al., 2009). The equation for computing the opacity from the inversion transitions has 14 free parameters. Two sets of free-parameters were empirically derived by data fitting (Tables 5.5 and 5.6) and the appropriate set of values should be used for calculating the ammonia opacity for a given pressure.

Table 5.5: Values of the low-pressure inversion model constants used for computing the H_2/He-broadened NH_3 absorptivity when $P <= 15$ bar.

	i=H_2	i=He	i=NH_3
γ_i	1.7465	0.9779	0.7298
Γ_i	0.8202	1	1
ζ_i	1.2163	0.0291	0.5152
Z_i	0.8873	0.8994	2/3
d		-0.0627	
D_{inv}		0.9862	

Table 5.6: Values of the high-pressure inversion model constants used for computing the H_2/He-broadened NH_3 absorptivity when $P > 15$ bar.

	i=H_2	i=He	i=NH_3
γ_i	1.6361	0.4555	0.7298
Γ_i	0.8	0.5	1
ζ_i	1.1313	0.1	0.5152
Z_i	0.6234	0.5	2/3
d		0.2	
D_{inv}		1.3746	

The opacity from the rotational transitions is calculated using a modified Gross lineshape and is given as

$$\alpha_{rot} = \frac{0.1 D_{rot} P_{NH_3}}{k_B T} \left(\frac{1}{\pi}\right) \left(\frac{T_0}{T}\right)^{\eta+1} \times \sum_j \left[I_j(T_0) \exp\left(\left(\tfrac{1}{T_0} - \tfrac{1}{T}\right) E_{(l,j)} \left(\tfrac{hc}{k_B}\right)\right) \left(\frac{\nu}{\nu_{(0,j)}}\right) \left(\frac{4\nu\nu_{(0,j)}\Delta\nu_j}{\left(\nu_{(0,j)}^2 - \nu^2\right)^2 + 4\nu^2\Delta\nu_j^2}\right)\right] \quad (\mathrm{cm}^{-1}), \tag{5.17}$$

where for the rotational line j, $\nu_{(0,j)}$ is the frequency of transition, $\Delta\nu_j$ is the linewidth parameter, and D_{rot} is an empirically derived unitless scale factor. The linewidth parameter is given as

Table 5.7: Values of the model constants of the new model used for computing the H_2/He-broadened NH_3 absorptivity from the rotational transitions.

	i=H_2	i=He	i=NH_3
c_i	0.2984	0.75	3.1789
ξ_i	0.8730	2/3	1
D_{rot}		2.4268	

$$\Delta\nu_j = c_{H_2}\Delta\nu_{(H_2,j)}P_{H_2}\left(\frac{300}{T}\right)^{\xi_{H_2}} + c_{He}\Delta\nu_{(He,j)}P_{He}\left(\frac{300}{T}\right)^{\xi_{He}} + c_{NH_3}\Delta\nu_{(NH_3,j)}P_{NH_3}\left(\frac{300}{T}\right)^{\xi_{NH_3}} \quad \text{(GHz)}, \quad (5.18)$$

where for i = H_2, He, and NH_3, c_i and ξ_i are the empirically derived model constants, P_i are the ideal partial pressures in bar, and $\Delta\nu_{(i,j)}$ are the broadening parameters in GHz/bar. The units of $\Delta\nu_j$ should be converted from GHz to cm^{-1} before it is used in the equation for computing the opacity from the rotational lines (Equation 5.17). The self-broadened linewidth for the $J = 1 \leftarrow 0$ transition of the ammonia molecule is assigned the value measured by Belov et al. (1983), and the hydrogen- and helium-broadened linewidths for the $J = 1 \leftarrow 0$ transition are assigned values measured by Bachet (1973). The self- and hydrogen-broadened linewidths for each of the other rotational lines are assigned values measured by Brown and Peterson (1994). The linewidths for the lines that were not measured by Brown and Peterson were assigned values computed using their extrapolation formula. The helium-broadened linewidths are assigned the values computed using the formula given by Pine et al. (1993). The empirically derived model constants for the rotational transitions are listed in Table 5.7.

The opacity from the ν_2 roto-vibrational transitions is calculated using a modified

Gross lineshape and is given as

$$\alpha_{\nu_2} = \frac{0.1 D_{\nu_2} P_{NH_3}}{k_B T} \left(\frac{1}{\pi}\right) \left(\frac{T_0}{T}\right)^{\eta+1} \times \sum_j \left[I_j(T_0) \exp^{\left(\left(\frac{1}{T_0}-\frac{1}{T}\right) E_{(l,j)} \left(\frac{hc}{k_B}\right)\right)} \left(\frac{\nu}{\nu_{(0,j)}}\right) \left(\frac{4\nu\nu_{(0,j)}\Delta\nu}{\left(\nu^2_{(0,j)} - \nu^2\right)^2 + 4\nu^2\Delta\nu^2}\right)\right] \quad (\mathrm{cm}^{-1}), \tag{5.19}$$

where, for the ν_2 roto-vibrational line j, $\nu_{(0,j)}$ is the frequency of transition, $\Delta\nu$ is the linewidth parameter, and D_{ν_2} is an empirically derived unitless scale factor. The linewidth parameter is given by

$$\Delta\nu = \Delta\nu_{H_2} P_{H_2} \left(\frac{300}{T}\right)^{\xi_{H_2}} + \Delta\nu_{He} P_{He} \left(\frac{300}{T}\right)^{\xi_{He}} + \Delta\nu_{NH_3} P_{NH_3} \left(\frac{300}{T}\right)^{\xi_{NH_3}} \quad (\mathrm{GHz}), \tag{5.20}$$

where for $i = \mathrm{H_2}$, He, and $\mathrm{NH_3}$, ξ_i are the empirically derived temperature coefficients, P_i are the ideal partial pressures in bar, and $\Delta\nu_i$ are the empirically derived broadening parameters for the ν_2 transitions in GHz/bar. The units of $\Delta\nu$ should be converted from GHz to cm^{-1} before it is used in the equation for computing the opacity (Equation 5.19). The self-broadening parameter of the strongest ν_2 transition in the millimeter-wavelength region (ν_0 = 140.14 GHz) was theoretically calculated by Belli et al. (1997). However, the theoretically calculated value of 13.72 GHz/bar was too large to fit the opacity measurements. The self-broadening parameter of the 466 GHz ν_2 transition was measured by Belov et al. (1982). The self-, hydrogen-, and helium-broadening parameters of most of the ν_2 transitions have not been measured. Hence, the broadening parameters were made free variables during model optimization and empirically derived constant values are used for all lines. The empirically derived model constants for the ν_2 roto-vibrational transitions are listed in Table 5.8.

The values of the model constants listed in this paper were optimized to the latest JPL spectral line catalogs (Pickett et al., 1998) (Version 5, September 2010). The

Table 5.8: Values of the model constants of the new model used for computing the H_2/He-broadened NH_3 absorptivity from the ν_2 roto-vibrational transitions.

	i=H_2	i=He	i=NH_3
Δv_i (GHz/bar)	1.4	0.68	9.5
ξ_i	0.73	0.5716	1
D_{ν_2}		1.1206	

frequency, line intensity, and lower state energy of the various transitions of ammonia given in the latest JPL catalogs along with the self- and hydrogen-/helium- broadening parameters for these transitions are provided online (*ammonia_inversion.dat*, *ammonia_rotational.dat*, and *ammonia_rotovibrational.dat*) at `http://users.ece.gatech.edu/~psteffes/palpapers/models.html`. Software for running the model in Matlab® is also provided online ($nh3devarajsteffesmodel.m$). This model can be used to estimate the opacity of ammonia under jovian conditions in the centimeter-wavelength range at pressures up to 100 bar and temperatures in the 200 to 500 K range and in the millimeter-wavelength range at pressures up to 3 bar and temperatures in the 200 to 300 K range.

5.5 Model Performance

Assessing the performance of the model with respect to the measured data provides insights into the goodness of fit of the model and the conditions of its effectiveness. The model was compared with the 1431 data points of the 1.5–27 GHz opacity of ammonia and the 250 data points of the 22–40 GHz opacity of ammonia measured by Hanley et al. (2009), in addition to the 1013 data points of the 75–150 GHz opacity of ammonia and the 1176 data points of the 1.5–6 GHz opacity of ammonia measured as part of this work.

The new ammonia opacity model fits 66.84% of the 1.5–6 GHz high-pressure cavity resonator measurements, 66.14% of the 75–150 GHz FPR measurements, 93.92% of the 1.5–27 GHz cavity resonator measurements, and 90.4% of the 22–40 GHz

FPR measurements within 2σ uncertainty. Overall, the model fits 78.2% of the 3870 measurements in the 1.5–150 GHz range within 2σ uncertainty. Comparison of the new model peformance with the models of Berge and Gulkis (1976), Spilker (1990), Joiner and Steffes (1991), Mohammed and Steffes (2003), Mohammed and Steffes (2004), Hanley et al. (2009), Hanley (2008) with rotational lines, and Devaraj et al. (2011) is listed in Table 5.9. Plots comparing some of the measured data to the different models are shown in Figures 5.2–5.57. The error bars shown in the plots are the 2σ measurement uncertainties. In the implementation of the model by Joiner and Steffes (1991), there were difficulties in matching the numerical values given by the author. Hanley et al. (2009) describe similar difficulties in reproducing the original numerical values given by Joiner and Steffes (1991). However, the numerical values estimated by Hanley et al. (2009) for the various models are consistent with the values estimated in this work. The Hanley et al. (2009) model includes only the inversion transitions of ammonia and was developed using their centimeter-wavelength measurements conducted at pressures up to 12 bar. Hanley (2008) provided a modification to this model for use in the high-pressure regime by including the lowest 20 rotational transitions of ammonia in addition to the inversion transitions, and both the models are shown in the figures for comparison.

Table 5.9: The percentage of the $NH_3/He/H_2$ measurement data points within 2σ uncertainty of the new model in comparison with the existing models.

NH_3 opacity model	Cavity (1.5–27 GHz)	FPR (22–40 GHz)	FPR (75–150 GHz)	High Pressure (1.5–6 GHz)	Total
Berge and Gulkis (1976)	53.11	89.2	23.59	56.72	48.81
Spilker (1990)	70.23	48.4	8.69	25.6	39.15
Joiner and Steffes (1991)	82.88	84.4	19.84	60.03	59.53
Mohammed and Steffes (2003)	57.16	55.2	3.95	37.5	37.13
Mohammed and Steffes (2004)	49.13	86.4	25.07	52.55	46.28
Hanley et al. (2009)	96.09	85.2	10.46	61.73	62.5
Hanley (2008) w/ rot. lines	96.09	85.6	12.04	61.82	62.99
Devaraj et al. (2011)	95.11	94.8	66.44	35.46	69.46
This work	**93.92**	**90.4**	**66.14**	**66.84**	**78.19**

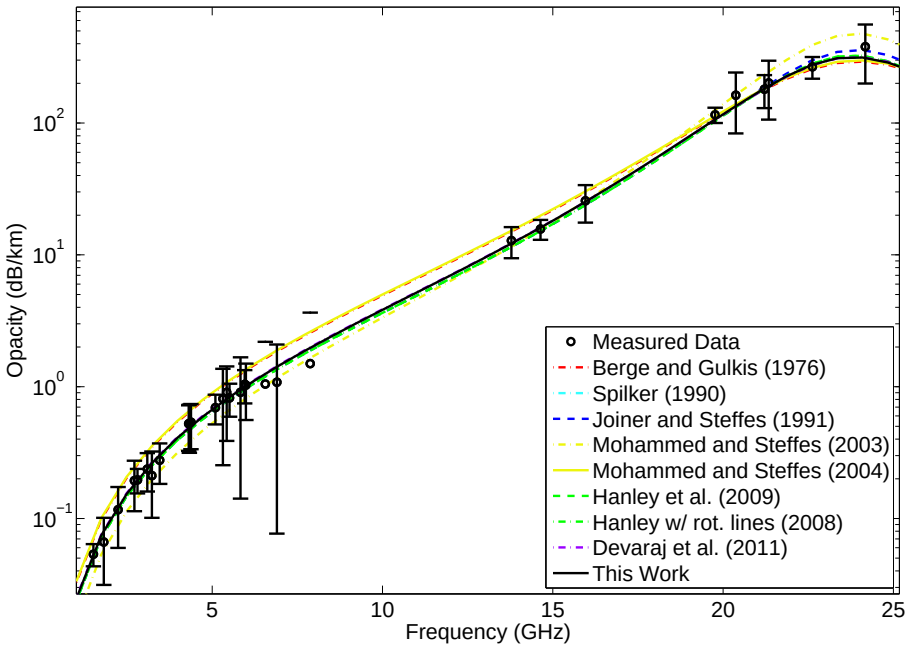

Figure 5.2: Opacity data measured by Hanley et al. (2009) using the cavity resonators for a mixture of $NH_3 = 0.95\%$, $He = 13.47\%$, $H_2 = 85.58\%$ at a pressure of 1.009 bar and temperature of 216.4 K compared to various models.

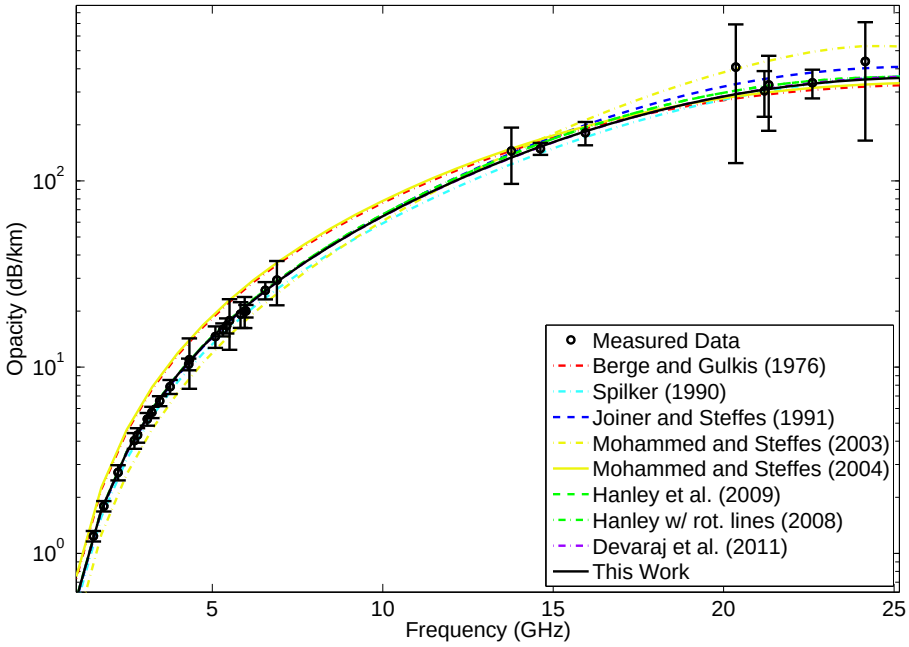

Figure 5.3: Opacity data measured by Hanley et al. (2009) using the cavity resonators for a mixture of $NH_3 = 0.77\%$, $He = 13.5\%$, $H_2 = 85.73\%$ at a pressure of 5.782 bar and temperature of 216.3 K compared to various models.

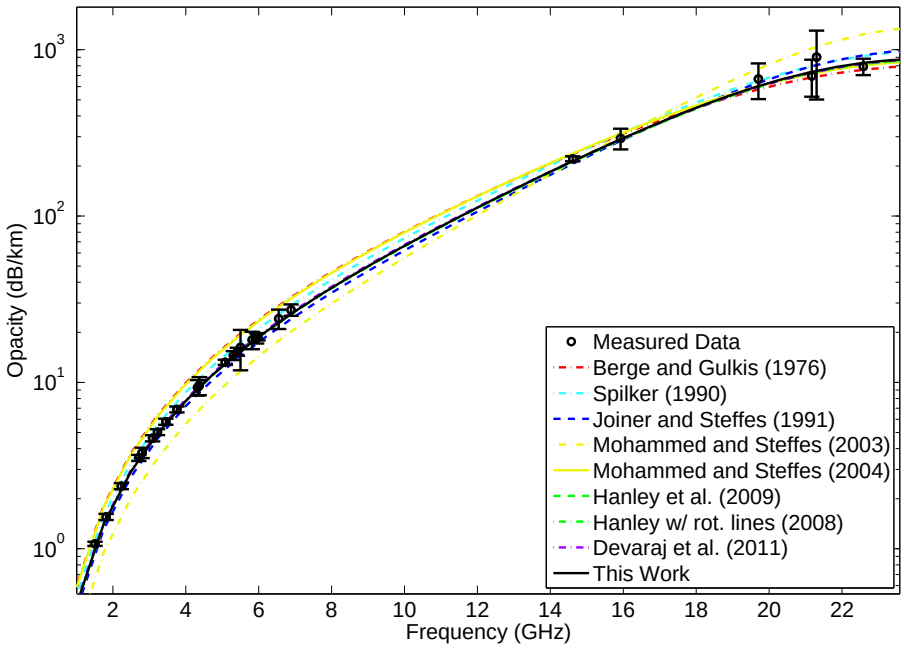

Figure 5.4: Opacity data measured by Hanley et al. (2009) using the cavity resonators for a mixture of $NH_3 = 4\%$, $He = 13.06\%$, $H_2 = 82.94\%$ at a pressure of 2.96 bar and temperature of 293.6 K compared to various models.

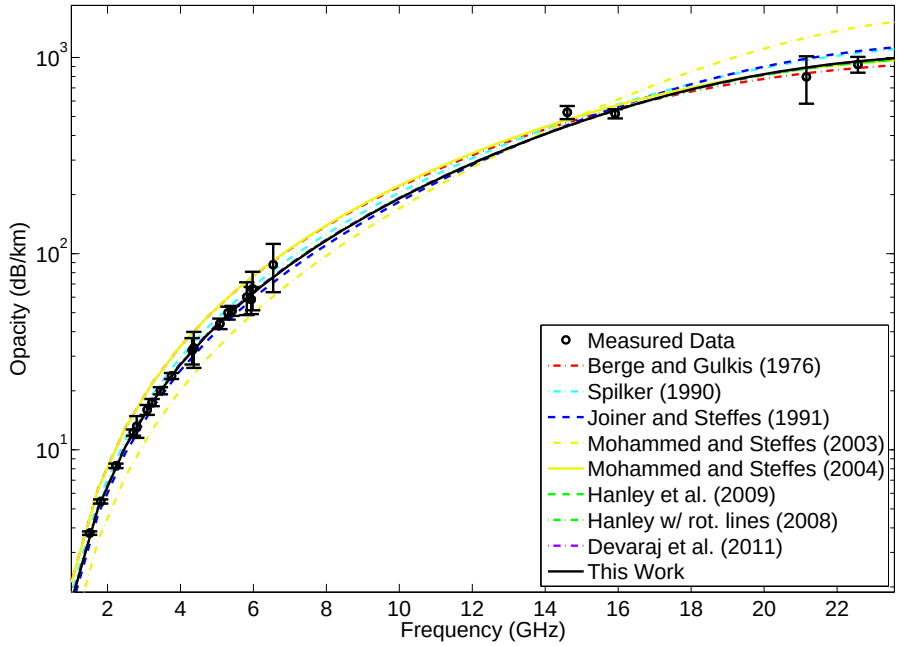

Figure 5.5: Opacity data measured by Hanley et al. (2009) using the cavity resonators for a mixture of $NH_3 = 4\%$, $He = 13.06\%$, $H_2 = 82.94\%$ at a pressure of 5.927 bar and temperature of 293.3 K compared to various models.

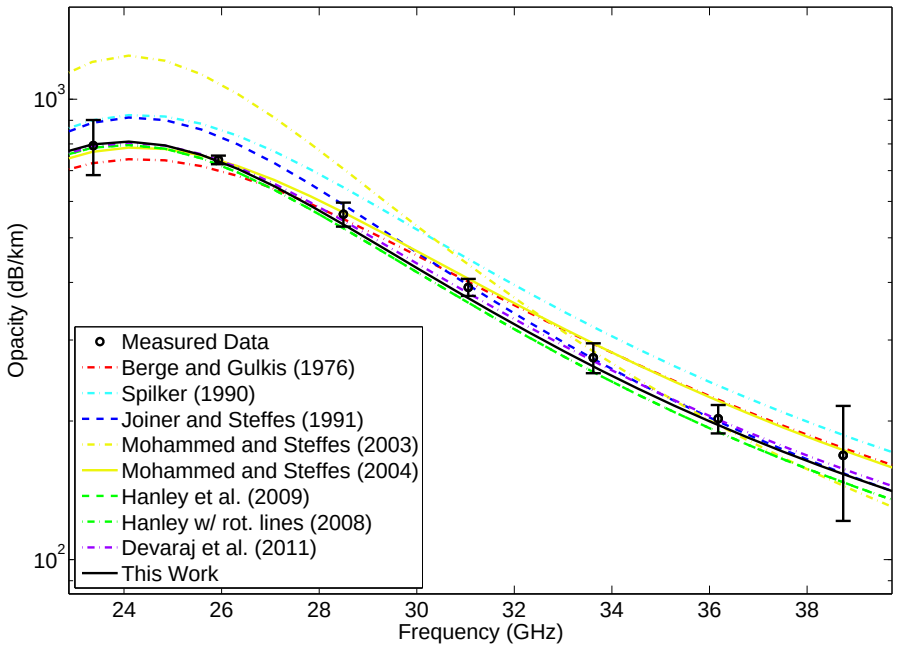

Figure 5.6: Opacity data measured by Hanley et al. (2009) using the Fabry-Perot resonator for a mixture of $NH_3 = 4\%$, $He = 13.06\%$, $H_2 = 82.94\%$ at a pressure of 2 bar and temperature of 295.3 K compared to various models.

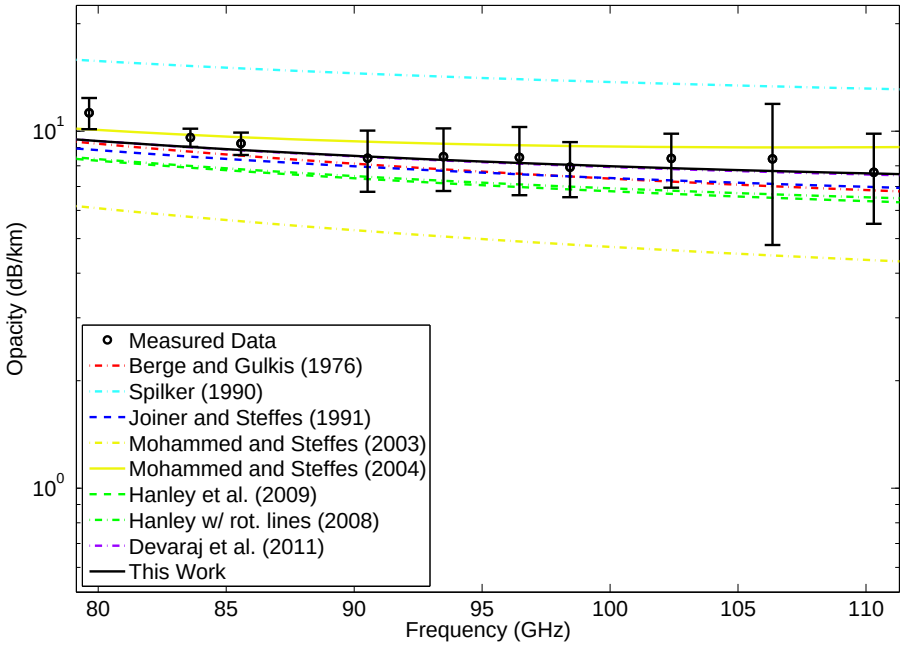

Figure 5.7: Opacity data measured using the 3–4 mm-wavelength system for a mixture of $NH_3 = 4\%$, $He = 13.06\%$, $H_2 = 82.94\%$ at a pressure of 0.976 bar and temperature of 296.3 K compared to various models.

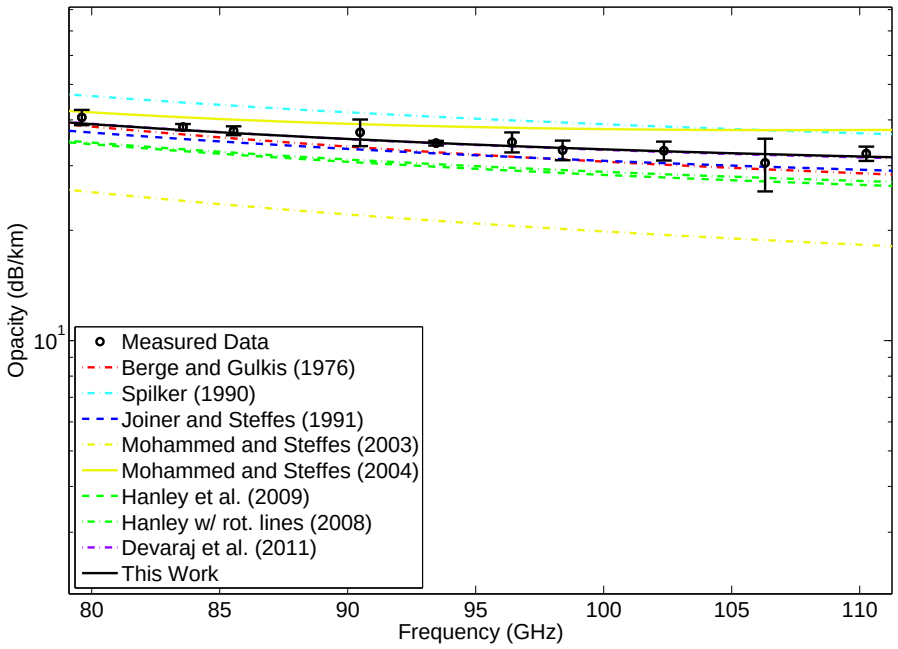

Figure 5.8: Opacity data measured using the 3–4 mm-wavelength system for a mixture of NH_3 = 4%, He = 13.06%, H_2 = 82.94% at a pressure of 1.999 bar and temperature of 296.2 K compared to various models.

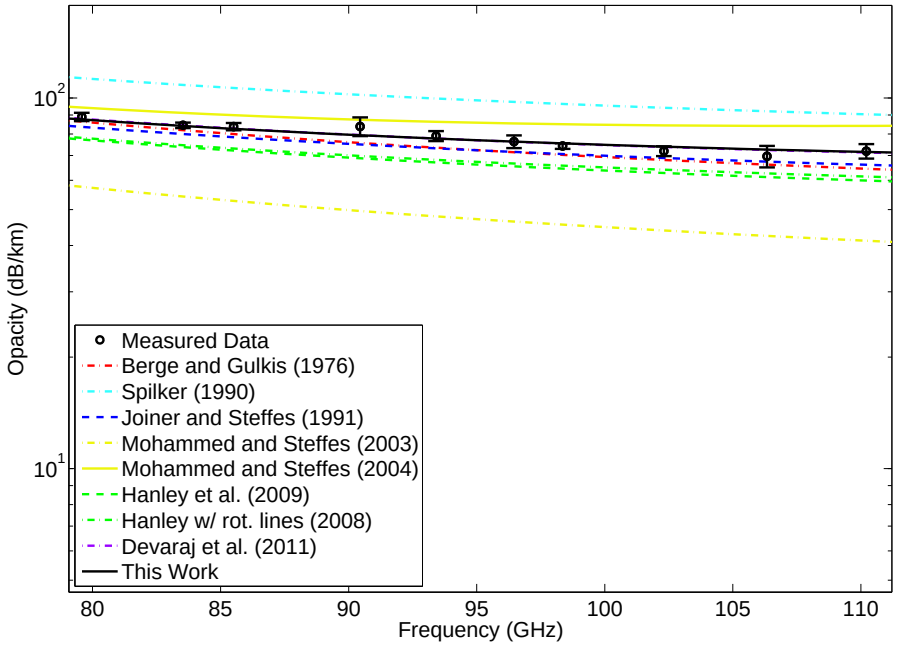

Figure 5.9: Opacity data measured using the 3–4 mm-wavelength system for a mixture of NH_3 = 4%, He = 13.06%, H_2 = 82.94% at a pressure of 3.009 bar and temperature of 296.3 K compared to various models.

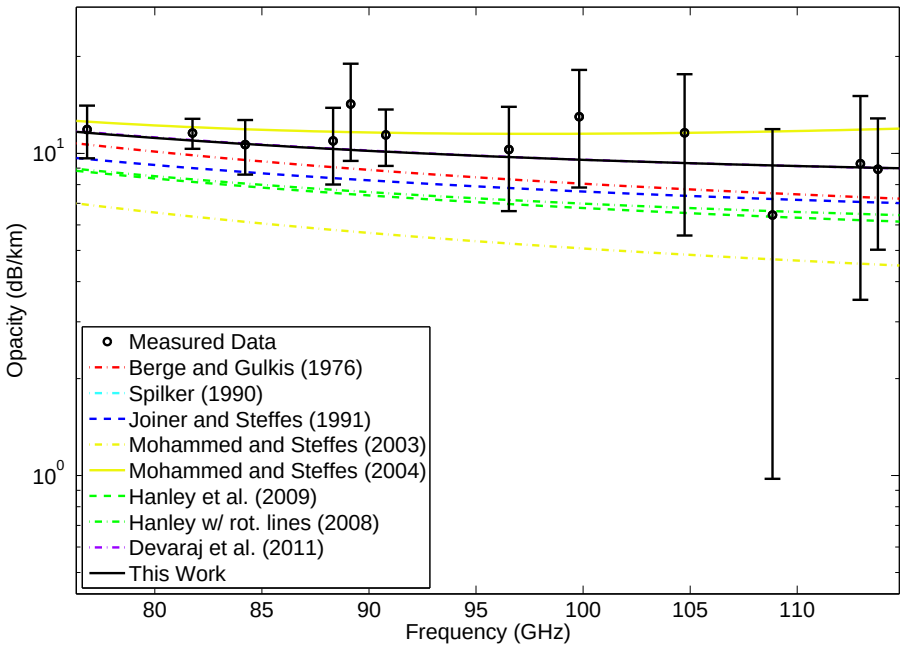

Figure 5.10: Opacity data measured using the 3–4 mm-wavelength system for a mixture of NH_3 = 2%, He = 13.33%, H_2 = 84.67% at a pressure of 1.041 bar and temperature of 219.3 K compared to various models.

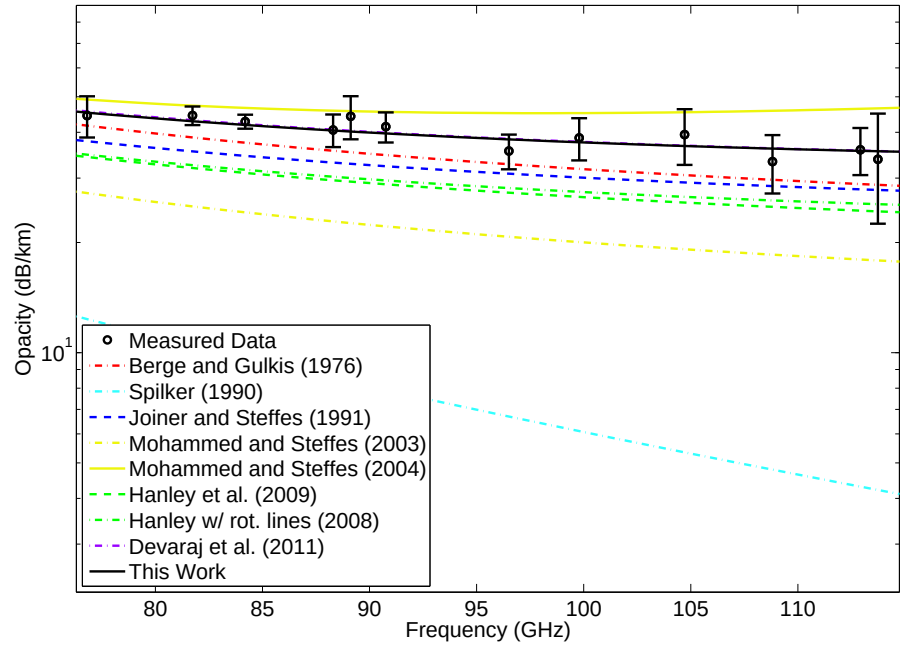

Figure 5.11: Opacity data measured using the 3–4 mm-wavelength system for a mixture of NH_3 = 2%, He = 13.33%, H_2 = 84.67% at a pressure of 2.07 bar and temperature of 219.2 K compared to various models.

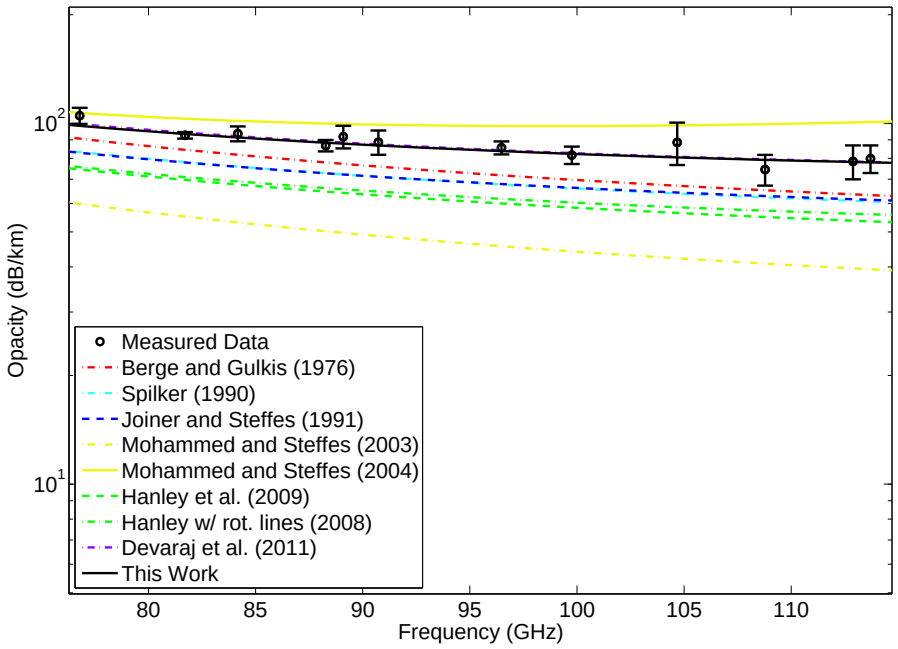

Figure 5.12: Opacity data measured using the 3–4 mm-wavelength system for a mixture of NH_3 = 2%, He = 13.33%, H_2 = 84.67% at a pressure of 3.085 bar and temperature of 219.6 K compared to various models.

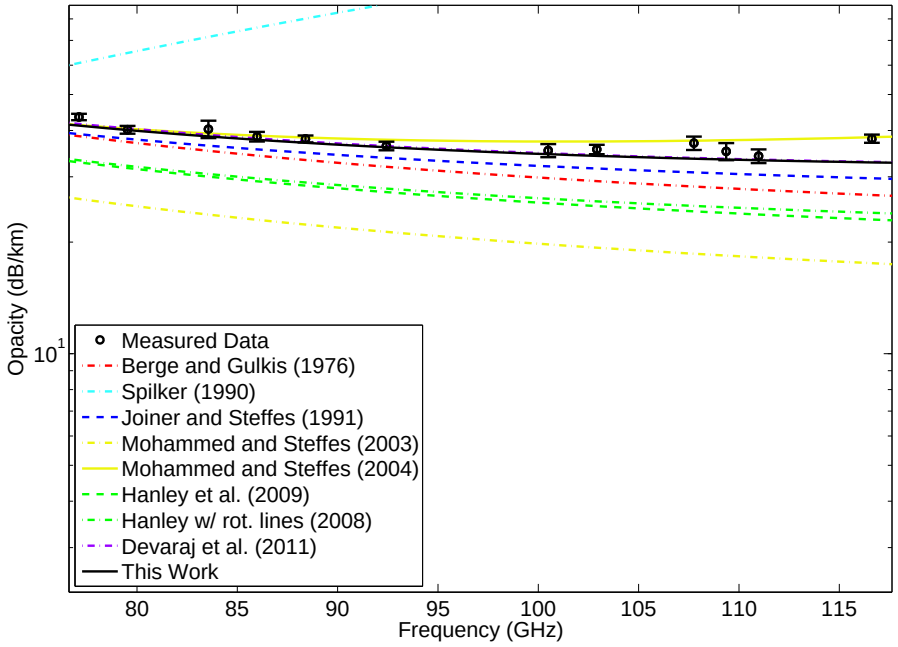

Figure 5.13: Opacity data measured using the 3–4 mm-wavelength system for a mixture of NH_3 = 6.04%, He = 12.78%, H_2 = 81.18% at a pressure of 0.994 bar and temperature of 221.5 K compared to various models.

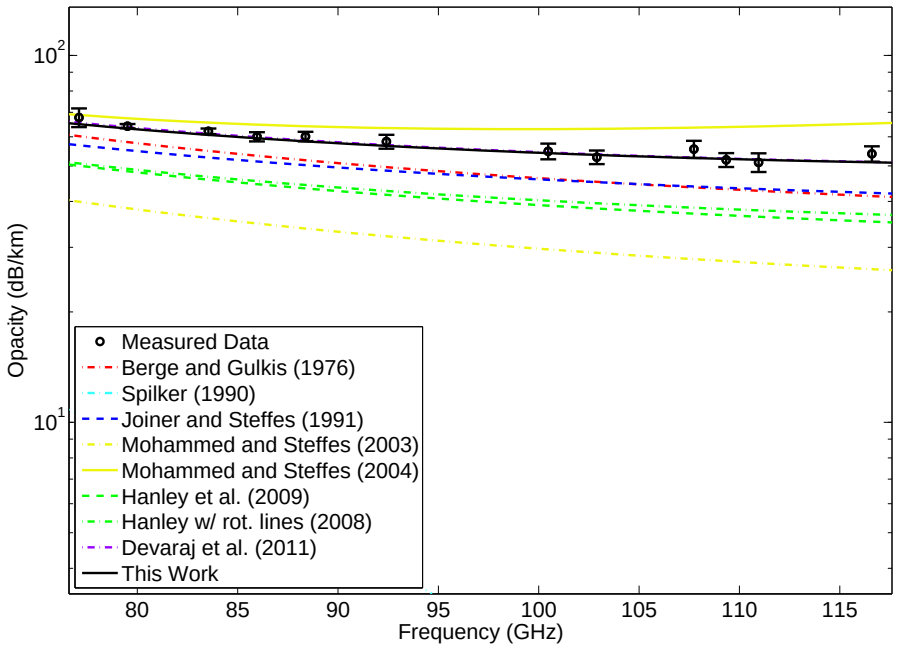

Figure 5.14: Opacity data measured using the 3–4 mm-wavelength system for a mixture of $NH_3 = 3.12\%$, $He = 13.18\%$, $H_2 = 83.7\%$ at a pressure of 1.925 bar and temperature of 221.1 K compared to various models.

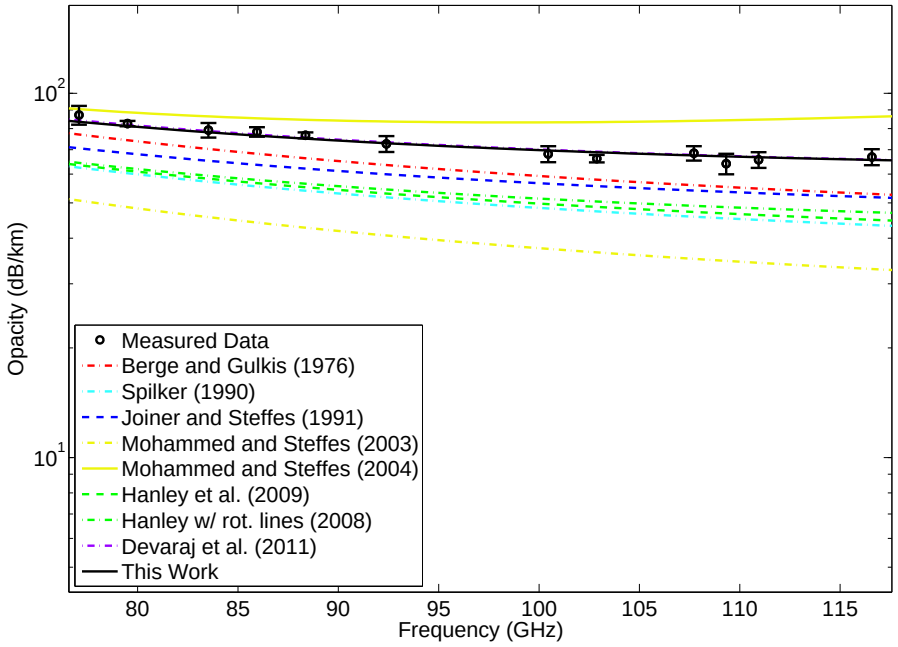

Figure 5.15: Opacity data measured using the 3–4 mm-wavelength system for a mixture of $NH_3 = 2.14\%$, $He = 13.31\%$, $H_2 = 84.55\%$ at a pressure of 2.766 bar and temperature of 221.6 K compared to various models.

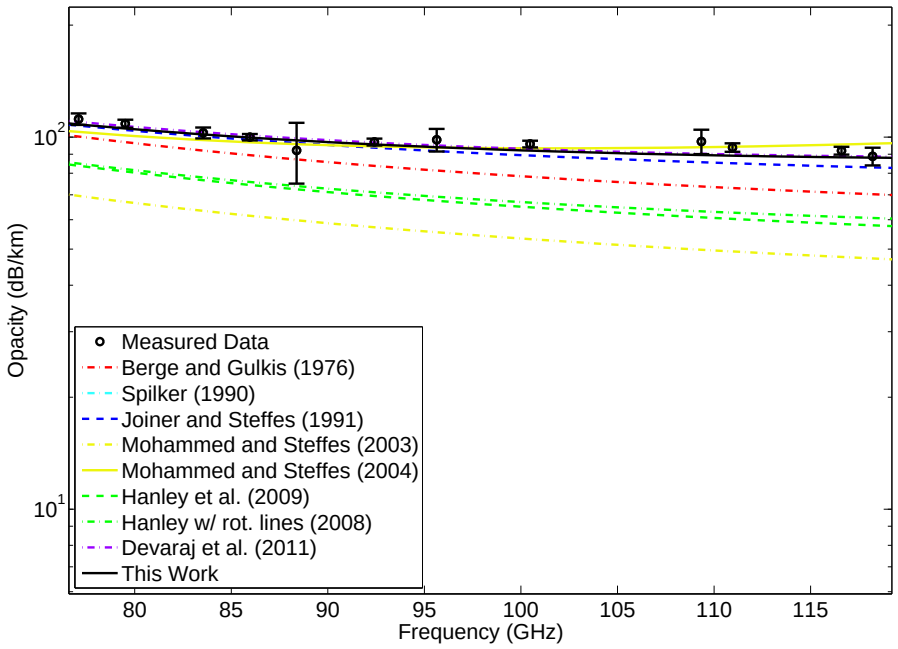

Figure 5.16: Opacity data measured using the 3–4 mm-wavelength system for a mixture of $NH_3 = 9.17\%$, $He = 12.35\%$, $H_2 = 78.48\%$ at a pressure of 1.083 bar and temperature of 207.7 K compared to various models.

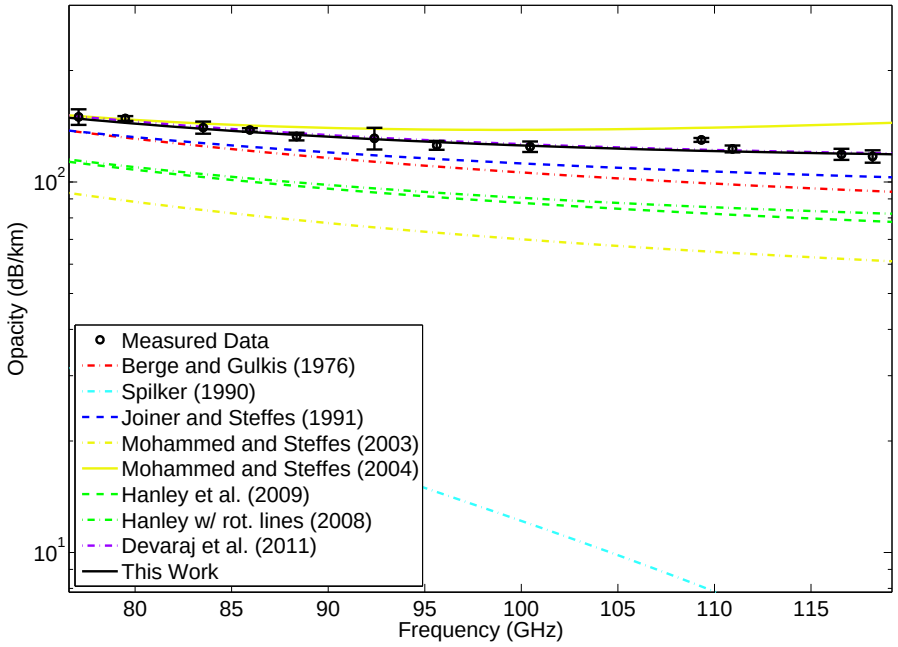

Figure 5.17: Opacity data measured using the 3–4 mm-wavelength system for a mixture of $NH_3 = 5.06\%$, $He = 12.91\%$, $H_2 = 82.03\%$ at a pressure of 1.943 bar and temperature of 207.7 K compared to various models.

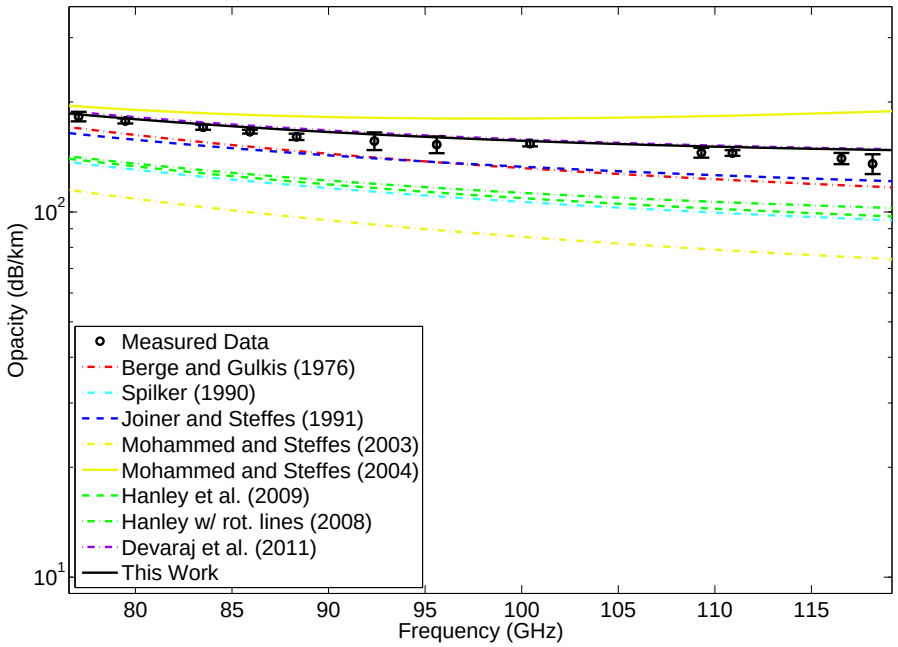

Figure 5.18: Opacity data measured using the 3–4 mm-wavelength system for a mixture of NH_3 = 3.36%, He = 13.14%, H_2 = 83.5% at a pressure of 2.855 bar and temperature of 207.7 K compared to various models.

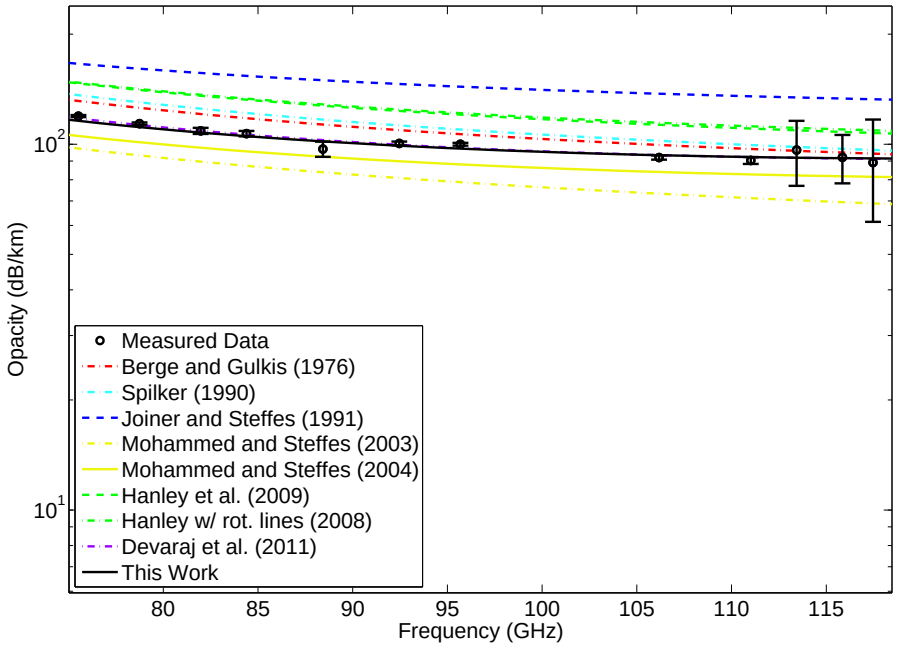

Figure 5.19: Opacity data measured using the 3–4 mm-wavelength system for pure ammonia gas at a pressure of 0.255 bar and temperature of 295.1 K compared to various models.

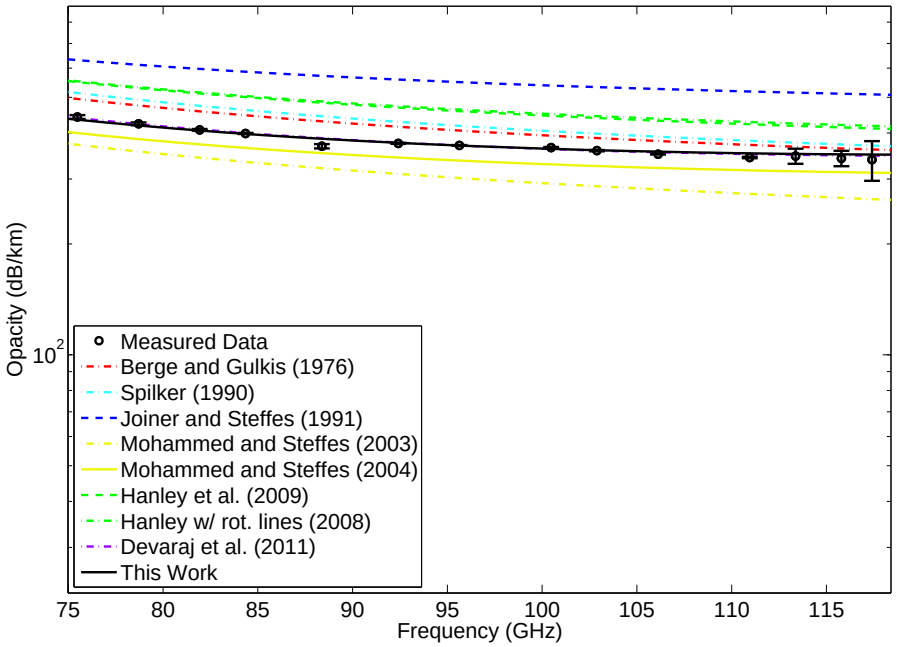

Figure 5.20: Opacity data measured using the 3–4 mm-wavelength system for pure ammonia gas at a pressure of 0.505 bar and temperature of 296.7 K compared to various models.

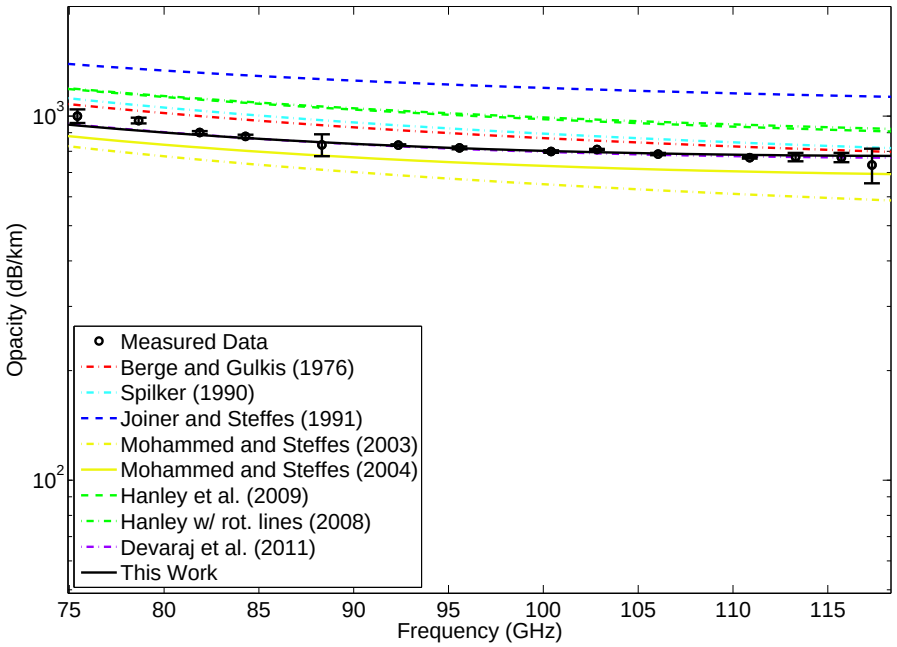

Figure 5.21: Opacity data measured using the 3–4 mm-wavelength system for pure ammonia gas at a pressure of 0.755 bar and temperature of 296.8 K compared to various models.

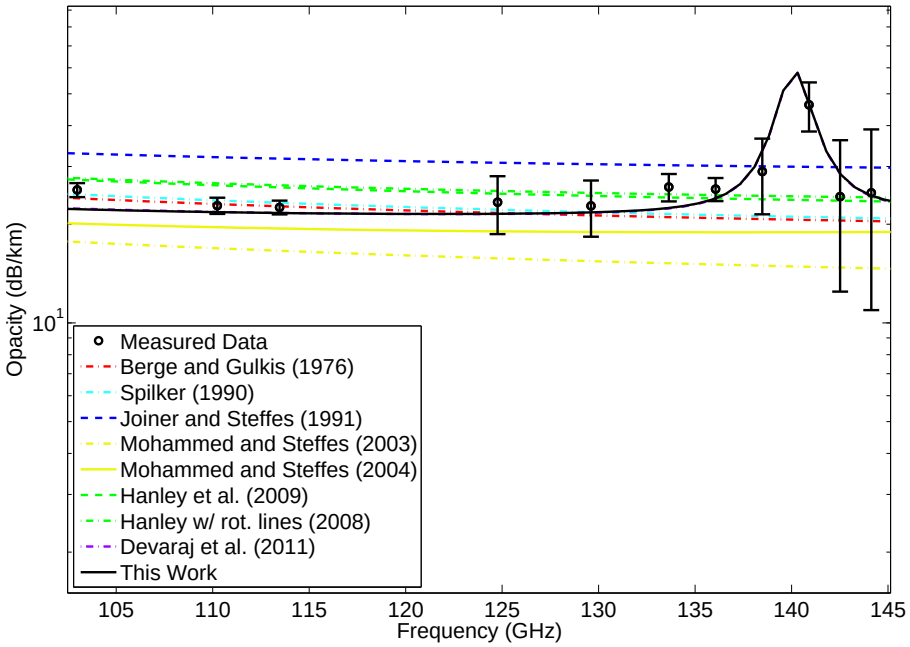

Figure 5.22: Opacity data measured using the 2–3 mm-wavelength system for pure ammonia gas at a pressure of 0.124 bar and temperature of 295.9 K compared to various models.

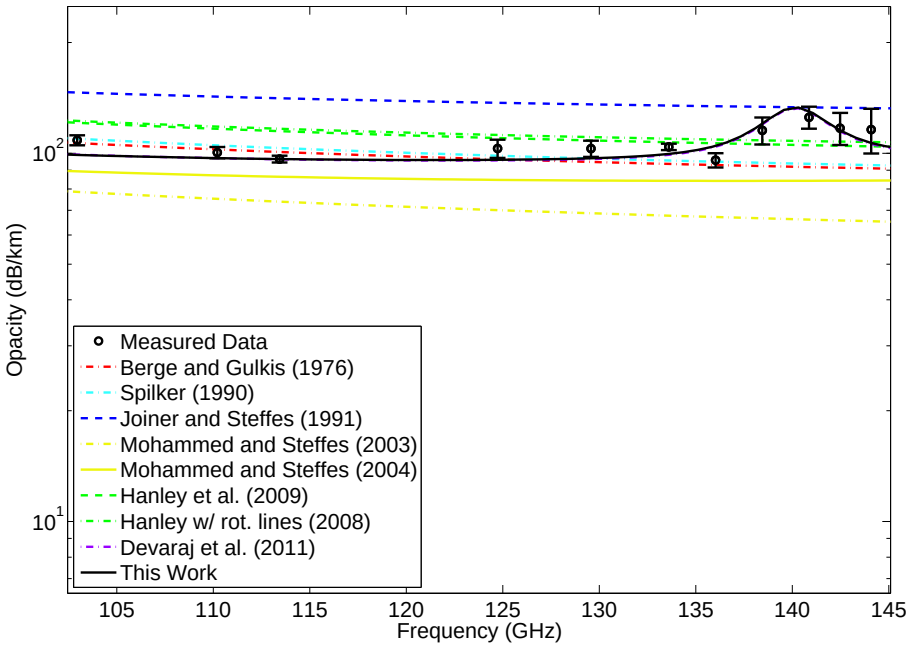

Figure 5.23: Opacity data measured using the 2–3 mm-wavelength system for pure ammonia gas at a pressure of 0.262 bar and temperature of 295.5 K compared to various models.

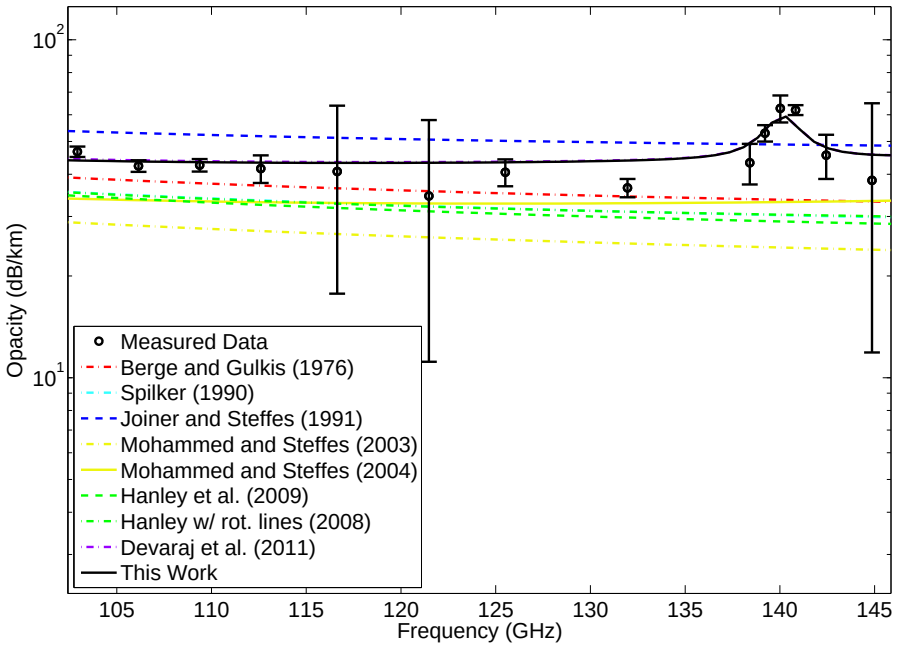

Figure 5.24: Opacity data measured using the 2–3 mm-wavelength system for pure ammonia gas at a pressure of 0.103 bar and temperature of 220.9 K compared to various models.

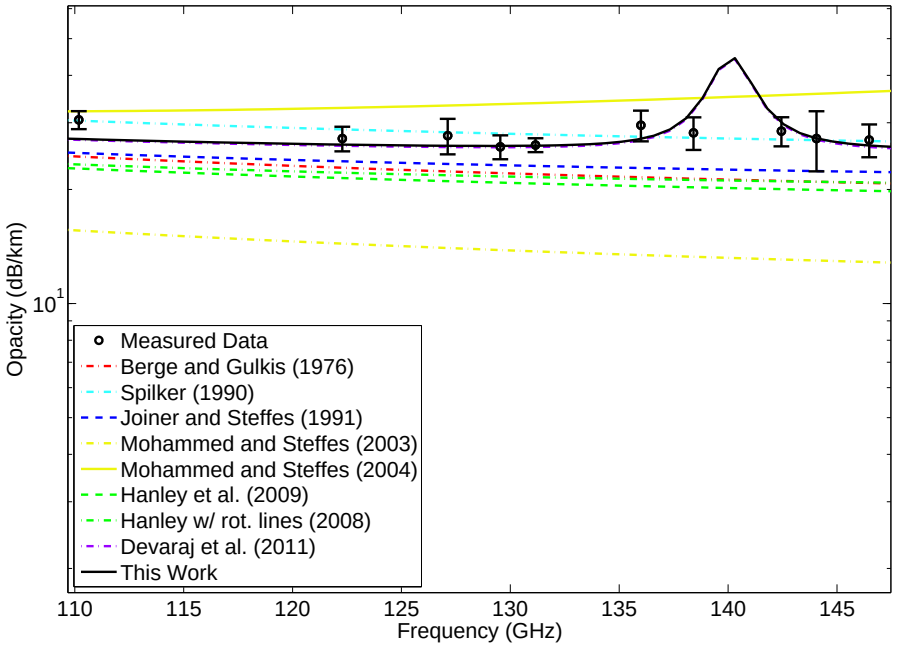

Figure 5.25: Opacity data measured using the 2–3 mm-wavelength system for a mixture of NH_3 = 3.97%, He = 13.06%, H_2 = 82.97% at a pressure of 1.854 bar and temperature of 296 K compared to various models.

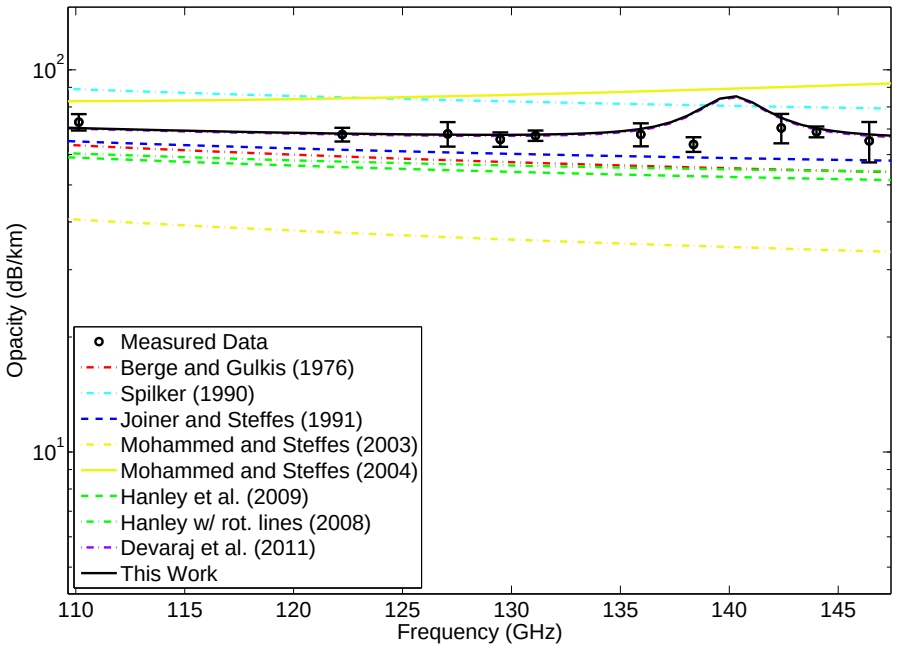

Figure 5.26: Opacity data measured using the 2–3 mm-wavelength system for a mixture of $NH_3 = 3.97\%$, $He = 13.06\%$, $H_2 = 82.97\%$ at a pressure of 2.998 bar and temperature of 296.2 K compared to various models.

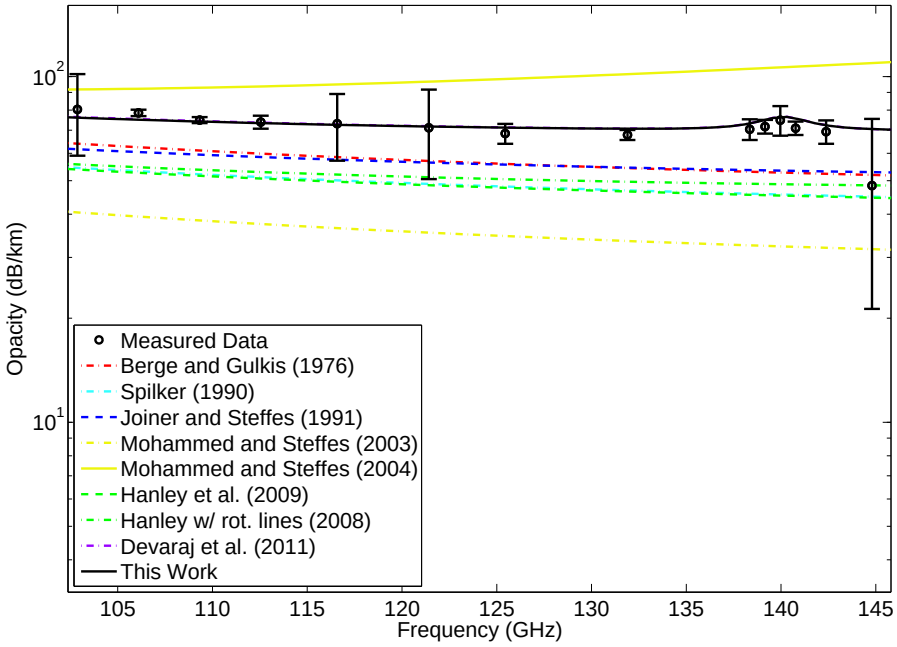

Figure 5.27: Opacity data measured using the 2–3 mm-wavelength system for a mixture of $NH_3 = 2.21\%$, $He = 13.3\%$, $H_2 = 84.49\%$ at a pressure of 2.841 bar and temperature of 220.9 K compared to various models.

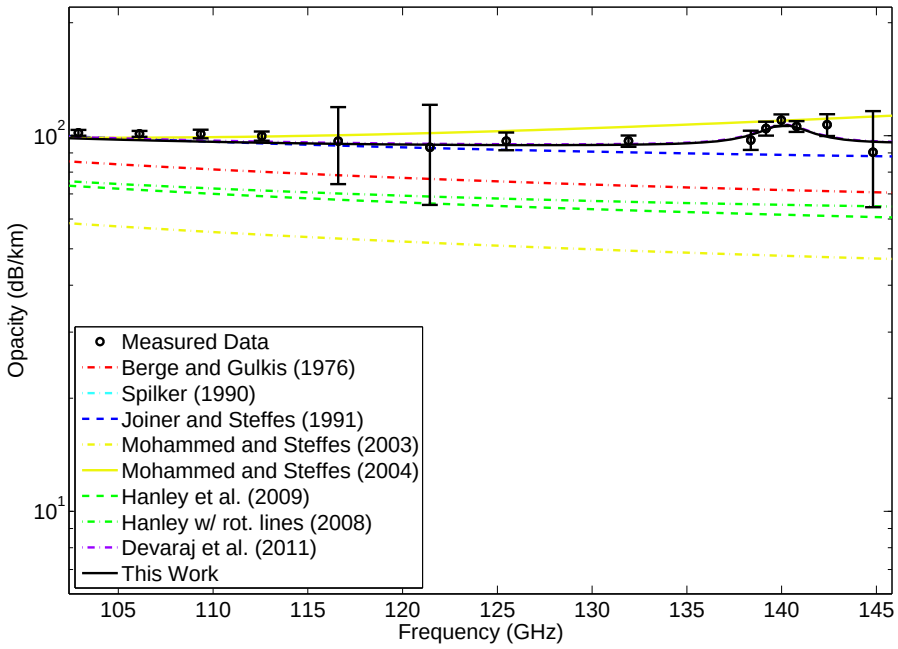

Figure 5.28: Opacity data measured using the 2–3 mm-wavelength system for a mixture of $NH_3 = 10.89\%$, $He = 12.12\%$, $H_2 = 76.99\%$ at a pressure of 1.089 bar and temperature of 220.7 K compared to various models.

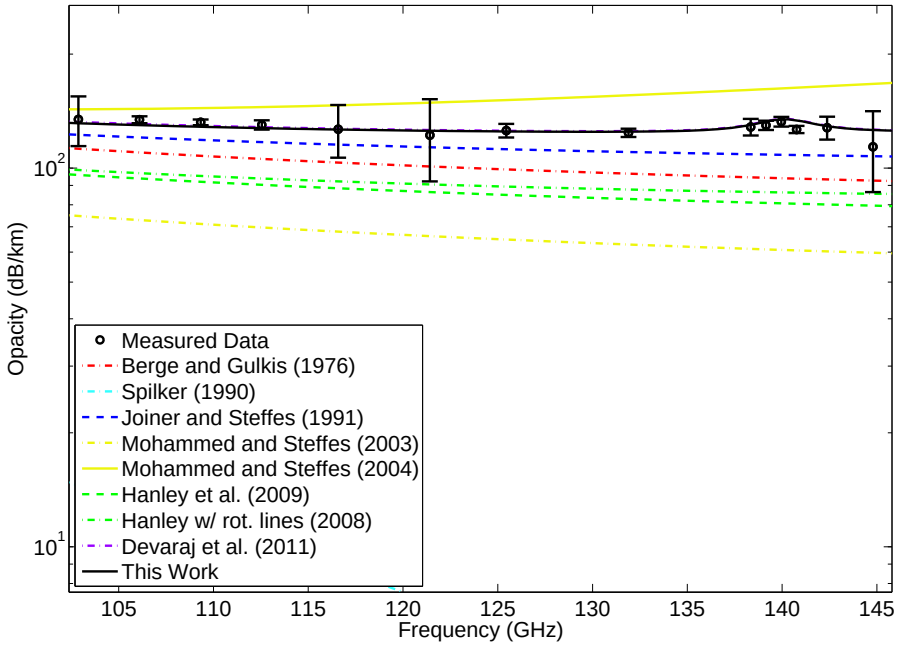

Figure 5.29: Opacity data measured using the 2–3 mm-wavelength system for a mixture of $NH_3 = 6.2\%$, $He = 12.76\%$, $H_2 = 81.04\%$ at a pressure of 1.909 bar and temperature of 220.7 K compared to various models.

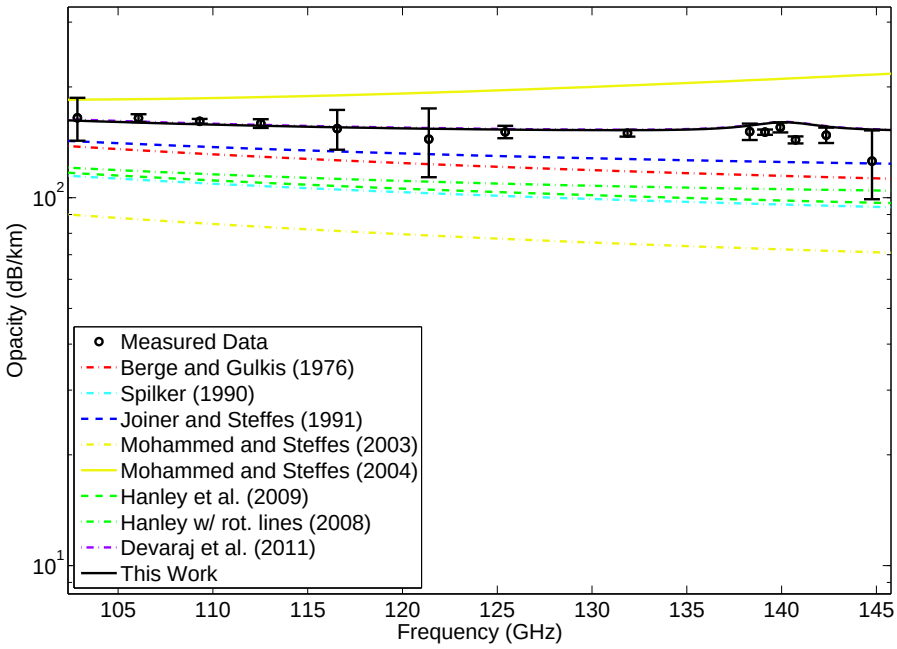

Figure 5.30: Opacity data measured using the 2–3 mm-wavelength system for a mixture of $NH_3 = 4.07\%$, He = 13.05%, $H_2 = 82.88\%$ at a pressure of 2.862 bar and temperature of 220.6 K compared to various models.

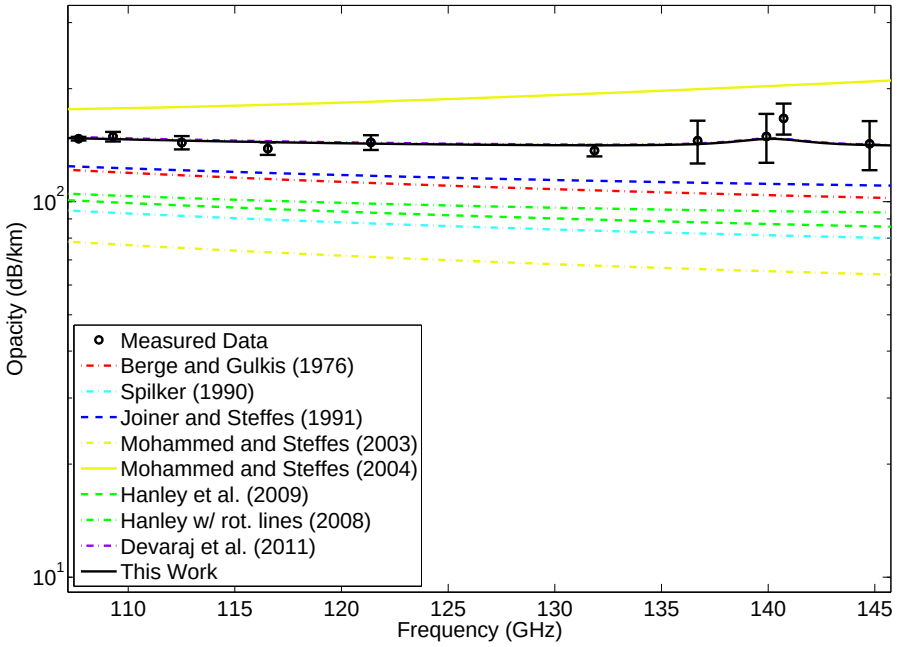

Figure 5.31: Opacity data measured using the 2–3 mm-wavelength system for a mixture of $NH_3 = 3.41\%$, He = 13.14%, $H_2 = 83.45\%$ at a pressure of 2.791 bar and temperature of 208.1 K compared to various models.

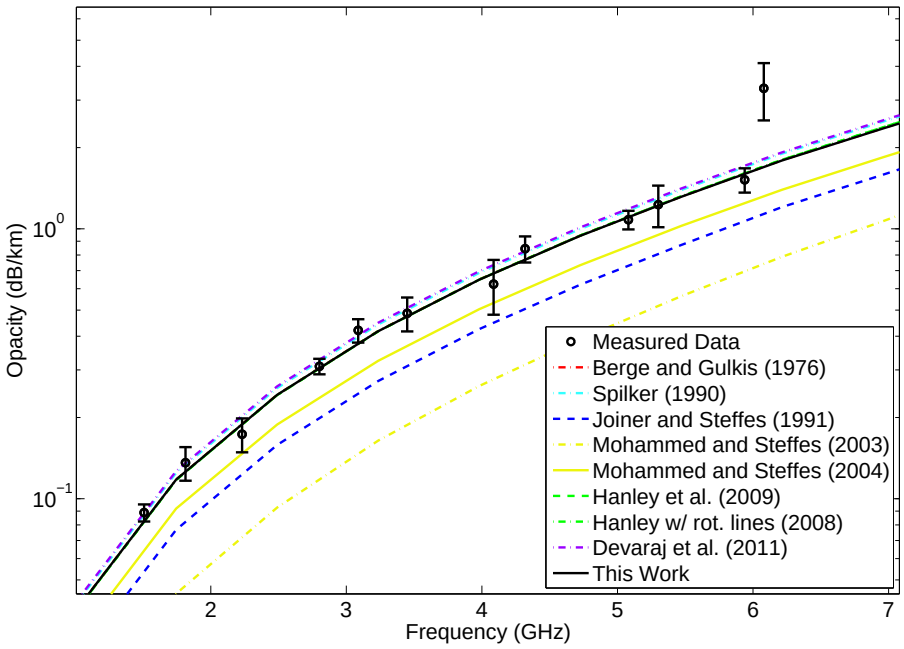

Figure 5.32: Opacity data measured using the high-pressure centimeter-wavelength system for a mixture of $NH_3 = 100\%$, $He = 0\%$, $H_2 = 0\%$ at a pressure of 0.09 bar and temperature of 376 K compared to various models.

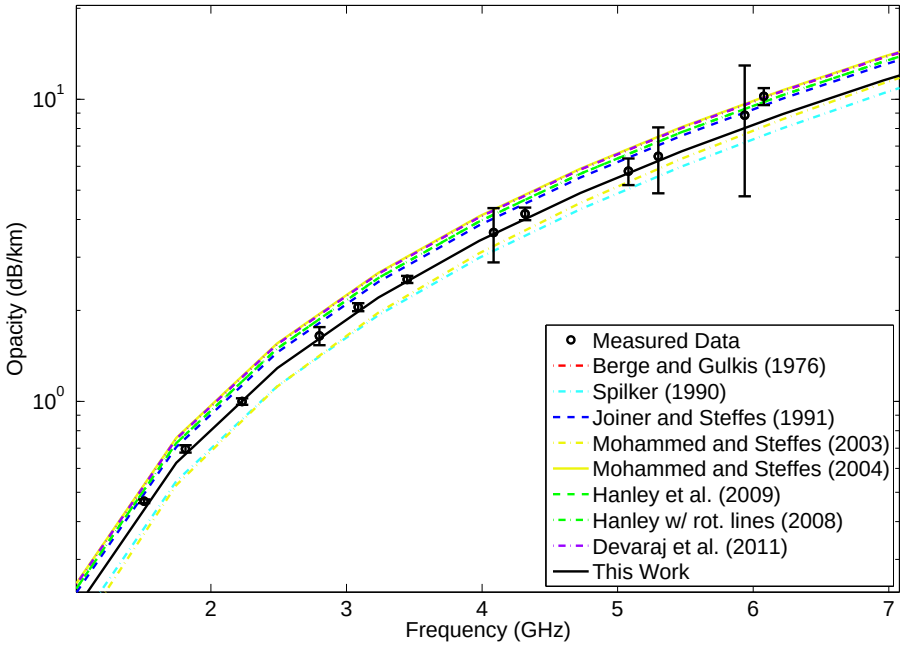

Figure 5.33: Opacity data measured using the high-pressure centimeter-wavelength system for a mixture of $NH_3 = 0.71\%$, $He = 99.29\%$, $H_2 = 0\%$ at a pressure of 12.618 bar and temperature of 375.9 K compared to various models.

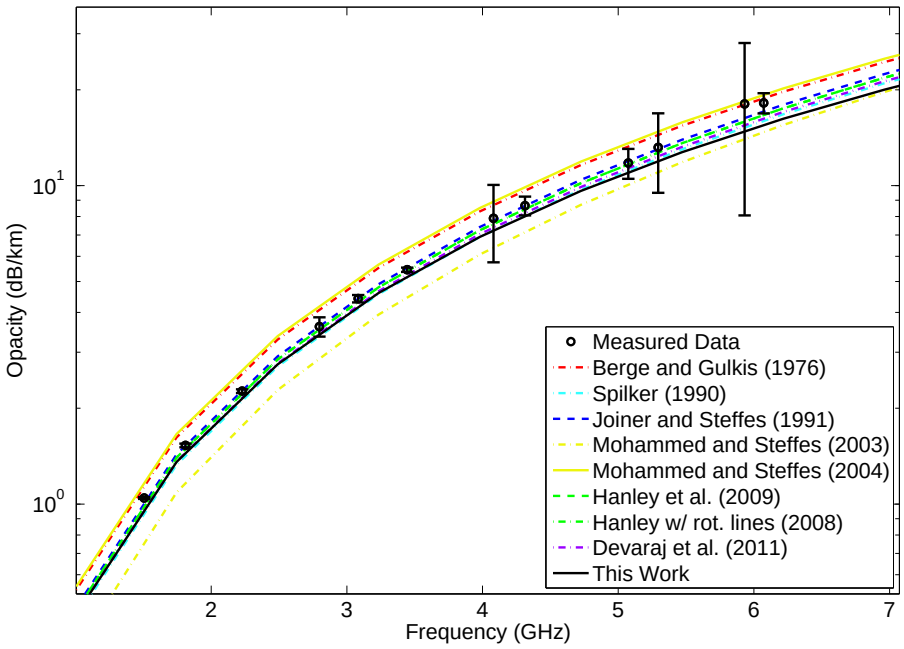

Figure 5.34: Opacity data measured using the high-pressure centimeter-wavelength system for a mixture of NH_3 = 0.42%, He = 58.51%, H_2 = 41.07% at a pressure of 21.411 bar and temperature of 376 K compared to various models.

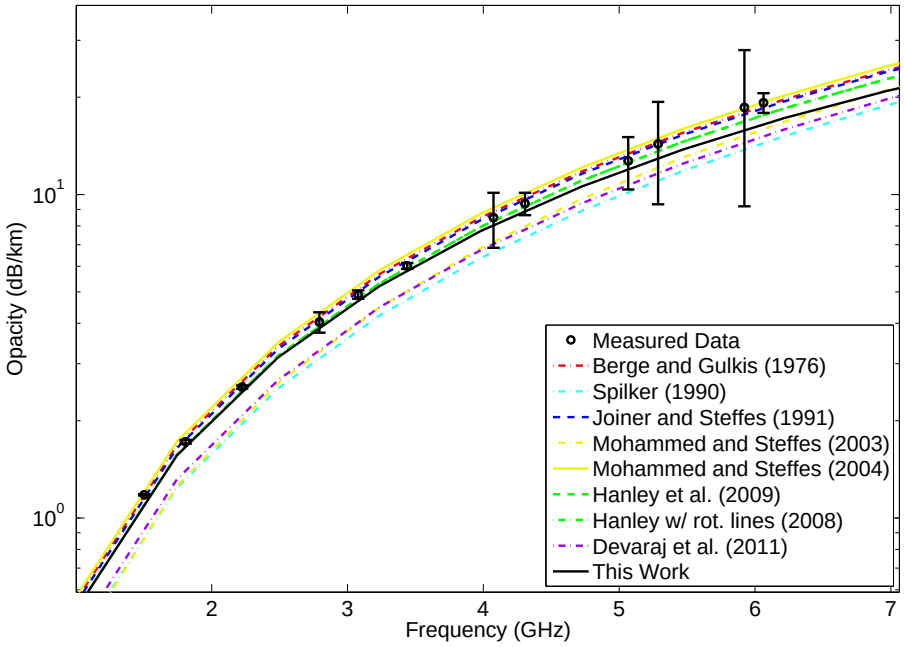

Figure 5.35: Opacity data measured using the high-pressure centimeter-wavelength system for a mixture of NH_3 = 0.23%, He = 31.6%, H_2 = 68.18% at a pressure of 39.649 bar and temperature of 375.9 K compared to various models.

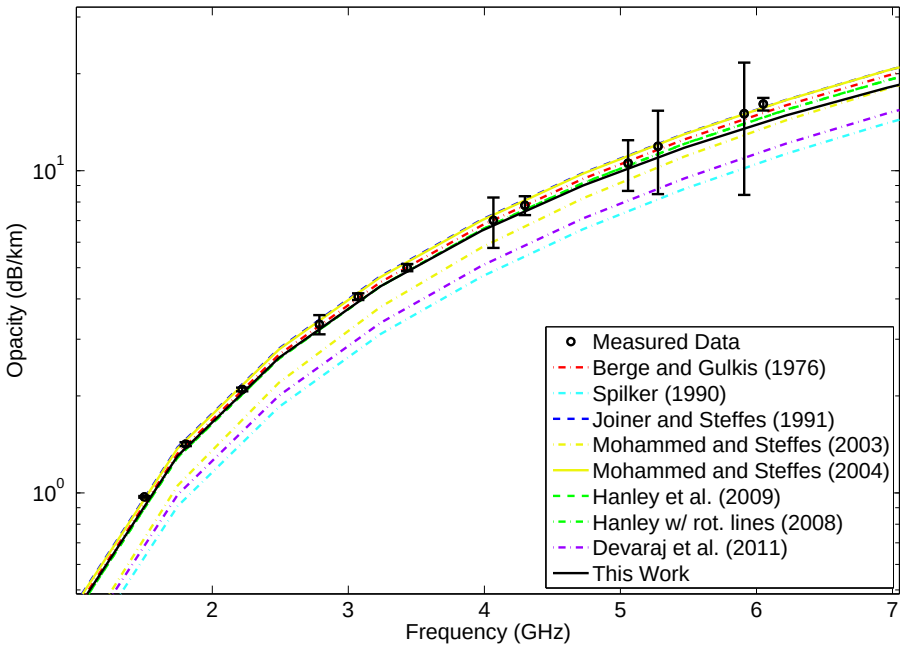

Figure 5.36: Opacity data measured using the high-pressure centimeter-wavelength system for a mixture of NH_3 = 0.15%, He = 20.34%, H_2 = 79.52% at a pressure of 61.608 bar and temperature of 376 K compared to various models.

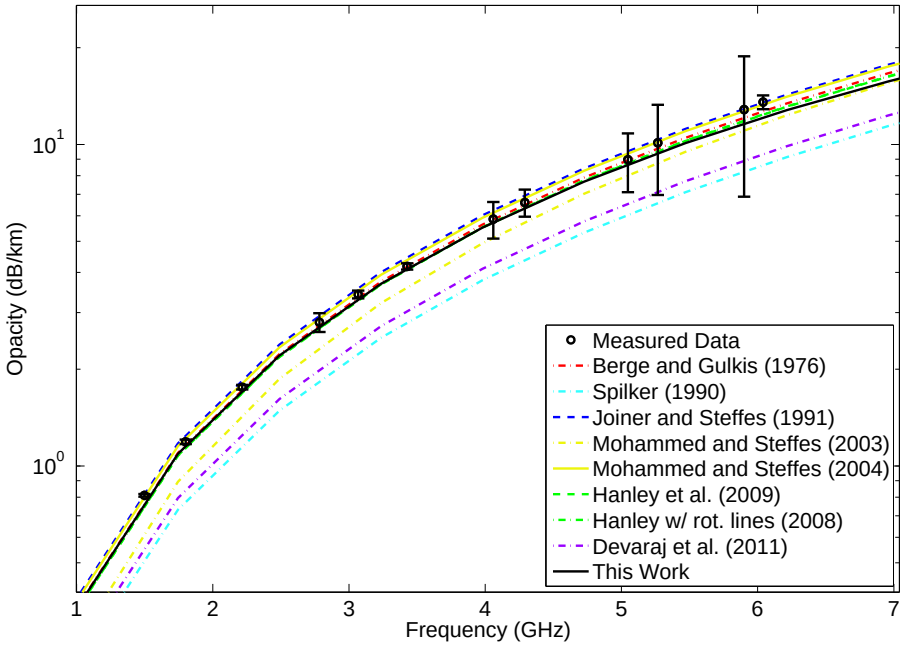

Figure 5.37: Opacity data measured using the high-pressure centimeter-wavelength system for a mixture of NH_3 = 0.11%, He = 15.77%, H_2 = 84.12% at a pressure of 79.454 bar and temperature of 376.1 K compared to various models.

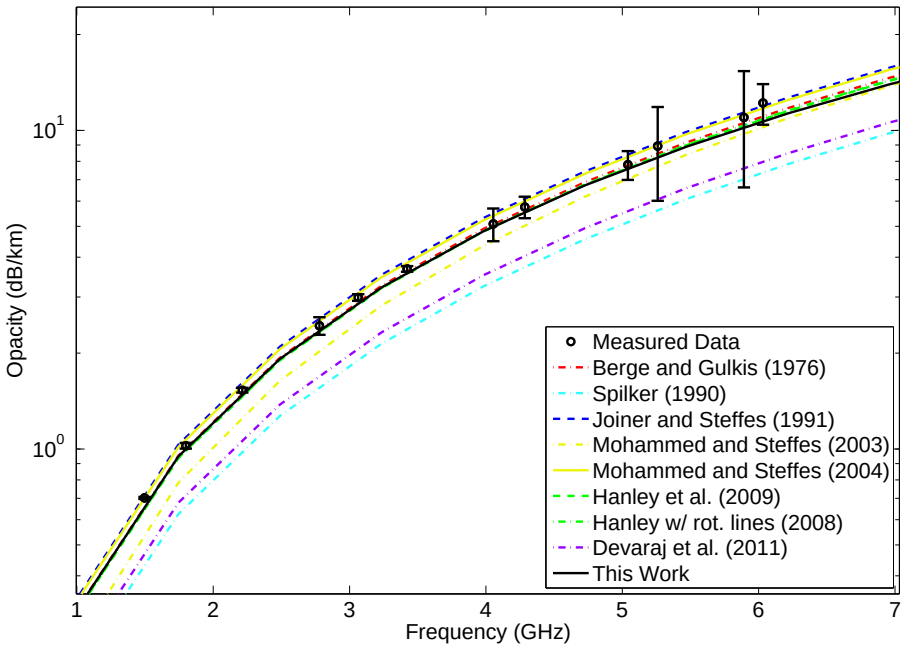

Figure 5.38: Opacity data measured using the high-pressure centimeter-wavelength system for a mixture of NH_3 = 0.09%, He = 13.23%, H_2 = 86.67% at a pressure of 94.665 bar and temperature of 376 K compared to various models.

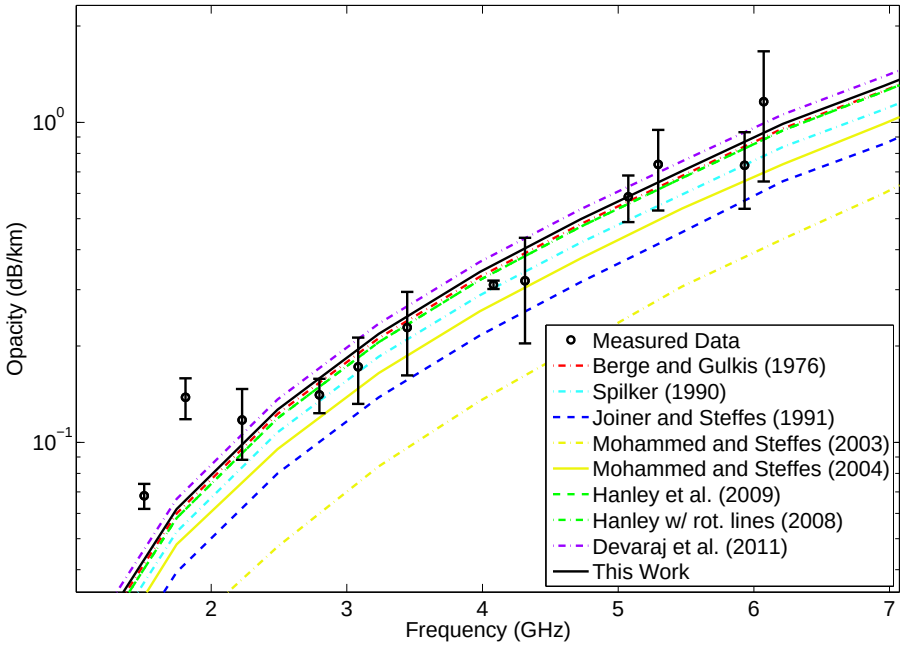

Figure 5.39: Opacity data measured using the high-pressure centimeter-wavelength system for a mixture of NH_3 = 100%, He = 0%, H_2 = 0% at a pressure of 0.082 bar and temperature of 446.8 K compared to various models.

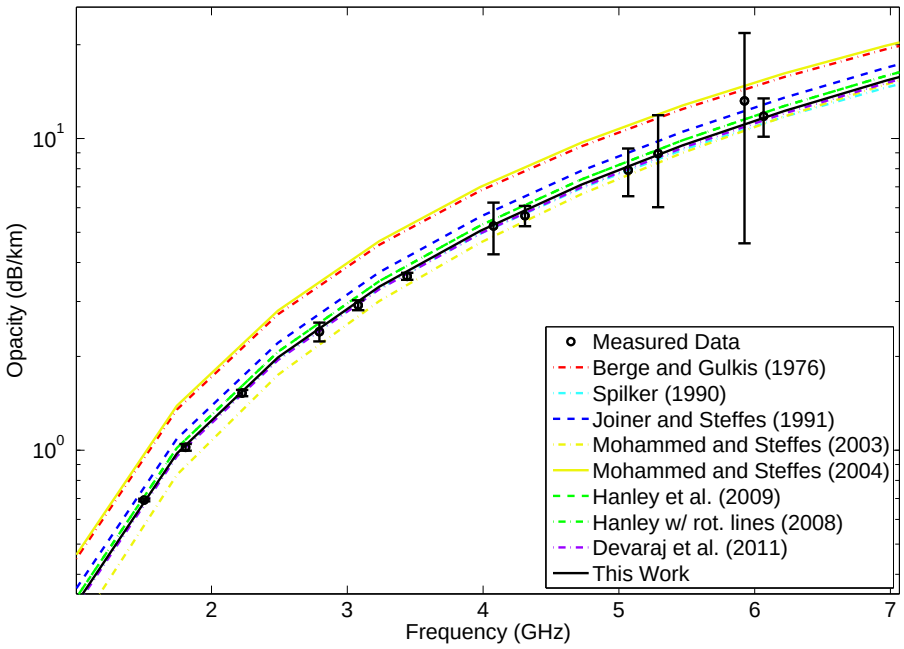

Figure 5.40: Opacity data measured using the high-pressure centimeter-wavelength system for a mixture of $NH_3 = 0.59\%$, $He = 0\%$, $H_2 = 99.41\%$ at a pressure of 14.025 bar and temperature of 446.9 K compared to various models.

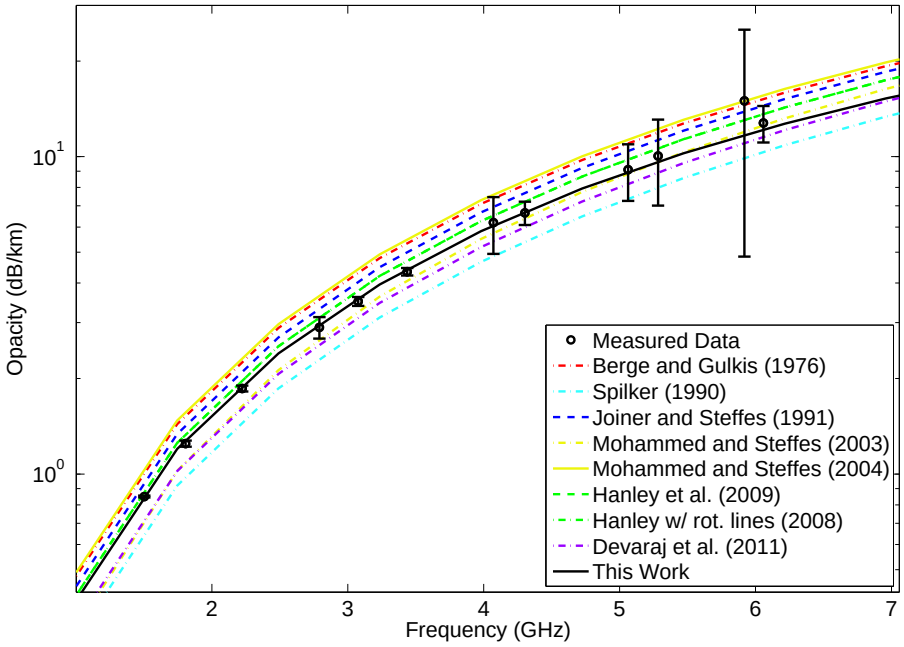

Figure 5.41: Opacity data measured using the high-pressure centimeter-wavelength system for a mixture of $NH_3 = 0.28\%$, $He = 0\%$, $H_2 = 99.72\%$ at a pressure of 29.862 bar and temperature of 446.9 K compared to various models.

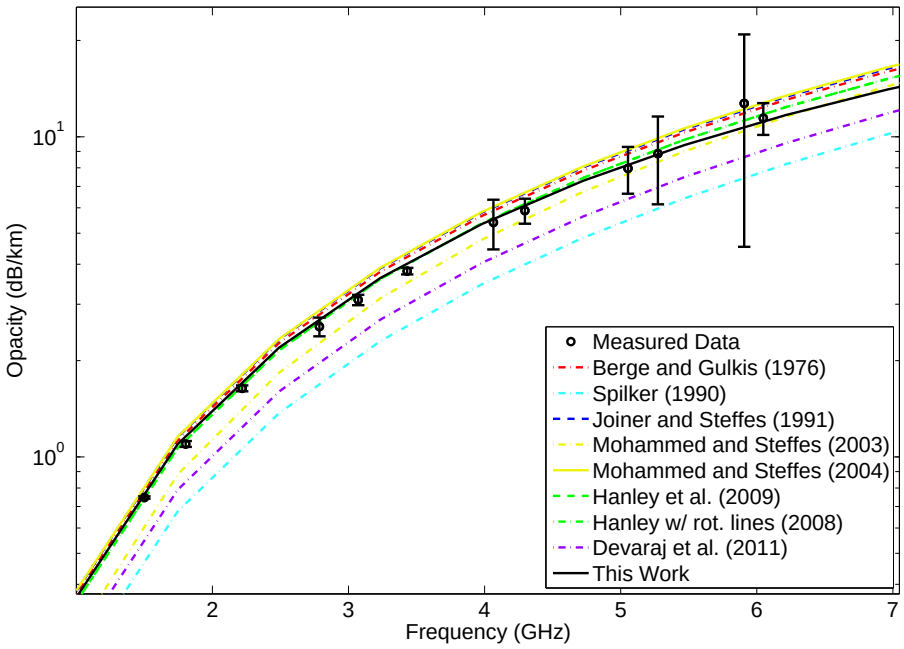

Figure 5.42: Opacity data measured using the high-pressure centimeter-wavelength system for a mixture of $NH_3 = 0.16\%$, $He = 0\%$, $H_2 = 99.84\%$ at a pressure of 51.48 bar and temperature of 446.9 K compared to various models.

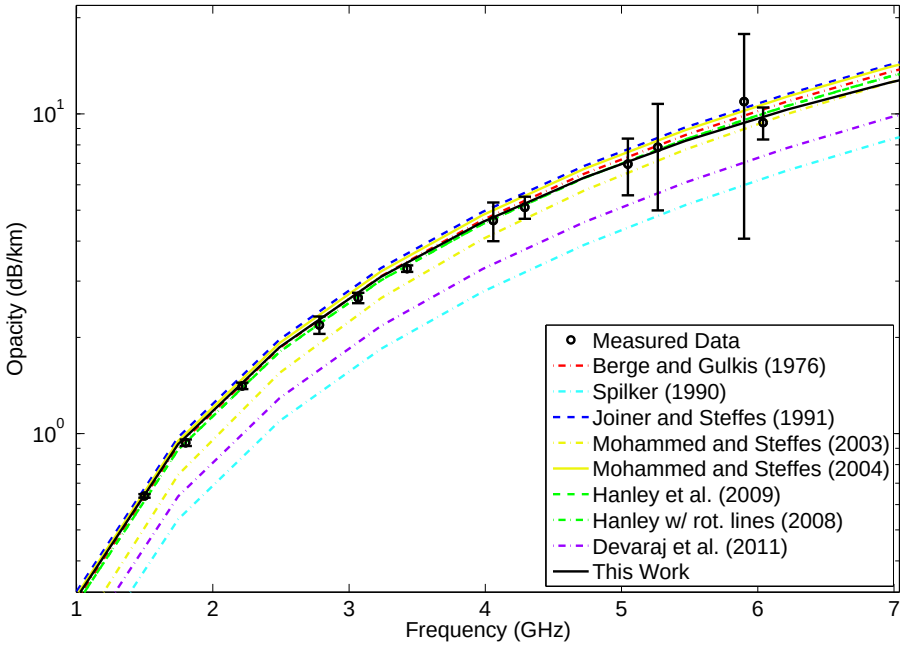

Figure 5.43: Opacity data measured using the high-pressure centimeter-wavelength system for a mixture of $NH_3 = 0.12\%$, $He = 0\%$, $H_2 = 99.88\%$ at a pressure of 69.01 bar and temperature of 446.8 K compared to various models.

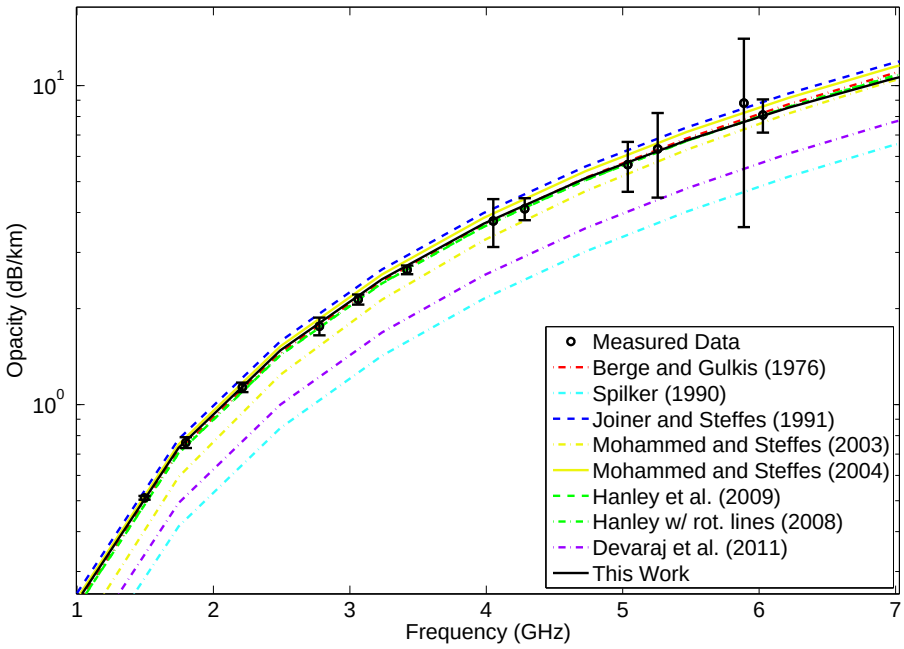

Figure 5.44: Opacity data measured using the high-pressure centimeter-wavelength system for a mixture of $NH_3 = 0.09\%$, $He = 0\%$, $H_2 = 99.91\%$ at a pressure of 93.545 bar and temperature of 446.9 K compared to various models.

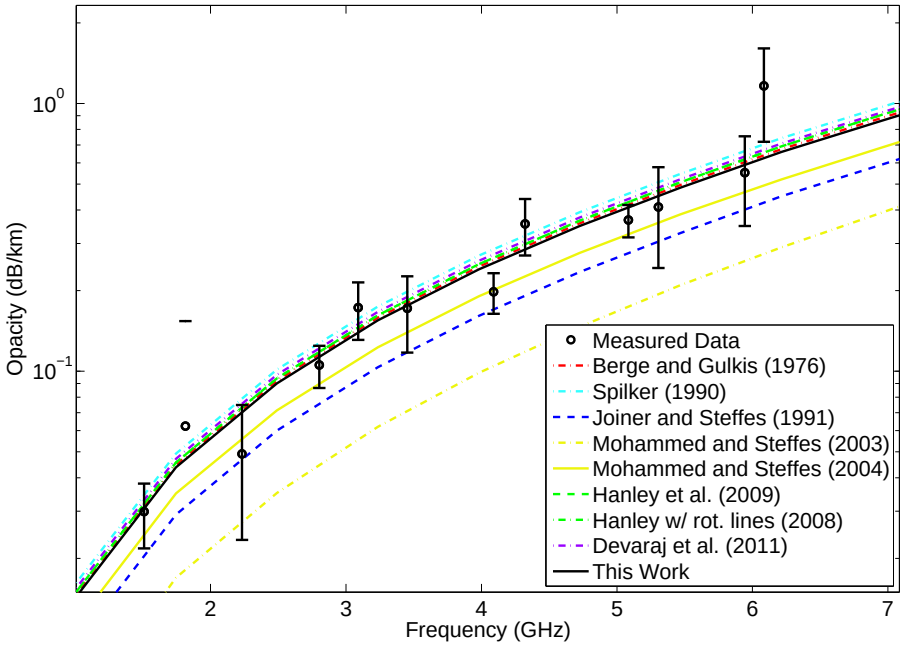

Figure 5.45: Opacity data measured using the high-pressure centimeter-wavelength system for a mixture of $NH_3 = 100\%$, $He = 0\%$, $H_2 = 0\%$ at a pressure of 0.046 bar and temperature of 332.9 K compared to various models.

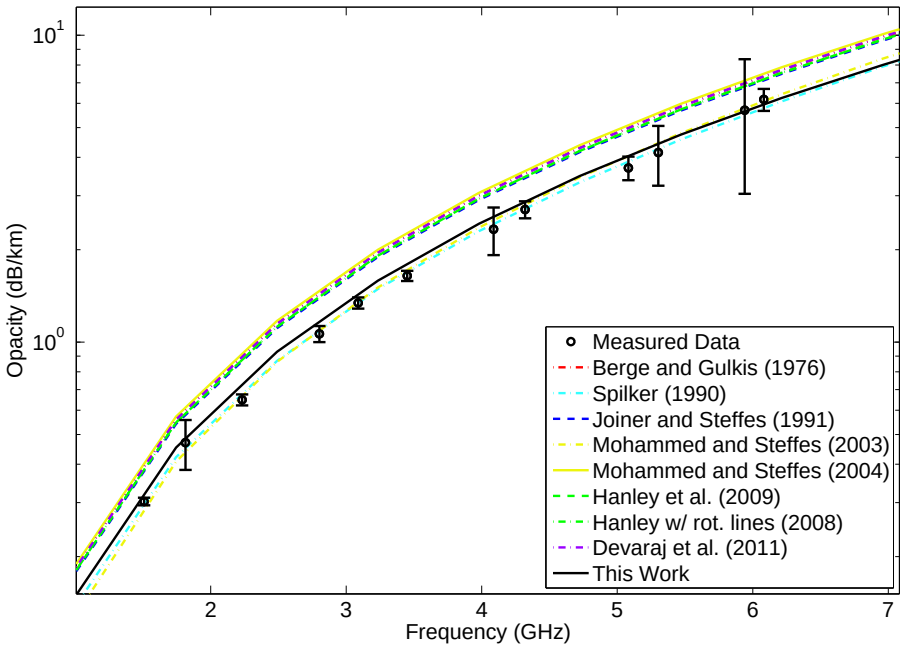

Figure 5.46: Opacity data measured using the high-pressure centimeter-wavelength system for a mixture of $NH_3 = 0.3\%$, He $= 99.7\%$, $H_2 = 0\%$ at a pressure of 15.628 bar and temperature of 333.2 K compared to various models.

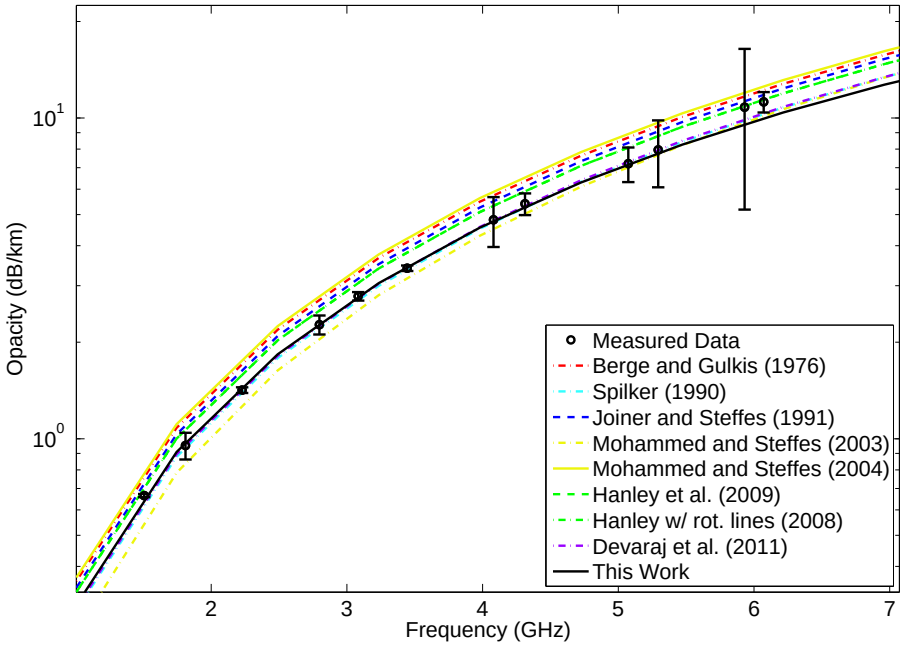

Figure 5.47: Opacity data measured using the high-pressure centimeter-wavelength system for a mixture of $NH_3 = 0.15\%$, He $= 49.1\%$, $H_2 = 50.76\%$ at a pressure of 31.738 bar and temperature of 333 K compared to various models.

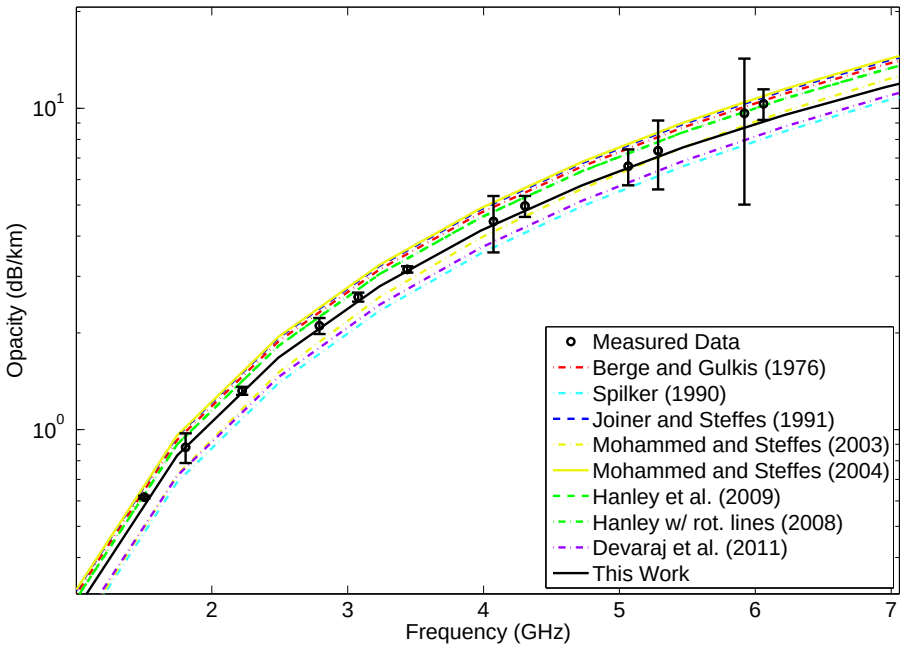

Figure 5.48: Opacity data measured using the high-pressure centimeter-wavelength system for a mixture of $NH_3 = 0.09\%$, He $= 31.44\%$, $H_2 = 68.47\%$ at a pressure of 49.567 bar and temperature of 333.1 K compared to various models.

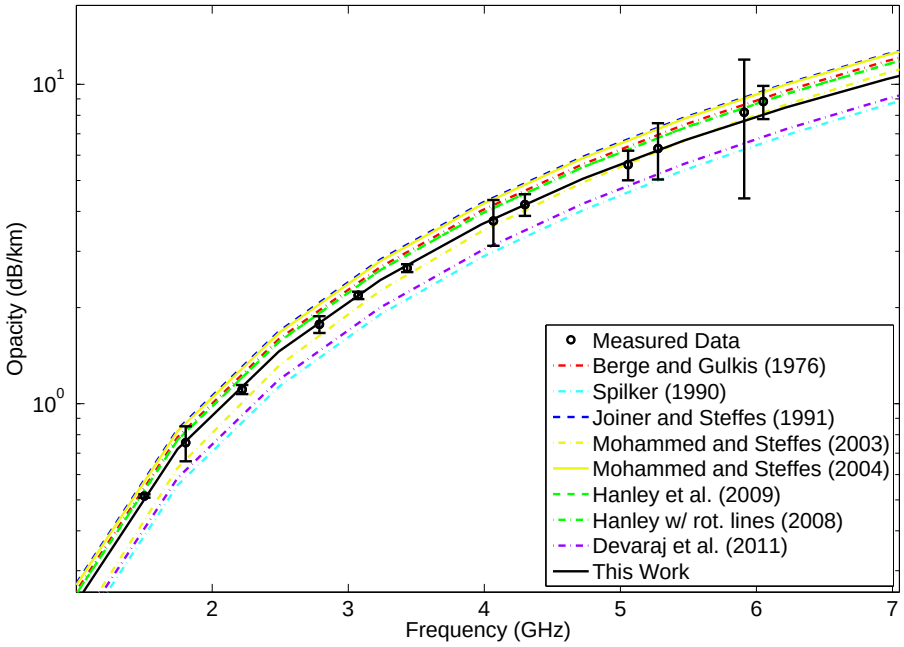

Figure 5.49: Opacity data measured using the high-pressure centimeter-wavelength system for a mixture of $NH_3 = 0.07\%$, He $= 24.28\%$, $H_2 = 75.65\%$ at a pressure of 64.177 bar and temperature of 333.1 K compared to various models.

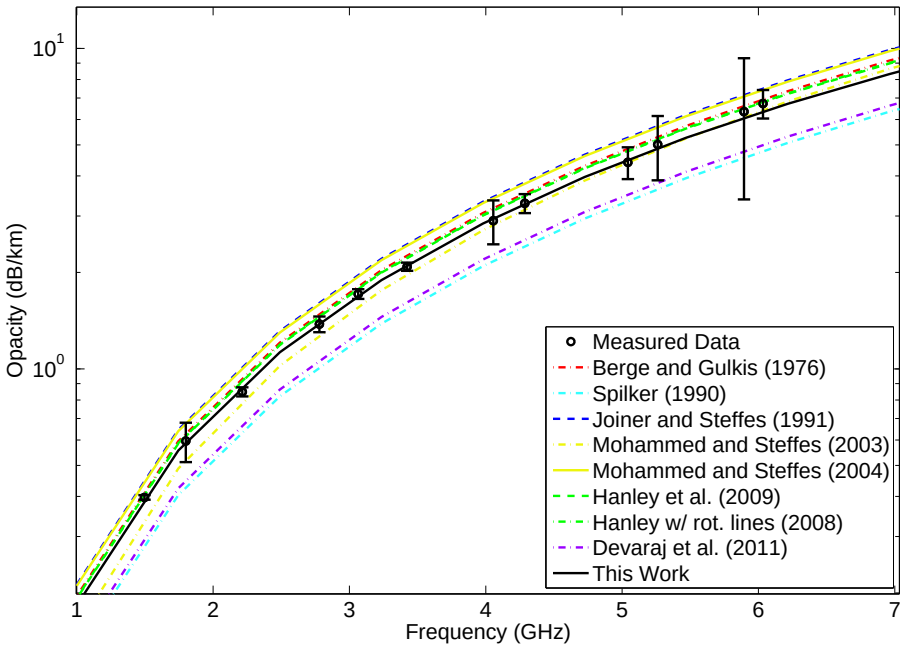

Figure 5.50: Opacity data measured using the high-pressure centimeter-wavelength system for a mixture of NH_3 = 0.05%, He = 16.99%, H_2 = 82.96% at a pressure of 91.728 bar and temperature of 332.9 K compared to various models.

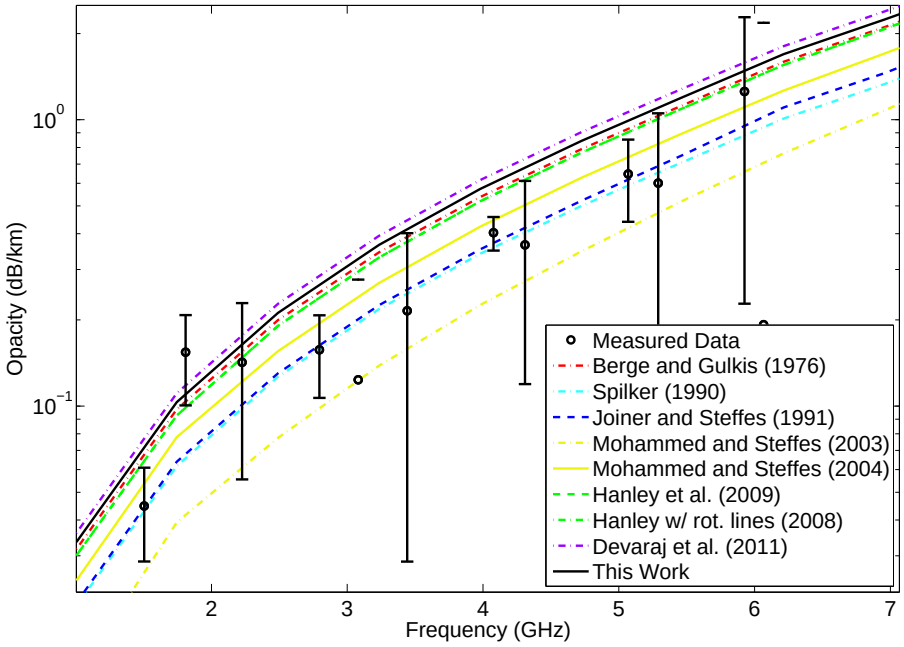

Figure 5.51: Opacity data measured using the high-pressure centimeter-wavelength system for a mixture of NH_3 = 100%, He = 0%, H_2 = 0% at a pressure of 0.125 bar and temperature of 502.4 K compared to various models.

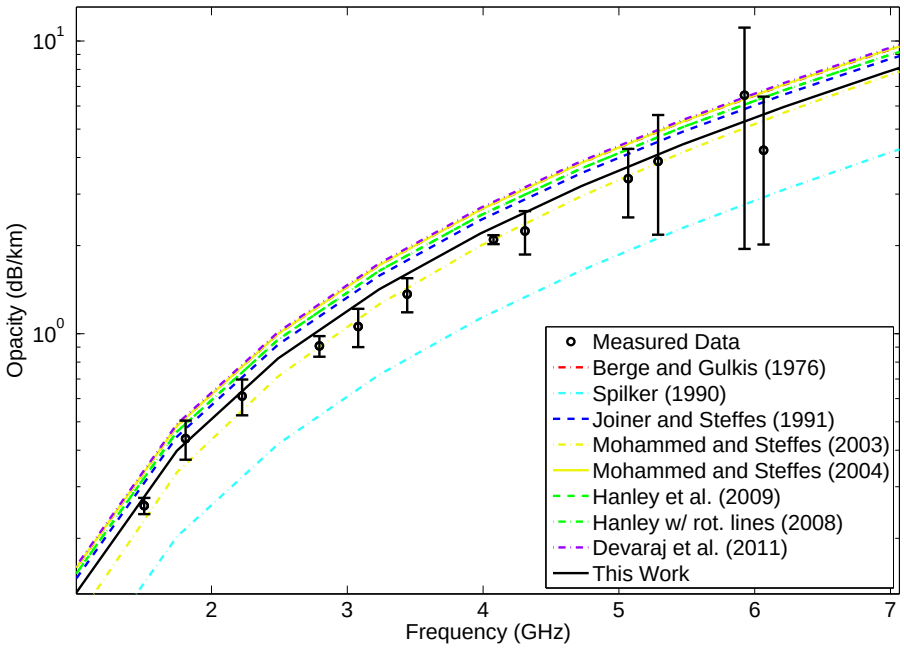

Figure 5.52: Opacity data measured using the high-pressure centimeter-wavelength system for a mixture of $NH_3 = 1.15\%$, $He = 98.85\%$, $H_2 = 0\%$ at a pressure of 10.877 bar and temperature of 502.6 K compared to various models.

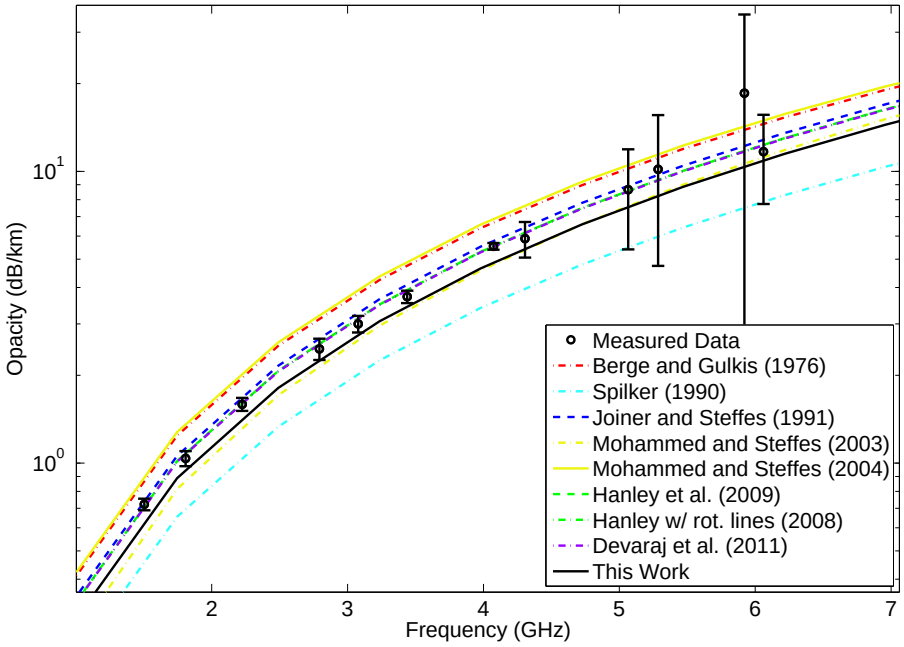

Figure 5.53: Opacity data measured using the high-pressure centimeter-wavelength system for a mixture of $NH_3 = 0.63\%$, $He = 54.08\%$, $H_2 = 45.29\%$ at a pressure of 19.882 bar and temperature of 502.5 K compared to various models.

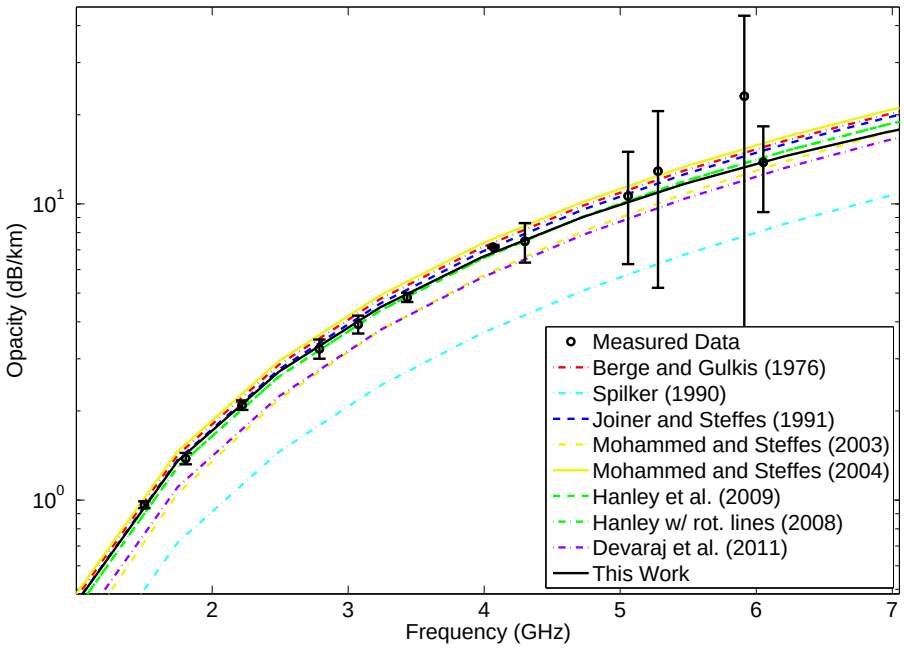

Figure 5.54: Opacity data measured using the high-pressure centimeter-wavelength system for a mixture of NH_3 = 0.3%, He = 25.59%, H_2 = 74.11% at a pressure of 42.01 bar and temperature of 502.3 K compared to various models.

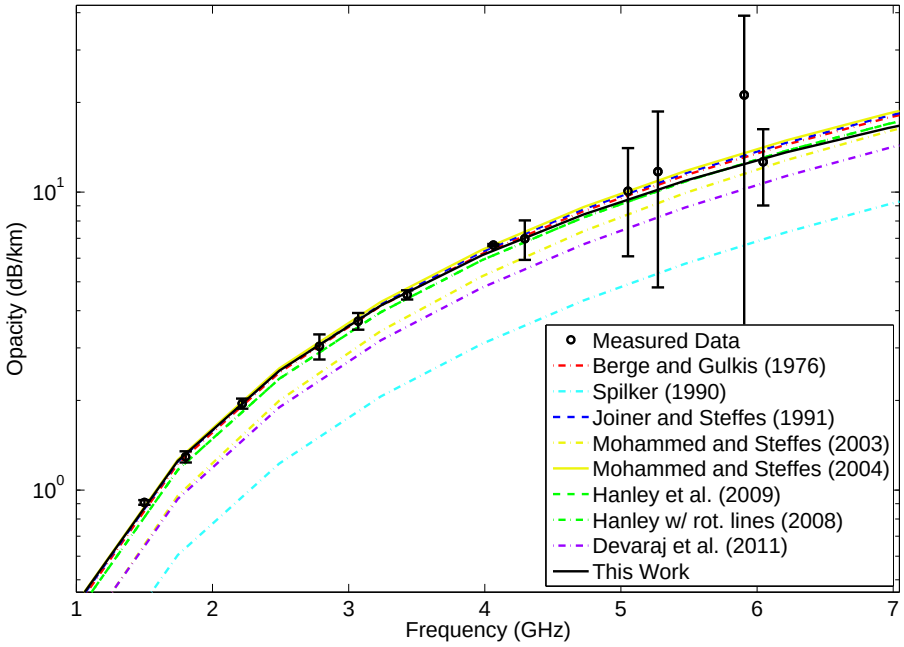

Figure 5.55: Opacity data measured using the high-pressure centimeter-wavelength system for a mixture of NH_3 = 0.21%, He = 18.44%, H_2 = 81.34% at a pressure of 58.305 bar and temperature of 502.4 K compared to various models.

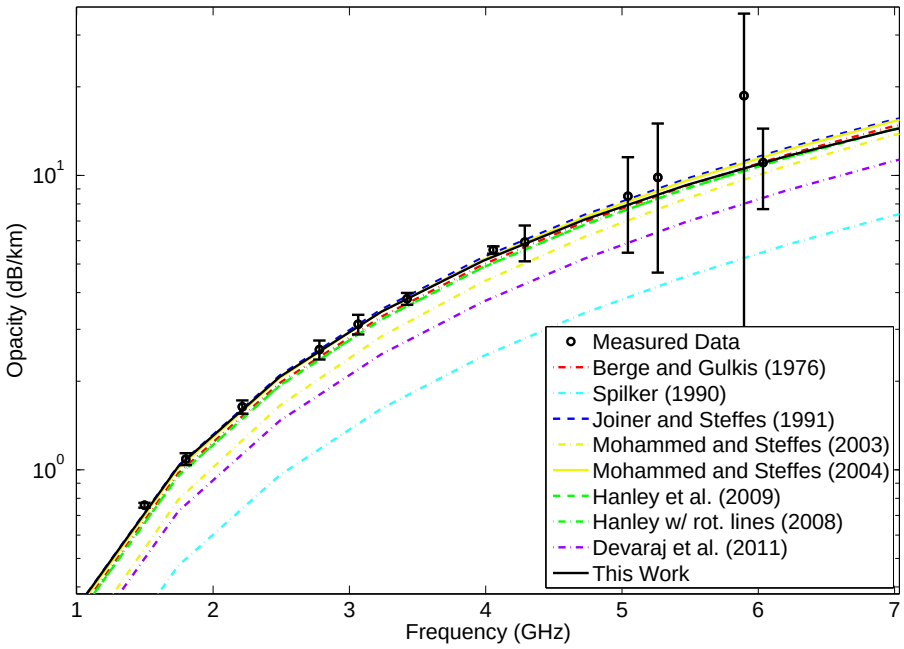

Figure 5.56: Opacity data measured using the high-pressure centimeter-wavelength system for a mixture of NH_3 = 0.15%, He = 13.04%, H_2 = 86.8% at a pressure of 82.432 bar and temperature of 502.1 K compared to various models.

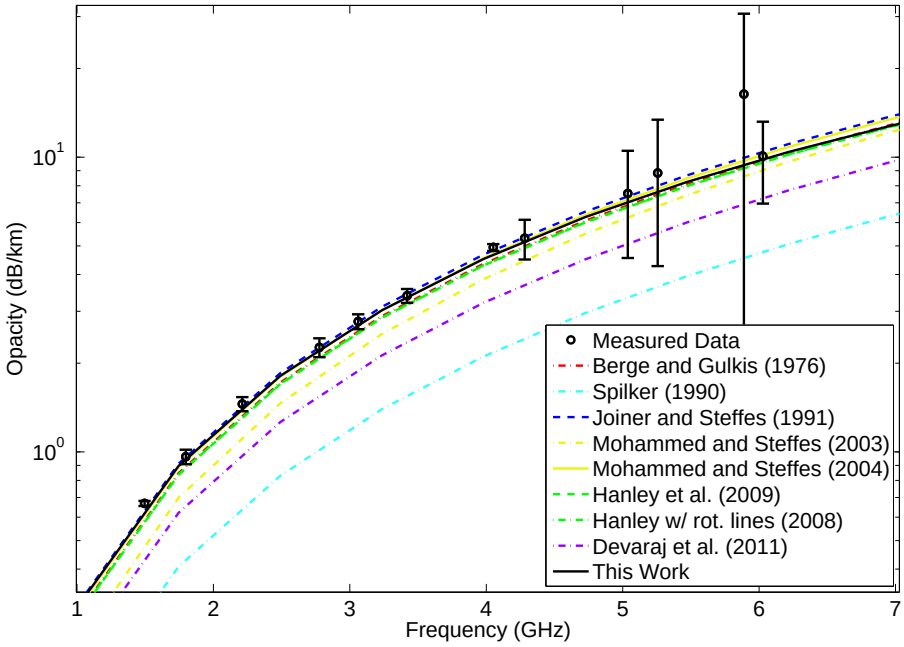

Figure 5.57: Opacity data measured using the high-pressure centimeter-wavelength system for a mixture of NH_3 = 0.13%, He = 10.92%, H_2 = 88.95% at a pressure of 98.439 bar and temperature of 502.1 K compared to various models.

5.5.1 Ultra-High-Pressure Extrapolation

The new consistent ammonia opacity model was developed for use under jovian conditions in the centimeter-wavelength range at pressures up to 100 bar and in the millimeter-wavelength range at pressures up to 3 bar. The new model corrects for the non-ideal pure fluid behavior under high-pressure conditions and the high-pressure inversion model parameters were empirically derived by data fitting to a high-pressure data set ($P > 15$ bar). While this model can be extrapolated with reasonable certainty to slightly higher pressures, some caution must be exercised when using the model under ultra-high-pressure conditions (pressures much greater than 100 bar).

When modeling the microwave emission from a planetary atmosphere, weighting functions (or contribution functions) indicate the altitudes (pressure layers) that contribute most to the brightness temperature at a particular frequency. The weighting functions probe less deep into the atmosphere at the limb of the planet than at nadir (the path length through the atmosphere at the limb is longer than at nadir). For example, the nadir-viewing weighting function for Jupiter show that at 1 GHz the atmospheric layers from 20 to 300 bar contribute to the brightness temperature. At even lower frequencies, the jovian atmospheric layers at hundreds of bar of pressure contribute to the brightness temperature. The normalized nadir-viewing weighting function in the 0.5–25 GHz range computed by Karpowicz (2010) using a radiative transfer model for the atmosphere of Jupiter without contribution from cloud opacity is shown in Figure 5.58.

Morris and Parsons (1970) made measurements of the microwave absorption of ammonia in a predominantly hydrogen or helium atmosphere at 295 K and pressures up to 700 bar. A tunable resonant cavity which was operated in the TE_{013} mode was used for these measurements and the binary mixture absorption measurements were conducted at 9.58 GHz. These measurements show a steep increase in opacity with pressure up to around 80 bar, and then the opacity increases less steeply. Morris

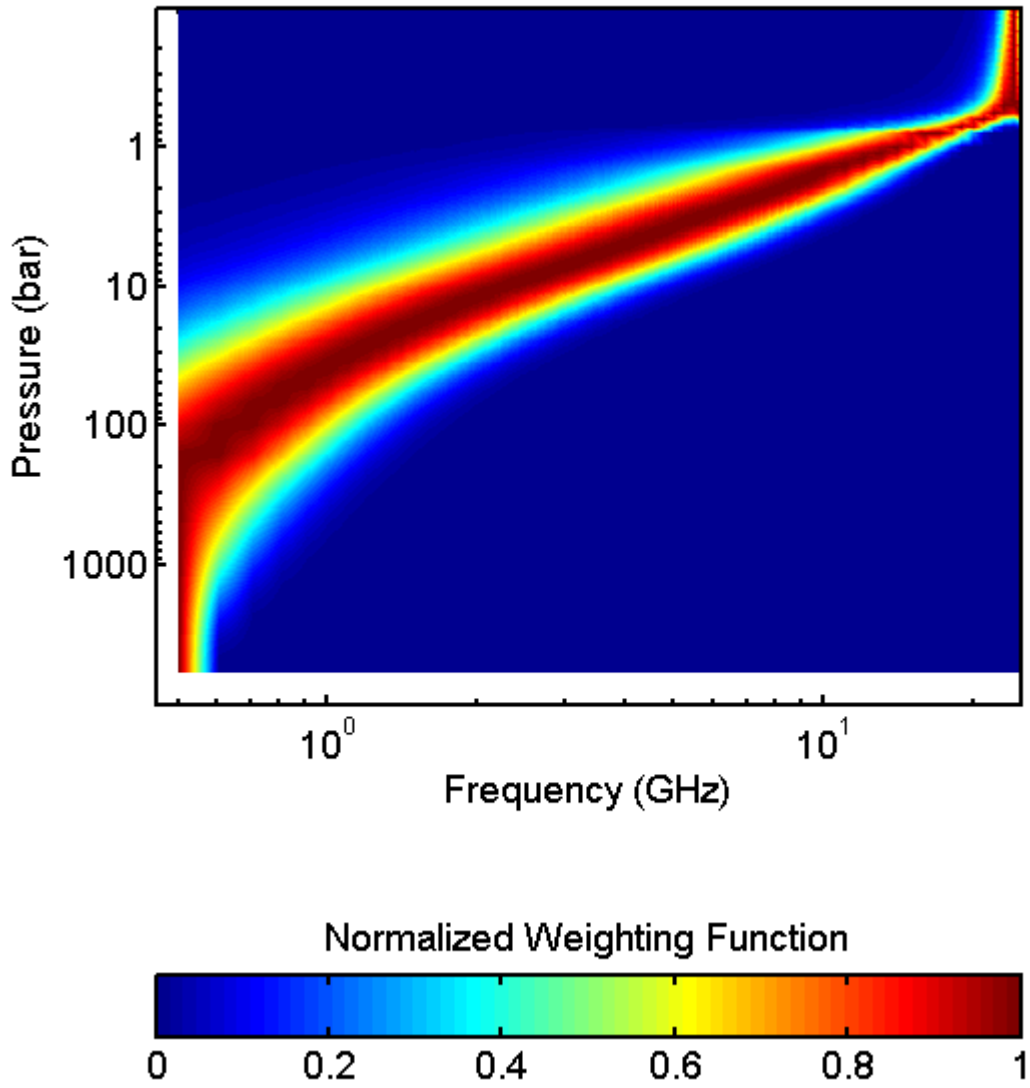

Figure 5.58: Normalized nadir-viewing weighting functions in the 0.5–25 GHz range computed by Karpowicz (2010) using a radiative transfer model for a mean jovian atmosphere without cloud contribution.

(1971) attempts to explain this behavior as a shift from resonant to non-resonant Debye absorption along with greater frequency of collision of molecules. Berge and Gulkis (1976) developed a model that was fit to the Morris and Parsons (1970) ammonia/hydrogen data using a correction factor for hydrogen. However, this model does not include a correction factor for helium, which behaves in a similar fashion to hydrogen. Hanley (2008) attempted to fit to the Morris and Parsons (1970) data by including the lowest 20 rotational transitions of ammonia. The Berge and Gulkis (1976), Hanley (2008) with rotational lines, and the new model developed as part of this work are shown along with the Morris and Parsons (1970) measured data in Figures 5.59 and 5.60. Since the absolute uncertainties of the Morris and Parsons (1970) ammonia measurements are not precisely known, the measurements were assumed to be accurate within $\pm 10\%$. There could be some additional uncertainties in the Morris and Parsons (1970) data since they did not account for the adsorption of ammonia on the walls of their system. Additionally, the measurements were made only at one resonant frequency and that resonance might have been contaminated by other resonances.

Although the new model performs very well in its consistency with the Morris and Parsons (1970) data, some caution must be exercised when using the new model at pressures much greater than 100 bar. The new model accounts for the non-ideal behavior of pure fluids, but does not account for the non-ideal behavior of fluid mixtures. Additionally, only the inversion transitions of the new model were optimized for use under high-pressure conditions (pressures up to 100 bar). The parameters for the rotational transitions described in this work were not optimized to perform under high-pressure conditions. Finally, the assumptions underlying most lineshape theories, such as binary and elastic collisions of molecules, might become invalid under ultra-high-pressure conditions. All of the possible shortcomings of the new model at pressures much greater than 100 bar indicate that some caution must be exercised

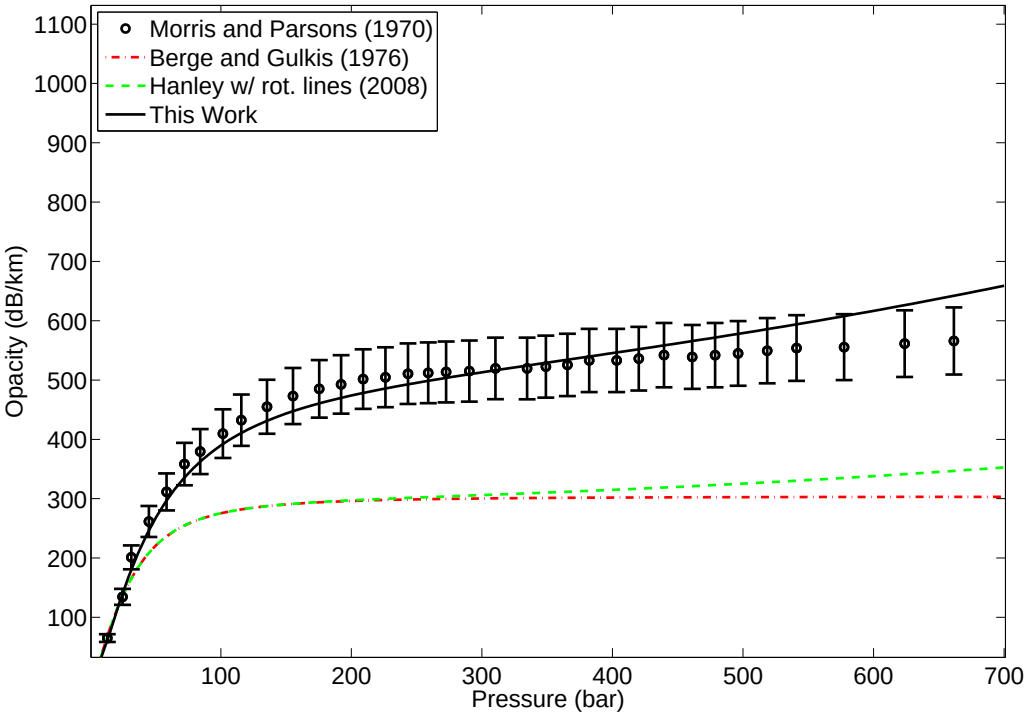

Figure 5.59: Opacity data by Morris and Parsons (1970) for a mixture of NH_3 = 0.9%, He = 99.1%, H_2 = 0% at a frequency of 9.58 GHz and temperature of 295 K compared to this work, Hanley (2008) with rotational lines and Berge and Gulkis (1976)

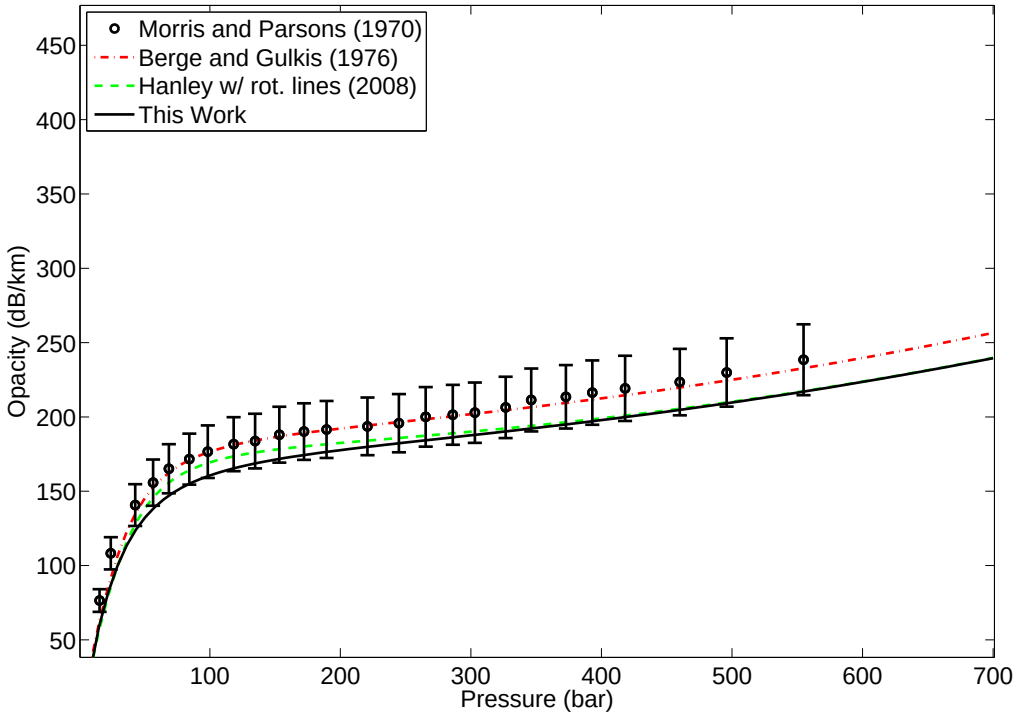

Figure 5.60: Opacity data measured by Morris and Parsons (1970) for a mixture of $NH_3 = 0.44\%$, He $= 0\%$, $H_2 = 99.56\%$ at a frequency of 9.58 GHz and temperature of 295 K compared to this work, Hanley (2008) with rotational lines, and Berge and Gulkis (1976)

when extrapolating the new model to ultra-high-pressure conditions characteristic of the very deep atmospheres of jovian planets.

5.6 The Influence of Water Vapor on the Ammonia Absorption Spectrum

Water vapor is the third most abundant constituent deep in the atmosphere of Jupiter after hydrogen and helium (see, e.g., Karpowicz, 2010). Current ammonia opacity models for jovian conditions, including the new model that was described earlier in this chapter, account for the self-broadening and foreign-gas-broadening due to hydrogen and helium. While the broadening effects of hydrogen and helium are well characterized, it is critical to investigate any possible pressure-broadening effects of water vapor on the ammonia absorption spectrum. Karpowicz and Steffes (2011) made extensive measurements of the centimeter-wavelength opacity of water vapor under jovian conditions and found that the self-broadening from water vapor dominates its absorption spectrum. Water vapor, with its a large broadening cross-section (collision diameter), has the potential to broaden the ammonia transitions. Hence, it is important to study the influence of water vapor on the ammonia absorption spectrum.

Preliminary experimental investigation of the pressure-broadening of ammonia by water vapor in the centimeter-wavelength region has been conducted in the 375–450 K temperature range. Prior to this investigation, there was at least one laboratory measurement study which indicated that water vapor can efficiently broaden the 572 GHz rotational transition of ammonia (Belov et al., 1983). Hence, understanding the enhanced opacity of ammonia due to the presence of water vapor is crucial to the determination of the abundance of water vapor in the jovian atmospheres.

5.6.1 Ammonia/Water Vapor Opacity Measurements

Laboratory measurements of the centimeter-wavelength properties of ammonia pressure-broadened by water vapor have been conducted using the high-pressure system. The measurement process involved four sequences of measurements of the 5–20 cm-wavelength opacity of ammonia/water vapor mixture in the 375–450 K temperature range. The measurements at 450 K were conducted by this author and the measurements at 375 K were conducted by fellow graduate student Danny Duong. Certified UHP grade ammonia and argon gas cylinders from Airgas, Inc. were used for the experiments and dielectric matching. A water reservoir (similar to the one used by Karpowicz and Steffes, 2011), filled with distilled water, ACS Reagent Grade with ASTM D 1193 specifications for reagent water, type II (manufactured by Ricca Chemical Company), was connected to the pressure vessel and placed inside the oven to generate the required amount of water vapor for the experiments. The water vapor adsorption is very small (see, e.g., Karpowicz, 2010) when compared to ammonia under our experimental conditions. Hence, ammonia was added first to the system and the walls of the pressure vessel and cavity resonator were presaturated with ammonia before the pure ammonia measurements were made.

Each measurement sequence first involved vacuum measurements, followed by the addition of gaseous ammonia to the evacuated chamber up to the desired pressure and pure ammonia measurements were made. Water vapor was then added to the system up to the desired pressure, by opening the oven door and quickly opening and closing the valve on the water reservoir, and ammonia/water vapor mixture measurements were made. Since there is a possibility of water vapor condensing in the pipes exterior to the oven (which are at room temperature), the high-temperature inlet and outlet valves that are inside the oven were closed before water vapor is added into the pressure vessel. A coarse estimate of the water vapor pressure, while adding water vapor to the system, was obtained from the pressure transducer readings

Table 5.10: Listing of all experiment sequences of the 5–20 cm-wavelength opacity measurements of the NH_3/H_2O mixture.

Experiment Dates	Temperature (K)	NH_3 Pressure (bar)	H_2O Pressure (bar)
12/2010	452.11	0.0902	0.945
12/2010	452.52	0.0462	1.0912
02/2011	373.85	0.0295	0.1499
03/2011	373.85	0.0473	0.2065

to ensure that its partial pressure was well below the saturation vapor pressure at the measurement temperature. After the measurements of the water vapor/ammonia mixture were conducted, the pressure was measured using a "buffer method". A small amount of helium was added to the pipe section connecting the DPI 10430A gauge to the inlet valve to a pressure known to be slightly greater than that in the pressure vessel. Then, while monitoring the DPI 10430A gauge, the oven was quickly opened and the inlet valve to the pressure vessel was opened and the pressure quickly read before closing the valve and shutting the oven door. The pressure reading stabilizes very quickly and the possibility of any water vapor entering and condensing in the pipes external to the oven is very low. Since the volume of the pipe section between the DPI 10430A gauge and the inlet valve is very small relative to the volume of the pressure vessel, which is approximately 32 liters, no additional corrections were needed to account for the true pressure in the vessel prior to opening the inlet valve. After this step, a vacuum was drawn in the pressure vessel and a second set of vacuum measurements were conducted. After this step, dielectric matching measurements were conducted followed by a third set of vacuum measurements. Finally, three sets of straight-through measurements of signal levels were conducted. Table 5.10 lists the measurements and the experiment dates.

5.6.2 Preliminary Ammonia/Water Vapor Opacity Model

Based on the initial four sequences of the ammonia+water vapor measurements, a preliminary model of the opacity of ammonia pressure-broadened by water vapor has been developed in a fashion similar to that explained in Section 5.4.2. The preliminary model for the water vapor-broadened opacity of ammonia uses a modified Ben-Reuven lineshape (Ben-Reuven, 1966) for the inversion transitions. The opacity of ammonia broadened by water vapor in the centimeter-wavelength region is given by Equation 5.12. The linewidth and the coupling parameter of the lines are calculated by summing the contribution from ammonia and water vapor and are given by

$$\gamma_j = \gamma_{H_2O} P_{H_2O} \left(\frac{300}{T}\right)^{\Gamma_{H_2O}} + \gamma_{NH_3}\gamma_{(0,j)} P_{NH_3} \left(\frac{295}{T}\right)^{\Gamma_{NH_3}} \quad \text{(GHz)}, \tag{5.21}$$

$$\zeta_j = \zeta_{H_2O} P_{H_2O} \left(\frac{300}{T}\right)^{Z_{H_2O}} + \zeta_{NH_3}\gamma_{(0,j)} P_{NH_3} \left(\frac{295}{T}\right)^{Z_{NH_3}} \quad \text{(GHz)}, \tag{5.22}$$

where for the inversion line j and i = H_2O and NH_3, γ_i and ζ_i are constant scale terms, and Γ_i and Z_i represent the constant temperature dependences of the broadening of each of the gases, P_i are the ideal partial pressures in bar, and $\gamma_{(0,j)}$ are the self-broadening linewidths of the inversion transitions of ammonia in MHz/Torr. The pressure shift parameter is calculated by

$$\delta_j = d \times \gamma_j \quad \text{(GHz)}, \tag{5.23}$$

where d is an empirically derived constant. The free parameters for water vapor were empirically derived using the four sequences of measurements, while the free parameters for ammonia were assigned the same values derived in Section 5.4.2. Table 5.11 lists the values of the water vapor and ammonia model constants of the preliminary NH_3/H_2O model.

Table 5.11: Values of the H_2O model constants used for computing the H_2O-broadened NH_3 absorptivity from the inversion transitions.

	i=H_2O	i=NH_3
γ_i	8.4993	0.7298
Γ_i	1	1
ζ_i	1.364	0.5152
Z_i	2/3	2/3
d	-0.0627	
D_{inv}	0.9862	

The laboratory measurements and the preliminary model of the opacity of ammonia in a water vapor atmosphere have given insights into the pressure broadening effects of water vapor on ammonia opacity and can potentially improve retrievals of the atmospheric abundance of water vapor at Jupiter from MWR measurements. Plots comparing some of the measured data to the preliminary NH_3/H_2O model, along with the models for pure ammonia opacity (this work) and pure water vapor opacity (Karpowicz and Steffes, 2011) are shown in Figures 5.61–5.62. The error bar shown in the plots are the 2σ measurement uncertainties. It can be seen that there is a significant influence of water vapor on the centimeter-wavelength opacity of ammonia. An aggressive campaign of laboratory measurements of the opacity of ammonia pressure-broadened by water vapor/hydrogen/helium mixture under simulated deep jovian conditions are currently being conducted by fellow graduate student Danny Duong. An updated model of the opacity of ammonia pressure-broadened by water vapor/hydrogen/helium mixture will be developed by a future graduate student after the measurements are completed.

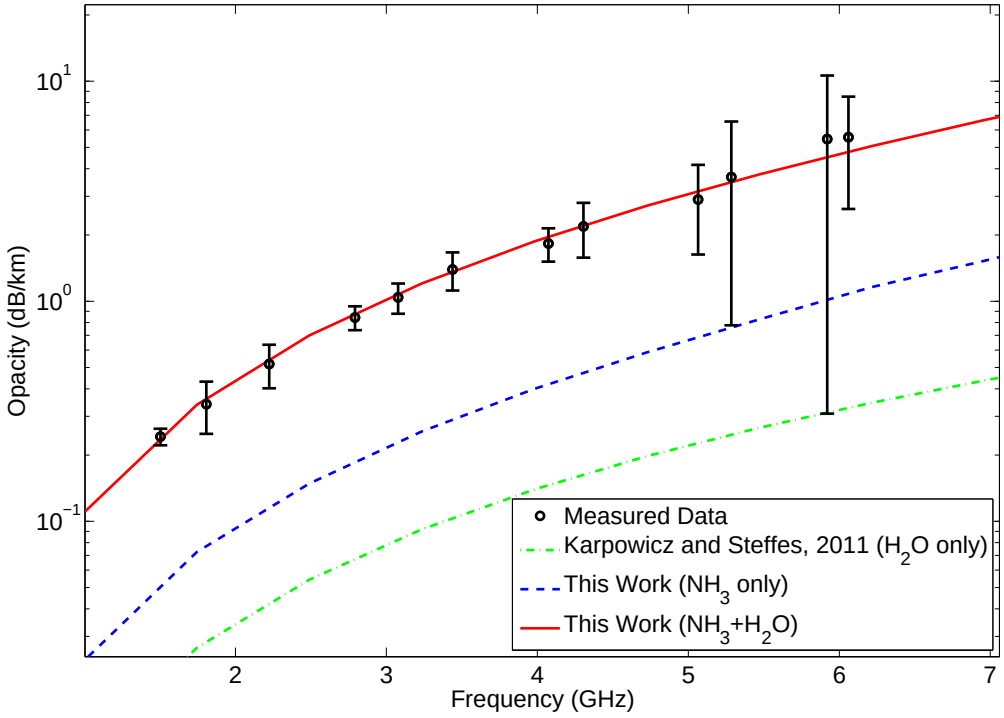

Figure 5.61: Opacity data measured using the high-pressure centimeter-wavelength system for a mixture of NH_3 = 8.71% and H_2O = 91.29% at a pressure of 1.041 bar and temperature of 452 K compared to Karpowicz and Steffes (2011) H_2O model, the NH_3 model described in Section 5.4.2 and the preliminary NH_3+ H_2O model that includes the interaction between NH_3 and H_2O.

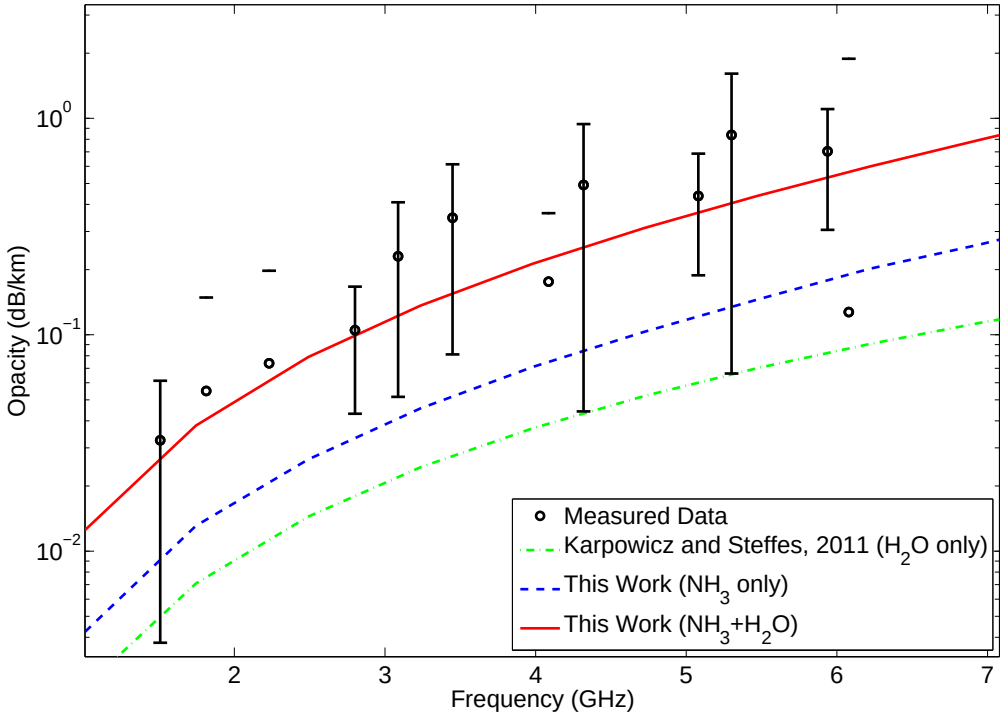

Figure 5.62: Opacity data measured using the high-pressure centimeter-wavelength system for a mixture of NH_3 = 16.44% and H_2O = 83.56% at a pressure of 0.18 bar and temperature of 373.9 K compared to Karpowicz and Steffes (2011) H_2O model, the NH_3 model described in Section 5.4.2 and the preliminary NH_3+ H_2O model that includes the interaction between NH_3 and H_2O.

CHAPTER VI

MILLIMETER-WAVELENGTH OBSERVATIONS OF JUPITER

Radiative transfer simulations of the atmosphere of Jupiter performed early in this work (Devaraj et al., 2011) predicted that the jovian brightness temperature at 140.14 GHz corresponding to the $\nu_2 = 1$ inversion transition of ammonia was at least 4 K lower than the continuum brightness temperature at these wavelengths. Hence, in an attempt to detect the line, millimeter-wavelenth observations of Jupiter were conducted with the Institut de Radioastronomie Millimétrique (IRAM) 30 m telescope facility as described below. The disk-averaged brightness temperature spectrum of Jupiter obtained from these observations showed no features corresponding to the absorption line. Recently, the ammonia spectral line catalogs were significantly improved (Yu et al., 2010a,b,c). New radiative transfer simulations of the atmosphere of Jupiter were performed using the ammonia absorption model presented in this work (with the new spectral line catalogs for the ammonia ground-state and ν_2 transitions) and the simulations predict that the 140 GHz transition is only < 0.5 K darker than the continuum. As discussed below, this is consistent with the latest observations of Jupiter (non-detection of the line)[1].

6.1 IRAM Observations

The IRAM 30 m telescope located on Pico Veleta in the Spanish Sierra Nevada at an elevation of 2850 m is one of the most sensitive millimeter-wave telescopes. The 30 m single dish parabolic antenna has a Cassegrain-Nasmyth configuration supported

[1]Observations were carried out with the IRAM 30 m Telescope. IRAM is supported by INSU/CNRS (France), MPG (Germany) and IGN (Spain)

on an alt-azimuth mount. Eight MIxer heterodyne Receivers (EMIR) that operate in the 0.8–3.6 mm-wavelength range were recently installed on the telescope and used for this study. Observations of Jupiter were conducted using two E1 band (120–170 GHz) horizontal (H) and vertical (V) polarization receivers tuned to 140.142 GHz on two consecutive nights (September 17 and 18) in 2010. The half-power beamwidth (HPBW) of a single dish telescope with a 70% illumination efficiency is given by

$$\text{HPBW} = 1.22 \times \frac{\lambda}{D} \quad \text{(radians)}, \tag{6.1}$$

where λ is the observation wavelength and D is the diameter of the telescope. The antenna HPBW at 140 GHz is approximately 17.5 arcsec and the spectral resolution is 4 MHz. An IF bandwidth of 4 GHz was used for the observations. During the observations, Jupiter was approximately 3.95 AU from Earth and had an angular diameter of 49.8 arcsec. The astrometric right ascension was $\sim$ 23 h 58 m and declination was $\sim$ -01 deg 55 m. The Moon was chosen as the calibration source for these observations since it is a constant radiator without any features at millimeter wavelengths, and the night side of the Moon is approximately at the same temperature as Jupiter. It was also at a convenient elevation in the sky during the observation period. The observations of the Moon were used for calibration, and disk-averaged antenna temperature measurements of Jupiter were made. It was possible to remove part of the standing waves inherent to the receiver by comparing the antenna temperature spectra of Jupiter and the Moon.

Figures 6.1 and 6.2 show the observed antenna temperature spectra of Jupiter and the Moon for the H and V polarizations on September 17, 2010, and Figures 6.3 and 6.4 show the observed antenna temperature spectra of Jupiter and the Moon for the H and V polarizations on September 18, 2010. These antenna temperature spectra have been corrected for the system temperature. It can be seen that the spectra between the two days are quite reproducible. It can also be seen that on both days H polarization spectra have much better SNR than V polarization spectra.

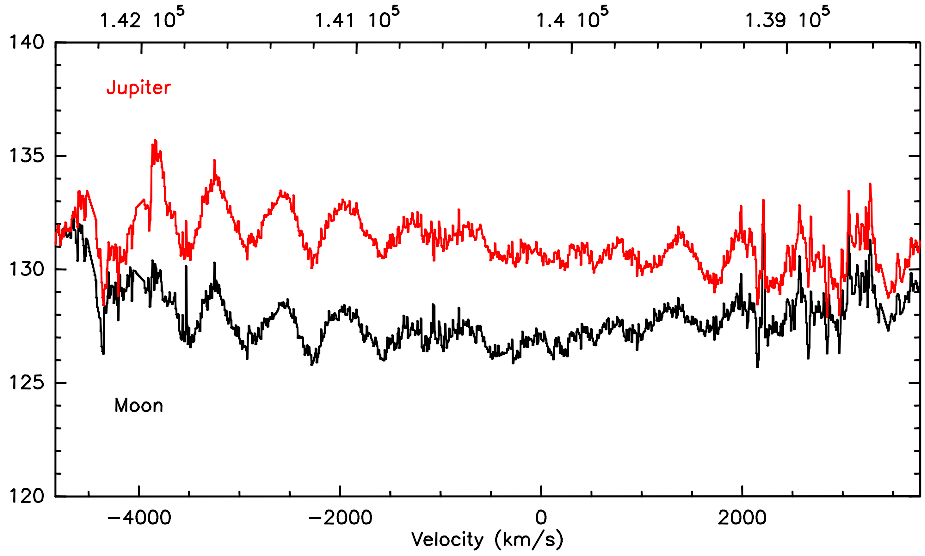

Figure 6.1: Antenna temperature spectra obtained with the H polarization receiver on September 17, 2010 for Jupiter and the Moon. The abscissa on top is frequency in MHz and the ordinate is antenna temperature in K.

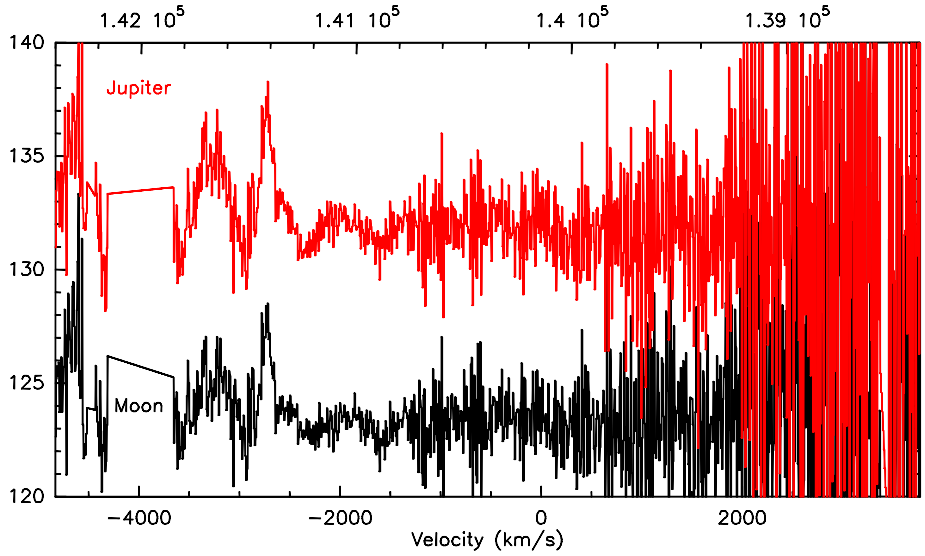

Figure 6.2: Antenna temperature spectra obtained with the V polarization receiver on September 17, 2010 for Jupiter and the Moon. The abscissa on top is frequency in MHz and the ordinate is antenna temperature in K.

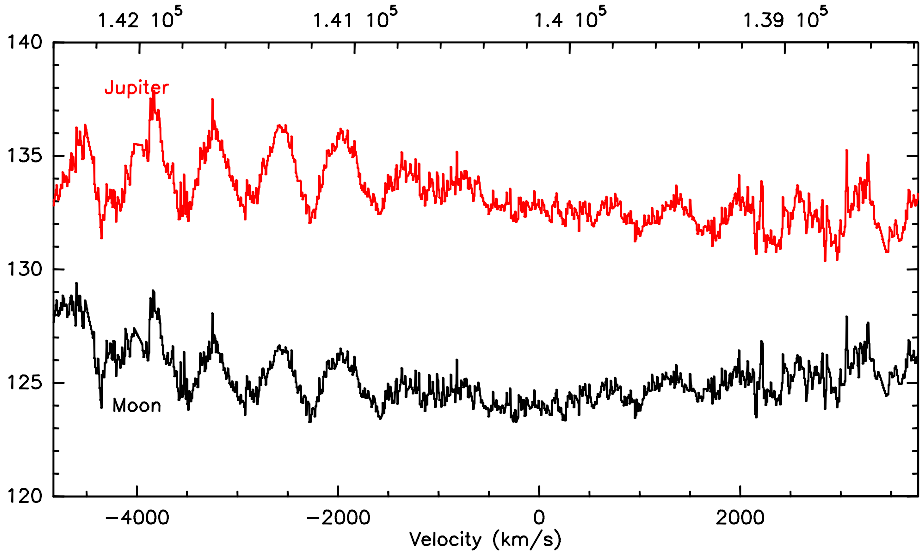

Figure 6.3: Antenna temperature spectra obtained with the H polarization receiver on September 18, 2010 for Jupiter and the Moon. The abscissa on top is frequency in MHz and the ordinate is antenna temperature in K.

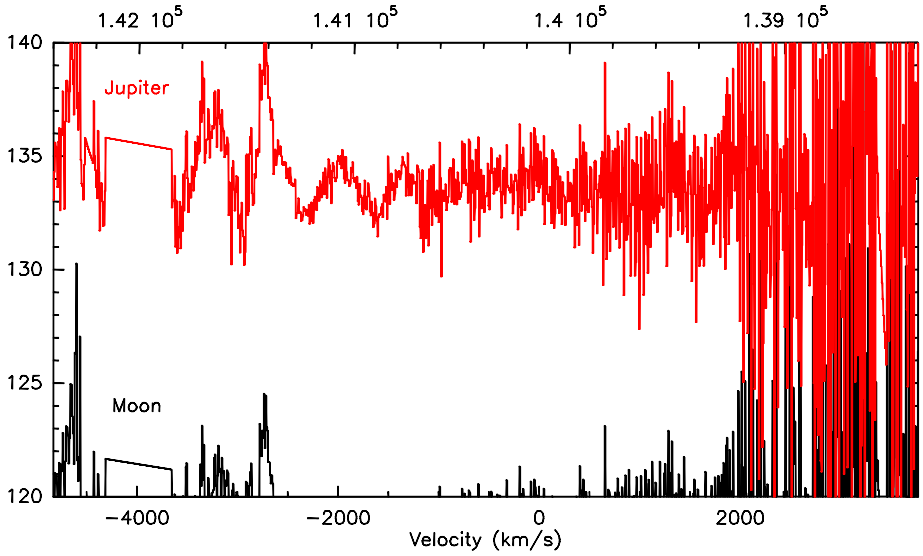

Figure 6.4: Antenna temperature spectra obtained with the V polarization receiver on September 18, 2010 for Jupiter and the Moon. The abscissa on top is frequency in MHz and the ordinate is antenna temperature in K.

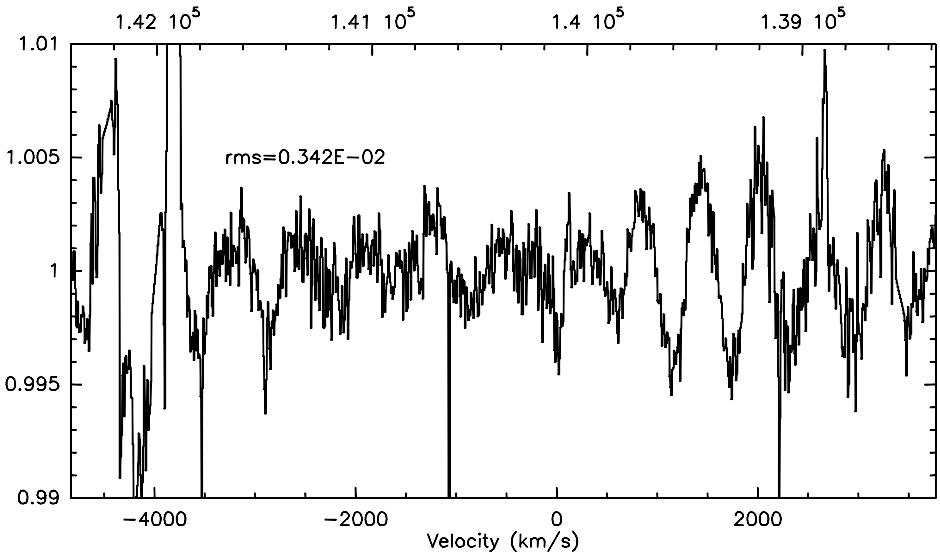

Figure 6.5: Ratio of the 140.14 GHz line to continuum spectrum (H polarization) obtained on September 17, 2010. The abscissa on top is frequency in MHz.

The primary objective of the observations was to detect a potential dip in Jupiter's emission spectrum resulting from the 140 GHz line. Standing waves inherent to the receivers ($\sim$ 300 MHz) can be seen on both the Jupiter and Moon observations. After removing most of the standing waves by dividing the Jupiter spectrum with that of the Moon, the ratio of the line (4 MHz spectral resolution centered at 140.142 GHz) to continuum spectrum (4 GHz) was obtained. The final spectra of the ratio of the line and continuum for the two observations are shown in Figures 6.5 and 6.6. Only the H polarization spectra are shown here since the V spectra were very noisy. These spectra have a typical rms of $\sim$0.2–0.3% mainly due to the residual of the standing waves. It can be seen from the figures that there is no dip in the spectrum corresponding to the 140 GHz ν_2 inversion transition of ammonia.

Ulich (1974) conducted very high-precision absolute brightness temperature measurements of the new Moon at 2.1 mm (140 GHz) and reported a value of 145 $\pm$ 9 K. Since the night-side of the Moon is a constant radiator at millimeter-wavelengths, it serves as an excellent calibration source at millimeter-wavelengths. The measured

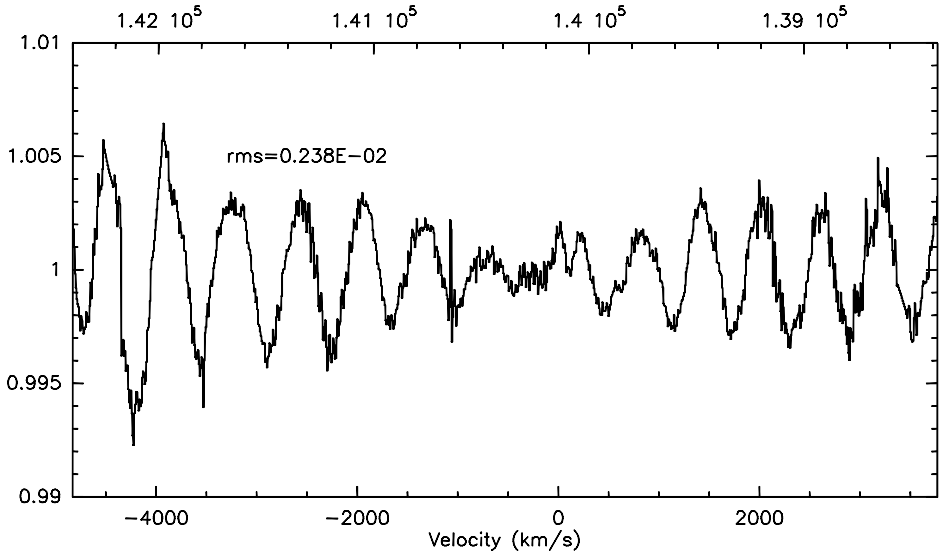

Figure 6.6: Ratio of the 140.14 GHz line to continuum spectrum (H polarization) obtained on September 18, 2010. The abscissa on top is frequency in MHz.

antenna temperature at 140 GHz (corrected for the system temperature) for the night-side of the Moon is $\sim$ 125 K and for Jupiter is $\sim$ 133 K. Since the brightness temperature of the new Moon is available to a very-high precision (145 $\pm$ 9 K), it is possible to calibrate the corrected antenna temperature measurements of Jupiter with that of the Moon. The computed disk-averaged brightness temperature of Jupiter at 140 GHz is $\sim$ 155 $\pm$ 15 K.

6.2 Radiative Transfer Model

A radiative transfer model (RTM) can be used to simulate the millimeter-wavelength emission spectrum of Jupiter as observed from Earth. By incorporating the new ammonia opacity formalism in the radiative transfer calculations of Jupiter, it is possible to analyze the effects of the new formalism on the modeled brightness temperature of the planet. The RTM used for this analysis was developed by Hesman et al. (2007) and modified by this author. The RTM relies on a thermochemical model (TCM) to define the distribution and abundances of the constituent elements and

the temperature-pressure (TP) profile of the atmosphere of Jupiter. The construction begins, in general, from some assumption of the deep abundance of atmospheric constituents. The TP profile is then computed using a wet adiabatic extrapolation in discrete layers of pressure, starting at the deepest layer and ending at the 1 bar pressure level. For pressures less than 1 bar, the Voyager radio occultation results summarized in tabular form by Lindal (1992) are used. The assumed mole fraction of various constituents in the deep atmosphere of Jupiter for the RTM construction are as follows: X_{He}=0.1346, X_{H_2O}=0.0055, X_{H_2S}=66.01 ppm, X_{NH_3} = 800 ppm, and rest H_2. These abundance values are based on recent studies of the composition of Jupiter (e.g., Atreya et al., 2003). Since the abundance of PH_3 in Jupiter is very small (e.g., Kunde et al., 1982), and because there are no strong absorption lines of PH_3 in the 2–4 mm-wavelength range (e.g., Pickett et al., 1998), it is not included in the RTM simulations.

Once the constituent abundances, temperature, and pressure in each layer has been defined, the absorption of each layer is calculated. The collision induced absorption between H_2–H_2, H_2–He, and H_2–CH_4 are calculated using a model given by Orton et al. (2007). Absorption from NH_3 is computed using the latest formalism described in this paper. Absorption from H_2O is computed using a formalism developed by Karpowicz (2010), and absorption from H_2S is computed using a formalism developed by DeBoer and Steffes (1994). The formalisms for H_2O and H_2S are based on centimeter-wavelength laboratory measurements. The outgoing electromagnetic radiation exiting the atmosphere of Jupiter at the measurement frequency is predicted by the black body thermal emission of each layer and the absorption of its constituents.

6.3 Search for the 140 GHz Line

Based on the results of radiative transfer simulations of the atmosphere of Jupiter performed early in this work (Devaraj et al., 2011), observations were conducted with the IRAM 30 m telescope to search for a potential dip in Jupiter's spectrum resulting from the 140 GHz ammonia line transition. However, no feature was detected in the observed spectrum of Jupiter. Since then, the ammonia line catalogs have been extensively updated (Yu et al., 2010a,b,c). New radiative transfer simulations were performed using the ammonia model described in this dissertation.

Based on the attenuation of the Galileo Probe's radio signal in Jupiter's atmosphere, the deep atmospheric ammonia abundance was estimated as 800 ppm (Folkner et al., 1998; Hanley et al., 2009). The low temperatures in the upper troposphere of Jupiter cause ammonia to condense and form ammonia ice clouds, thereby depleting gaseous ammonia from the atmosphere. Another mechanism by which a relatively large amount of ammonia gets depleted is by combining with hydrogen sulfide resulting in the formation of ammonium hydrosulfide cloud (see, e.g., Sromovsky and Fry, 2010). A range of ammonia abundance profiles from a variety of sources were used in these simulations so as to study their impact on the millimeter-wavelength emission spectrum of Jupiter. If ammonia is assumed to follow a saturation profile (Sat), then ammonia abundance should be constant in the troposphere until it reaches the saturation layer; at that point the ammonia abundance profile follows the vapour pressure curve. The saturation vapor pressure equation for ammonia used in this study is given by Overstreet and Giauque (1937). The Galileo Probe (GP) ammonia profile includes the abundance values inferred from thermal net flux measurements in the 0.5–3 bar range (Sromovsky et al., 1998), and from the attenuation of radio signals during the probe descent in the 4.3–15 bar range (Folkner et al., 1998; Hanley et al., 2009). The probe results were from the edge of a 5 μm hotspot (Orton et al., 1998) and display a substantial decrease in ammonia mixing ratio with altitude and never reach the

saturation level of ammonia. The Sat and GP profiles along with three other profiles, the hot spot (HS), north equatorial belt (NEB), and equatorial zone (EZ) profiles listed by Sromovsky and Fry (2010) were used for modeling the ammonia abundance in Jupiter's atmosphere. The temperature-pressure (TP) profile of Jupiter and the ammonia abundance profiles used in the RTM simulations are shown in Figure 6.7. Figure 6.8 shows the TP profile of Jupiter overlayed with the normalized weighting functions (which indicate the atmospheric layers that contribute most to the brightness temperature at a particular frequency) at 140.1 GHz for the different ammonia abundance profiles.

The RTM simulations were performed for various ammonia abundance profiles and the predicted disk-averaged brightness temperature of Jupiter in the 138–142 GHz range is shown in Figure 6.9. The model predicts that irrespective of the assumed ammonia abundance profile, the brightness temperature of Jupiter at 140 GHz (corresponding to the ν_2 transition of ammonia) is only < 0.5 K darker than the continuum. With the current capabilities of millimeter-wavelength telescopes, this shallow line cannot be detected. Future generation of high-sensitivity telescopes such as the ALMA might help in detecting the line at Jupiter. Of particular interest is the predicted brightness temperature of Jupiter for various ammonia abundance profiles. The disk-averaged brightness temperature varies by approximately 50 K for the two extreme cases of ammonia abundance profiles used in the simulations (saturation profile and hot spot profile which is highly subsaturated). Even among the other profiles, there is a variation in the predicted brightness temperature of at least 5 K. Hence, highly accurate millimeter-wavelength observations of Jupiter can potentially be used to retrieve the global abundance profile of ammonia in the 0.5–5 bar region.

The brightness temperature of Jupiter was estimated to be $\sim 155 \pm 15$ K from the latest observations using the "relative" calibration technique described earlier.

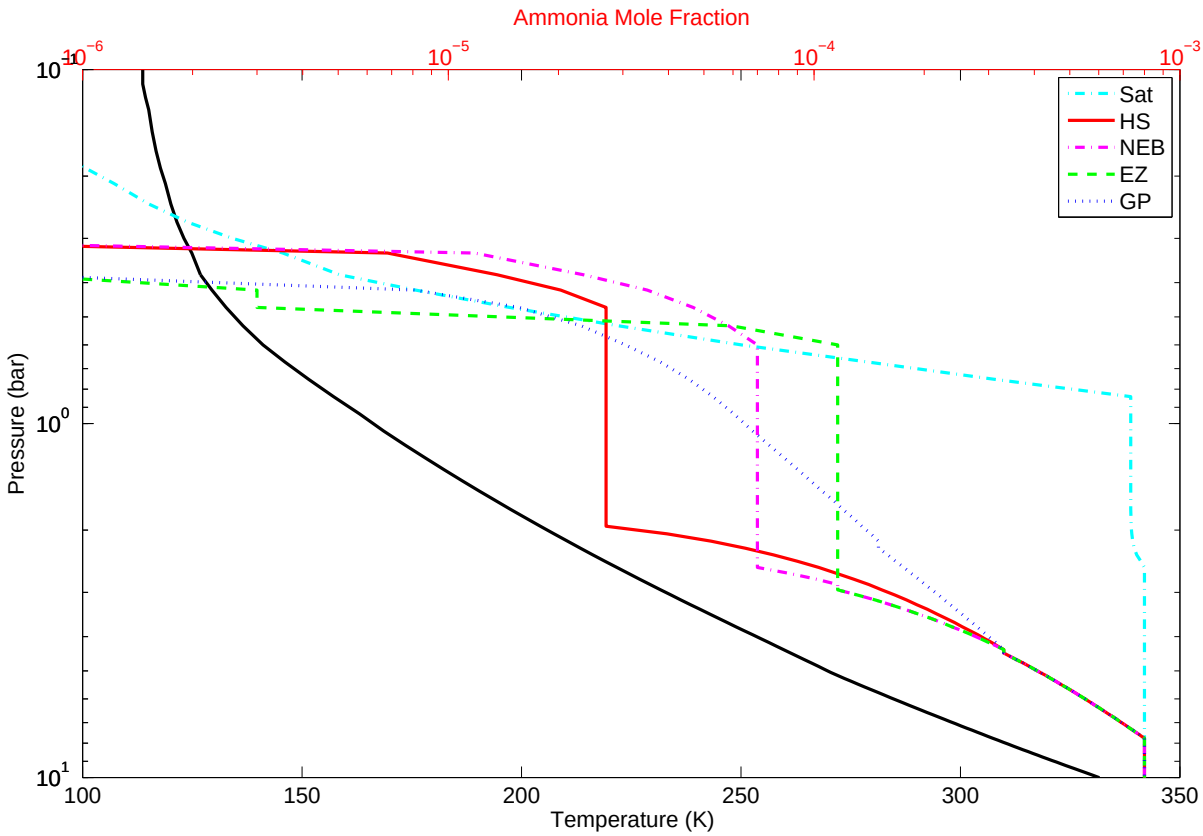

Figure 6.7: The temperature-pressure (TP) profile of Jupiter is shown as a black line. The TP profile above the 1-bar level represents the Voyager radio occultation results summarized by Lindal (1992), and the TP profile below the 1-bar level represents the results of a wet-adiabatic extrapolation using the thermochemical model. The deep ammonia abundance is fixed at 800 ppm and the ammonia abundance profiles corresponding to the saturation (Sat), hot spot (HS), north equatorial belt (NEB), equatorial zone (EZ), and Galileo Probe (GP) models are also shown.

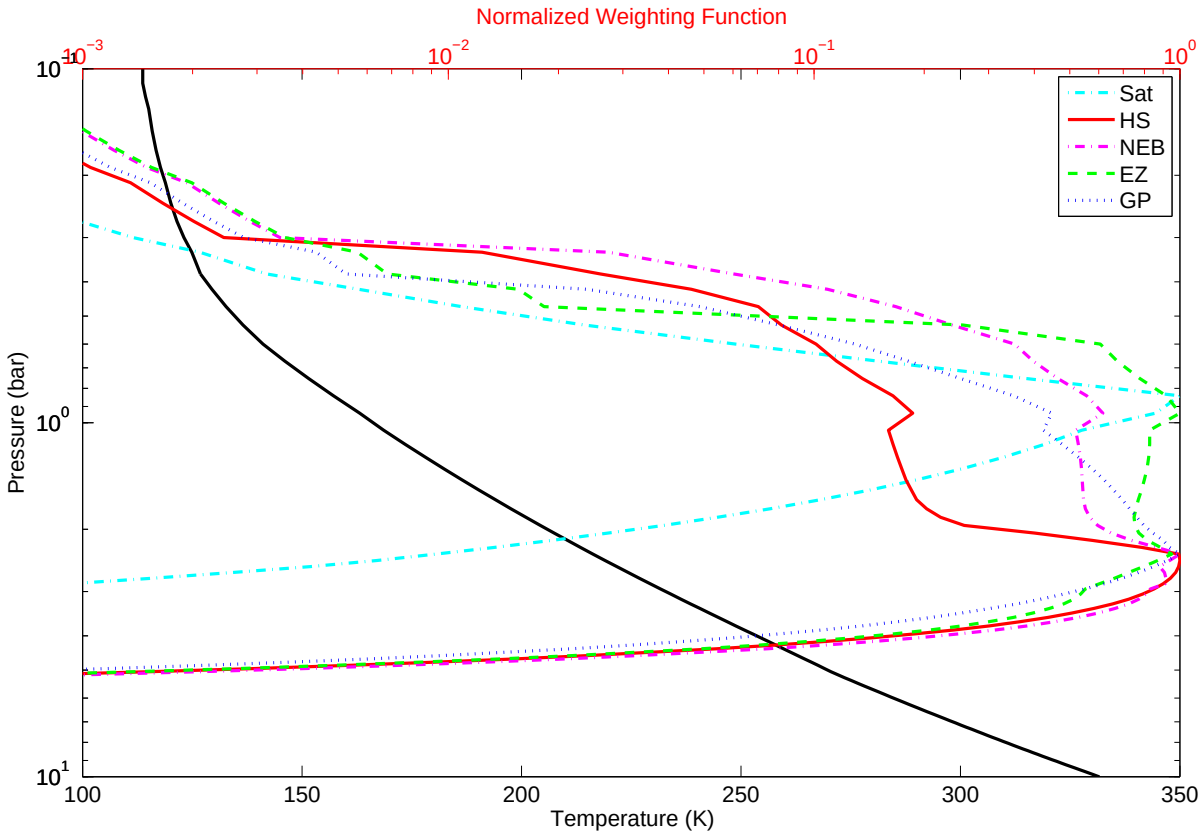

Figure 6.8: The TP profile of Jupiter (black line) and the normalized weighting functions at 140.1 GHz for various ammonia abundance profiles.

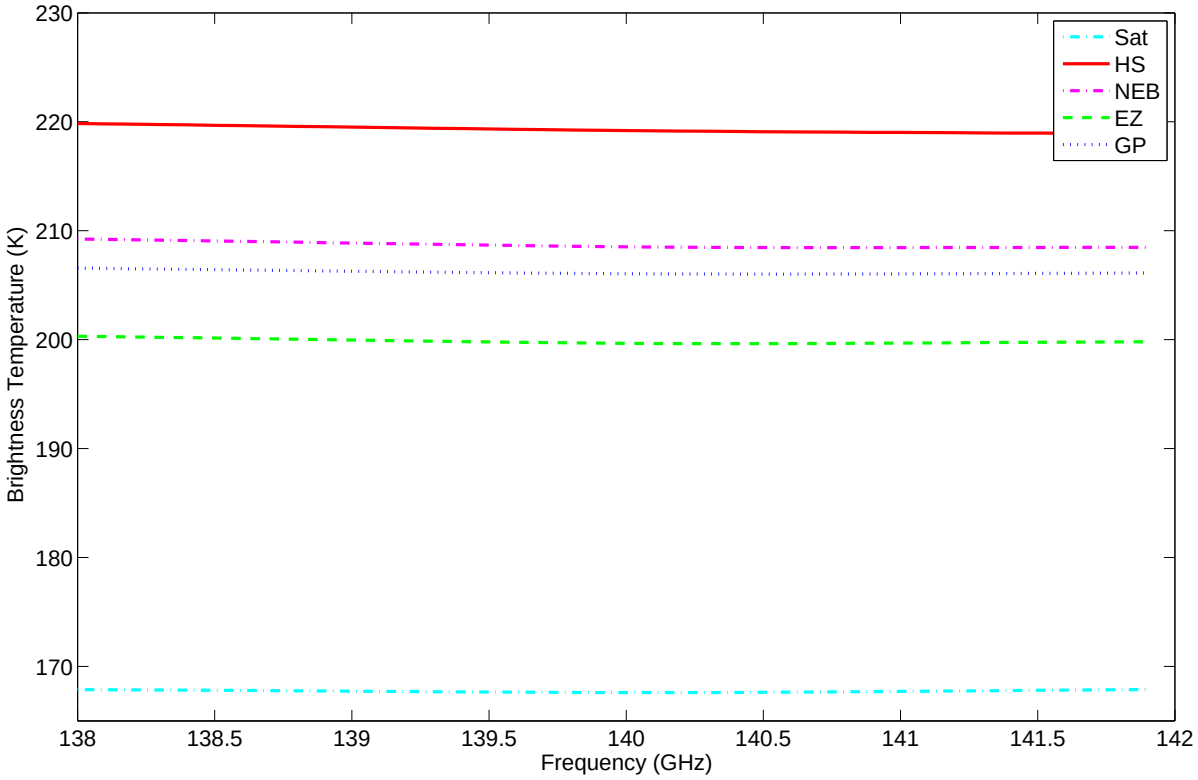

Figure 6.9: Modeled disk-averaged brightness temperature of Jupiter for various ammonia profiles.

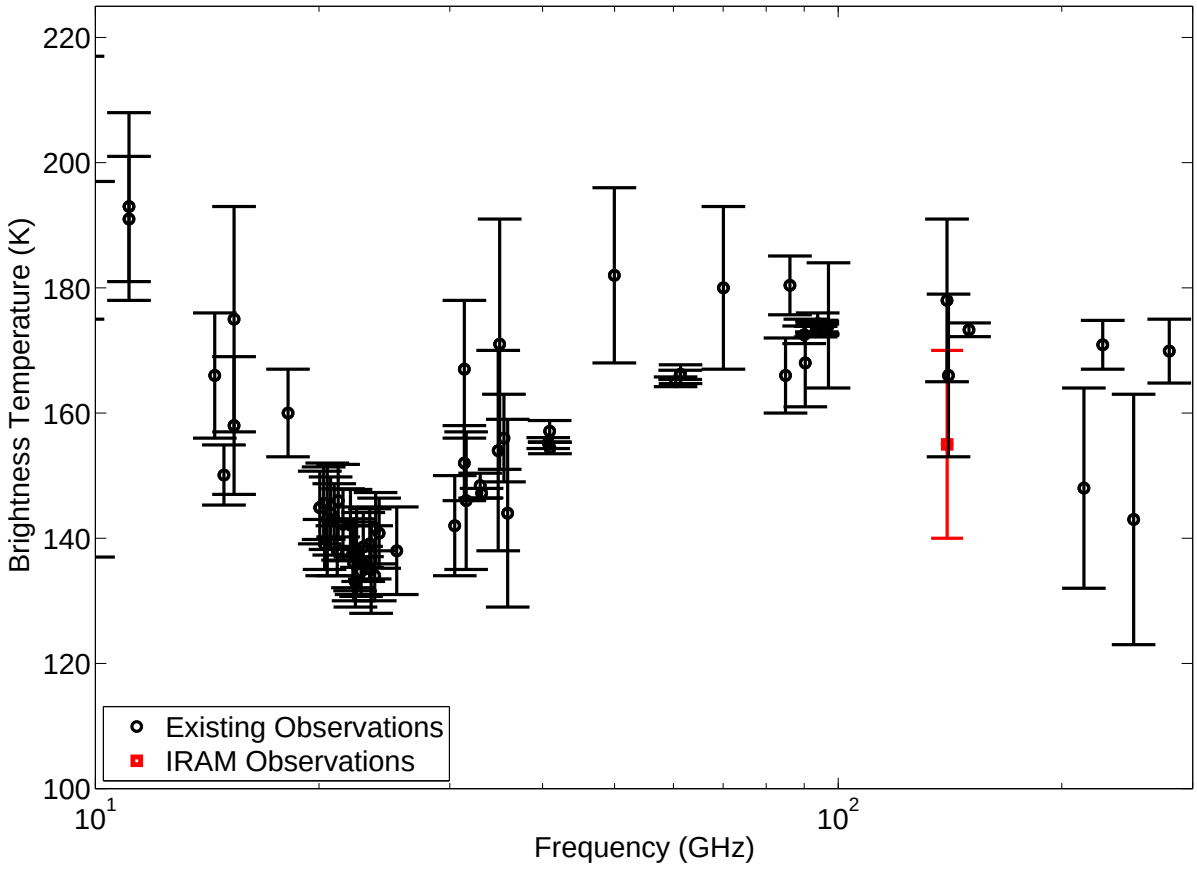

Figure 6.10: Disk-averaged brightness temperature measurements of Jupiter.

Although these observations had large uncertainties, the measurements are still consistent with the existing brightness temperature measurements. The latest measured Jupiter brightness temperature is graphically compared against those in the literature in Figure 6.10. The existing values are taken from the compilations by Berge and Gulkis (1976) and Joiner and Steffes (1991) along with individual observations from de Pater et al. (1982), Griffin et al. (1986), de Pater et al. (2001), Gibson et al. (2005), and Weiland et al. (2011).

CHAPTER VII

CONCLUSIONS

The objective of this doctoral research has been to advance the understanding of the centimeter- and millimeter-wavelength properties of gaseous ammonia under jovian conditions. As part of this research, extensive laboratory measurements of the 2–4 mm-wavelength properties of ammonia under simulated upper and middle tropospheric conditions of the jovian planets, and the 5–20 cm-wavelength properties of ammonia under simulated deep tropospheric conditions of the jovian planets were conducted. These and pre-existing laboratory measurements (Hanley et al., 2009) were utilized to develop the most accurate and consistent model to date to represent the opacity of ammonia pressure-broadened by hydrogen/helium in the centimeter-wavelength range at pressures up to 100 bar and temperatures up to 500 K and in the millimeter-wavelength range at pressures up to 3 bar and temperatures up to 300 K. Additionally, preliminary laboratory investigation of the 5–20 cm-wavelength opacity of ammonia pressure-broadened by water vapor were made and an initial model for the centimeter-wavelength opacity of ammonia broadened by water vapor was developed.

7.1 Contributions

The main focus of this doctoral research work was to better understand the centimeter- and millimeter-wavelength opacity spectra of ammonia under jovian conditions. During the course of this work, several unique contributions were made to the fields of microwave spectroscopy and planetary science.

7.1.1 Millimeter-wavelength measurement system

A high-sensitivity millimeter-wavelength measurement system was developed as part of this work, to accurately measure the propagation properties of gases under simulated planetary atmospheric conditions. The measurement system operates in the 2–4 mm-wavelength range and withstands up to 3 bar of pressure. This system was employed in the measurements of the 2–4 mm-wavelength opacity of ammonia under jovian conditions as part of this work. With minor modifications, this system can be used to study the properties of various gases such as hydrogen sulfide under Neptune atmospheric conditions, and sulfur dioxide and sulfuric acid vapor under Venus atmospheric conditions (Devaraj and Steffes, 2011).

7.1.2 Laboratory measurements and model

As part of the laboratory measurement campaign, extensive measurements of the centimeter- and millimeter-wavelength properties of ammonia under simulated jovian conditions were made. The millimeter-wavelength measurements contributed to the empirical estimation of the self-, hydrogen-, and helium-broadening parameters of the 140.14 GHz ν_2 inversion transition of ammonia for the first time in a laboratory setting. Efforts toward developing a unified formalism to estimate the centimeter- and millimeter-wavelength opacity spectra of ammonia at the pressures, temperatures, and mixing ratios characteristic of the outer planets have been on-going for more than 30 years since the work by Berge and Gulkis (1976) (see, e.g., Mohammed and Steffes, 2004). As part of this research, a consistent absorption formalism was developed to accurately characterize the opacity of ammonia in the centimeter-wavelength range at pressures up to 100 bar and temperatures up to 500 K, and millimeter-wavelength range at pressures up to 3 bar and temperatures up to 300 K. This model represents the first successful attempt at reconciling the centimeter- and millimeter-wavelength opacity spectra of ammonia under jovian conditions. This model can

be used for accurate interpretation and modeling of the broad emission spectrum of jovian planets and for accurate retrievals of ammonia and other constituents in the jovian planetary atmospheres from ground-based and spacecraft-based radio observations. The influence of water vapor on the ammonia absorption spectrum in the centimeter-wavelength region was studied in the laboratory for the first time as part of this research and this work will aid in the retrievals of the atmospheric abundance of water vapor and ammonia at Jupiter from the Juno MWR measurements.

7.1.3 Search for the 140 GHz line

Observations of Jupiter were conducted at 140 GHz to search for the ν_2=1 inversion transition of ammonia using the IRAM 30 m telescope facility and the ν_2 transition was not detected. Radiative transfer simulations using the new ammonia model show that the 140 GHz line is < 0.5 K darker than the continuum, and this result is consistent with the non-detection of the line from the IRAM observations. The disk-averaged brightness temperature of Jupiter was estimated to be $\sim 155 \pm 15$ K based on the observations.

7.2 Recommendations for Future Work

7.2.1 Millimeter-wavelength laboratory work

Ground based millimeter-wavelength astronomy is very powerful in probing planets because of the low attenuation millimeter waves suffer in Earth's atmosphere compared to submillimeter waves. New millimeter arrays such as the ALMA are capable of providing an unprecedented combination of sensitivity, angular resolution, spectral resolution, and imaging fidelity. Hence, accurate data concerning the absorptive properties of various atmospheric constituents are required to interpret those observations and derive planet-wide abundances of those constituents. The new millimeter-wavelength measurements of ammonia have proven that the pre-existing models did not accurately predict the opacity of ammonia in the millimeter-wavelength range

under relevant planetary conditions. Hence, there is a need to accurately study the properties of other millimeter-wavelength absorbing gases under those planetary conditions. The system described in this paper can be used for making such high-precision measurements. Future work will involve modifying the measurement system for studying the millimeter-wavelength properties of sulfur dioxide and sulfuric acid vapor under simulated Venus atmospheric conditions (Devaraj and Steffes, 2011).

Measurements of gas properties at shorter wavelengths can yield much information about the behavior of the rotational transitions of various molecules. The FPR that was built for the measurements of ammonia opacity has the capability to operate in the 1–4 mm-wavelength range. A G band (140–220 GHz) planar frequency doubler along with the active multiplier chain (AMC) can be used to generate signals in the 1.5–2 mm-wavelength range and a series of harmonic mixers can be used for down-conversion. Such a system can be used for studying the rotational transitions of gases such as hydrogen sulfide under simulated planetary atmospheric conditions.

7.2.2 Centimeter-wavelength laboratory work

Based on preliminary results of the ammonia/water vapor experiments, it is clear that there is a necessity to understand the enhancement of the opacity of ammonia due to the presence of water vapor. Extensive measurements of the properties of ammonia in a hydrogen/helium/water vapor atmosphere under jovian conditions are currently being conducted by fellow graduate student Danny Duong. The initial measurements made as part of this study and the current measurements that are being conducted will be used to update the preliminary model described in Section 5.6 to more accurately characterize the centimeter-wavelength properties of ammonia under jovian conditions. In addition, high-pressure measurements of other centimeter-wavelength absorbing gases with relatively large abundance, such as hydrogen sulfide, can provide unique insights into the behavior of those gases under the deep jovian

conditions and also help limit uncertainties in the Juno MWR retrievals at Jupiter.

An accurate ammonia opacity model for jovian atmospheres should include the effects of broadening from all the major atmospheric constituents. For example, the third most abundant constituent in the atmosphere of Uranus is methane ($\sim 2.3\%$). Although methane is non-polar and its inherent centimeter-wavelength opacity is very small (Jenkins and Steffes, 1988), because of its large abundance and broadening cross-section it could potentially broaden ammonia under Uranus conditions. Hence, laboratory measurements of the centimeter-wavelength opacity of ammonia in the presence of methane under the deep atmospheric conditions of Uranus can yield information about the potential broadening nature of methane.

7.3 List of Publications

Journal Articles

K. Devaraj and P. Steffes (2011), "A new consistent model for the microwave opacity of ammonia under deep jovian conditions," *Icarus*, in preparation.

K. Devaraj and P. Steffes (2011), "The Georgia Tech millimeter-wavelength measurement system and some applications to study of planetary atmospheres," *Radio Sci.*, 46, RS2014, doi:10.1029/2010RS004433.

K. Devaraj, P. Steffes, and B. Karpowicz (2011), "Reconciling the centimeter- and millimeter-wavelength ammonia absorption spectra under jovian conditions: Extensive millimeter-wavelength measurements and a consistent model," *Icarus*, 212, pp. 224–235.

Conference Proceedings

K. Devaraj and P. Steffes, "Laboratory measurements and a consistent model of the microwave properties of ammonia under jovian conditions,". To be presented at the EPSC-DPS Joint Meeting 2011, Nantes, France, October 7, 2011.

K. Devaraj, D. Duong, and P. Steffes, "Preliminary results for the 5-20 cm wavelength opacity of ammonia pressure broadened by water vapor under jovian conditions,". To be presented at the EPSC-DPS Joint Meeting 2011, Nantes, France, October 5, 2011.

P. Steffes and **K. Devaraj**, "VLA observations of Venus at X band," *Workshop on New Results from Venus Express, Ground-Based Observations and Future Missions*. To be presented at the 2011 VEXAG International Workshop, Chantilly, Virginia, August 31, 2011.

K. Devaraj and P. Steffes, "New laboratory measurements of the centimeter-wavelength properties of ammonia under deep jovian atmospheric conditions," *Bulletin of the American Astronomical Society*, vol. 42, 2010, p.1040. Presented at the 42nd Annual Meeting of the Division for Planetary Sciences of the American Astronomical Society, Pasadena, CA, October 7, 2010.

K. Devaraj, B. Butler, B. Hesman, P. Steffes, and R. Sault, "VLA observations of the Jupiter impact," *Geophysical Research Abstracts*, vol. 12, 7661. Presented at the EGU General Assembly, Vienna, Austria, May 2010 (Invited Talk).

K. Devaraj and P. Steffes, "The 2–4 millimeter-wavelength opacity of ammonia," *Geophysical Research Abstracts*, vol. 12, 7675. Presented at the EGU General Assembly, Vienna, Austria, May 2010.

K. Devaraj and P. Steffes, "Laboratory measurements of microwave properties of ammonia under deep jovian atmospheric conditions," *Lunar and Planetary Institute*, Contribution No. 1553, pp. 1875 -1876, 2010. Presented at the 41st Lunar and Planetary Science Conference, The Woodlands, TX, March 4, 2010.

K. Devaraj and P. Steffes, "The 2–4 millimeter-wavelength opacity of ammonia: Extensive laboratory measurements and a new model," *Bulletin of the*

American Astronomical Society, vol. 41, no. 3, 2009, p. 1049. Presented at the 41st Annual Meeting of the Division for Planetary Sciences of the American Astronomical Society, Fajardo, PR, October 7, 2009.

B. Butler, **K. Devaraj**, P. Steffes, and B. Hesman, "Observations of the Jupiter impact with the VLA," *Bulletin of the American Astronomical Society*, vol. 41, no. 3, 2009, p. 1194. Presented at the 41st Annual Meeting of the Division for Planetary Sciences of the American Astronomical Society, Fajardo, PR, October 7, 2009.

B. Hesman, M. Hofstadter, B. Butler, and **K. Devaraj**, 'Microwave observations of Neptune," *Bulletin of the American Astronomical Society*, vol. 41, no. 3, 2009, p. 196. Presented at the 41st Annual Meeting of the Division for Planetary Sciences of the American Astronomical Society, Fajardo, PR, October 7, 2009.

K. Devaraj and P. Steffes, "A new laboratory system for measurement of the millimeter-wave properties of gases and preliminary results for the continuum opacity of ammonia," *Bulletin of the American Astronomical Society*, vol. 40, no. 3, 2008, p. 497. Presented at the 40th Annual Meeting of the Division for Planetary Sciences of the American Astronomical Society, Ithaca, NY, October 14, 2008.

M. Hofstadter, B. Butler, M. Gurwell, B. Hesman, and **K. Devaraj**, 'The tropospheres of Uranus and Neptune as seen at microwave wavelengths," *Bulletin of the American Astronomical Society*, vol. 40, no. 3, 2008, p. 488. Presented at the 40th Annual Meeting of the Division for Planetary Sciences of the American Astronomical Society, Ithaca, NY, October 14, 2008.

K. Devaraj and P. Steffes, "Laboratory measurements of w-band continuum

opacity of ammonia using a fully confocal Fabry-Perot resonator," *International Union of Radio Science Programs and Abstracts: 2008 National Radio Science Meeting*, pp. J1-4. Presented at the 2008 URSI National Radio Science Meeting, Boulder, CO, January 3, 2008.

K. Devaraj and P. Steffes, 'Preliminary results for the 2–4 millimeter wavelength continuum opacity of ammonia based on new laboratory measurements under simulated jovian conditions," *Bulletin of the American Astronomical Society*, vol. 39, no. 3, 2007, p. 447. Presented at the 39th Annual Meeting of the Division for Planetary Sciences of the American Astronomical Society, Orlando, FL, October 9, 2007.

P. Steffes, T. Hanley, B. Karpowicz, and **K. Devaraj**, "Laboratory measurements of the microwave and millimeter-wave properties of planetary atmospheric constituents: The Georgia Tech system," *Workshop on Planetary Atmospheres*, pp. 117-118. LPI Contribution No. 1376, Lunar and Planetary Institute, Houston. Presented at the 2007 Workshop on Planetary Atmospheres, Greenbelt, MD, November 6, 2007.

APPENDIX A

MILLIMETER-WAVELENGTH COMPONENTS

The millimeter-wavelength subsystem consists of a Fabry–Perot resonator and the W band and F band components (signal generators and receivers). This appendix provides an overview of the characteristics of the W band and F band components. Complete design and construction information of the millimeter-wavelength components can be obtained from the manufacturer's websites.

A.1 W band Components

The W band subsystem consists of the following components along with the Fabry–Perot resonator.

. Signal Generator (HP 83650B)

. Active Multiplier Chain (Millitech AMC-10-RFH00)

. Harmonic Mixer (QMH 922WHP/387)

. Diplexer (MD1A)

. Spectrum Analyzer (HP 8564E)

The first stage of the two-stage active multiplier chain (AMC) consists of a Ku band (12–18 GHz) amplifier followed by a frequency doubler, and the second stage of the AMC consists of a Ka band (26.5–40 GHz) amplifier followed by a frequency tripler. The output power of the AMC varies as a function of frequency and it is shown in Figure A.1. The harmonic mixer can be used either in an "external mixer" mode with a spectrum analyzer LO and an MD1A diplexer or as a down-converter

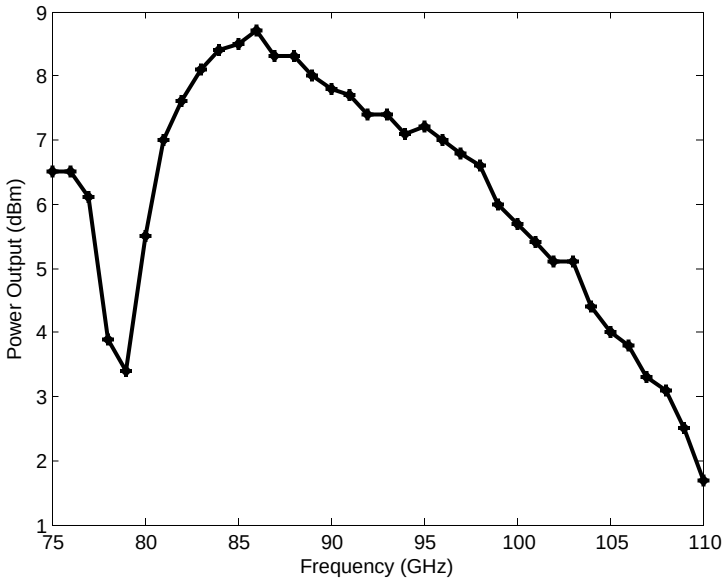

Figure A.1: Power output of the AMC for P_{in}=+10 dBm.

with an external LO (f_{LO} up to 18 GHz) and MD2A diplexer. The AMC, mixer, and diplexer are are shown in Figure A.2. Tables A.1 and A.2 list some of the parameters of the AMC and mixer, respectively.

When the components are placed at cold temperatures, bias is continuously provided to the AMC, even if the system is not under operation, to ensure that the heat dissipated by the AMC along with the thermal insulation layers maintain the

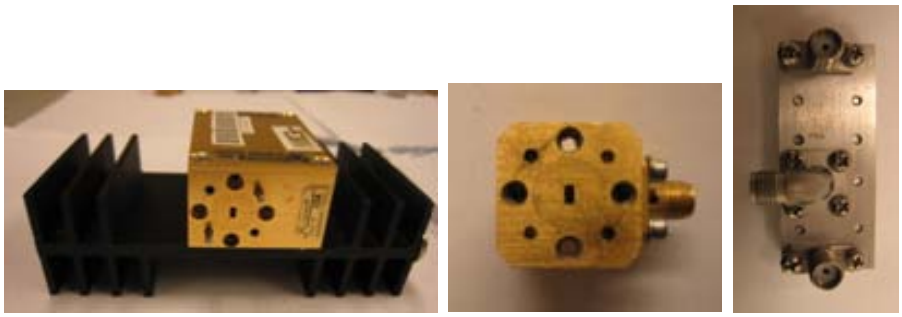

(a) Active multiplier chain. (b) Harmonic mixer (QMH). (c) Diplexer (MD1A).

Figure A.2: Components of the W band subsystem.

Table A.1: AMC-10-RFH00 parameters.

Output frequency	75–110 GHz
Input frequency	12.50–18.33 GHz
Multiplication factor	6
Input power	+10 dBm (nom)
Output power	see Figure A.1
Maximum input power	+13 dBm
Signal purity (max)	-20 dBc
DC input	8–12 V @ 600 mA (typ)
Operating temperature	0°C to +45°C

Table A.2: Quinstar QMH 922WHP/387 parameters in "external mixer" mode.

Input frequency	75–110 GHz
Input power	-10 dBm (max)
LO frequency (from spectrum analyzer)	3–6.1 GHz
LO power (from spectrum analyzer)	15 dBm
Harmonic number	18
Conversion loss	40 dB (nom)
Operating temperature	-55°C to +125°C

AMC within its operating temperature at all times. It is critical to prevent condensation from occurring inside the components when they are used at cold temperatures. Hence, all the components are hermetically sealed in an enclosure with some silica gel to prevent condensation. The silica gel beads are periodically replaced to ensure minimum water vapor content inside the enclosure.

A.2 F band Subsystem

The F band subsystem consists of the following components along with the Fabry–Perot resonator.

. Signal Generator (HP 83650B)

. Q band Amplifier (Spacek SG4413-15-16W)

. Frequency Tripler (Pacific Millimeter Products D3WO)

. Harmonic Mixer (Pacific Millimeter Products DM)

(a) Spacek amp.

(b) Tripler.

Figure A.3: F band components: Spacek amplifier and frequency tripler.

. Diplexer (Pacific Millimeter Products MD2A)

. LO Amplifier (JCA 1920-612)

. Local Oscillator (HP 83712B)

. Bias Tee

. Low Noise Amplifier (MITEQ AMF-3F-012017)

. Spectrum Analyzer (HP 8564E)

A swept signal generator (HP 83650B) is used to generate the input signal in the 37 to 50 GHz range (Q band) that is amplified (Spacek amplifier) and fed to a frequency tripler to generate the desired RF in the 2 to 3 mm-wavelength range (Figure A.3). The output power of the Spacek amplifier and the tripler are shown in Figure A.4 and some additional parameters are listed in Table A.3.

A harmonic mixer and the diplexer (model MD2A) are used for down-converting the RF signals (Figure A.5). The conversion loss of the harmonic mixer when used with the spectrum analyzer LO in the "external mixer" mode is > 70 dB. Hence, the harmonic mixer is used in the "down-converter" mode with an MD2A diplexer and an external LO. Increasing the LO frequency reduces the conversion loss, for $f_{\rm LO}$ up to 18 GHz. Hence, the lowest possible harmonic (7–10) is chosen for down-converting

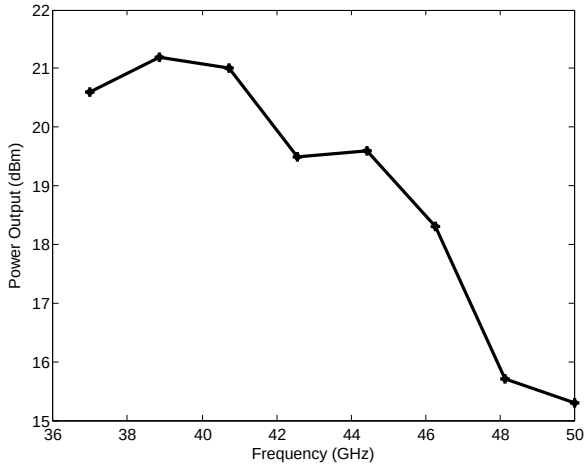

(a) Power output of the Spacek amplifier ($\mathrm{P1dB_{output}}$).

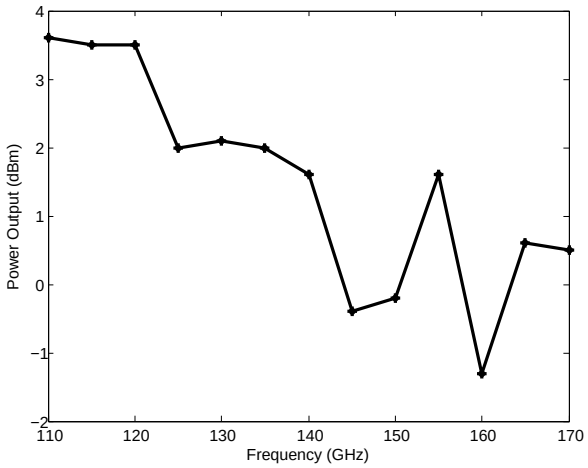

(b) Power output of the tripler (P_{in}=+20 dBm).

Figure A.4: Power output of the Spacek amplifier and the tripler.

Table A.3: Spacek amplifier and tripler parameters.

Spacek amplifier	Frequency	33–50 GHz
	Gain	15 dB (min) / 19 dB (typ)
	P-1dB	17.5 dBm (typ) / 15 dBm (min)
	Psat	19 dBm (typ)
	VSWR in/out	2:1 typ
	Bias	375 mA @ +8 to +12 VDC
	RF connectors	K-female In / WR-22 Out
	Operating temperature	0°C to +50°C
Frequency tripler	Input frequency	33–56.7 GHz
	Output frequency	100–170 GHz
	Input power	+15 dBm

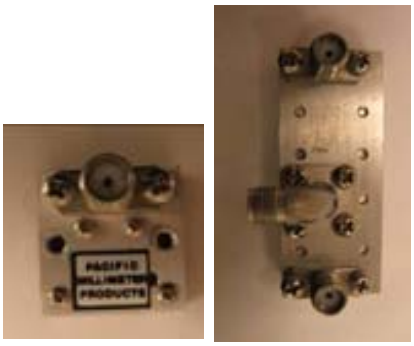

(a) Harmonic mixer. (b) Diplexer.

Figure A.5: F band harmonic mixer and diplexer.

(a) JCA amp. (b) LNA. (c) Bias tee.

Figure A.6: JCA/Miteq amplifiers and bias tee.

the RF signal while keeping the IF constant at 1 GHz. A JCA amplifier is used to amplify the LO signals and a spectrum analyzer is used to view the IF via a MD2A diplexer. Bias is provided to the harmonic mixer via a bias tee. An LNA amplifies the signals prior to displaying in the spectrum analyzer. The JCA amplifier, bias tee, and the LNA are shown in Figure A.6. The power output of the JCA amplifier and the S-parameters of the bias tee are shown in Figure A.7.

RFI was reduced by wrapping aluminum foil tapes around the bias tee, LNA, and all the microwave adapters. A 1 k ohm series resistor was added to the biastee and a bias voltage of $8V_{DC}$ was provided. Without this series resistance, the optimum bias-voltage that maximizes the system sensitivity is 388 mV_{DC}. The amplifiers and the mixer must be biased before any millimeter wave energy can be provided to the components.

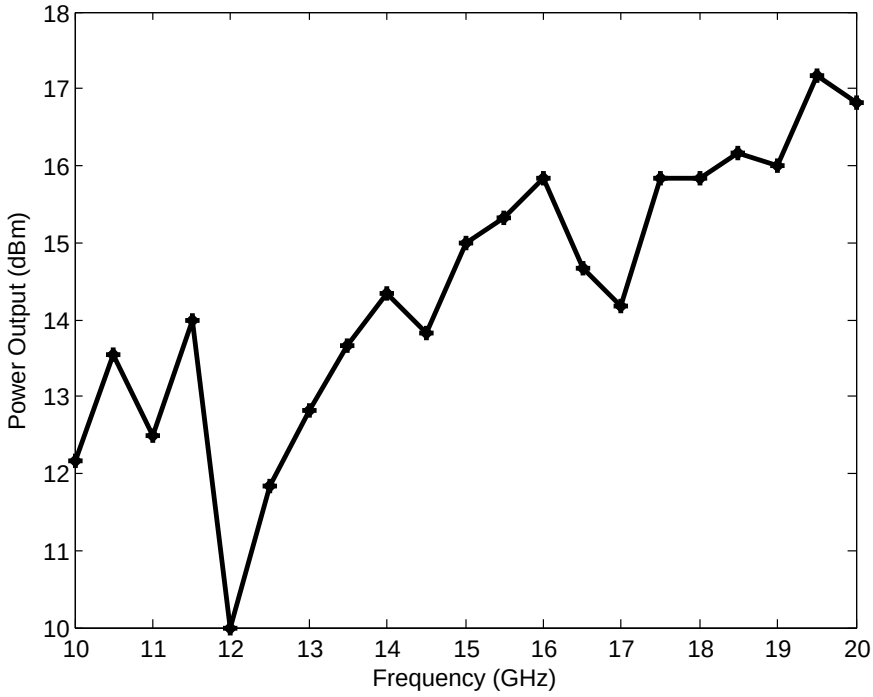

(a) Power output of the JCA amp (P_{in}=-5 dBm).

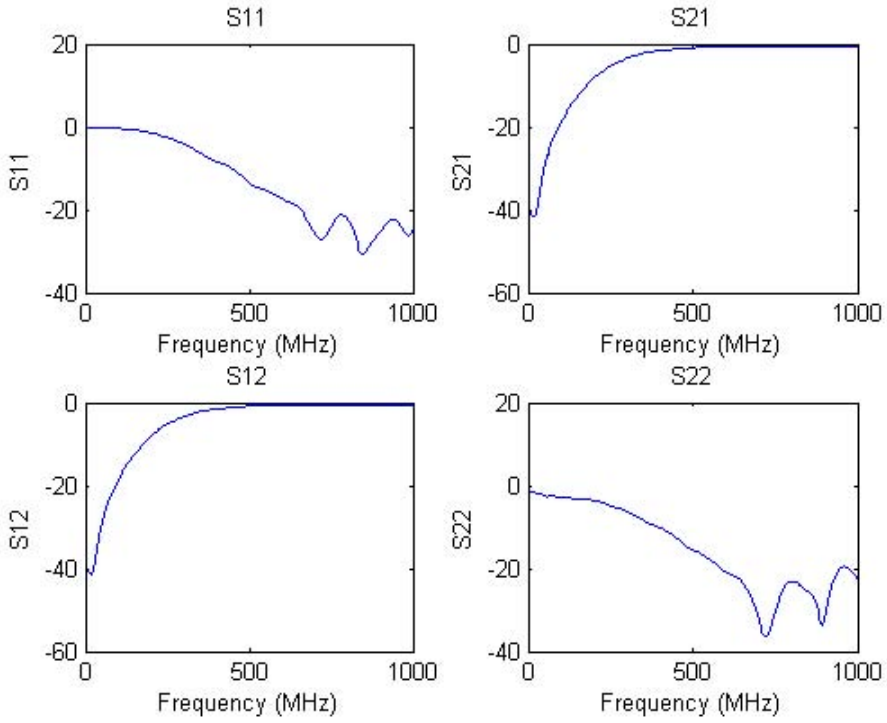

(b) S-parameters of the bias tee.

Figure A.7: Output component parameters.

APPENDIX B

VLA OBSERVATIONS OF THE 2009 JUPITER IMPACT EVENT

Jupiter was bombarded by an object of unknown origin on UT July 19, 2009 (Sánchez-Lavega et al., 2010). The collision itself was not recorded, but Anthony Wesley (an amateur astronomer) spotted an anomalous feature centered at $\sim 305^{\circ}$ W longitude and $\sim 58\ ^{\circ}$ S planetographic latitude in System III (λ_{III}) coordinates within hours after the impact. The Hubble image of Jupiter and its impact spot is shown in Figure B.1. Visible and infrared observations that followed confirmed that the feature was exogenic and it spanned a total area of $\sim$ 4800 km (east-west) x 2500 km (north-south) (de Pater et al., 2010; Sánchez-Lavega et al., 2010; Fletcher et al., 2010). Since different wavelengths probe different regions in the atmosphere of Jupiter, multi-wavelength observations of the impact, spanning radio, infrared, and visible wavelengths, are best suited for studying the impact characteristics, such as the impact dynamics, direction from which the impactor arrived, depth penetration of the impactor, and the type of body involved.

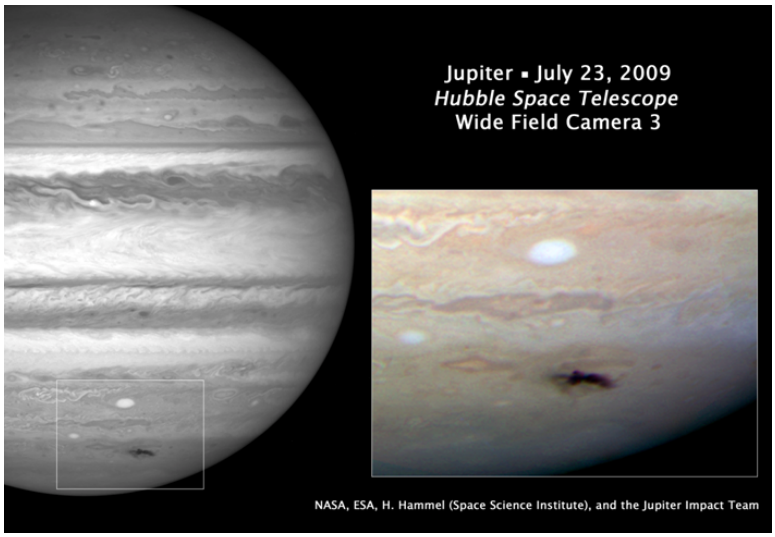

Figure B.1: Hubble image of Jupiter and its impact spot. Image credit: NASA, ESA, H. Hammel (Space Science Institute, Boulder, CO), and the Jupiter impact team.

B.1 VLA Observations of the Impact Event

The Jupiter impact event of 2009 was observed with the Very Large Array (VLA) situated on the Plains of San Agustin near Socorro, New Mexico, operated by the National Radio Astronomy Observatory (NRAO). The VLA consists of 27 antennas, each with a diameter of 25 m. The antennas are arranged in a Y-shape with nine antennas on each arm of the Y. There are four basic configurations for the VLA: A, B, C, and D. The A-configuration is the largest (highest resolution) and D-configuration is the most compact. In order to observe Jupiter using the VLA immediately after the impact, three rapid response-target of opportunity proposals were written and submitted to NRAO (VLA proposal IDs: VLA/09B-205, VLA/09B-206, VLA/09B-208). The proposals were reviewed by a panel of scientists and later accepted by the NRAO scheduling committee and a total of 38.5 hours of observation time was alloted between July 22, 2009 and August 10, 2009.

The VLA observations of Jupiter were conducted when the array was in the C-configuration, with a maximum physical antenna separation of 3.4 km. The observations were conducted at L, C, X, and K bands. During the observations, the L band electronics were tuned to 1.3851 and 1.4649 GHz, C band to 4.86 GHz, X band to 8.44 GHz, and K band to 22.46 GHz. Continuum mode was used in all the observations, and the four Stokes parameters were measured in two 50 MHz passbands. This provides an equivalent bandwidth of 100 MHz when the two passbands are averaged together (except the two L band frequencies, where the IFs are not averaged together), and the total intensity images (Stokes I) are formed (see, e.g., Butler et al., 2001). During the observations, Jupiter was approximately 4 AU from Earth and had an angular diameter of 48 arcsec. The astrometric right ascension was $\sim$ 21 h 45 m and the declination was $\sim$ -14 deg 36 m. Quasar 3C286 or 3C48 was used as the primary calibrator (flux), while the secondary calibrator (phase) was selected depending on which phase calibrator was approximately at the same elevation in the sky during the time of observation.

A summary of the observations along with the geometry of the planet visible from Earth and the duration of observations is listed in Table B.1. The observations were split into 1-4 hour time slots such that the impact site was visible as viewed from Earth at the time of the observation. The sidereal rotation rate of Jupiter is approximately 9 h 55 m, so the coordinates of the impact location rotate across the disk during the course of the observation. An example of the 1.3 cm observation made on August 1, 2009 is shown in Figure B.2.

The total emission from Jupiter at radio wavelengths is due to the thermal component from the planet as well as the synchrotron component from the relativistic electrons spiraling in the magnetosphere of the planet (see, e.g., Berge and Gulkis, 1976). At long wavelengths, synchrotron emission dominates and at short wavelengths thermal emission dominates. The cross-over is at approximately 10 cm (Berge and

Table B.1: Summary of the VLA observations of Jupiter along with the duration of observation and the geometry of the planet visible from Earth.

Date	**Wavelength (cm)**	λ_{III} **longitude**	**Duration (hours)**
July 22, 2009	3.5	197-288	1.5
July 23, 2009	3.5	257-293	1
July 26, 2009	3.5	258-7	3
July 27, 2009	3.5	261-327	2
July 29, 2009	6, 20	87-232	4
July 30, 2009	6, 20	153-292	4
August 1, 2009	6, 20	82-227	4
August 1, 2009	1.3	227-336	3
August 5, 2009	1.3	259-7	3
August 6, 2009	6, 20	104-249	4
August 6, 2009	1.3	249-358	3
August 10, 2009	1.3	268-340	2
August 10, 2009	6, 20	340-125	4

Gulkis, 1976). For the L and C band observations, the contribution to the total emission is mostly from the synchrotron radiation, and for the X and K band observations, the major contribution is from Jupiter's atmospheric thermal emission. Different wavelengths have different thermal and synchrotron contributions and they also probe to different depths in the atmosphere, with the longer wavelengths probing deeper into the atmosphere of the planet (see, e.g., Janssen et al., 2005). The weighting functions indicate the altitudes (pressure layers) that contribute most to the brightness temperature at a particular frequency. The normalized nadir-viewing weighting function in the 0.5–25 GHz range computed by Karpowicz (2010) using a radiative transfer model for the atmosphere of Jupiter is shown in Figure 5.58. The 3.5 cm wavelength probes the atmospheric layers between 0.8 bar and 3 bar and the 1.3 cm wavelength probes the atmospheric layers between 0.3 bar and 0.8 bar.

When an object bombards Jupiter, a plume of material from the object as well as from Jupiter's atmosphere is brought up from Jupiter's troposphere into the stratosphere. Hence, there will be a change in the composition of the stratosphere as well

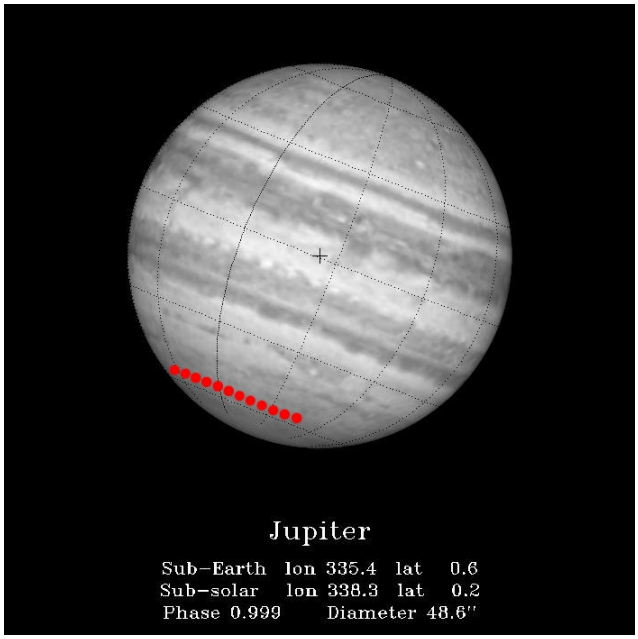

Figure B.2: Jupiter observation geometry on August 1, 2009. The red dots show the progression of the coordinates of the impact site as the location rotates across the disk during the observation.

as the troposphere at the impact site. Enhanced emission associated with ammonia gas and an increase in temperature in the upper troposphere at the site of the impact were observed in Jupiter following the 2009 impact event (de Pater et al., 2010; Fletcher et al., 2010). The 1.3 and 3.5 cm wavelengths probe the upper and middle troposphere of Jupiter. The VLA is capable of measuring changes due to the impact because of its sensitivity and resolution. Unfortunately the array was not in a high-resolution configuration at the time of the impact. The VLA resolution in C-configuration at 3.5 cm is $\sim$ 2.3 arcsec (6800 km linear at Jupiter) and at 1.3 cm is $\sim$ 0.8 arcsec (2300 km linear at Jupiter). Additionally, it was summer in New Mexico; so observing at high frequencies was difficult because of the North American Monsoon. In spite of these difficulties, observations were conducted at 1.3 and 3.5 cm wavelengths to study the changes to the thermal emission from Jupiter, and at 6 and 20 cm wavelengths to study the changes to the synchrotron emission from Jupiter.

B.2 Data Reduction and Analysis

The calibration of the data was performed in the normal fashion for VLA data, using the AIPS reduction package (`http://www.cv.nrao.edu/aips/`). A detailed description of the initial calibration and self-calibration of the visibilities obtained for the observations of Venus is provided by Butler et al. (2001) and a similar approach was followed for the calibration of Jupiter observations in this study. After the self-calibration process, the data product is a set of fully calibrated visibilities for Jupiter. These visibilities were used to make maps of the received flux density, in units of Jy, across the visible disk of Jupiter. Initial data reductions were performed for the 1.3 and 3.5 cm observations. The synchrotron component of the emission at 3.5 cm is approximately 10% and at 1.3 cm is $< 1\%$. Hence, at 3.5 cm, it is possible to observe both thermal and synchrotron emissions. Some approximations about the spatial extent of the synchrotron belts were made, and post processing was done on the reduced 3.5 cm maps of Jupiter to seperate the thermal and synchrotron components. Figure B.3 shows the maps of the thermal and synchrotron component of Jupiter at 3.5 cm wavelength made on July 26, 2009. Figure B.4 shows the maps of the thermal component of Jupiter at 1.3 cm wavelength made on August 01, 2009 and August 06, 2009. Work is in progress to reduce and analyze the 6 and 20 cm observations and to study the changes to the synchrotron emission due to the impact at these wavelengths.

Initial data reduction and analysis show no significant changes to the thermal component because of the impact at both the observation wavelengths (Devaraj et al., 2010). Using the method by Sault et al. (2004), the 3.5 cm images of Jupiter obtained over four days between July 22–27, 2009 were rotationally deprojected into a planetary cartographic system. The resulting images were averaged together and is shown in Figure B.5 and the impact site is highlighted with a black oval. It can be seen from the figure that no signature of the impact on the thermal emission at 3.5 cm, at a depth

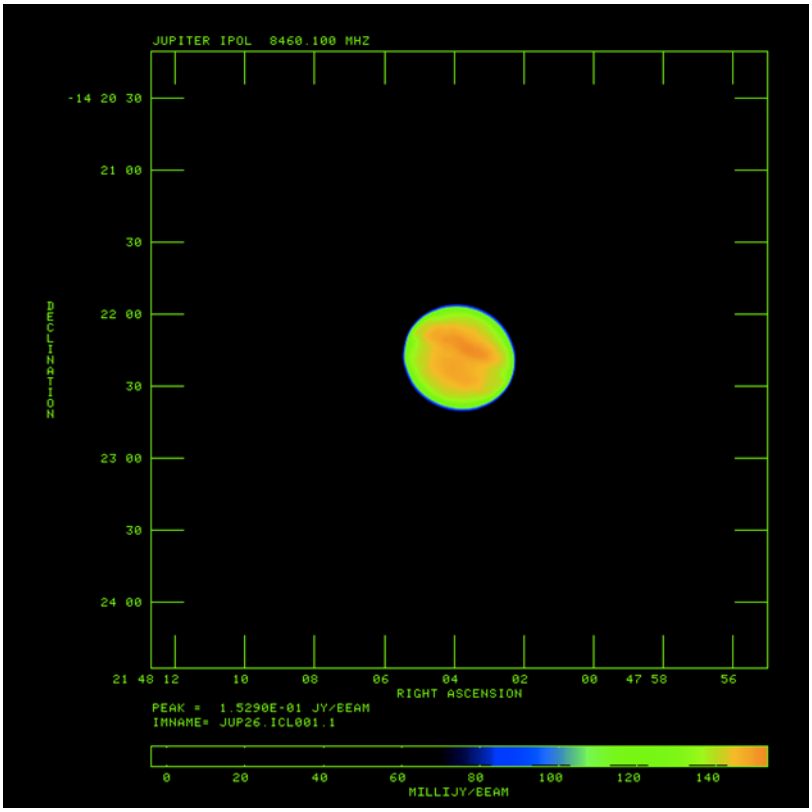

(a) Thermal component.

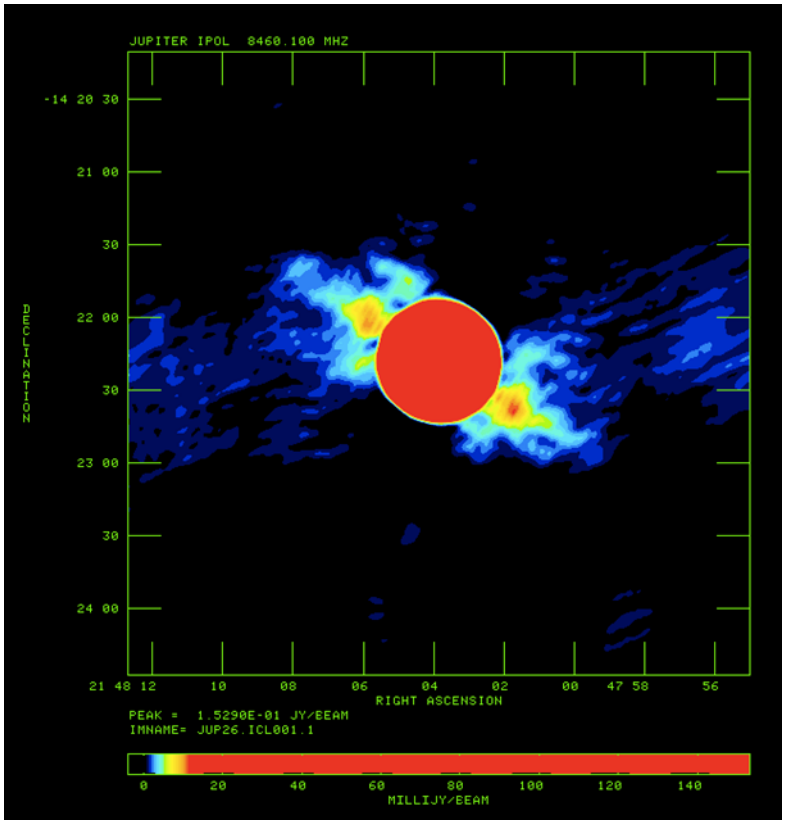

(b) Synchrotron component.

Figure B.3: Maps of Jupiter at 3.5 cm made on July 26, 2009.

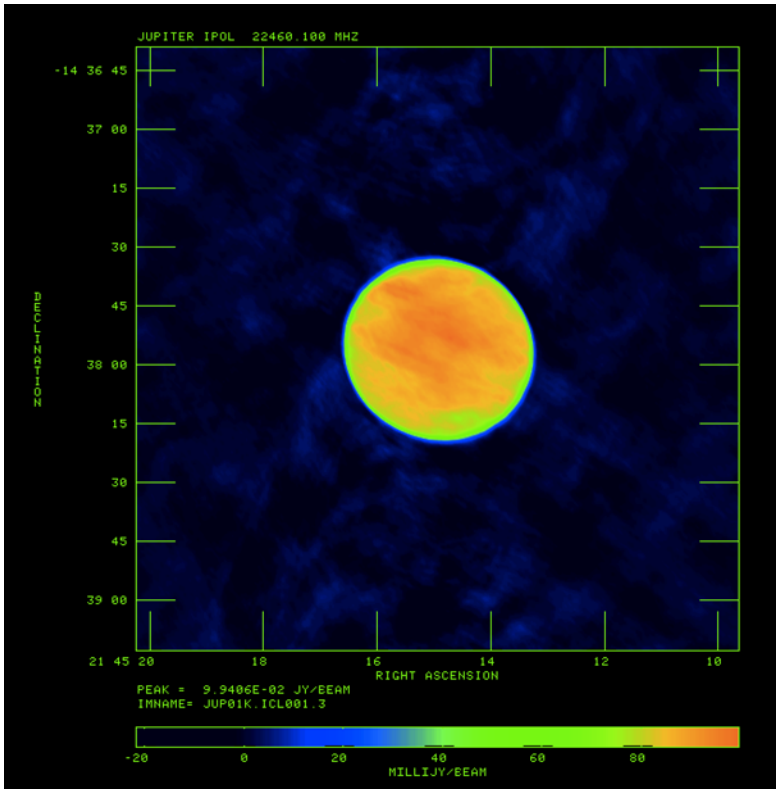

(a) August 01, 2009.

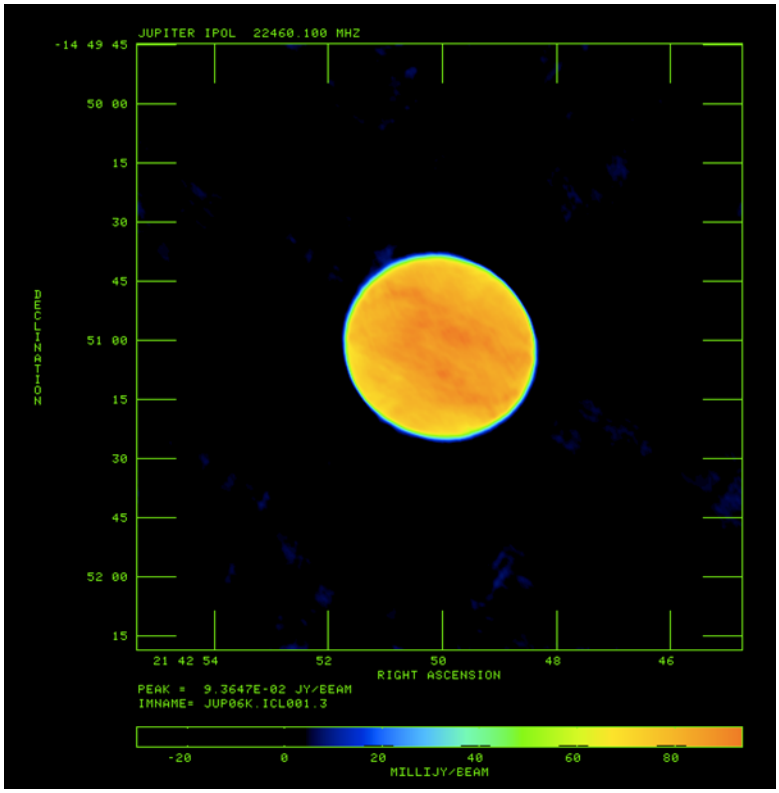

(b) August 06, 2009.

Figure B.4: Maps of Jupiter showing the thermal emission at 1.3 cm.

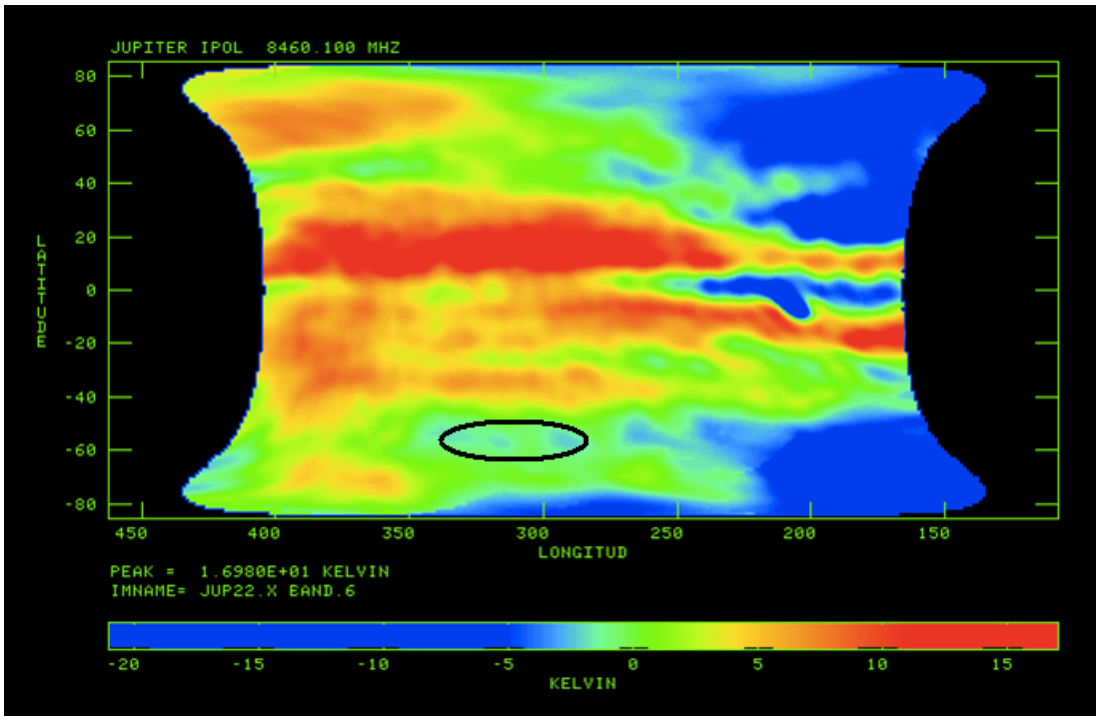

Figure B.5: Rotationally deprojected map of Jupiter at 3.5 cm averaged over observations from July 22–27, 2009. A black oval highlights the impact site. No signature of the impact on the thermal emission at 3.5 cm, at a depth of $\sim$ 1 bar, and with effective resolution of $\sim$ 6800 km, was detected.

of $\sim$ 1 bar, and with effective resolution of $\sim$ 6800 km, was detected. Preliminary analysis of the 1.3 cm thermal emission data (depth of $\sim$ 500 mbar and an effective resolution of $\sim$ 2300 km) also indicates that no signature of the impact was detected.

APPENDIX C

VLA OBSERVATIONS OF VENUS AT X BAND

Previous observations of Venus were conducted at X band (3.6 cm) in 1996 and new observations were conducted as part of this work in 2009 with the NRAO VLA. These observations have now been calibrated, reduced, and analyzed in a consistent fashion. Spatial variations were observed in the microwave emission from Venus originating from the deep atmosphere.

C.1 VLA Observations

Observations of Venus were made at X band using the VLA on April 30, 1996 by Butler et al. (2001) and July 07, 2009 by this author. The VLA was in C-configuration during both the observations, and at 3.6 cm, the angular resolution of the array is $\sim$ 2.3 arcsec. Continuum mode was used in all the observations. A summary of the ephemeris information and the calibrators used for the observations is listed in Table C.1.

Table C.1: Ephemeris information and the calibrators for Venus observations.

Observation Date	**April 30, 1996**	**July 07, 2009**
Time range (UT)	0148-0224	0240–0450
Right ascension	05 h 21 min	04 h 03 min
Declination	+27 deg 39 min	+18 deg 05 min
Distance from Earth (AU)	0.486	0.947
Angular diameter (arcsec)	34.28	17.61
Primary calibrator	3C286	3C48
Secondary calibrator	0555+398	0344+159

Figure C.1 shows the disk of Venus as seen from Earth (left) and the radar map of the surface of Venus on April 30, 1996 and Figure C.2 shows the disk and radar maps of Venus on July 07, 2009.

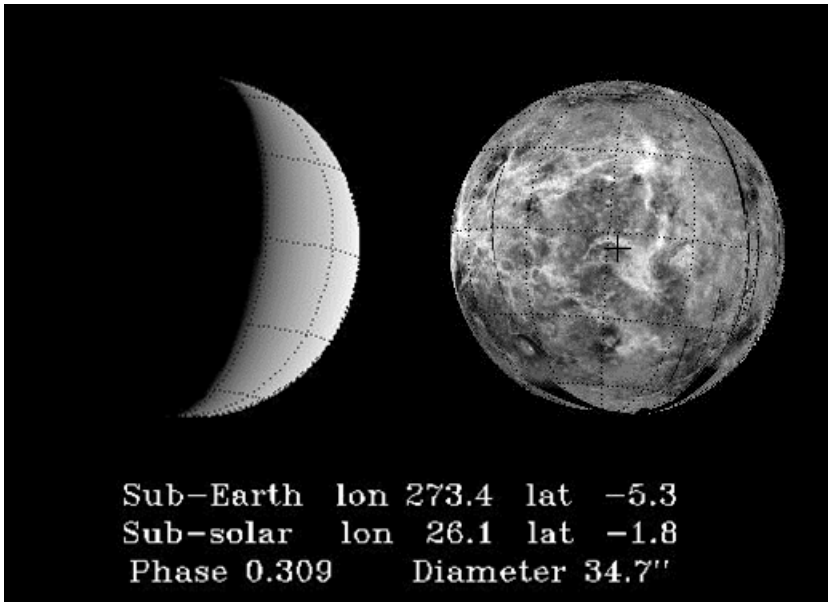

Figure C.1: Disk map of Venus as seen from Earth (left) and radar surface map of Venus (right) on April 30, 1996. Image source: US Naval Observatory.

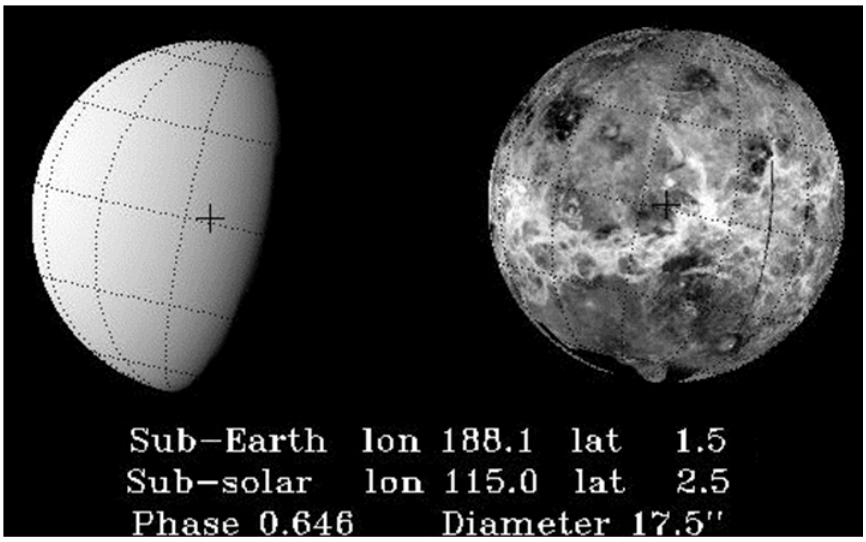

Figure C.2: Disk map of Venus as seen from Earth (left) and radar surface map of Venus (right) on July 07, 2009. Image source: US Naval Observatory.

C.2 Data Analysis

Calibration and reduction of the Venus observations were performed using the AIPS data-reduction package in a fashion similar to the Jupiter observations explained in Appendix B.2, and maps of the 3.6 cm emission from Venus were created. Figure C.3 shows the reduced X band map of Venus for the 2009 observation. The reduced maps of Venus were referenced to a radially-averaged, limb-darkened disk and residual maps were created. These residual maps are shown in Figures C.4 and C.5 for the two observations.

Significant structures are visible on the residual maps. Of note are the bright/dark regions around the limb of the planet, which correspond to the variations in the abundance of microwave-opaque sulfuric acid vapor below the cloud base, caused by the Hadley cell circulation. (The limb-viewing weighing functions correspond to such altitudes.) However, the features in the center of the disk correspond to variations in either temperature or microwave absorbing gases in the deepest part of the troposphere. At X band, emission from the disk center is from the 0-15 km altitude range (see, Figure C.6).

Sulfur dioxide (SO_2) and gaseous sulfuric acid (H_2SO_4) dominate the centimeter-wavelength emission from Venus (see, e.g., Butler et al., 2001; Jenkins et al., 2002). At altitudes below 35 km, gaseous H_2SO_4 thermally dissociates and forms H_2O and SO_3, both of which exhibit relatively small amounts of microwave absorption at the abundance levels present in the Venus atmosphere. Thus, in the deep atmosphere of Venus, only SO_2, and to a lesser extent OCS have the potential to affect the observed microwave emission. The collisionally-induced absorption from CO_2 has a significant effect on the microwave emission from Venus, but it is not in any way localized since CO_2 is the dominant atmospheric constituent ($\sim 96\%$). Hence, it is critical to study the centimeter-wavelength properties of SO_2 in the deep Venus atmospheric conditions.

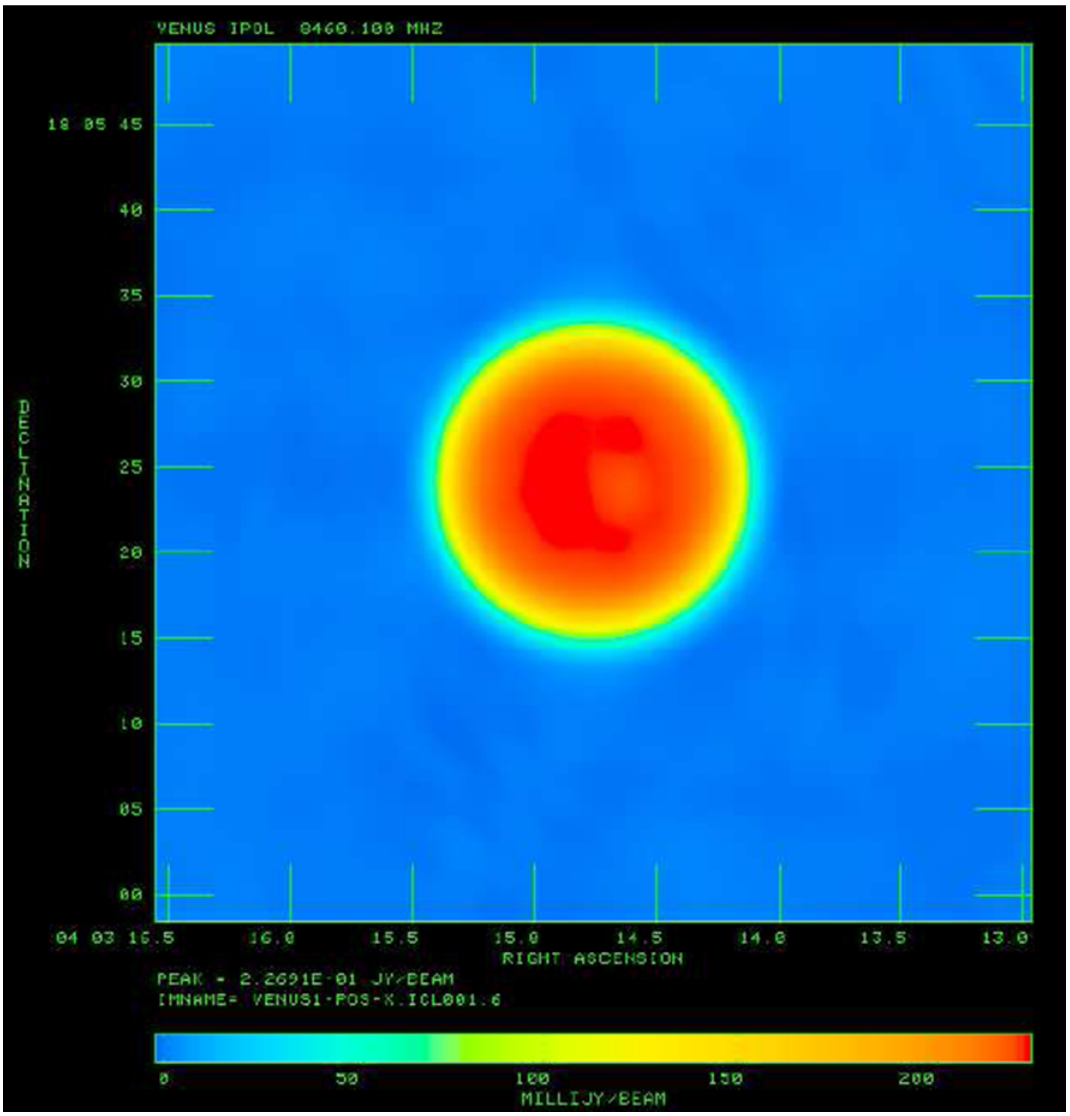

Figure C.3: X band map of Venus taken with the VLA on July 07, 2009.

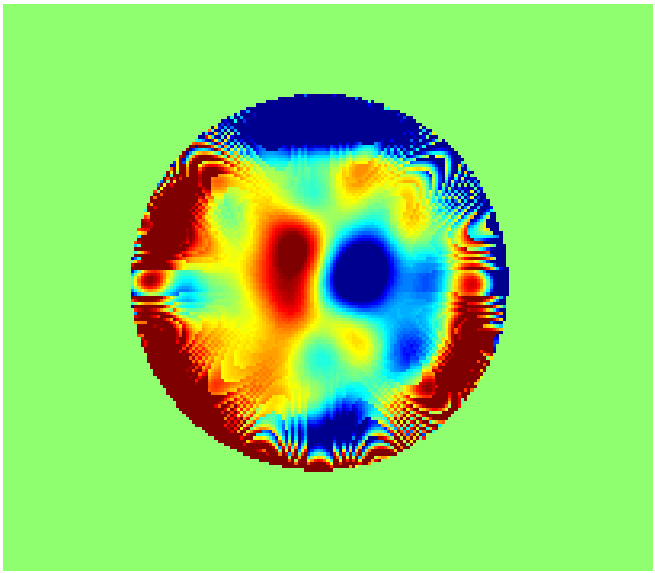

Figure C.4: Residual X band map of Venus for the July 07, 2009 observation.

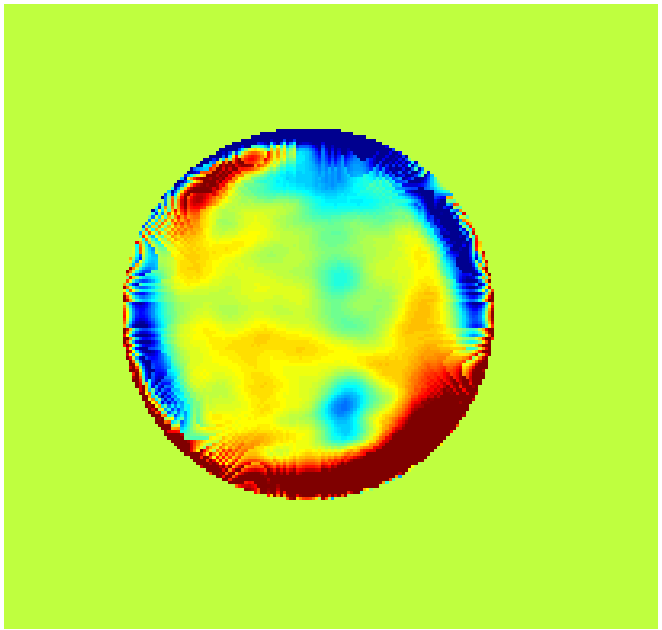

Figure C.5: Residual X band map of Venus for the April 30, 1996 observation.

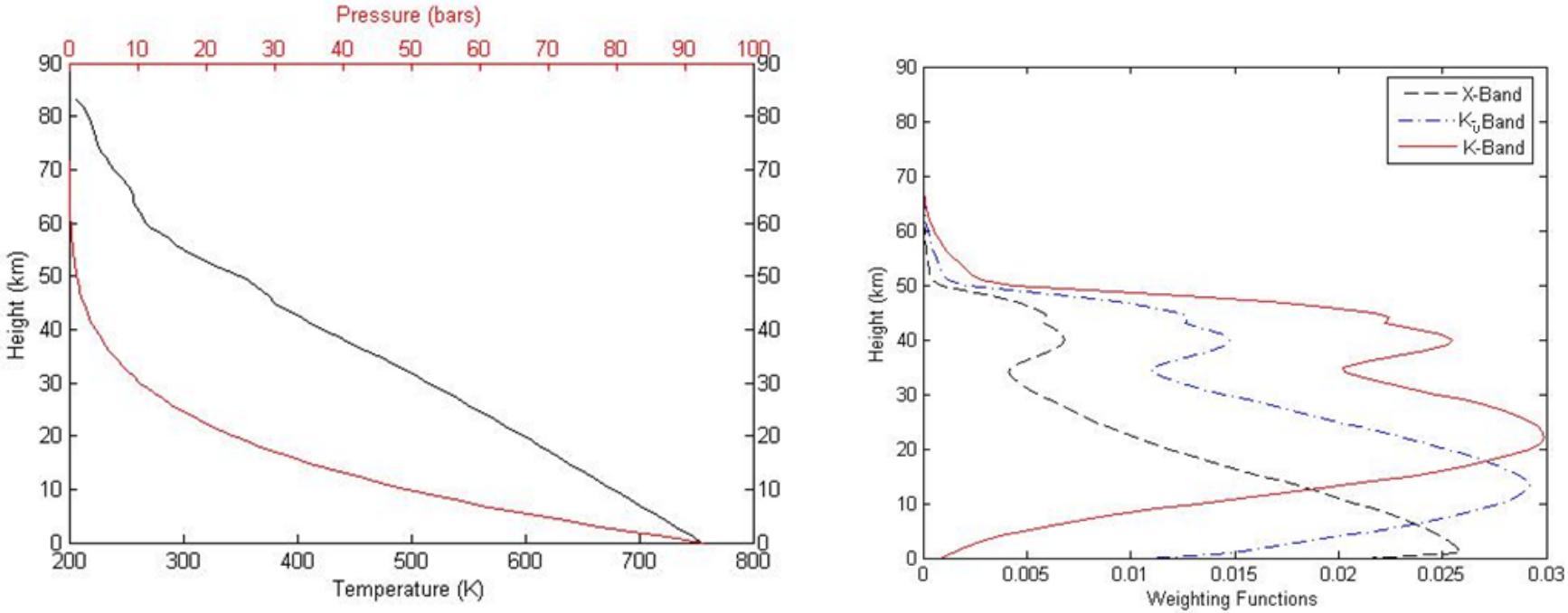

Figure C.6: The TP profile of Venus (left) and the weighting functions at the disk center (right).

Laboratory measurements of the centimeter-wavelength opacity of SO_2 under Venus atmospheric conditions were conducted by Suleiman et al. (1996) at pressures up to 4 bar. However, the weighting functions for Venus central disk show that the contribution to the 3.6 cm emission is from altitudes with pressures in the 40–92 bar region (Figure C.6). Hence, laboratory measurements of the microwave properties of SO_2 under simulated deep tropospheric conditions of Venus are currently being planned with the high-pressure laboratory system described in this dissertation. The results of the laboratory study will aid in interpreting the observed spatial variations in the microwave emission from Venus originating from the deep atmosphere.

Bibliography

Atreya, S., Mahaffyy, P., Niemann, H., Wong, M., Owen, T., 2003. Composition and origin of the atmosphere of Jupiter–an update, and implications for the extrasolar giant planets. Planet. Space Sci. 51, 105–112.

Bachet, G., 1973. Etude des elargissements de la raie de rotation a 19 cm^{-1} de NH_3 perturbee par des gaz etrangers comprimes. J. Quant. Spectrosc. Radiat. Transfer 13, 1305–1308.

Becker, G. E., Autler, S. H., 1946. Water vapor absorption of electromagnetic radiation in the centimeter wave-length range. Phys. Rev. 70, 300–307.

Belli, S., Buffa, G., Tarrini, O., 1997. On the extension of the Rydberg-Ritz principle to the collisional relaxation of molecular and atomic lines. Chem. Phys. Lett. 193, 277–284.

Belov, S. P., Kazakov, V. P., Krupnov, A. F., Markov, V. N., Mel'nikov, A. A., Skvortsov, V. A., Tret'yakov, M. Y., 1982. The study of microwave pressure linewidths. J. Mol. Spectrosc. 94, 264–282.

Belov, S. P., Krupnov, A. F., Markov, V. N., Mel'nikov, A. A., Skvortsov, V. A., Tret'yakov, M. Y., 1983. Study of microwave pressure lineshifts: dynamic and isotopic dependences. J. Mol. Spectrosc. 101, 258–270.

Ben-Reuven, A., 1966. Impact broadening of microwave spectra. Phys. Rev. 145, 7–22.

Berge, G. L., Gulkis, S., 1976. Earth-based radio observations of Jupiter: millimeter to meter wavelengths. In: Gehrels, T. (Ed.), Jupiter: Studies of the Interior, Atmosphere, Magnetosphere, and Satellites. Univ. of Arizona Press, Tuscon, AZ, pp. 621–692.

Bleaney, B., Penrose, R. P., 1947. The inversion spectrum of ammonia at centimeteric wavelengths. Proc. Roy. Soc. A189, 358.

Brown, L. R., Peterson, D. B., 1994. An empirical expression for linewidths of ammonia from far-infrared measurements. J. Mol. Spectrosc. 168, 593–606.

Burke, B. F., Franklin, K. L., 1955. Observations of a variable radio source associated with the planet Jupiter. J. Geophys. Res. 60, 213–217.

Butler, B. J., Steffes, P. G., Suleiman, S. H., Kolodner, M. A., Jenkins, J. M., 2001. Accurate and consistent microwave observations of Venus and their implications. Icarus 154, 226–238.

Cleeton, C. E., Williams, N. H., 1934. Electromagnetic waves of 1.1 cm wave-length and the absorption spectrum of ammonia. Phys. Rev. 45, 234–237.

Culshaw, W., 1960. High resolution millimeter wave Fabry-Perot interferometer. IRE Trans. Microwave Theory Tech. 8, 182–189.

Culshaw, W., 1961. Resonators for millimeter and submillimeter wavelengths. IRE Trans. Microwave Theory Tech. 9, 135–144.

Culshaw, W., 1962. Futher considerations on Fabry-Perot type resonators. IRE Trans. Microwave Theory Tech. 10, 331–339.

Danos, M., Geschwind, S., 1953. Broadening of microwave absorption lines due to wall collisions. Phys. Rev. 91, 1159–1162.

de Pater, I., DeBoer, D., Marley, M., Freedman, R., Young, R., 2005. Retrieval of water in Jupiter's deep atmosphere using microwave spectra of its brightness temperature. Icarus 173, 425–438.

de Pater, I., Dunn, D., Romani, P., Zahnle, K., 2001. Reconciling Galileo Probe data and ground-based radio observations of ammonia on Jupiter. Icarus 149, 66–78.

de Pater, I., Fletcher, L. N., Pérez-Hoyos, S., Hammel, H. B., Orton, G. S., Wong, M. H., Luszcz-Cook, S., Sánchez-Lavega, A., Boslough, M., 2010. A multi-wavelength study of the 2009 impact on Jupiter: Comparison of high resolution images from Gemini, Keck and HST. Icarus 210, 722–741.

de Pater, I., Kenderdine, S., Dickel, J. R., 1982. Comparison of the thermal and nonthermal radiation characteristics of Jupiter at 6, 11, and 21 cm with model calculations. Icarus 51, 25–38.

de Pater, I., Mitchell, D., 1993. Radio observations of the planets: the importance of laboratory measurements. J. Geophys. Res. 98, 5471–5490.

DeBoer, D. R., Steffes, P. G., 1994. Laboratory measurements of the microwave properties of H_2S under simulated Jovian conditions with an application to Neptune. Icarus 109, 352–366.

DeBoer, D. R., Steffes, P. G., 1996. Estimates of the tropospheric vertical structure of Neptune based on microwave radiative transfer studies. Icarus 123, 323–335.

Debye, P. J. W., 1929. Polar Molecules. The Chemical Catalog Company Inc., New York.

Devaraj, K., Butler, B., Hesman, B., Steffes, P., Sault, R., 2010. VLA observations of the Jupiter impact. Geophys. Res. Abs. 12.

Devaraj, K., Steffes, P. G., 2011. The Georgia Tech millimeter-wavelength measurement system and some applications to the study of planetary atmospheres. Radio Sci., RS2014, doi:10.1029/2010RS004433.

Devaraj, K., Steffes, P. G., Karpowicz, B. M., 2011. Reconciling the centimeter- and millimeter-wavelength ammonia absorption spectra under jovian conditions: Extensive millimeter-wavelength measurements and a consistent model. Icarus 212, 224–235.

Dowling, T. E., Muhleman, D. O., Berge, G. L., 1987. Aperture synthesis observations of Saturn and its rings at 2.7-mm wavelength. Icarus 70, 506–516.

Dunn, D. E., de Pater, I., Wright, M., Hogerheijde, M. R., Molnar, L. A., 2005. High-quality BIMA-OVRO images of Saturn and its rings at 1.3 and 3 millimeters. Astron. J. 129, 1109–1116.

Fahd, A. K., Steffes, P. G., 1992. Laboratory measurements of the microwave and millimeter-wave opacity of gaseous sulfur-dioxide (SO_2) under simulated conditions for the Venus atmosphere. Icarus 97, 200–210.

Fletcher, L. N., Orton, G., de Pater, I., Edwards, M., Yanamandra-Fisher, P., Hammel, H., Lisse, C., , Fisher, B., 2010. The aftermath of the July 2009 impact on Jupiter: Ammonia, temperatures and particulates from Gemini thermal infrared spectroscopy. Icarus 211, 568–586.

Folkner, W. M., Woo, R., Nandi, S., 1998. Ammonia abundance in Jupiter's atmosphere derived from the attenuation of the Galileo Probe's radio signal. J. Geophys. Res. 103, 22847–22856.

Gibson, J., Welch, W. J., de Pater, I., 2005. Accurate jovian radio flux density measurements show ammonia to be subsaturated in the upper troposphere. Icarus 173, 439–446.

Gordy, W., 1948. Microwave spectroscopy. Rev. Mod. Phys. 20.

Griffin, M. J., Ade, P. A. R., Orton, G. S., Robson, E. I., Gear, W. K., Nolt, I. G., Radostitz, J. V., 1986. Submillimeter and millimeter observations of Jupiter. Icarus 65, 244–256.

Griffin, M. J., Orton, G. S., 1993. The near-millimeter brightness temperature spectra of Uranus and Neptune. Icarus 105, 537–547.

Gross, E. P., 1955. Shape of collision-broadened spectral lines. Phys. Rev. 97, 395–403.

Hanley, T. R., 2008. The microwave opacity of ammonia and water vapor: Application to remote sensing of the atmosphere of Jupiter. PhD dissertation, Georgia Institute of Technology, Atlanta, GA.

Hanley, T. R., Steffes, P. G., 2007. A high-sensitivity laboratory system for measuring the microwave properties of gases under simulated conditions for planetary atmospheres. Radio Sci. 42 (RS6010).

Hanley, T. R., Steffes, P. G., Karpowicz, B. M., 2009. A new model of the hydrogen and helium-broadened microwave opacity of ammonia based on extensive laboratory measurements. Icarus 202, 316–335.

Herriott, D. R., Kogelnik, H., Kompfner, R., 1964. Off axis paths in spherical mirror interferometers. Appl. Opt. 3, 523–526.

Hesman, B. E., Davis, G. R., Matthews, H. E., Orton, G. S., 2007. The abundance profile of CO in Neptune's atmosphere. Icarus 186, 342–353.

Hewlett-Packard, 1997. HP 8560 E-Series Spectrum Analyzer Calibration Guide. Santa Rosa, CA.

Hoffman, J. P., Steffes, P. G., DeBoer, D. R., 2001. Laboratory measurements of the microwave opacity of phosphine: Opacity formalism and application to the atmospheres of the outer planets. Icarus 152, 172–184.

Irwin, P., 2003. Giant planets of our solar system: Atmospheres, composition, and structure. Springer-Praxis, Chichester, UK.

Jacquinet-Husson, N., Crepeau, L., Armante, R., Boutammine, C., Chédin, A., Scott, N. A., Crevoisier, C., Capelle, V., Boone, C., Poulet-Crovisier, N., Barbe, A., Campargue, A., Benner, D. C., Benilan, Y., Bézard, B., Boudon, V., Brown, L. R., Coudert, L. H., Coustenis, A., Dana, V., Devi, V. M., Fally, S., Fayt, A., Flaud, J. M., Goldman, A., Herman, M., Harris, G. J., Jacquemart, D., Jolly, A., Kleiner, I., Kleinböhl, A., Kwabia-Tchana, F., Lavrentieva, N., Lacome, N., Xu, L.-H., Lyulin, O. M., Mandin, J. Y., Maki, A., Mikhailenko, S., Miller, C. E., Mishina, T., Moazzen-Ahmadi, N., Müller, H. S. P., Nikitin, A., Orphal, J., Perevalov, V., Perrin, A., Petkie, D. T., Predoi-Cross, A., Rinsland, C. P., Remedios, J. J., Rotger, M., Smith, M. A. H., Sung, K., Tashkun, S., Tennyson, J., Toth, R. A., Vandaele, A. C., , Auwera, J. V., 2011. The 2009 edition of the GEISA spectroscopic database. J. Quant. Spectrosc. Radiat. Transfer 112, 2395–2445.

Janssen, M. A., Hofstadter, M. D., Gulkis, S., Ingersoll, A. P., Allison, M., Bolton, S. J., Levin, S. M., Kamp, L. W., 2005. Microwave remote sensing of Jupiter's atmosphere from an orbiting spacecraft. Icarus 173, 447–453.

Jenkins, J. M., Kolodner, M. A., Butler, B. J., Suleiman, S. H., G.Steffes, P., 2002. Microwave remote sensing of the temperature and the distribution of sulfur compounds in the Venus atmosphere. Icarus 158, 312–328.

Jenkins, J. M., Steffes, P. G., 1988. Constraints on the microwave opacity of gaseous methane and water vapor in the jovian atmosphere. Icarus 76, 378–382.

Joiner, J., Steffes, P. G., 1991. Modeling of Jupiter's millimeter wave emission utilizing laboratory measurements of ammonia (NH_3) opacity. J. Geophys. Res. 96, 17,463–17,470.

Karpowicz, B. M., 2010. In search of water vapor on Jupiter: Laboratory measurements of the microwave properties of water vapor and simulations of Jupiter's microwave emission in support of the Juno mission. PhD dissertation, Georgia Institute of Technology, Atlanta, GA.

Karpowicz, B. M., Steffes, P. G., 2011. In search of water vapor on Jupiter: Laboratory measurements of the microwave properties of water vapor under simulated jovian conditions. Icarus 212, 210–223.

Kramer, C., Moreno, R., Greve, A., 2008. Long-term observations of Uranus and Neptune at 90 GHz with IRAM 30 m telescope. Astron. Astrophys. 482, 359–363.

Kunde, V., Hanel, R., Maguire, W., Gautier, D., Baluteau, J. P., Marten, A., 1982. The tropospheric gas composition of Jupiter's north equatorial belt ($NH_3, PH_3, CH_3D, GeH_4, H_2O$) and the Jovian D/H isotopic ratio. Astrophys. J. 263, 443–467.

Lamarre, J. M., Puget, J. L., Bouchet, F., Ade, P. A. R., Benoit, A., Bernard, J., Bock, J., Bernardis, P. D., Charra, J., Couchot, F., Delabrouille, J., Efstathiou, G., Giard, M., Guyot, G., Lange, A., Maffei, B., Murphy, A., Pajot, F., Piat, M., Ristorcelli, I., Santos, D., Sudiwala, R., Sygnet, J., Torre, J., Yurchenko, V., Yvon, D., 2003. The Planck high frequency instrument, a third generation CMB experiment, and a full sky submillimeter survey. New Astron. Rev. 47, 1017–1024.

Law, S. E., Staelin, D. H., 1968. Measurements of Venus and Jupiter near 1-cm wavelength. Astrophys. J. 154, 1077–1086.

Leachman, J. W., Jacobsen, R. T., Penoncello, S. G., Lemmon, E. W., 2009. Fundamental equations of state for parahydrogen, normal hydrogen, and orthohydrogen. J. Phys. Chem. Ref. Data 38, 721–748.

Lemmon, E. W., Huber, M. L., McLinden, M. O., 2007. NIST Standard Reference Database 23: Reference Fluid Thermodynamic and Transport Properties-REFPROP, *Standard Reference Data Program Version 8.0*. National Institute of Standards and Technology, Gaithersburg.

Levenberg, K., 1944. A method for the solution of certain nonlinear problems in least squares. Quart. Appl. Math. 2, 164–168.

Lindal, G. F., 1992. The atmosphere of Neptune - an analysis of radio occultation data acquired with Voyager 2. Astron. J. 103, 967–982.

Lindal, G. F., Sweetnam, D. N., Eshleman, V. R., 1985. The atmosphere of Saturn - an analysis of the voyager radio occultation measurements. Astron. J. 90, 1136–1146.

Lorentz, H. A., 1906. The width of spectral lines. Proc. Neth. Acad. Arts Sci. 18, 134–150.

Marquardt, D., 1963. An algorithm for least-squares estimation of nonlinear parameters. SIAM J. Appl. Math. 11, 431–441.

Matthaei, G. L., Young, L., Jones, E., 1980. Microwave filters, impedance matching networks and coupling structures. McGraw-Hill, New York.

McCarty, R. D., Arp, V. D., 1990. A new wide range equation of state for helium. Advances in Cryogenic Engineering 35, 1465–1475.

Mohammed, P. N., Steffes, P. G., 2003. Laboratory measurements of the Ka-band (7.5 to 9.2 mm) opacity of phosphine (PH_3) and ammonia (NH_3) under simulated conditions for the Cassini-Saturn encounter. Icarus 166 (423–435).

Mohammed, P. N., Steffes, P. G., 2004. Laboratory measurements of the W band (3.2 mm) properties of phosphine (PH_3) and ammonia (NH_3) under simulated conditions for the outer planets. J. Geophys. Res. 109 (E07S13).

Morris, E. C., 1971. Microwave absorption by gas mixtures at pressures upto several hundred bars. II. Discussion of results. Aust. J. Phys. 24, 157–175.

Morris, E. C., Parsons, R. W., 1970. Microwave absorption by gas mixtures at pressures upto several hundred bars. I. Experimental technique and results. Aust. J. Phys. 23, 335–349.

Muhleman, D. O., Berge, G. L., 1991. Observations of Mars, Uranus, Neptune, Io, Europa, Ganymede and Callisto at a wavelength of 2.66 mm. Icarus 92, 263–272.

Nethercot, A. H., Klein, J. A., Loubser, J. H. N., Townes, C. H., 1952. Spectroscopy near the boundary between the microwave and infrared regions. Suppl. Nuovo Cimento 9, 358–363.

Niemann, H. B., Atreya, S. K., Carignan, G. R., Donahue, T. M., Haberman, J. A., Harpold, D. N., Hartle, R. E., Hunten, D. M., Kasprzak, W. T., Mahaffy, P. R., Owen, T. C., Spencer, N. W., Way, S. H., 1996. The Galileo probe mass spectrometer: Composition of Jupiter's atmosphere. Science 272, 846–849.

Orton, G. S., Fisher, B. M., Baines, K. H., Stewart, S. T., Friedson, A. J., Ortiz, J. L., Marinova, M., Ressler, M., Dayal, A., Hoffmann, W., Hora, J., Hinkley, S., Krishnan, V., Masanovic, M., Tesic, J., Tziolas, A., Parija, K. C., 1998. Characteristics of the Galileo Probe entry site from Earth-based remote sensing observations. J. Geophys. Res. 103, 22791–22814.

Orton, G. S., Gustafsson, M., Burgdorf, M., Meadows, V., 2007. Revised ab initio models for $H_2 - H_2$ collision-induced absorption at low temperatures. Icarus 189, 544–549.

Overstreet, R., Giauque, W. F., 1937. Ammonia. The heat capacity and vapor pressure of solid and liquid. Heat of caporization. The entropy values from thermal and spectroscopic data. J. Am. Chem. Soc. 59, 254–259.

Pickett, H. M., Poynter, R. L., Cohen, E. A., Delitsky, M. L., Pearson, J. C., Müller, H. S. P., 1998. Submillimeter, millimeter, and microwave spectral line catalog. J. Quant. Spectrosc. Radiat. Transfer 60, 883–890.

Pine, A. S., Markov, V. N., Buffa, G., Tarrini, O., 1993. N_2, O_2, H_2, Ar and He broadening in the ν_1 band of NH_3. J. Quant. Spectrosc. Radiat. Transfer 50, 337–348.

Poynter, R. L., Kakar, R. K., 1975. The microwave frequencies, line parameters, and spectral constants for $14NH_3$. Astrophys. J. Suppl. Ser. 29, 87–96.

Pozar, D. M., 1998. Microwave Engineering. 2nd ed., Wiley and Sons, New York.

Ramo, S., Whinnery, J. R., Duzer, T. V., 1994. Fields and Waves in Communications Electronics. Wiley and Sons, New York.

Rodrigues, C. C., Moraes Jr., D., 2002. Control of the emission of ammonia through adsorption in a fixed bed of activated carbon. Adsorpt. Sci. Technol. 20, 1013–1022.

Rosenkranz, P. W., 1998. Water vapor microwave continuum absorption: A comparison of measurements and models. Radio Sci. 33, 919–928.

Sánchez-Lavega, A., Wesley, A., Orton, G., Hueso, R., Perez-Hoyos, S., Fletcher, L. N., Yanamandra-Fisher, P., Legarreta, J., de Pater, I., Hammel, H., Simon-Miller, A., Gomez-Forrellad, J. M., Ortiz, J. L., Garca-Melendo, E., Puetter, R. C., Chodas, P., 2010. The impact of a large object with Jupiter in July 2009. Astrophys. J. 715, 155–159.

Sault, R. J., Engel, C., de Pater, I., 2004. Longitude-resolved imaging of Jupiter at λ=2 cm. Icarus 168, 336–343.

Smith, H. J., Douglas, J. N., 1957. First results of a planetary radio astronomy program of the Yale Observatory. Astron. J. 62, 247.

Span, R., 2000. Multiparameter Equations of State. Springer, New York.

Spilker, T. R., 1990. Laboratory measurements of the microwave absorptivity and refractivity spectra of gas mixtures applicable to giant planet atmospheres. PhD dissertation, Stanford University, CA.

Sromovsky, L. A., Collard, A., Fry, P., Orton, G., Lemmon, M., Tomasko, M., Freedman, R., 1998. Galileo Probe measurements of thermal and solar radiation fluxes in the jovian atmosphere. J. Geophys. Res. 103, 22929–22978.

Sromovsky, L. A., Fry, P. M., 2010. The source of 3-μm absorption in Jupiter's clouds: Reanalysis of ISO observations using new NH_3 absorption models. Icarus 210, 211–229.

Student, 1908. The probable error of a mean. Biometrika 6, 1–25.

Suleiman, S. H., Kolodner, M. A., Steffes, P. G., 1996. Laboratory measurement of the temperature dependence of gaseous sulfur dioxide (SO_2) microwave absorption with application to the Venus atmosphere. J. Geophys. Res. 101, 4623–4635.

Tillner-Roth, R., Harms-Watzenberg, F., Baehr, H. D., 1993. Eine neue fundamentalgleichung für ammoniak. DKV-Tagungsbericht 20, 167–181.

Townes, C. H., Schawlow, A. L., 1955. Microwave Spectroscopy. McGraw-Hill, New York.

Tyler, G. L., Howard, H. T., 1969. Refractivity of carbon dioxide under simulated Martian conditions. Radio Sci. 4, 899–904.

Ulich, B. L., 1974. Absolute brightness temperature measurements at 2.1-mm wavelength. Icarus 21, 254–261.

Ulich, B. L., 1981. Millimeter-wavelength continuum calibration sources. Astron. J. 86, 1619–1626.

Valdes, F., Welch, W. J., Haber, D., 1982. The Jovian ammonia abundance from interferometric observations of limb darkening at 3.4 mm. Icarus 49, 17–26.

Valkenburg, E. P., Derr, V. E., 1966. A high-Q Fabry-Perot interferometer for water vapor absorption measurements in the 100 Gc/s to 300 Gc/s frequency range. Proceedings of the IEEE 54, 493–498.

van der Tak, F., de Pater, I., Silva, A., Millan, R., 1999. Time variability in the radio brightness distribution of Saturn. Icarus 142, 125–147.

van der Waals, 1873. On the continuity of the gaseous and liquid states. PhD dissertation, Universiteit Leiden, Leiden, Netherlands.

Van Vleck, J. H., Weisskopf, V. F., 1945. On the shape of collision-broadened lines. Rev. Mod. Phys. 17, 227–236.

von Zahn, U., Hunten, D. M., Lehmacher, G., 1998. Helium in Jupiter's atmosphere: Results from the Galileo probe helium interferometer experiment. J. Geophys. Res. 103, 22815–22829.

Wagner, W., Pruß, A., 2002. The IAPWS formulation 1995 for the thermodynamic properties of ordinary water substance for general and scientific use. J. Phys. Chem. Ref. Data 31, 387–535.

Waters, J. W., 1976. Absorption and emission by atmospheric gases. In: Meeks, M. L. (Ed.), Methods of Experimental Physics. Vol. 12B. New York Academic Press, New York, NY.

Weidner, R. T., 1947. Microwave spectrum of iodine monochloride at 4.5 centimeters wavelengths. Phys. Rev. 72, 1268.

Weiland, J. L., Odegard, N., Hill, R. S., Wollack, E., Hinshaw, G., Greason, M. R., Jarosik, N., Page, L., Bennett, C. L., Dunkley, J., Gold, B., Halpern, M., Kogut, A., Komatsu, E., Larson, D., Limon, M., Meyer, S. S., Nolta, M. R., Smith, K. M., Spergel, D. N., Tucker, G. S., , Wright, E. L., 2011. Seven-year Wilkinson microwave anisotropy probe (WMAP) observations: Planets and celestial calibration sources. Astrophys. J. Suppl. Ser. 192, doi: 10.1088/0067–0049/192/2/19.

Young, D. M., Crowell, A. D., 1962. Physical Adsorption of Gases. Butterworths, London.

Yu, S., Drouin, B. J., Pearson, J. C., 2010a. Species tag: 17002 Version 5. URL `http://spec.jpl.nasa.gov/ftp/pub/catalog/doc/d017002.pdf`

Yu, S., Drouin, B. J., Pearson, J. C., 2010b. Species tag: 17004 Version 5. URL `http://spec.jpl.nasa.gov/ftp/pub/catalog/doc/d017004.pdf`

Yu, S., Pearson, J. C., Drouin, B. J., Sung, K., Pirali, O., Vervloet, M., Martin-Drumel, M.-A., Endres, C. P., Shiraishi, T., Kobayashi, K., Matsushima, F., 2010c. Submillimeter-wave and far-infrared spectroscopy of high-J transitions of the ground and $\nu_2 = 1$ states of ammonia. J. Chem. Phys. 133, doi:10.1063/1.3499911, 174317.

Zimmerer, R. W., 1963. Spherical mirror Fabry-Perot resonators. IRE Trans. Microwave Theory Tech. 11, 371–379.

VITA

Kiruthika Devaraj was born in Coimbatore, Tamil Nadu, India. After completing her Bachelor's degree in Electronics and Communication Engineering from PSG College of Technology, Coimbatore, she enrolled at the Georgia Institute of Technology and earned a Master's degree in Electrical and Computer Engineering in May 2009, followed by a doctorate in December, 2011. As a PhD candidate, Kiruthika Devaraj conducted laboratory measurements of centimeter- and millimeter-wavelength opacity of gases under simulated planetary atmospheric conditions.